THESIS

HIGH HEAT FLUX PHASE CHANGE THERMAL MANAGEMENT OF LASER DIODE

ARRAYS

Submitted by

Taylor A. Bevis

Department of Mechanical Engineering

In partial fulfillment of the requirements

For the Degree of Master of Science

Colorado State University

Fort Collins, Colorado

Spring 2016

Master's Committee:

    Advisor: Todd M. Bandhauer

    John D. Williams
    Michael A. De Miranda

ABSTRACT

HIGH HEAT FLUX PHASE CHANGE THERMAL MANAGEMENT OF LASER DIODE

ARRAYS

Laser diodes are semiconductor devices than convert electrical work into light emitted at a specific wavelength over a small spectral bandwidth at a high intensity. A small array of laser diodes can be fabricated on an internally reflective bar that emits light through one edge. If a large number of edge-emitting bars are packed closely together and arrayed to emit light towards the same target, a very high brightness (*i.e.*, light power per unit area) can be achieved, which is useful for a wide range of applications, including advanced manufacturing, inertial confinement fusion energy, and pumping laser gain media. The principle limit for achieving higher brightness is thermal management. State of the art laser diodes generate heat at fluxes in excess of 1 kW cm^{-2} on a plane parallel to the light emitting edge. As the laser diode bars are packed closer together, it becomes increasingly difficult to remove the heat generated by the diodes in the diminishing space between neighboring diode bars. In addition, the wavelength of the laser diode changes with temperature, and minimizing the variation in wavelength among diodes in very large arrays is very challenging. Thermal management of these diode arrays using conduction and natural convection is practically impossible, and therefore, some form of forced convective cooling must be utilized. Cooling large arrays of laser diodes using single-phase convection heat transfer has been investigated for more than two decades by multiple investigators. Unfortunately, either large temperature increases or very high flow velocities must be utilized to reject heat to a single phase fluid, and the practical threshold for single phase convective cooling of laser diodes appears to

have been reached. In contrast, liquid-vapor phase change heat transport can occur with a negligible increase in temperature and, due to a high enthalpy of vaporization, at comparatively low mass flow rates. However, there have been no prior investigations at the conditions required for high brightness edge emitting laser diode arrays: heat fluxes >1 kW cm^{-2} and a volumetric heat generation rate >10 kW cm^{-3}.

In the current investigation, flow boiling heat transfer at heat fluxes up to 1.1 kW cm^{-2} was studied in a microchannel heat sink with plurality of very small channels (45×200 μm) for a phase change fluid (R134a). The high aspect ratio channels (5:1) were manufactured using MEMS fabrication techniques, which yielded a large heat transfer surface area to volume ratio in the vicinity of the laser diode. To characterize the heat transfer performance, a test facility was constructed that enabled testing over a wide range of fluid properties and operating conditions. Due to the very small geometric features, significant heat spreading was observed, necessitating numerical methods to determine the average heat transfer coefficient from test data. The heat transfer correlations were predicted well (mean absolute error, *MAE*, of ±38.7%) by the correlation of Bertsch et al. This correlation was modified to account for the effect of fin conduction, in the calculation of average heat flux, which yielded an improved *MAE* of ±8.1%. The new correlation was then used to investigate a range of potential phase change fluids and an alternative microchannel geometry for the laser diode phase change heat exchanger. Finally, a next generation test section design and operating conditions are proposed which are expected to improve diode array brightness up to 5.3× over the state of the art with R134a. If ammonia is used at the working fluid instead of R134a, the brightness could potentially increase by more than 17× over the state of the art.

ACKNOWLEDGEMENTS

TABLE OF CONTENTS

LIST OF TABLES

LIST OF FIGURES

NOMENCLATURE

Symbol	Description	Units	Dimensionless Number Expression
A_B	Base area	m^2	
A_{ch}	Wetted surface area	m^2	
A_H	Heated surface area	m^2	
$A_{H,act}$	Corrected heated surface area	m^2	
$B_{\bar{X}}$	Bias uncertainty in "x"	-	
Bo	Boiling number	-	$q^{"}/(Gh_{fg})$
Bd	Bond number	-	$(g_a(\rho_l - \rho_v)D_h^2)/\sigma$
Br	Simplified brightness	W m^{-2}	q_{He}/A_{unit}
Co	Confinement number	-	$[\sigma/(g_a(\rho_l - \rho_v)D_h^2)]^{1/2}$
C_p	Heat capacity at constant pressure	J K^{-1}	
D_H	Hydraulic diameter	m	$4A_{ch}/P_{ch}$
e_a	Approximated error	-	
f	Friction factor (Darcy)	-	$\dfrac{2dPD_h}{\rho u^2 L}$
G	Mass flux	kg m^{-2} s^{-1}	
GCI	Grid-convergence index	-	
h_{fg}	Latent heat of vaporization	J kg^{-1}	
h_f	Frictional head loss	m	
h	Heat transfer coefficient	W m^{-2} K^{-1}	

Symbol	Description	Units	Dimensionless Number Expression
h_t	Enthalpy	J kg^{-1}	
I	Current	A	
K	Thermal conductivity	W m^{-1} K^{-1}	
L	Length	m	
M	Fin parameter	m^{-1}	
$\dot{m}$	Mass flow rate	kg s^{-1}	
MAE	Mean Absolute Error	-	
N	Number of channels	-	
Nu_d	Nusselt number	-	hD_h / k
P	Pressure	kPa	
P_{ch}	Wetted perimeter	m	
P_H	Heated perimeter	m	
$P_{H,act}$	Corrected heated perimeter	m	
P_R	Reduced pressure	-	$P / P_{critical}$
Pr	Prandtl number	-	$c_p \mu / k$
$P_{\bar{X}}$	Precision uncertainty in "x"	-	
q	Heat transport rate (power)	W	
q''	Heat flux	W m^{-2}	
Ra	Rayleigh number	–	$g\beta L^3 \Delta T / \nu \alpha_t$
R_e	Electrical resistance	Ω	

Symbol	Description	Units	Dimensionless Number Expression
R_{th}	Thermal resistance	K W^{-1}	
Re_f	Superficial Reynolds number	-	$G(1-\chi)D_h / \mu_l$
Re_l	Liquid-only Reynolds number	-	GD_h / μ_l
Re_v	Vapor-only Reynolds number	-	GD_h / μ_v
S_x	Standard deviation of variable x	-	
SEE	Standard Error of Estimate	-	
t	Thickness	-	
tol	Tolerance	-	
u	Velocity	m s^{-1}	
U_R	Uncertainty in "R"	-	
V	Voltage	V	
$\dot{V}$	Volumetric flow rate	m^3 s^{-1}	
w	Width	m	
We	Weber number	-	$G^2 D_h / \rho_l \sigma$
x	Stream-direction coordinate	m	
X_{tt}	Martinelli parameter (turbulent-turbulent)	-	$(\frac{\mu_l}{\mu_v})^{0.1}(\frac{1-\chi}{\chi})^{0.9}(\frac{\rho_v}{\rho_l})^{0.5}$
X_{vv}	Martinelli parameter	-	$(\frac{\mu_l}{\mu_v})^{0.5}(\frac{1-\chi}{\chi})^{0.5}(\frac{\rho_v}{\rho_l})^{0.5}$
Greek Symbols			
α	Geometric aspect ratio	-	w_{ch} / h_{ch}

Symbol	Description	Units	Dimensionless Number Expression
α_e	Temperature coefficient of resistivity	K^{-1}	
α_s	Statistical significance level	-	
α_t	Thermal diffusivity	$m^2\ s^{-1}$	
β	Thermal expansion coefficient	K^{-1}	
χ	Vapor quality	-	$\dot{m}_v / \dot{m}_{tot}$
ε	Emissivity	-	
γ	Contact angle	°	
η_{fin}	Fin efficiency	-	
φ	Scaling Parameter	-	
μ	Dynamic viscosity	$kg\ m^{-1}\ s^{-1}$	
ν	Kinematic viscosity	$m^2\ s^{-1}$	
ρ	Density	$kg\ m^{-3}$	
ρ_e	Electrical resistivity	$\Omega\ m$	
σ	Surface Tension	$N\ m^{-1}$	
Subscripts			
amb	Ambient		
app	Applied		
au	Gold		
B	Base		
cal	Calibration		

Symbol	Description	Units	Dimensionless Number Expression
CB	Convective boiling		
ch	Channel		
cp	Contact pad		
Di	Diode		
eq	Equivalent		
exp	Experiment		
f	Fluid		
FB	Forced boiling		
H	Heated interface		
He	Heater		
HTM	Heat transfer model		
i	Inner		
int	interface		
l	liquid		
man	manifold		
NB	Nucleate boiling		
NC	Natural convection		
ni	Nickel		
o	Outer		
orf	Orifice		
pt	Platinum		
surf	surface		

Symbol	Description	Units	Dimensionless Number Expression
sat	Saturated		
si	Silicon		
SP	Single-phase		
SS	Stainless steel		
std	Standard		
ti	Titanium		
tot	Total		
TP	Two-phase		
unit	Unit cell		
v	vapor		
web	Web between channels		

1.1. Background

Laser diodes are semiconductor devices than convert electrical work into light emitted at a specific wavelength over a small spectral bandwidth at a high intensity. As shown in Figure 1-1, various layers of dopants are deposited onto a substrate (*e.g.*, GaAs) using semiconductor fabrication techniques to create a p-n junction. In the absence of an external potential applied across this junction, excess electrons (n) and holes (p) are separated by a depletion region at the interface of these two layers, which is called the space charge or active layer. In solid state physics, the band gap is the potential difference between the conduction and valence bands within a material. The valence band is defined as the highest energy state which an electron can occupy in
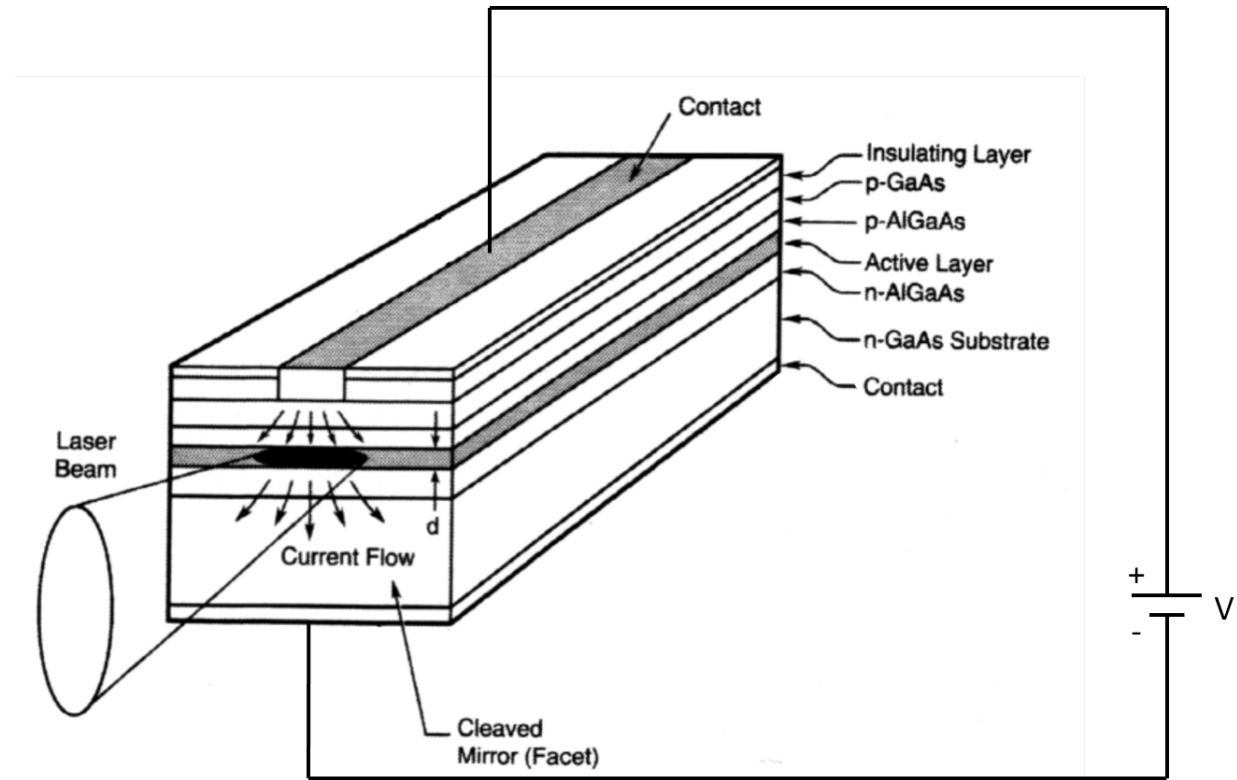
Figure 1-1:   Diagram of a double heterostructure semiconductor emitter [1]

a semiconductor at a temperature of absolute zero; the conduction band is a region of elevated energy states that can contain electrons at all temperatures greater than absolute zero [1]. When a potential is applied across the junction that exceeds the band gap, current is induced, which results in a population inversion of electrons and holes that stimulates the emission of a photon when they recombine in the depletion zone. A forbidden energy region separates the valance and conduction bands that has an extent equal to the band gap energy of the material. The energy of an emitted photon is wavelength dependent, where the frequency required for this stimulation event is equivalent to the bandgap in the material. Because more electrons are in the higher energy conduction band when this potential is applied, additional stimulated emission events occur and yield a light gain. When this phenomenon occurs within an internally reflective cavity, the light intensity becomes very high. To confine this radiation to a particuar cavity geometry a highly reflective second semiconductor material is introduced, typically aluminum gallium arsenide (AlGaAs), in what is termed a double heterostructure. At an external face the surface is cleaved to create a nearly perfect mirror that allows transmission of a fraction of this coherent radiation through the facet. For a gallium arsenide (GaAs) semiconductor material, the emitted radiation can be nominally between 870–900 nm [2].

A small array of individual emitters can be fabricated on an internally reflective bar that emits light through a common edge. Typical dimensions for the laser diode bar are shown in Figure 1-2: a width of 10 mm, a cavity length of 1 mm, and a thickness
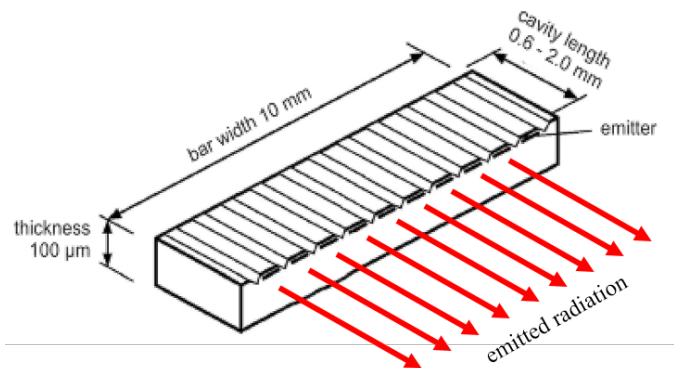
Figure 1-2:   Representative geometry of a single edge emitting laser diode bar with multiple individual emitters [3]

of 100 μm. In this configuration, a potential is applied and current passes through the diode perpendicular to the bar thickness, and heat is generated at the top surface in the figure. Light is generated at a specific wavelength along the entire cavity length, which is internally reflective, and it escapes in a direction that is parallel to the bar width. Once the light leaves, it can pass through optics that focus the beam and direct it towards the target (*e.g.*, a fiber).

One of the many applications for laser diodes is pumping of laser gain media. As compared to flashlamps, which only convert ~1% of their operating power into light usable by laser gain media (*e.g.*, Nd:YAG lasers). In comparison, laser diodes are extremely efficient and they generally operate at an efficiency of 50% [1]. In spite of this high efficiency, however, the thermal management challenges associated with laser diodes operating at high power are very challenging. There are two primary operation schemes for laser diodes: pulsed and continuous wave (CW). Laser diodes operating in CW mode emit light at a constant power output, while pulsed diodes emit light at very high instantaneous rates for a short time duration followed by a rest period. In both cases, thermal management can be difficult. Because of the length of the optical cavity, the amount of light power emanating from a single bar operating in CW mode can exceed 100 W.

Assuming a 50% efficiency, this means that 100 W of heat will need to be dissipated over an area approximately equal to the cavity length multiplied by the bar width. Using the typical dimensions in Figure 1-2, the heat flux can exceed 1 kW cm^{-2}, which is more than an order of magnitude larger than
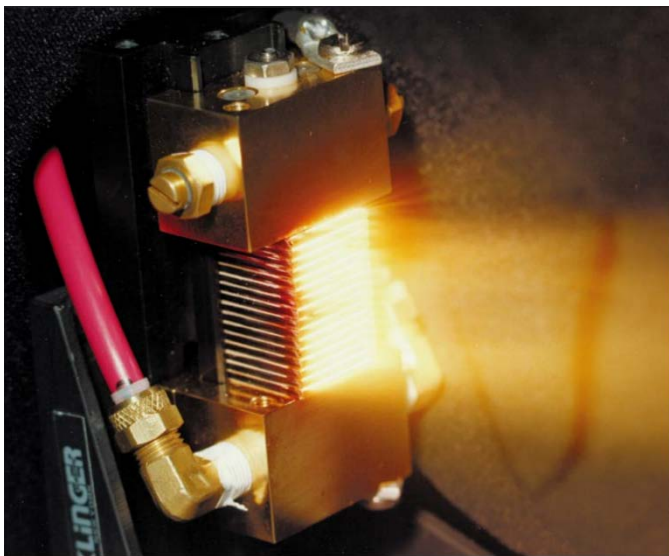
Figure 1-3:   Liquid-cooled laser diode array [4]

heat fluxes emanating from state of the art computer microprocessors. Furthermore, if a large number of edge-emitting bars are packed closely together and arrayed to emit light towards the same target, a very high brightness (*i.e.*, light power per unit area) can be achieved (Figure 1-3). High brightness diode arrays are useful for a wide range of applications, including advanced manufacturing, inertial confinement fusion energy, and pumping laser gain media. Commercially available products from manufacturers such as Northrup Grumman and Coherent can achieve output of 3 kW CW in a 30-bar stack. To attain high brightness on the target, the arrayed laser diode bars must be closely packed together. The spacing between diode bars in the thickness direction is called the pitch. For commercial products the pitch is typically between 2 and 3 mm for high powered laser diodes arrays. Table 1-1 summarizes high brightness diode array reported in the literature, it shows that a pitch of 1.7 mm and a heat flux of 1.49 kW cm^{-2} for a microchannel heat sink was demonstrated by Skidmore et al.; however, their highest efficiency was at 1 kW cm^{-2}, and thus, they only reported thermal performance at this condition [5]. The small spacing and large light power yields a high light intensity, but also causes a very high required volumetric cooling rate (~4 kW cm^3). Increasing the brightness further is highly desirable for many applications, which can be achieved by increasing the power applied to each diode, decreasing the diode bar pitch, or a combination of these approaches, which all exacerbate the already difficult thermal management challenges.

The primary constraints preventing high power operation at low diode bar pitch are peak temperature and temperature uniformity of the across the individual emitters in a large array multiple bars. The wavelength of light emitted from laser diodes changes with temperature at a rate of nominally 0.3 nm K^{-1}. Therefore, the maximum operational temperature of a laser diode is limited to maintain a desired wavelength for a particular application. It is also limited to avoid
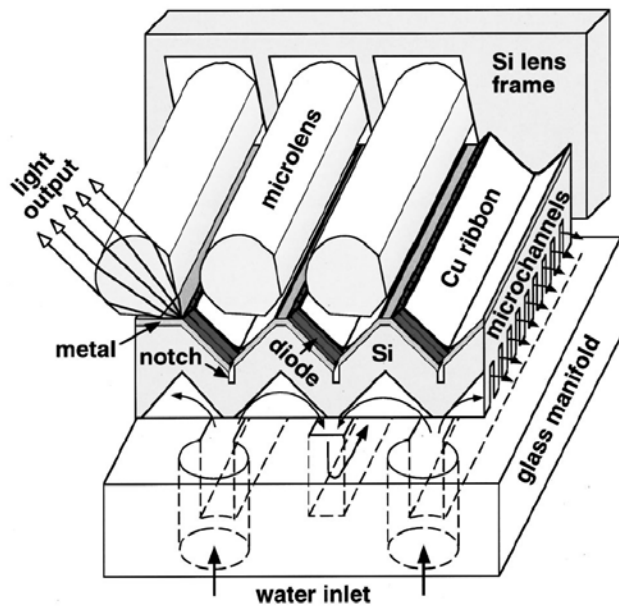
Figure 1-4: Heat sink design from the work of Skidmore et al. [5]

melting adhesives used to mount micro-lenses which focus the emitted light. Furthermore, congregating a large number of bars to increase the directed light power for specific applications makes thermal control even more difficult because the temperature of the emitters can be significantly different from bar to bar. To overcome these challenges, most prior investigations utilize microchannel heat sinks that have a large surface area to volume ratio, and, due to the small dimensions, can yield very high fluid heat transfer coefficients. A state of the art heat sink for a laser diode is shown in Figure 1-4, which utilizes a single phase coolant (water at 10°C) to reject heat from the back side of the laser diode. The diodes were mounted to a "v-grooved" silicon substrate that contained microchannels etched into the bottom surface. During their experiments, they achieved a minimum thermal resistance of 0.32 K W^{-1} per diode bar, at a temperature rise of 32°C while rejecting ~100 W CW [5]. This approach yielded the highest brightness of any laser diode system to date. However, to minimize the temperature maldistribution across an array of diodes, the mass flow rate is large to minimize the temperature rise of the coolant. At high flow rates, local fluid velocity can be high, causing a very large frictional pressure drop and/or increasing the likelihood of surface erosion. Both of these effects can limit the durability of the microchannel heat exchangers. This is perhaps

Table 1-1:   Existing single-phase high power laser diode array cooling studies

Authors (Year)	Description	Heat Flux (W cm^{-2})	Pitch (mm)
Beach et al. (1992) [6]	Microchannels-Silicon, diamond conductors	1000	1.85
Feeler et al. (2008) [7]	Impingement Jets-Ceramic	-	1.5-2.0
Karni et al. (2008) [8]	Microchannels-Copper	1000	-
Roy and Avanic (1996) [9]	Single Channel-Copper	650	~1.4
Skidmore et al. (2000) [5]	Microchannel V-groove-Silicon	1000**	~1.7*

* The authors reported a smaller pitch. However, the diodes were arranged at an angle, and the effective diode pitch is 1.7mm.

** The authors reported a maximum heat flux of 1490 W cm^{-2}, but provided no temperature or heat transfer performance data at this condition.

why no investigation has yielded improved brightness: the spacing and light emissive power are fundamentally limited by thermal management challenges associated with single phase cooling.

Evaporative cooling offers several advantages over single-phase liquid cooling. Single-phase fluids dissipates energy through a temperature rise (*i.e.*, sensible heat). In contrast, an evaporating fluid can reject heat proportional to its latent heat of vaporization (h_{fg}) without a rise in temperature. Also, a liquid will require a substantial increase in temperature to reject the same about of heat as an evaporating fluid because h_{fg} can be very large. For example, water has an h_{fg} of nominally 2,200 kJ kg^{-1} and a liquid specific heat of 4.2 kJ kg^{-1} K^{-1}. Therefore, by setting the temperature rise for a liquid to be 50°C, rejecting the same amount of heat would require a liquid flow rate of >10× that of the two-phase flow rate. As a result, evaporative liquid cooling systems can reject the same amount of heat as a liquid cooling system at a mass flow rate one order of magnitude lower than single phase cooling, potentially lowering fluidic pressure drop and, therefore, pumping requirements. This could allow even smaller channels to be used for laser diode cooling systems, which could enable a decrease in spacing between diode bars to yield unprecedented levels of brightness. Dramatically decreasing the mass flow rate of the cooling fluid

could also potentially reduce erosion, thereby increasing microchannel cooler operational lifetime. Furthermore, the heat rejection from the diode to an evaporating fluid can occur at a single temperature, which can minimize temperature variations across large diode arrays. Finally, convection heat transfer coefficients associated with liquid-vapor phase processes can be 10× higher than for liquids [10-12]. This causes the temperature difference between the diode and the fluid to be reduced, allowing the diodes to operate at much higher power levels at the same temperature.

To increase performance further, many investigators have employed the use of microchannels, which have two desirable effects. First, decreasing the channel size increases the number of possible channels in a given volume, which substantially increases the heat transfer surface area. Second, as the hydraulic diameter decreases, the convection heat transfer coefficient can increase. As shown in Figure 1-5, the channel dimensions need to be very small to facilitate
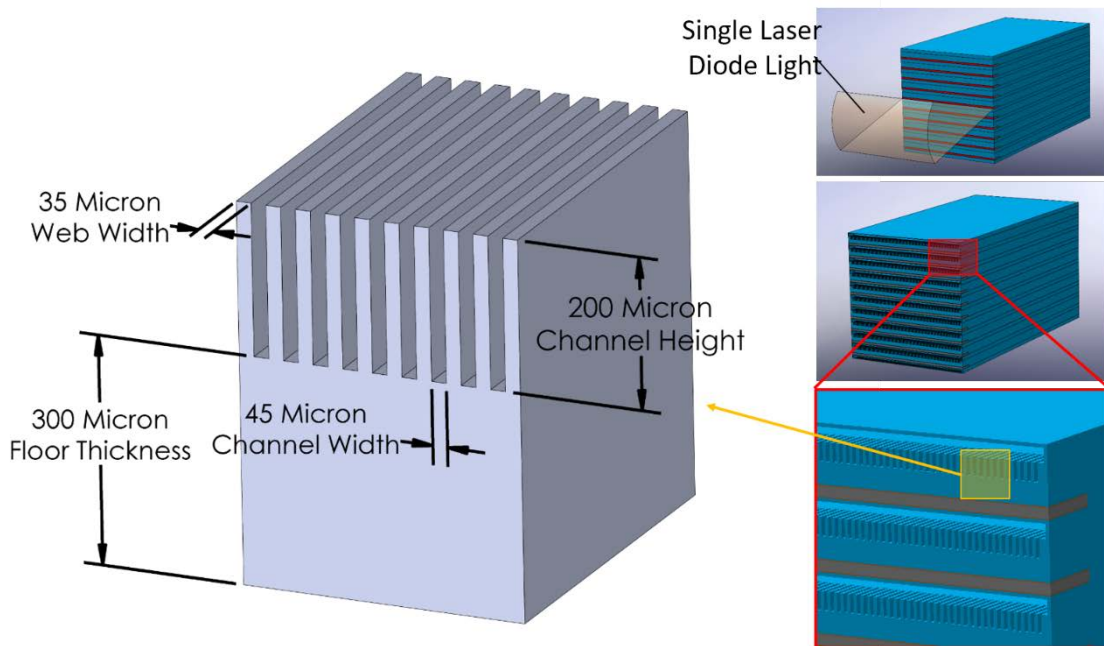
Figure 1-5:   Left: Channel array solid model with representative nominal dimensions and coordinate system; Top-Right: diode array solid model; Center-Right: section view of solid model; Bottom-Right: close-up of section view

small laser diode spacing. For this study, the hydraulic diameter is < 100 μm, which enables a substantial number of channels within the 10 mm diode width.

Liquid-vapor mixtures exhibit numerous flow regimes encountered as the fluid vapor quality increases from zero (all liquid) to unity (all vapor). While these regimes have been classified by many investigators, it has been found that they are highly dependent on geometry, fluid properties, and operating parameters. Furthermore, two-phase heat transfer is limited when the heat transfer surface area is no longer in contact with the liquid. This condition is known as dryout, which is accompanied by a significant rise in the surface temperature because the thermal conductivity of vapor is 10× lower than liquid. The heat flux corresponding to dryout is known as the Critical Heat Flux (CHF). CHF is dependent on many factors, and it is typically found from experiment. Studies have shown that CHF can occur at vapor qualities as low as 5-10% to as high as 80-90%. The purpose of the current work is to characterize the flow boiling heat transfer performance at the very high heat fluxes and small hydraulic diameters applicable to laser diodes. To guide the current research, specific targets for the laser diode operation with microchannel liquid-vapor phase change coolers were developed. These are discussed in the next section.

1.2. Target Performance

The current work represents the first part of a multi-year heat sink development effort to yield a 10× increase in brightness over the existing state of the art diode array. As shown in Figure 1-6, the work conducted by Skidmore et al. yielded a diode power of 100 W per bar for a temperature rise of 32°C, at an effective diode pitch of 1.7 mm. The target of this research is to establish a path toward doubling the diode power to 200 W per bar while decreasing the diode pitch to 0.34 mm, and minimizing the temperature rise. Laser diodes are able to operate at higher power if properly cooled, or operated in a pulsed operation; for example, a peak power of 500 W
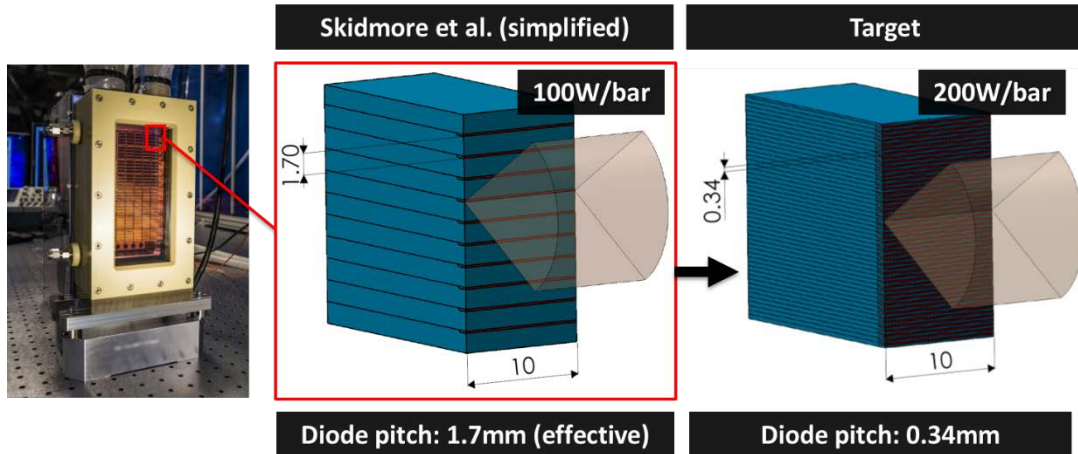
Figure 1-6: Comparison of laser diode arrays; Skidmore et al. is reduced to a planar model (center) of a sample laser diode array (left) [14] for comparison with the target of >10× increase in brightness in the current study (right).

was achieved by Traub et al. for a polymer welding application [13]. By increasing the continuous wave power per diode bar by 2× and decreasing the spacing by 5×, one can realistically increase brightness by 10× relative to the state of the art. These conditions would yield a heat flux of 2 kW cm^{-2}, and a volumetric cooling capacity of 13.3 kW cm^{-3}. In this investigation, it has been shown that a peak heat flux of 1.1 kW cm^{-2} was achieved in a controlled heat transfer experiment with R134a flowing through 45 μm × 200 μm rectangular channels while the diode temperature was maintained at an average temperature of 60°C. Using the data collected here, a path toward meeting the ultimate heat flux and volumetric cooling rate objectives has been established. In the following section, the organization of the remainder of this thesis is presented.

1.3. Thesis Organization

In the following chapters, the design, fabrication, testing, and analysis of a prototype two-phase heat sink geometry are presented. Using the experimental data collected on this device, a correlation that best predicts the heat transfer performance was developed. The current effort has improved the ability to predict performance of two-phase liquid-vapor phase change heat sinks for

fluid flowing through channels with small hydraulic diameters and subjected to very high heat fluxes. As a result, this allowed new fluids and geometries to be proposed for future investigation.

This thesis is organized as follows. Chapter Two includes a review of literature on two-phase microchannel cooling with a specific emphasis on high heat flux cooling relevant to laser diode applications, which motivates the current work at the appropriate scale and operating conditions. Chapter Three discusses the design of the prototype test sections, and the test facility built to characterize heat transfer performance, and the method of establishing the test conditions. This includes a discussion on the Micro Electrical Mechanical Systems (MEMS) fabrication techniques used to manufacture the prototypes used in the experiments, the details of the test facility, and an estimation of the environmental heat transfer loss from the test facility. Chapter Four presents the data analysis reduction techniques used to extract the average flow boiling heat transfer coefficient from the data collected. Due to a few limitations of the test section, an iterative numerical solution is required to calculate the heat transfer coefficients, which is descried in detail. Chapter Five presents a summary of the experimental test data and describes trends in the heat transfer coefficient data, which is followed by an assessment of the uncertainty in measured and calculated values, and a comparison to existing flow boiling correlations. A new correlation is then proposed, which was used to explore alternative operating parameters, working fluids, and microchannel geometry that warrant further investigation. Concluding remarks about the current work and implications for laser diode cooling is given in Chapter Six. Cited references are given in Chapter 7. In the Appendix A, additional details regarding the design of the thin film heater are presented. In Appendix B, documentation and operating procedures for the test facility and instrument calibration are presented. Finally, in Appendix C a representative calculation for a sample data point to evaluate existing flow boiling and pressure drop correlations is presented.

CHAPTER 2. LITERATURE REVIEW

Microchannel cooling has been the subject of significant research for the past few decades [15-19]. As advances in electronics and photonics have led to increased heat transfer rejection rates through diminished surface area, there have been many investigations that focus on improving convective single-phase cooling in microchannel geometries [5, 20, 21]. Studies have also shown that flow boiling in microchannels can offer improved performance over single phase cooling [18, 22, 23]. However, it has been shown that the heat transfer characteristics for flow boiling at the microscale are different than observed at the macroscale, and none of these investigations have been applied to conditions that are relevant to laser diode cooling: very high heat fluxes in small geometries [18, 23-25]. Many experiments have shown that local heat transfer is dependent on fluid properties, operating conditions, and geometry. Because analytical and numerical models have been used with limited success, flow boiling heat transfer coefficients are primarily predicted with empirical correlations developed from experimental data, and extrapolating these correlations beyond the range of conditions used to develop them can lead to significant errors [26, 27]. Prior to the present investigation, neither the required geometric scale ($D_H < 100$ μm) nor the heat flux ($q'' > 1$ kW cm^{-2}) required for laser diode applications have been studied in the literature for two-phase flows.

In this chapter, a review of existing literature on two-phase flow boiling in microchannel geometries is presented. General flow characteristics observed at these scales are discussed first, followed by a detailed review of prior microchannel flow boiling investigations. This chapter ends with a discussion of the focus of the present study, after the critical research needs for two-phase laser diode cooling are identified.

2.1. Flow Characteristics in Microchannel Flow Boiling

Flow boiling heat transfer has been shown by previous investigators to depend on geometry, test fluid transport and thermodynamic properties, heat flux, and local vapor quality [10, 29, 30]. Changes in these parameters affect the distribution of liquid and vapor, which impacts the interfacial shear between the two phases, and the shear of the surface being cooled. In addition to bubble nucleation and growth, the interaction between the two phases drives the rate of heat transport to the fluid mixture. The distribution of the two phases are often characterized by flow regimes, and the conditions which produce each are plotted on an operational map (Figure 2-1). At the macroscale, gravitational body forces can be significant, while surface tension forces are negligible. However, as the channel hydraulic diameter is reduced, surface tension forces can dominate gravity, and, in some cases, inertial forces can be significant at high liquid and vapor velocities. Consequently, numerous investigators have found that the existing macroscale flow regime maps are inaccurate at the microscale, and, as a result, several studies have developed new flow regime maps for flow through microscale geometries [18, 23, 28, 31]. However, it is
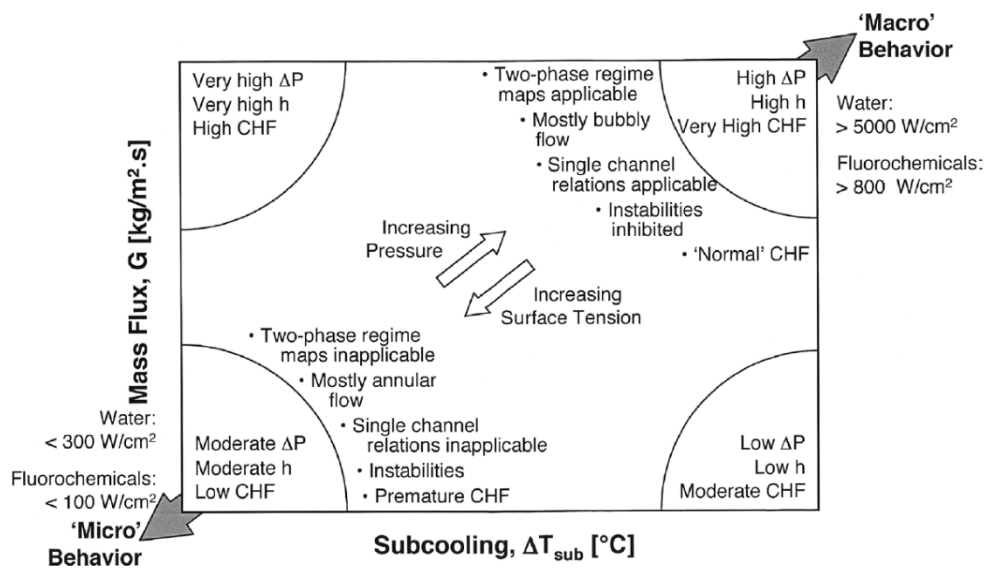
Figure 2-1:   Macro vs. micro comparison operational map [28]

12

uncertain if these maps are applicable to the geometry, hydraulic diameter, and applied heat flux used in the present study. As shown in the following discussion, the flow regime has a strong influence on heat transfer performance.

In general, there are two dominant heat transfer mechanisms for flow boiling in microchannels[1]: nucleate boiling and forced convective boiling [15]. When the wall superheat is higher than the saturation temperature of the fluid, vapor bubbles can nucleate on the surface, and the size of the vapor bubbles are dependent on many factors, including surface roughness, fluid properties, and applied heat flux [32]. Bubble nucleation, growth, and detachment into the bulk flow is associated with very high rates of heat transfer. In forced convective boiling, heat is transferred from the wall through the liquid film on the surface. Instead of continually increasing the temperature of the fluid, as is the case in sensible heat transfer, heat is dissipated by generating vapor at the liquid-vapor interface. The rate of vapor generation is strongly dependent on the fluid shear between the two phases. Harirchian and Garimella [18] noted that that the Confinement number (Co) is an accurate way of determining the relative importance of these two heat transfer mechanisms, and is defined as follows:

$$Co = Bo^{0.5} Re = [\frac{g_a(\rho_l - \rho_v)}{\sigma}]^{0.5} \frac{GD_h^2}{\mu} \tag{2.1}$$

The Bond number (Bo) is the ratio of body forces to surface tension forces, while the Reynolds number (Re) denotes the relative importance of inertial and viscous forces. Therefore, Co indicates the relative importance of these forces, and low values are associated with surface tension and viscous dominated flows inside small channels. For $Co > 160$, the vapor is "unconfined" by the

---

[1] In some cases, the wall superheat can be so high that the vapor bubbles are formed prior to the bulk fluid enthalpy reaching the saturated liquid state. In this case, bubbles are formed at the surface, detach, and are re-condensed by the bulk liquid flow. This effect is called subcooled nucleate boiling.

channel, and nucleate boiling is the dominant heat transfer mechanism. Harirchian and Garimella noted that for $Co < 160$, vapor generated during flow boiling forms elongated bubbles that are surrounded by a thin liquid film, which causes forced convective boiling to be the dominant heat transfer mechanism. This type of flow is called "confined" because the vapor cannot freely escape before it is trapped in the channel. In this case, the bulk of energy transport is from the extended thin meniscus region where fluid evaporates at the liquid-vapor interface [33].

As the vapor quality increases, it is possible that the surface of the channel is no longer covered by a thin liquid film, but it instead in direct contact with vapor. This condition is known as dryout. Because vapor has a much lower thermal conductivity that liquid, the rate of heat transfer from the surface decreases substantially. Figure 2-2 shows the classic pool boiling curve that demonstrates the consequences of dryout (transition from point 'C' to 'E'). As the applied surface heat flux increases, the temperature difference between the wall and the bulk fluid increases. Once the onset of boiling occurs, the applied heat flux can increase rapidly without requiring a
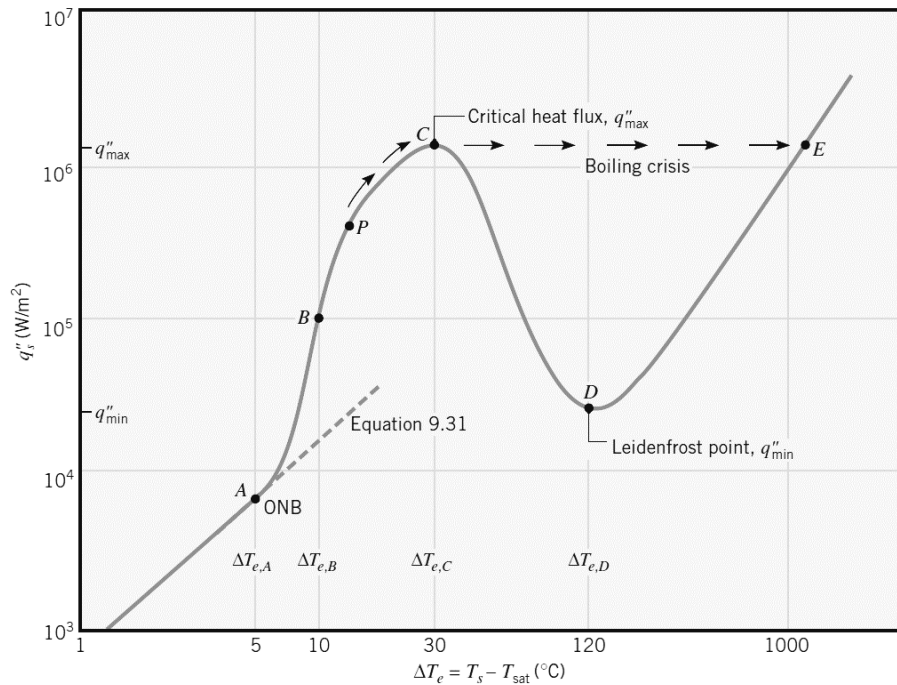
Figure 2-2:   Classical pool boiling curve for water at atmospheric pressure [34]

substantial rise in wall temperature due to the very high heat transfer coefficients associated with nucleate or force convective boiling. However, once dryout ensues, there is a significant drop in the heat transfer coefficient, and, as a result, the wall temperature must increase dramatically to reject higher heat fluxes. If a constant heat flux is applied to the wall, the temperature rise can be so high that it melts the wall material. The location on the boiling curve just before this temperature rise is observed is called the critical heat flux (CHF). For confined flow, this is attributed to the film thickness being comparable to the amplitude of interfacial waves generated by the shear between the liquid and vapor, yielding the so-called Kelvin-Helmholtz interfacial instability [35]. This instability is due to pressure-drop oscillations at the interface and cause cyclic dry-out when the liquid film is sufficiently thin, leading to a decay in heat transfer coefficient [36].

The trend in local heat transfer coefficient vs. flow regime for forced convective boiling is shown on Figure 2-3. After liquid enters the channel, nanoscale bubbles can begin to form at the wall and quickly coalesce, allowing the fluid remains below the saturation temperature. This is known as subcooled boiling, and it occurs at a thermodynamic quality of zero. As the bulk fluid temperature reaches the saturation temperature, vapor bubbles become stable and exist within the flow, eventually aggregating to form slugs of vapor. Because the vapor density is significantly lower than the liquid density, the vapor elongate, which yields transition to an annular flow. When the vapor quality increases, the thickness of the liquid films along the walls decreases, which increases heat transfer. As the vapor quality increases further, the liquid film can periodically disappear, and vapor comes in direct contact with the surface. Eventually this local dry-out is present over the entire surface, and the only liquid left is entrained in the vapor (mist flow). At this point, the heat transfer coefficient plummets and the CHF is reached. Representative images of these flow regimes are shown in Figure 2-4.
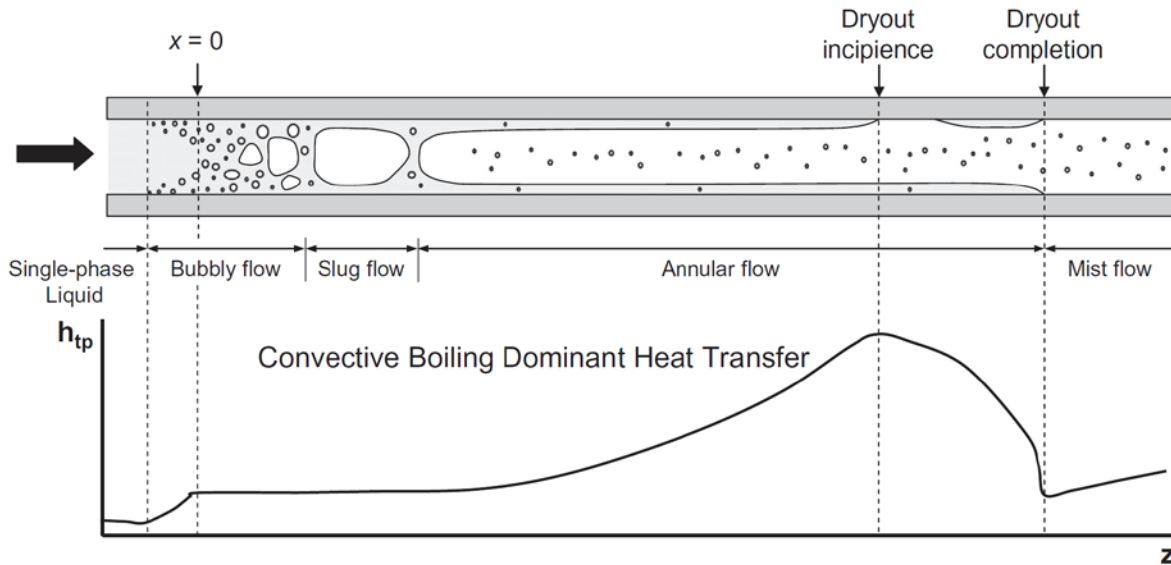
Figure 2-3:   Flow regime vs. heat transfer in convective boiling dominant channels [15]

In addition to heat transfer, the microchannel geometry also significantly impacts the flow stability, especially for multiple parallel channels. As the vapor quality increases during flow boiling in these devices, the growth of bubbles within a single channel can become so rapid that it blocks the flow and causes flow reversal in some cases. This phenomena is problematic as it causes temperature and pressure oscillations in the device, and can lead to partial or full channel dryout. Many investigators have found that the addition of a large pressure drop element at the inlet of each channel prevents flow reversal (Figure 2-5), but at the expense of additional pressure drop [23, 38-41]. However, if no restrictions are added to the channel inlets, the flow can also be significantly maldistributed. In a microchannel heat sink, the flow enters the cooler from a small inlet header which then distributes the flow
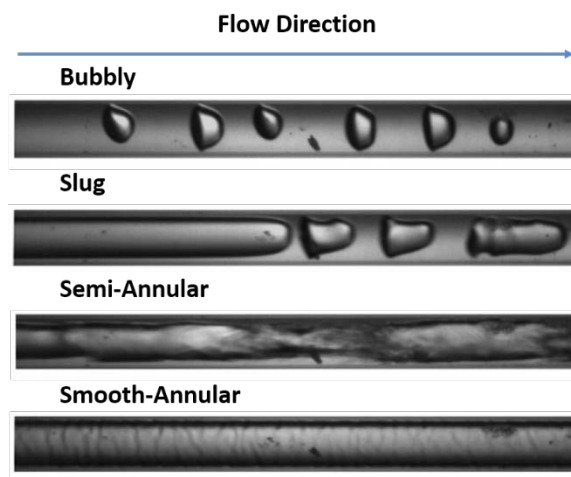
Figure 2-4:   Relevant flow regimes for convective dominant boiling [37]

16

across the array of parallel microchannels. Brandner and Maikowske showed that (without an inlet restriction) this type of arrangement leads to less flow some channels [42]. In their experiments, they noted that the location where the flow transitioned from single phase flow to two phase flow followed a parabolic profile

Figure 2-5:   Inlet restrictions by Szczukiewicz et al. [23]

across the channels, with more mass flow through the center channels. They then showed that (without an inlet restriction) to achieve stable and uniformly distributed flow within the microchannels, a complex bifurcating tree geometry would be required [42]. This result suggests that the simplicity of an inlet restriction to control flow distribution is worth the additional pressure drop.

The choice of working fluid and operating conditions also have a significant effect on heat transfer performance of the heat sink geometry. Prior investigators have studied a variety of working fluids, including water, alcohols, refrigerants, and dielectric fluids. It has been shown that the choice of fluid is a significant factor in determining CHF, with the ratio of liquid to vapor density (*i.e.*, the phase slip ratio) as a key determining factor. Fluids with a high phase slip ratio (water) are more likely to reach CHF at a lower vapor quality than those with a low phase slip ratio (refrigerants).

In summary, many factors can influence the heat transfer characteristics for flow boiling inside microchannels, including geometry, fluid thermodynamic and transport properties, fluid flow rate, and applied heat flux. In the following section, a detailed review of prior flow boiling

heat transfer studies in channel geometries with $D_H < 1$ mm are presented. Thereafter, a summary of the critical needs for flow boiling research relevant to laser diode cooling is presented, followed by an overview of the focus for the current investigation.

2.2. Prior Microchannel Flow Boiling Heat Transfer Studies

To decrease the diode pitch below the state of the art, it is imperative that the channels that contain the boiling fluid are small. Therefore, only prior investigations with channels that have a $D_H < 1$ mm were reviewed, which are summarized in Table 2-1. In the following discussion, observations from these studies are given, as well as a brief review of heat transfer performance prediction methodologies.

As shown in Table 2-1, although there have been many recent investigations for flow boiling heat transfer in microchannel geometries for a wide range of fluids, only one study has achieved a heat flux greater than the magnitude needed for laser diodes (> 1 kW cm^{-2}). In their investigation, Mudawar

Figure 2-6: Image of two-phase burnout in a circular channel from Mudawar and Bowers [43]

and Bowers [43] have reported the largest heat flux rejected in any study to date: 27.6 kW cm^{-2}. This was achieved during a large body of subcooled water boiling experiments in small stainless steel tubes ($406 \leq D_H \leq 2540$ μm). During these experiments, the heat rate was increased until the test section experienced dryout-induced failure at the critical heat flux (Figure 2-6). The water flow rate in these experiment was extremely high, yielding very large fluidic pressure drop: up to 153.4 bar (2,225 psi). In addition, the surface temperature was measured during these tests, and,

Table 2-1: Parallel rectangular microchannel ($D_h < 1$ mm) saturated flow boiling studies

Study [ref]	Microchannel Array Properties					Max q_B''	G [kg m^{-2} s^{-1}]		Working Fluid(s)	Notes
	Mat'l	N	w_{ch} [μm]	h_{ch} [μm]	D_H [μm]	[W cm^{-2}]	Min	Max		
Wang and Peterson [44]	Copper	4	1000	510	675	10	64	257	HFE 7000	Wire mesh added to channel floor; inlet restriction
Kuznetsov et al. [31]	Stainless Steel	10	1500	720	975	16	33	190	R-21, R-134a	Vertical and horizontal orientation
Nascimento et al. [45]	Copper	50	100	500	167	31	400	1500	R134a	
Hetsroni et al. [46]	Silicon	21	250	179	129	33	95	340	Water	Triangular Cross-Section; IR temperature field
Ritchey et al. [47]	Silicon	35	240	370	291	35	890	890	FC-77	5 × 5 individually controllable heaters
Szczukiewicz et al. [48]	Silicon	67	100	100	100	49	283	2370	R245fa, R236fa, R1234ze	Inlet orifices; IR temperature field; 50.3°C heater temperature
Bertsch et al. [49]	Copper	17-33	381 – 762	953 – 1,905	540 – 1090	66	20	350	R134a, R245fa	
Chen and Garimella [50]	Silicon	24	389	389	389	73	70	118	FC-77	5 × 5 heater / temperature array
Lee and Mudawar [28]	Copper	53	235	713	349	100	127	654	R-134a	Compared flow boiling and single-phase in the same test section
Chen and Garimella [51]	Silicon	60	100	389	159	110	254	1015	FC-77	Vapor backflow was present
Li et al. [52]	Silicon	14	250	200	222	115	238	571	Water	Monolithic nanowires grown from channel floor serve as webs/walls
Costa-Patry et al. [53]	Silicon	135	85	560	148	140	499	1100	R245fa, R236fa	
Buchling and Kandlikar [54]	Copper	17 - 25	200 - 400	200	200 - 267	217			Ethanol	Gravity-driven flow; mass flow not given
Qu and Mudawar [55]	Copper	21	215	821	341	217	86	368	Water, R113	Vapor backflow was present; no inlet restriction
Park et al. [41]	Copper	20-29	199	756	315 - 837	350	75	3750	R134a, R236fa, R245fa	Inlet orifices
Kuo and Peles [39]	Silicon	5	200	253	227	444	86	303	Water	Inlet restriction; 0.1 atm to 1 atm pressure

Table 2-1 (Cont.):   Parallel rectangular microchannel (D_H < 1 mm) saturated flow boiling studies

Study (year)	Microchannel Array Properties					Max $q_B^{''}$ [W cm^{-2}]	G [kg m^{-2} s^{-1}]		Working Fluid(s)	Notes
	Mat'l	N	w_{ch} [μm]	h_{ch} [μm]	D_H [μm]		Min	Max		
Kuo and Peles [22]	Silicon	5	200	253	223	643	83	303	Water	Reentrant cavities along the walls; inlet restrictions
Mudawar and Bowers [43]	Stainless Steel	1	n/a	n/a	406 - 2540	27,600	5000	134000	Water	Subcooled boiling; circular tube; high pressure drop; and high temperature
Present Study	Silicon	125	45	200	73.4	1100	735	2230	R134a	Inlet restrictions, IR temperature field

due to the extremely large heat fluxes, the tube temperature approached 800°C in the most extreme cases. Due to the exceptionally high pressure drop and surface temperature observed in this investigation, it is not likely that their approach – very high flow rates in single channel test sections with $D_H > 0.4$ mm – will be sufficient for laser diode cooling, even if scaled to lower heat fluxes. In contrast, distributing the flow into a parallel array of microchannels reduces pressure drop while still maintaining a low thermal resistance. Although no study using this approach has achieved a heat flux > 643 kW cm^{-2}, some key observations from these studies are useful to guide the present investigation.

While inlet restrictions have been shown to stabilize boiling and increase the critical heat flux, more extravagant approaches utilize surface features to enhance nucleate boiling have been employed [23, 38-41]. In a recent study by Li et al. [52], vertically oriented silicon nanowires on the floor of a microchannel
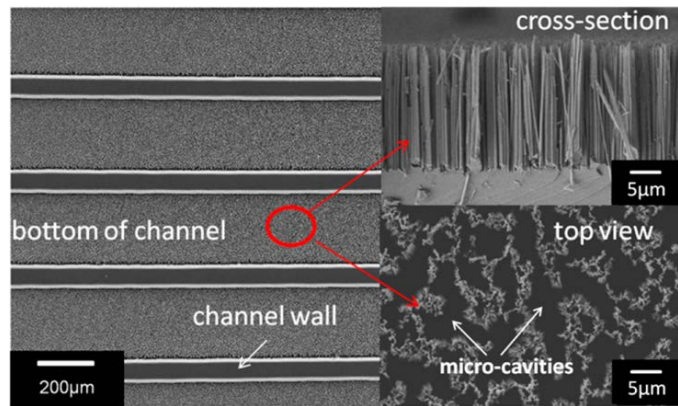
Figure 2-7:   Silicon nanowires grown from channel floor by Li et al. [52]

were shown to enhance heat transfer (Figure 2-7). The silicon nanowires create many micro-cavities that promote nucleate boiling, thus reducing the wall superheat[2] required for the onset of nucleate boiling. By increasing the rate of vapor generation, more bubbles are transported into the bulk flow, where they coalesce and create annular flow. In this flow regime, the thin liquid film interacts with vapor to enhance heat transfer, and pressure and temperature fluctuations are

---

[2] Wall super heat is characterized by the excess temperature which is defined as $T_e = T_{surf} - T_{sat}$

suppressed. The study showed that CHF was increased by 20% compared to a plain, untreated surface [52].

As shown in Table 2-1, the highest heat flux achieved for saturated flow boiling in a rectangular microchannel cooler with multiple parallel channels was 643 W cm^{-2} by Kuo and Peles [22]. Their
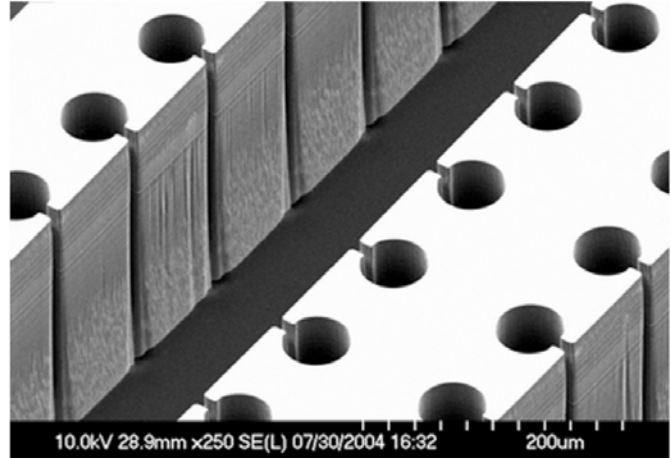
Figure 2-8:   Reentrant cavities along the channel walls by Kuo and Peles [22]

design featured both inlet restrictions for flow stabilization, and reentrant cavities along the channel wall to initiate vapor bubble nucleation (Figure 2-8). It was found that these reentrant cavities increase CHF more than inlet restrictions alone: the same test section without reentrant cavities achieved a heat flux of only 444 W cm^{-2} [39]. In addition to controlling the bubble nucleation size, these reentrant cavities may also cause recurring interruption of the thermal boundary layer, which can enhance heat transfer performance.

Lee and Mudawar [28] have challenged the premise that flow boiling exhibits enhanced heat transfer performance relative to single phase cooling. In their study, they compared flow boiling of R134a to single phase cooling with HFE-7100 in the same microchannel geometry (235 $\times$ 713 µm rectangular channels). During their R134a flow boiling experiments, the CHF was observed at 100 W cm^{-2}, which was primarily due to channel to channel instability. Conversely, single phase cooling with HFE-7100 achieved 840 W cm^{-2} without any problems. However, it should be noted that no inlet restrictions were used in the test section, which suggests that higher CHFs can be achieved by adding these to the channels.

In addition to exhibiting heat fluxes in excess of 1 kW cm^{-2}, it is critical that laser diodes operate at temperatures below nominally 60°C. To achieve a temperatures below this threshold, fluids must operate at a low saturation temperature, and hence low absolute pressure. Although it is an excellent heat transfer fluid, water must operate significantly below atmospheric pressure to achieve this. For example, at a saturation temperature of 10°C, the saturation pressure for water is only 1.23 kPa. Operating at such a low pressure limits the flow rate and channel geometry, necessitating relatively large channels and lower mass flow rates. Moreover, as the vapor quality increases, the frictional pressure drop increases. This further limits the maximum flow rate for flow boiling at conditions relevant to laser diode cooling, because the pressure drop allowed to force the flow through the channels must be lower than 1.23 kPa. Kuo and Peles [39] have studied the effect of decreasing water saturation pressure on heat transfer and critical heat flux. In their experiments, they measured CHF as a function of mass flow rate and vapor quality in a silicon microchannels cooler with a hydraulic diameter of 227 μm over a range of saturation pressures: between 0.1 and 1.0 atm. Their results showed that the low pressure had a minimal effect on the CHF, and they achieved an unusually high outlet vapor quality (0.72) at one set of operating conditions. Unfortunately, the investigators failed to provide surface temperature data, so it is unclear how the heat transfer coefficient would scale from these experiments or how relevant using subatmospheric water would be for laser diode cooling.

Refrigerants tend to have much smaller enthalpies of vaporization than water, which necessitates higher flow rates for the same vapor quality change and heat duty. However, medium and high pressure refrigerants can tolerate larger pressure drops because their saturation temperatures can be much lower than for water at reasonable pressures well above 1 atm. Furthermore, the saturation temperature does not change significantly with pressure for these

refrigerants, and, as a result, flow boiling experiments with refrigerants in microchannels have shown that the outlet vapor quality can approach unity without exhibiting dryout. For example, although it was for low heat flux (22 W cm^{-2}), Bertsch et al. [49] achieved an outlet quality of 0.9 with R134a for flow inside a 148 μm hydraulic diameter channel without experiencing CHF.

The surface area, heat duty, wall temperature, and fluid saturation temperature are required to calculate the heat transfer coefficient from an experiment. Typically, the test sections are electrically heated either by a heater deposited on the surface or joule heating the base material in the test section. The test section heat duty is then calculated by subtracting ambient heat loss from the electrical heat input. In these investigations, the external surface temperature was measured, and in some cases additional thermocouples were located between the heater and microchannel cooler to estimate the local heat flux. The fluid saturation temperature is estimated from the fluid pressure, which is measured at the inlet and outlet to the microchannel array, typically a linear fit is assumed between the two [56]. This is well executed by some authors who have placed static pressure taps directly on their test sections [22, 39, 57]. However, in other investigations, complex manifold geometries are located at the inlet and outlet of the microchannel array. This is significant as the pressure drop through these features typically dwarfs that of the microchannels themselves. Subtracting out the effect of these manifolds is exceedingly complex because of the combination of two-phase pressure drop and pressure recovery from expanding cross-sectional area within a complex geometry. Costa-Patry et al. have deduced pressure drop through their outlet manifold using an intricate combination of numerical models, empirically measured quantities, and assumptions of fluid temperature and vapor quality [58].

A direct measurement of the channel wall temperature in contact with the fluid is challenging, because it is encased within the test section. The approach typically utilized by

previous investigators is to use the measured external temperature and perform a conduction heat transport analysis in the base material to calculate the channel wall temperature. The measurement technique for the external surface temperature used by prior investigators ranges from a single bulk measurement of the heater temperature to discretized thermocouples placed on the test section or an infrared camera that maps the entire surface temperature. Cai et al. [59] measured the wall temperature by calibrating the resistance of the platinum heater with temperature, while Kuznetsov et al. [31] embedded thermocouples in the wall of the test section between the heater and the inside surface of the test section. The purpose of embedding these interim temperature measurements is to estimate the local channel surface temperature. However, in many cases an average heater temperature is used in conjunction with a uniform heat flux assumption. Assuming the latter is problematic because the heat transfer coefficient is expected to vary strongly with flow regime and vapor quality, as shown on Figure 2-3. Therefore, these two conditions cannot simultaneously exist: if the heat flux is uniform then the heater temperature with exhibit significant variation in the stream-direction. Therefore, the channel surface temperatures calculated in this way are inaccurate, which occurred in numerous investigations [22, 31, 46, 49]. For increased external surface temperature resolution, Ritchey et al. and Chen and Garimella utilize a 5×5 array of resistive heating elements to measure the wall temperature [47, 51], and Szczukiewicz et al. [60] used an infrared measurement technique to map in fine detail the external wall temperature of the entire test section. In the study by Szczukiewicz et al. the channel surface temperature was calculated from the local surface temperature and the average temperature rise through the base material assuming a uniform heat flux, which is an improvement over other investigations.

By mapping the wall temperature, it is possible to characterize heat spreading in the test section. For example, Ritchey et al. used their 5×5 array of heating elements (Figure 2-9) to

Flow direction
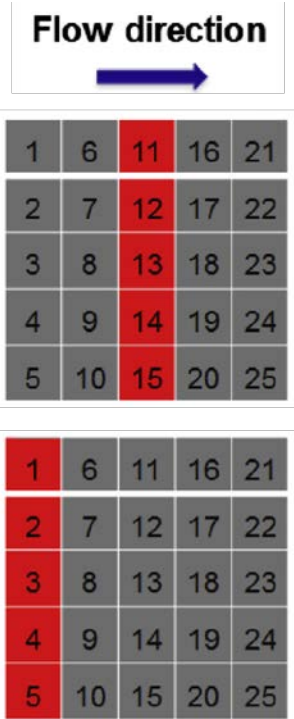
Figure 2-9: 5×5 Heater/RTD array from Ritchey et al. [47]

preferentially heat areas in the test section both in the parallel and across the test section [47]. They determined that non-uniform heat flux had a large effect on the measured heat transfer characteristics. For example, when the heat input was focused laterally across the entire microchannel array near the entrance (Bottom, Figure 2-9), 98% of the heat was transferred within the first 20% of the total flow length. In contrast, when the heat input was shifted downstream to the center of the array (Top, Figure 2-9), only 77.6% of the heat was dissipated over an equivalent area. While it appears clear that heat conduction within the test section plays a crucial role in some experiments, the heat spreading is under predicted by this method. In their study, Ritchey et al. assessed the heat spreading via conduction only at the back surface, where their discrete heaters and RTDs were located, and neglected any heat spreading within the 280 μm thick silicon floor between the heaters and microchannels. As a result, it appears that they over predict the heat dissipated within the area of the heated elements.

In these existing studies described above, the average heat transfer coefficient is calculated from the measured and calculated quantities by some form of the following general expression:

$$h_{TP} = \frac{q_{app} - q_{loss}}{\eta_o A_H (T_{s,ch} - T_{sat})} \tag{2.2}$$

In many cases the investigators have assumed an overall surface efficiency (η_o) of unity (*i.e.*, a uniform channel wall temperature), and have computed an average heat transfer coefficient [22, 49]. While Ritchey et al. and Kuo and Peles claimed to have computed a local heat transfer coefficient, they have inherent error in their data reduction as described above [22, 47].

26

Numerous investigators have developed correlations that fit their experimental data, and a few have even aggregated data from multiple studies to develop more universally applicable correlations [11, 12, 61]. The most notable example was Bertsch et al. [33], who developed a correlation using experimental data from 14 studies with 12 different fluids for a total of 3899 data points. The form of the correlation is the same as proposed by Chen [62], where the effective two-phase heat transfer coefficient correlation is the sum of the nucleate boiling and forced convective boiling effects, with enhancement and suppression factors. Because nucleate boiling can be lowered due the presence of vapor, its contribution multiplied by a suppression factor that reduces nucleate boiling as the vapor quality increases. Due to the difference in density between the two phases, interfacial shear increases, and, as a result, the forced convective boiling term is multiplied by an enhancement factor. While this correlation is developed for a wide range of fluid properties, mass fluxes, heat fluxes, and hydraulic diameters and predicted all of the data within a *MAE* of ±30%, the target heat flux in the present investigation exceeds their highest data point of 115 W cm^{-2} by an order of magnitude and at a hydraulic diameter less than half of their smallest (160 μm). Extrapolation to these conditions is uncertain, and further investigation is warranted.

This model, and all others to date, correlates the heat transfer coefficient to an average heat flux, which is based on the total heated channel surface area as follows:

$$q_H^{"} = \frac{q_{app}}{A_H} = \frac{q_{app}}{N(w_{ch} + 2h_{ch})L_{ch}} \tag{2.3}$$

This formulation is inaccurate in cases where the fin efficiency is less than unity, and this formulation under predicts the effective heat flux. In most cases, investigators have determined the heat transfer coefficient while including the effect of surface efficiency. However, in all cases, they correlate the data to the normalized average heat flux which neglects this effect. This is especially problematic for investigations which have used materials with low thermal conductivity,

27

such as stainless steel, had narrow/long fins geometry, or achieved a high heat transfer coefficient. All of these conditions are prevalent within the large databases of existing studies, and this effect is not captured by current models.

Purely analytical models are still in the early stages of development due to the complex nature of microscale fluid flow and heat transport. Recently, Zhang et al. [35] developed a separated flow model based the work of Revellin and Thome [63] to predict saturated flow boiling heat transfer, and this model showed excellent agreement with experimental data. In addition to mass, energy, and momentum balances on the liquid and vapor phases, they accounted for surface tension forces using the Young-Laplace equation. The primary limitation of their model is that it does not simulate subcooled nucleate boiling: bubble formed at a calculated critical size and suddenly expand into the bulk flow. Even with this assumption, the predicted pressure drop and heat transfer coefficients compared favorably to the experimental data presented by Qu and Mudawar [55] (*MAE* of ±5.89%). It remains to be seen if this type of approach can be applied to different experimental conditions, and flow regimes.

2.3. Critical Research Needs for Flow Boiling Thermal Management of Laser Diodes

As mentioned previously, the required heat flux for laser diode cooling is very high, and the temperature limit of practical laser diode systems is nominally 60°C. Furthermore, the surface area of laser diodes is very small: the length and width of a typical laser diode bar are 10 and 1 mm, respectively. As a result, the heat transfer coefficient and heat transfer surface area both need to be large to utilize fluids with reasonable saturation temperatures. For example, at a heat flux of 1 kW cm^{-2} and a temperature difference of 50 K between the diode and fluid saturation temperature, the effective heat transfer coefficient required is 200,000 W m^{-2} K^{-1} over the 0.1 cm^{-2} laser diode bar. Flow boiling heat transfer coefficients reported in literature have been as

high as 50,000 W m^{-2} K^{-1} [10]; therefore, a surface area increase of 4× would be needed to reject this heat from the laser diode across a temperature difference of 50 K. This would be achievable with 40 μm wide channels and 40 μm thick and 160 μm tall fins (125 total) with a fin efficiency of at least 88% for silicon (assuming an adiabatic tip). Unfortunately, as shown in Figure 2-10, there have been no studies in the literature that investigate flow boiling heat transfer for channels with dimensions smaller than 100 μm subjected to heat fluxes in excess of 1 kW cm^{-2}. In addition, the inlet fluid temperature in some cases was either far below 0°C, which may be impractical for some portable laser diode systems due to the need for an electrically powered chiller or causing unwanted condensation on the surface of the laser diode emitter, or have surface temperatures that exceed 100°C, which would drastically shift the emitted radiation wavelength and/or soften the epoxy holding the necessary optics. Therefore, flow boiling heat transfer studies in channels with $D_H < 100$ μm subjected to heat fluxes above 1 kW cm^{-2} for fluids with saturation temperatures ranging from 0°C to 60°C are warranted.

Furthermore, due to the large surface area-to-volume ratio required for laser diode heat sinks, it is anticipated that thermal conduction will have a significant impact on performance, as noted by Richey et al. [47]. The heat transfer coefficient profile in the stream direction, from single phase heat transfer up to the initiation of flow boiling, is expected to produce a non-uniform heat flux into the test section, which is contrary to the analysis of other investigators. Furthermore, the heat transfer coefficients for flow boiling can be very large, which can reduce fin efficiency, even for short fins. As a result, the channel surface temperature that the boiling fluid is exposed may be significantly non-uniform, which is in contrast to the uniform temperature assumption made by previous investigators. Accounting for these temperature variations are critical to measure flow boiling heat transfer coefficients accurately, and, without accounting for heat conduction in
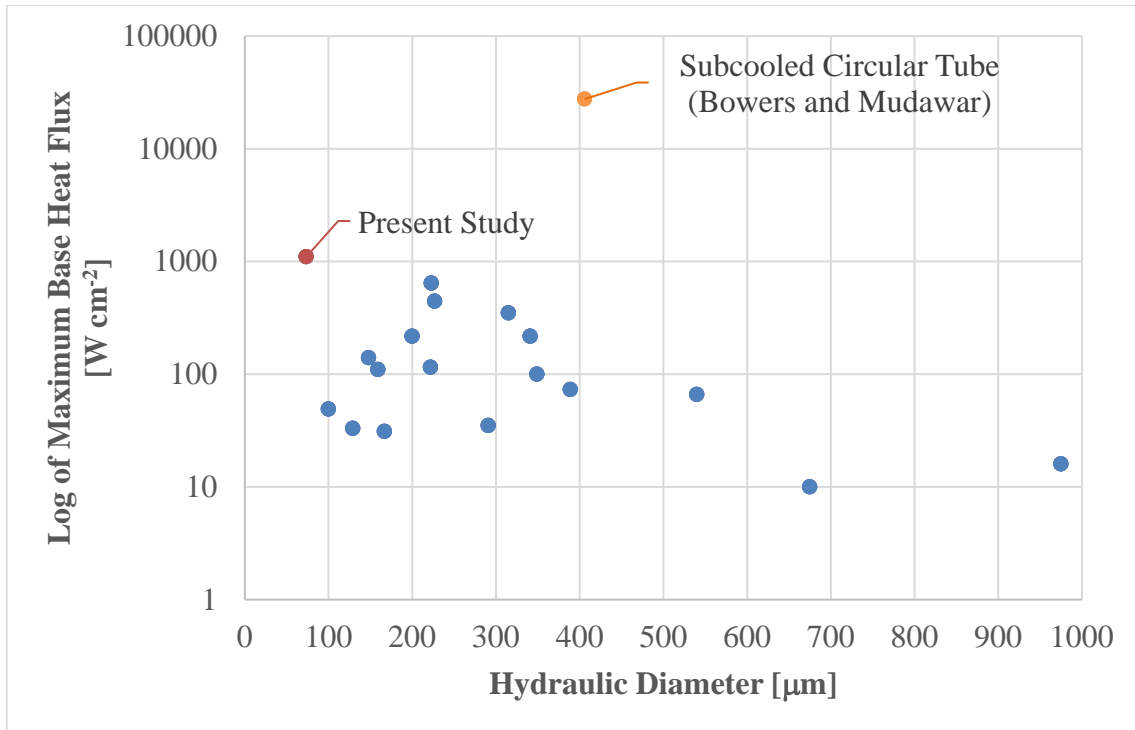
Figure 2-10:   Summary of parallel rectangular microchannel (D_H < 1 mm) saturated flow boiling experimental investigations: maximum heat flux achieved vs. channel hydraulic diameter

the microchannel substrate, it will be challenging to make coherent recommendations that improve microchannel heat sink performance.

2.4. Focus of Current Investigation

The purpose of the current study is to experimentally investigate flow boiling heat transfer characteristics for a medium pressure refrigerant (R134a) flowing in a microchannel heat sink with a D_H = 73.4 µm and subjected heat fluxes up to and greater than 1 kW cm^{-2}. Furthermore, because laser diode temperatures are limited, the temperature and flow rate of the refrigerant is adjusted so that a surrogate heater maintains a surface temperature < 60°C. The experimental results are then analyzed to calculate the effective two-phase heat transfer coefficient during flow boiling so that an accurate correlation can be developed, which will inform future design paths to improve the

ability of future microchannel heat sinks to absorb even higher heat fluxes. The following are the specific objectives for the current investigation:

- Accurately measure the overall heat transfer performance of a representative prototype silicon microchannel heat sink that contains 125 parallel channels that are nominally 45 μm wide and 200 μm tall, each separated by a 35 μm wide fin. Using a metal heater (10 mm × 1 mm) deposited onto the test section to serve as a surrogate for a laser diode, determine the maximum heat flux allowable for a surrogate heater temperature of 60°C over a range of flow rates (50 – 150 g min^{-1}) and saturation temperatures (15°C to 25°C) for a R134a test fluid.

- Using the gathered experimental data, calculate the two-phase heat transfer coefficient as a function of the input variables: heater current and voltage, fluid and surface temperature, fluid pressure, and location of transition from single-phase to boiling. Develop a method that accurately accounts for heat spreading in the test section, both temperature and heat flux non-uniformity. Compare the experimentally measured heat transfer coefficients to correlations available in the literature. Develop a new correlation that accurately predicts the data collected in the current study, using a corrected average channel heat flux.

- Use the experimental results and new correlation to recommend alternative heat transfer fluids and microchannel dimensions that can surpass the performance of the microchannel heat sink in the present study, and approach the targeted 10× improvement in diode array brightness.

In the next chapter, the experimental setup and procedures used to accomplish these objectives are discussed in detail.

CHAPTER 3. EXPERIMENTAL SETUP AND PROCEDURES

As discussed in the previous chapter, flow boiling in microchannels has not been characterized at the scale and heat fluxes required for laser diode cooling. In this chapter, the experimental facility and testing procedures used to measure flow boiling heat transfer coefficients inside 45 μm × 200 μm channels subjected to a base heat flux in excess of 1 kW cm^{-2} are described in detail. In the following sections, the fabrication and feature details of the test section used in the present study are described first, followed by a description of the test facility and the technique used to incorporate the test section into the facility. Because the wall temperature is a critical parameter required to calculate the boiling heat transfer coefficient, the system used to measure the heater and test section surface temperatures is then described in detail. Next, the test matrix executed in this study is described. In the last portion of the chapter, the methodology to establish the test condition is given, including sample calculations of the test section heat duty and outlet vapor quality and their associated uncertainties. With these critical parameters established, the flow boiling heat transfer coefficient can be calculated, which is described in Chapter 4.

3.1. Test Section Design and Fabrication

A picture of the microchannel test section used in the current study is given in Figure 3-1, which was fabricated at Lawrence Livermore National Laboratory (LLNL) using silicon MEMS fabrication techniques. The test section contains a plurality of high aspect ratio channels, and, to enable in-situ flow visualization and create a hermetic seal, a glass wafer bonded to the top surface of the silicon. As shown in the figure, the fluid enters an inlet hole etched through the silicon, and then is distributed to the channels in a manifold with five support features. Once the fluid exits the
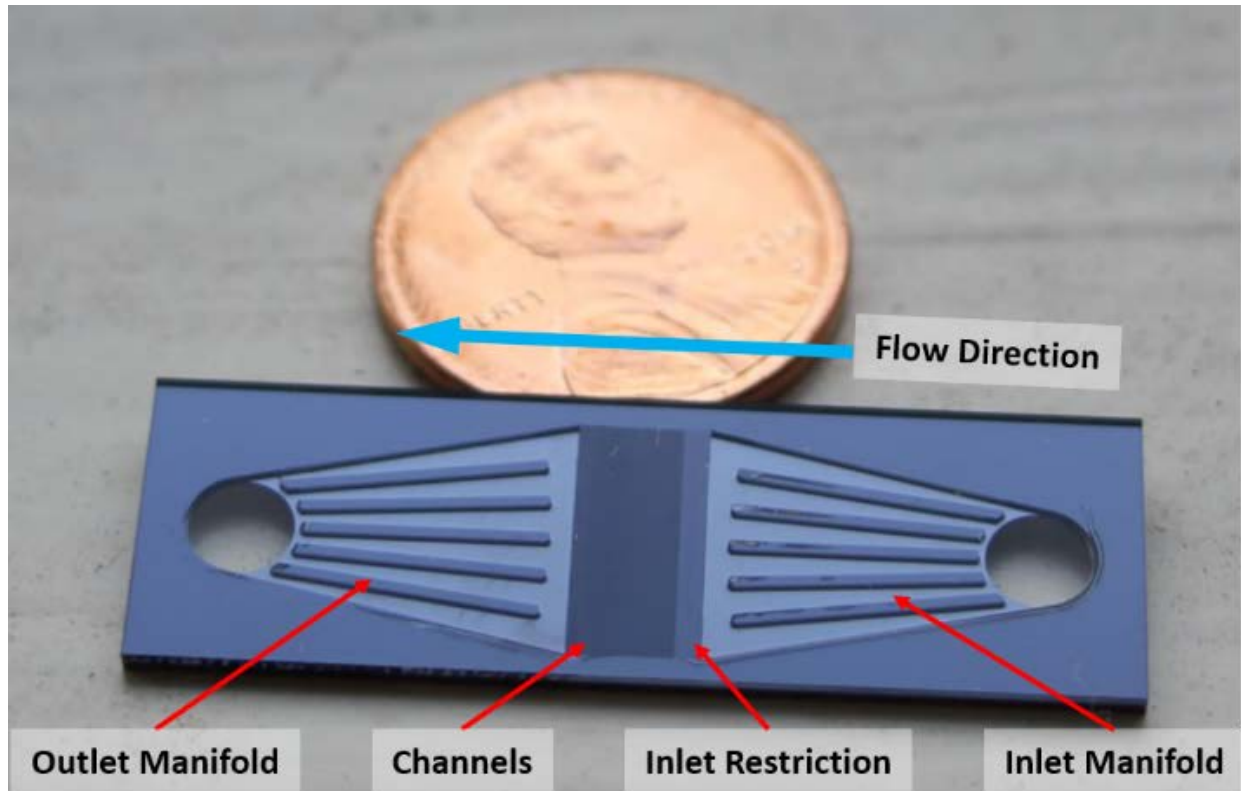
Figure 3-1:   Front view of the test section (penny for scale)

channels, it is redistributed in the outlet manifold and outlet hole. Similar to prior investigations, each channel contains a narrow section at each channel inlet to improve flow distribution and prevent backflow.

Heat input is provided by a thin film resistive heater deposited on the back-side of the test section. As shown in Figure 3-2, the heater has the same dimensions of a typical laser diode: 10 mm wide and 1 mm long. To ensure that joule heating is confined to the heater, 610 nm thick 1 mm^2 electrically conductive contact pads are placed at both extreme ends of the heater. The heater is located in the center of the nearly 5× longer microchannels to ensure that fluid flow is fully developed in the test section, and that the heater is directly below the channels. Using a surrogate heater instead of a laser diode is safer and less expensive, and allows the focus of the current study to remain on characterizing flow boiling heat transfer. This heater and surrounding silicon are coated in a high emissivity paint to enable accurate IR temperature measurement. In
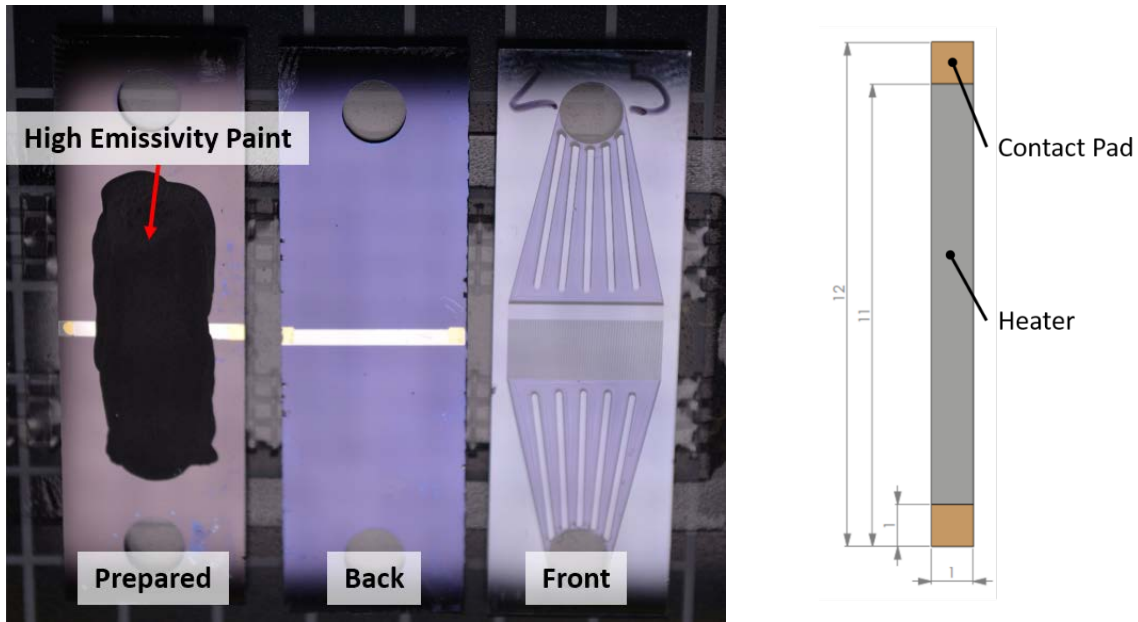
Figure 3-2:   Left: Three views of the test section, showing the high emissivity paint required for an accurate IR temperature measurement; Right: Heater design, dimensions in mm

the following two sections, the fabrication techniques and key geometric features are described in detail.

3.1.1. Test Section Fabrication

The test section channels are fabricated in standard 101.6 mm diameter 500 μm thick silicon wafers, and a 500 μm thick borosilicate glass wafer of the same diameter is used for the capping layer. Due to the size of the wafers, multiple test sections can be fabricated on a single wafer. In this section, the MEMS fabrication processes are discussed in the sequence required to fabricate the test section, which is as follows: (1) clean wafers, (2) mask off areas of the wafer to be protected from etching, (3) etch exposed areas, (4) bond silicon and glass wafers, (5) deposit thin film metal through a mask that defines the heater, and (6) cut into individual test sections.

The first step in fabrication is to clean both the silicon and glass wafers using an RCA cleaning regiment. In this process, organic materials and particulate matter are removed by a first soak in an oxidant, such as a mixture of sulfuric acid and hydrogen peroxide, followed by a second

soak in a mixture of water, hydrogen peroxide, and ammonium hydroxide. The wafers are then quickly dipped in hydrofluoric acid to remove oxides on the surface, if desired. Next, a soak in a mixture of water, hydrochloric acid, and hydrogen peroxide removes any metallic contaminates [64]. Finally, the part is rinsed with water and dried, and the silicon and glass wafers are now prepared for subsequent processing.

Etching is the process of removing material from a solid wafer, and two etching processes are required to create the features in the silicon wafer: one to fabricate the fluid channels, inlet restriction, and inlet and outlet manifolds, and a second to manufacture the inlet and outlet holes. As in standard MEMS fabrication processes, a mask is used to protect the portions of the wafer that are not etched during each process step. The masks consists of a photoresist polymer that is first uniformly coated on the wafer and then selectively cured by exposing portions of it to UV light. As shown in Figure 3-3, this light is projected onto the photoresist coating through a clear mask with chrome deposited on the surface to selectively cure the polymer in a pattern that is an inverse pattern of the etch. The features on the mask are typically 5× to 10× larger than image projected on the photoresist to facilitate manufacturability, and the projection optics determine the final size of the exposure on the photoresist. Once exposed to UV, the uncured photoresist polymer is then chemically removed from the wafer to expose the silicon surface for etching. After etching the channels, inlet restriction, and inlet and outlet manifolds,

Figure 3-3:   Projection lithography used to pattern the photoresist (not to scale)
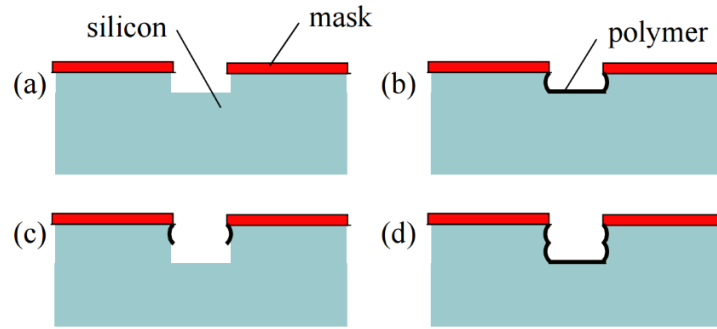
Figure 3-4:   DRIE process flow: (a) etch into silicon, (b) coat new surface in passivation polymer, (c) repeat etch into silicon, (d) recoat in passivation polymer and repeat until target depth is reached [65]

a similar etching process is performed on back side of the silicon wafer to form the inlet and outlet ports.
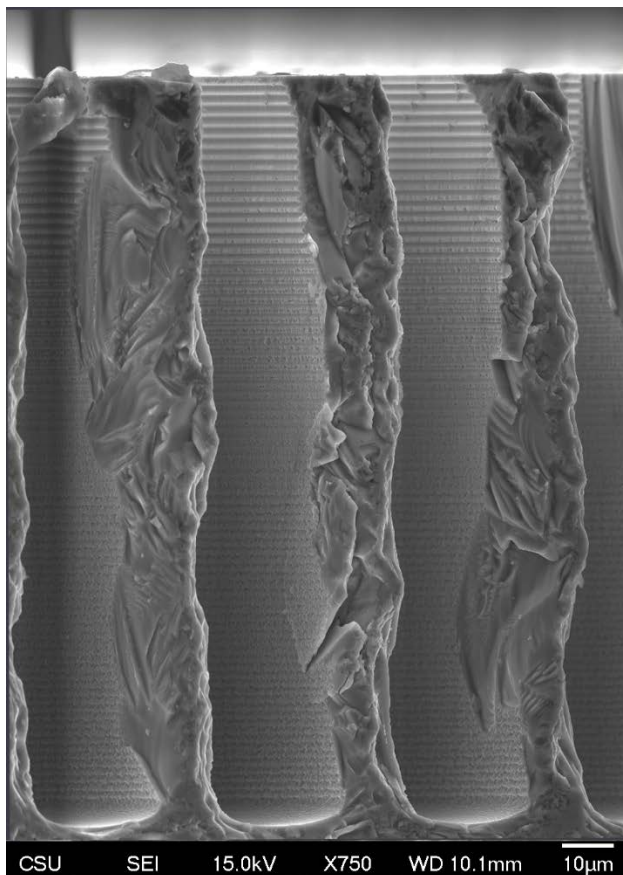
Figure 3-5:   Representative SEM cross section image of 20 μm wide microchannels; the rough edge is due to silicon fracture for sample preparation

As discussed above, it is necessary to have high aspect ratio channels to increase the surface area to volume ratio, and the method used to create these features is the Bosch Deep Reactive Ion Etch (DRIE) process. As illustrated by Figure 3-4, this process employs alternating plasma etching and surface passivation. Etching is accomplished by exciting a low-pressure sulfur hexafluoride (SF_6) into a plasma, then directing a stream of the glow-discharge toward the part. Silicon is removed both by direct sputtering and chemical reaction. In the latter process, ions react with the surface to produce volatile

36

species that are removed by the vacuum pump [64]. This etching process is directional: surfaces which are normal to the plasma source etch faster than those at an angle. Following each etch step, a passivation layer of perflurocyclobutane polymer (C_4F_8) is deposited on the surface. During etching,

Figure 3-6: Schematic of anodic bonding [64]

this coating is rapidly removed from the surface normal to the source, while perpendicular surfaces remain protected for a period of time. These two steps are alternated until the desired depth into the wafer is achieved, creating highly anisotropic features. When the etching process continues past the passivation layer, the silicon is "undercut" leading to a condition known as scalloping (Figure 3-5). Scalloping leaves a rough wavy pattern on the edges parallel to the etch direction, which may be beneficial in some cases due to the increase in heat transfer surface area, which warrants further investigation.

Once the front and back side etches are complete, all of the cured photoresist and any residual passivation polymer are chemically removed from the silicon wafer. The silicon and glass wafers are then anodically bonded together to create a hermetic seal. This process is accomplished by pressing the two wafers together while heating them from both sides and simultaneously applying a large voltage across the wafers (Figure 3-6). At an applied potential of 300 – 700 V, the sodium ions in the glass are repelled away from the interface, and a net charge between the silicon and glass wafers brings the surfaces into intimate contact. At temperatures on the order of 500°C, the two wafers fuse together and create a hermetic bond [64].

Electron beam evaporation
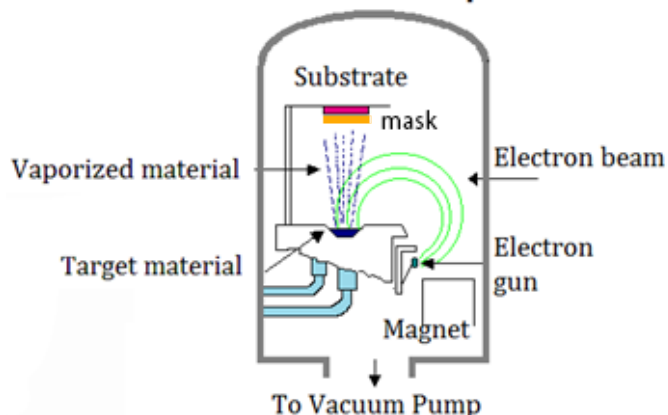
Figure 3-7:   Schematic of an evaporation physical vapor deposition process [66]

The next processing step is metal deposition on the back side of the silicon wafer to create the surrogate laser diode heater. The thin film heater on the back surface of the silicon is added by a physical vapor deposition (PVD) process (Figure 3-7). In this process, a source metal is evaporated from a crucible by heating it with an electron beam. This atomic vapor is then directed toward the target surface through a mask [64], and the metal is then deposited on the surface where it is left exposed. For this process, a direct contact mask was used instead of the photoresist polymer and projection lithography process used for etching, which avoids trapping polymer in the inlet and outlet ports. As shown in Figure 3-8, a direct contact mask is a plate machined to leave through holes for direct access to the wafers for the metal. During this process, the mask itself is also coated in the metal, and, when the mask is lifted off the surface after deposition is completed, the thin film at the mask-wafer interface shears, leaving only the desired pattern of metal. Because the
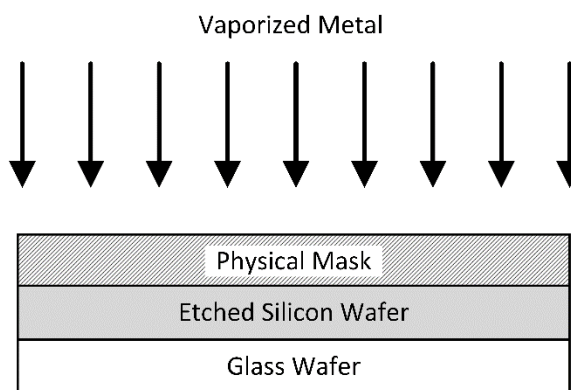
Figure 3-8:   Direct contact masking

heater and contact pads have a different shape, separate masks were required to produce the heater and contact pads. After the heaters and contact pads are deposited, the wafers were diced into

individual test sections using a high speed diamond wheel saw. The following section describes the feature details and a geometric characterization of test section used in the present study.

3.1.2. Feature Details

Figure 3-9 shows a cross-sectional view of test section focused on the etched silicon channels. During operation, liquid phase coolant enters the narrow passages (orifices) at the inlet to each channel. This creates a "bottle-neck" which distributes flow evenly across the microchannel array and prevents backflow, similar to the study by Park et al. [67]. For the present study, the fin thickness is 35 μm, the channel width is 45 μm, and the orifice width is 10 μm. Because etch speed and, therefore, depth is a strong function of feature width, a sacrificial part in the silicon wafer was cut along the stream-direction to measure the depth profile in a digital microscope (Figure 3-10). As feature width decreases, the quantity of plasma that reaches the bottom decreases. Because the entire fluid domain (*i.e.*, channels, orifices and manifolds) was etched simultaneously using a single mask, a nearly 100 μm difference in etch depth occurred between the 10 mm wide manifold and 10 μm wide orifice.
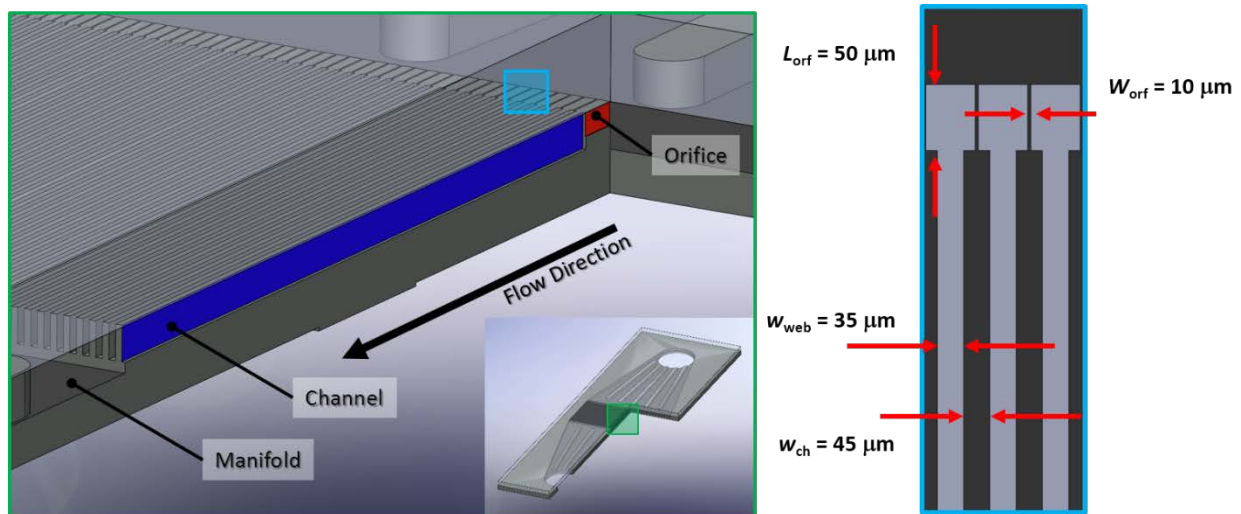
Figure 3-9:   Left: Solid model cross-sectional view of a test section showing depth variation; red is the orifice, and blue is the channel; Right: Top down view of the channel and orifice dimensions
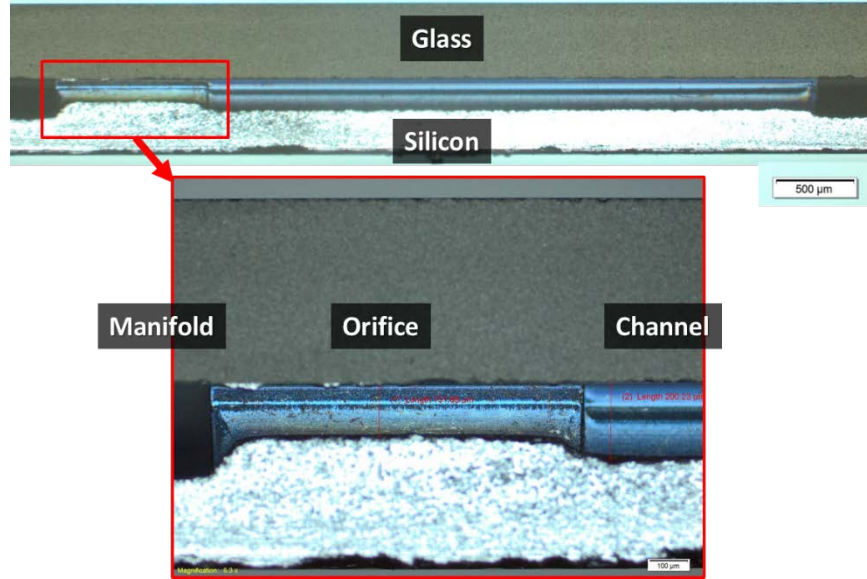
Figure 3-10: Digital microscope image of the test section cut in the stream-direction

To determine the width of the channels and webs between them, a microchannel array sample was cut laterally and inspected in a Scanning Electron Microscope, SEM. An actual test section was not used for this measurement: instead two sections of 20 and 60 μm channel widths at the same 200 μm depth were examined. The channel width was widest at bottom, which was caused by the plasma etching process. At the start of etching, plasma impinges on the surface and residual plasma is swept away. As feature depth increases, the plasma is contained by the side walls, which increases the amount of plasma further down the channel depth. The channels
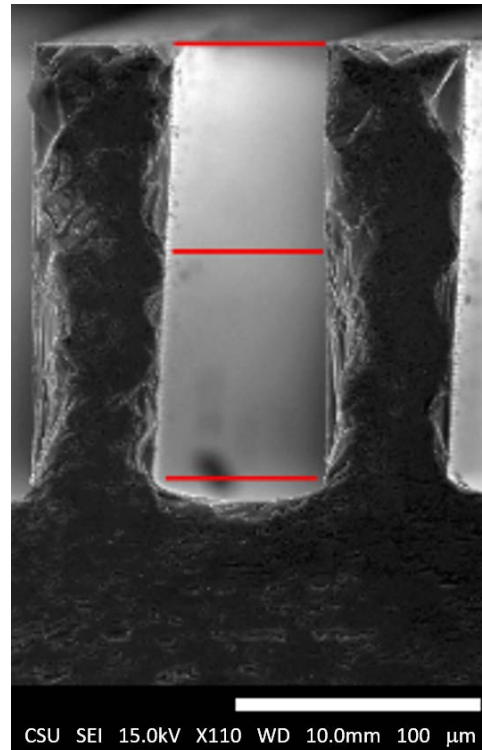
Figure 3-11: SEM image showing channel depth variation on a 60 μm wide channel; all red lines are 60 μm long to show the width variation

40

were both 10 µm wider on average at the bottom for both the 20 and 60 µm channels (Figure 3-11).

Therefore, the average channel width is assumed to be the nominal dimension plus a 5 µm offset.

A summary of all the target and actual dimensions is presented in Table 3-1.

Table 3-1:   Target and average produced dimensions for each fluid feature

Location	Dimension	Design [µm]	Actual [µm]
Manifold	Depth	200	230.00
	Inlet/Outlet Diameter	4,000	*
Channel	Depth	200	200.23
	Width	40	45
	Hydraulic Diameter	66.6	73.4
	Length	4,950	*
Web	Width	40	35
Orifice	Depth	200	131.69
	Width	10	15
	Length	50	*
* Dimension not measured			
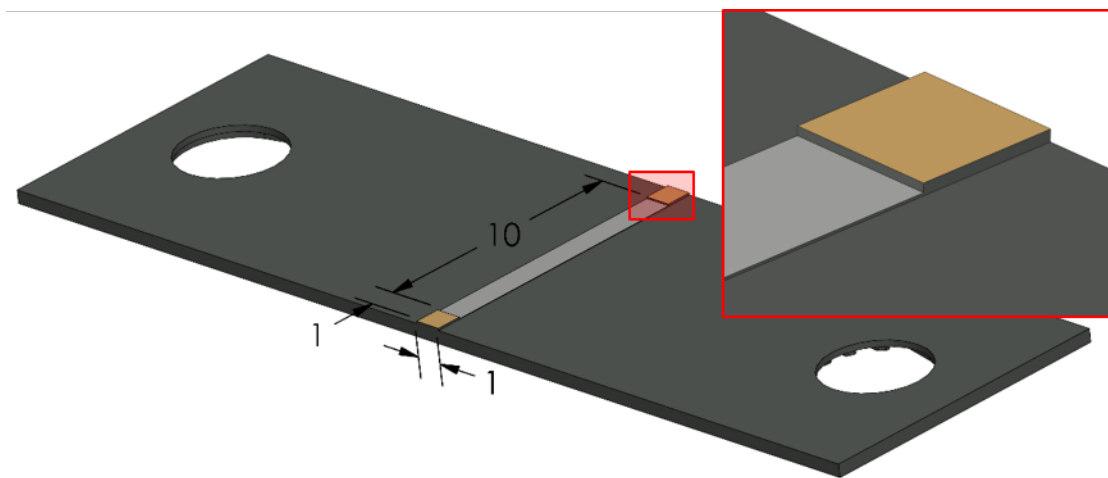
Figure 3-12:   Test section back side with heater and contact pad, dimensions in mm (thickness not to scale)

Table 3-2:   Heater and contact pad layer thicknesses

Layer	Material	Thickness [nm]	Location	Purpose
0	Si		Base Material	
1	SiO_2	~1	Back of Wafer	Electrical Isolation
2	Ti	10	Heater + Contact Pad	Adhesion
3	Pt	200	Heater + Contact Pad	Heater
4	Ti	10	Contact Pad	Adhesion
5	Ni	500	Contact Pad	Electrical Interface
6	Au	100	Contact Pad	Prevent Oxidation

The heater was carefully designed to dissipate heat into the test section at a very high heat flux and to enable accurate measurement the test section heat duty. (A detailed discussion on the design calculations are given in Appendix A.) The heater and contact pad dimensions are summarized in Table 3-2 and Figure 3-12. The various metals are deposited onto the silicon wafer, which is exposed to ambient air at room temperature prior to metal deposition to form a thin silicon dioxide layer (~1nm). Silicon dioxide is electrically insulating, which prevents current applied at the contact pads from short circuiting through the silicon instead of through the thin platinum heater. The heater consists of two layers: 200 nm Pt on top of a 10 nm layer of Ti. The platinum layer is the heater, but it does not adhere well to the silicon dioxide. Therefore, a thin layer of titanium is applied prior to the deposition of the platinum heater because it adheres well to both. The contact pads include these two layers and an additional three layers to decrease electrical resistance and ensure that the nearly all of the joule heating occurs in the platinum heater. The second titanium promotes adhesion of the nickel, and the gold capping layer prevents oxidation of the nickel. The electrical resistance of the contact pads are much lower than the heater, which allows current to spread from the current conducting wires uniformly such that the current distribution is uniform across the platinum heater. This was confirmed by a finite element model, and additional details are given in Appendix A. The following section describes the test facility used to control the test conditions for the test section.
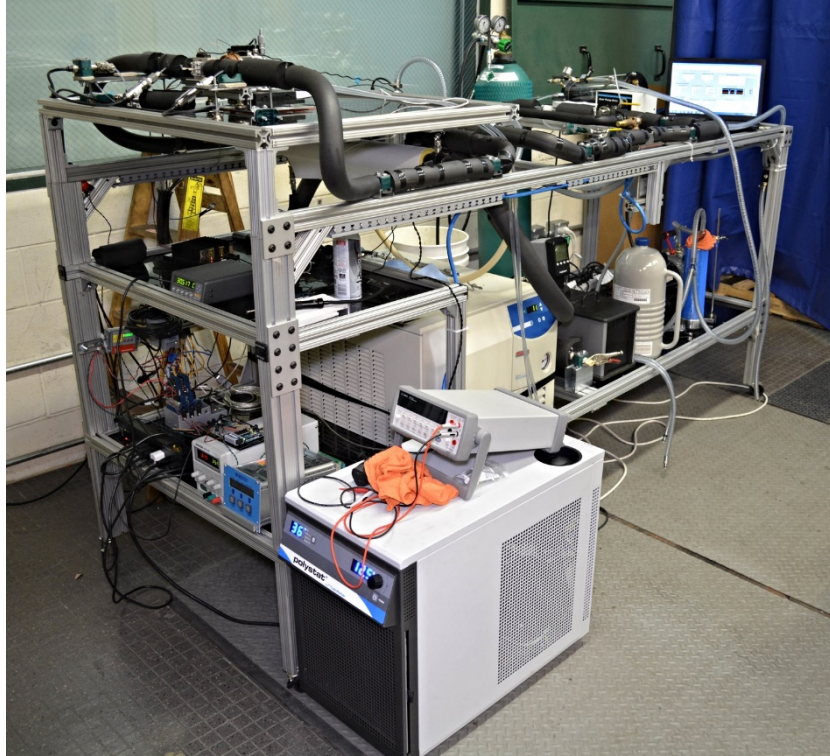
Figure 3-13:   Overview image of the test facility

3.2. Test Facility

The purpose of the test facility is to characterize heat transfer performance of the test section under conditions relevant to laser diode cooling. As stated in Chapter 2, no existing correlation or analytical model is applicable at the hydraulic diameter or applied heat flux in the current study. The aim of this facility is to collect relevant data to determine if existing heat transfer correlations can be used or if they need to be modified for these conditions

The test facility shown in Figure 3-13 was designed to recirculate a working fluid (R134a) at precise operating conditions while acquiring representative measurements. Figure 3-14 shows the process flow diagram of the test facility, and Table 3-3 shows a list of all the equipment and instrumentation used in this facility, and their associated range of operation. A list of all the calibrated uncertainties is then given on Table 3-4. In this facility, R134a is subcooled by the first heat exchanger (HX1, Koolance HXP-193) to a target subcooled condition prior to entering the

43

test section. Here, the degree of subcooling is measured by a calibrated type-K thermocouple and a pressure transducer (Omega, MMA100C1P3C0T4A6), and the existence of a single phase condition is verified through a flow sight (McMaster, 5071K41). The degree of subcooling is controlled by the temperature and flow rate of the chilled water line, which is circulated through a
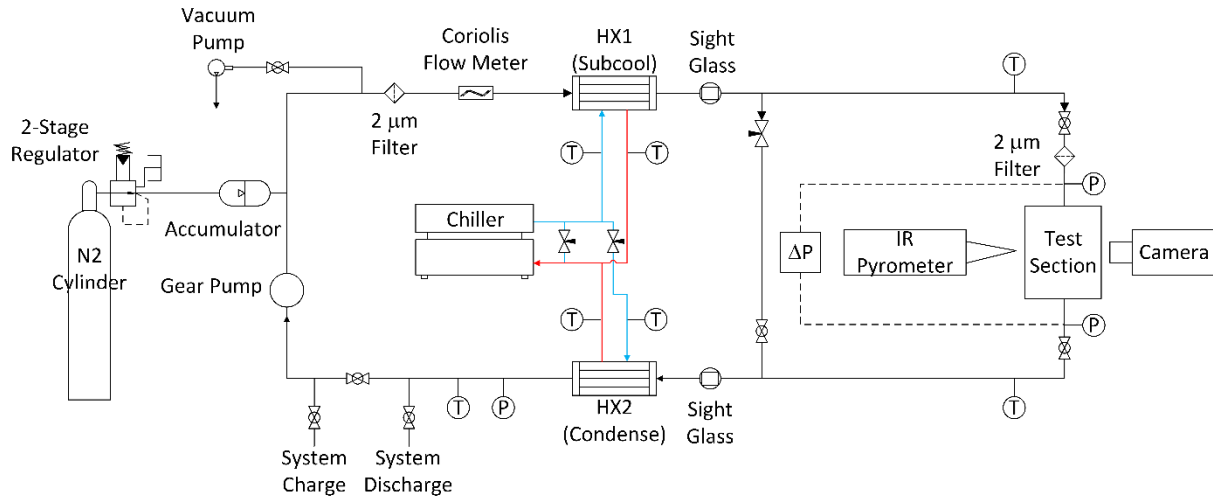
Figure 3-14:   Test facility process flow diagram

chiller (ThermoFisher, M150).

Prior to the fluid entering the test section, it passes through a 2 μm filter to remove particles that could block the orifices. In the test section, which can be isolated by a series of bypass valves, the fluid is heated to a two-phase liquid-vapor mixture by the thin film heater bonded to the back surface of the silicon. The heater is energized by a power supply (Instek SPS-606, 0 to 60 V, 6 A max). The voltage drop across the heater is measured by the data acquisition system, and current to the heater is measured using a high accuracy shunt resistor (Ohm Labs, CS-10). In addition, the surface temperature of the heater is measured using a calibrated IR pyrometer (MicroEpsilon, CTL-CF1-C8), which allows the flow boiling heat transfer coefficient to be calculated using the

Table 3-3:   List of equipment and instrumentation used in the test facility

Items	Description	Manufacturer	Supplier	Part Number
Gear Pump Head (High Flow)	GA series - T32 gear set (0.092 ml/rev) PEEK	MicroPump	Cole-Parmer	GA-T32
Gear Pump Console Drive	50-5000 rpm; A-Mount Console Drive	MicroPump	Cole-Parmer	wu-75211-10
Accumulator	Air/Water Bladder Cylinder; P(max):150 psi	Humboldt	Humboldt	HM-4151A
Vacuum Pump	High Vacuum; 15 micron; 3 cfm (Free)	McMaster		4396K21
Chiller	Merlin M150LR w/ CP 55 pump, 3.5 kW cooling, 0.5 gal res	Thermofisher		M150LR-CP55
Heated Bath	Heater: 1.1 kW; Res: 7L	PolyScience	Cole-Parmer	MX 7L
Heat Exchanger	Compact Plate Heat Exchanger	Koolance		HXP-193
Thermocouples	Type K; 0.5" length; Pipe process ungrounded	Omega		TC-K-NPT-UG-72
	Type T; 0.5" length; Pipe process ungrounded	Omega		TC-T-NPT-UG-72
	Type T; Surface mount adhesive backed (5 Pk)	Omega		SA1XL-T
IR Pyrometer	Non-contact IR; Spot 0.9mm; Range 50-975C	MicroEpsilon		CTL-CF1-C8
Flow Meter	Coriolis flow meter; 8-600g/min <0.5% accuracy	Rheonik		RHM015
	Coriolis flow transmitter; RS232 interface	Rheonik		RHE07
Power Supply	DC Power Supply; 360W (60V/6A)	Instek	Cole-Parmer	SPS-606
Pressure Transducers	0-50psia; 0.08% accuracy; 4-20 mA; 1/4" NPT	Omega		PX409-005AI
	0-100psia; 0.08% accuracy; 4-20 mA; 1/4" NPT	Omega		MMA100C1P3C0T4A6
	50 psid; 121degC max; 0.08% Accuracy	Omega		PX409-100DWUI
Shunt Resistor	10A, 1V, 0.1 ohm <0.01% accuracy	Ohm-Labs		CS-10
Data Acquisition System	4-slot USB Chassis	National Instruments		cDAQ-9174
	Thermocouple module; 16ch	National Instruments		NI 9214
	Analog current and voltage +/-10V; +/-21.5mA; 16ch	National Instruments		NI 9207
	Analog voltage +/-60V; 8ch	National Instruments		NI 9221

Table 3-4:   List of test facility instrumentation accuracy

Measurement	Equipment	Bias		
		Source	Value	Unit
Supplied Voltage	NI 9221 (+/-60V DAQ module)	% of Reading (Gain)	0.26	%
		Range (Offset)	0.156	V
Heater Voltage Drop	NI 9221 (+/-60V DAQ module)	% of Reading (Gain)	0.26	%
		Range (Offset)	0.156	V
Shunt Voltage Drop	NI 9207 (+/-10V DAQ module)	% of Reading (Gain)	0.52	%
		Range (Offset)	0.00416	V
Shunt Resistance	Ohm Labs CS-10	Manufacture	0.01	%
Mass flow rate	GE Rheonik Coriolis Meter	RHE07	0.50	%
Fluid Temperature	NPT K-type TC NI 9214 TC module	Calibration Curves	0.258 - 0.385	°C
Surface Temperature	MicroEpsilon IR Pyrometer	Calibration Curve	0.671	°C
Fluid Absolute Pressure	0-100 psia Transducer	Transducer BSL	0.08	%
	0-5 psia Transducer	Transducer BSL	0.08	%
	NI 9207 (4-20 mA DAQ module)	% of Reading	0.87	%
		Range (Offset)	0.011	mA
Fluid Differential Pressure	0-50 psid Transducer	Transducer	0.08	%
	NI 9207 (4-20 mA DAQ module)	% of Reading	0.87	%
		Range (Offset)	0.011	mA

procedure described in the next chapter. The inlet, outlet, and differential pressures of the test section are also measured (Omega: absolute transducer MMA100C1P3C0T4A6, and differential transducer PX409-100DWUI). On the front side of the test section, the fluid flow field is photographed and videotaped by a digital camera (Nikon D5200) with a microscope objective lens (Figure 3-15). The microscope objective has a fixed focal length, and magnification is increased by adding zoom tubes between the camera and the objective. Video clips are taken at a frame rate of 60 f s^{-1}, which was deemed sufficient to capture the boiling transition location.

Figure 3-15:   Left: Image of the camera with LED bar light and lens; Right: sample image

Once the fluid leaves the test section, the fluid is completely condensed in a second heat exchanger (HX2, same make and model as HX1). The degree of subcooling is measured by a calibrated type-K thermocouple and a pressure transducer (Omega, MMA100C1P3C0T4A6). This is controlled by the temperature of the chilled water line, which is conditioned by the same chiller used for the fluid connected to HX1. The test fluid is then circulated using a positive displacement gear pump head (MicroPump, GA-T32) that is magnetically coupled to a variable speed drive (Cole-Parmer, wu-75211-10). The mass flow rate of the fluid is measured by a Coriolis mass flow meter (Rheonik, RHM015) located downstream of the pump. An accumulator (Humboldt, HM-4151A) is located at the outlet of the gear pump. Excess fluid in the loop is contained in a bladder inside the accumulator, and the pressure of the fluid is controlled by pressurized nitrogen that fills the space inside the accumulator between the bladder and its housing (Figure 3-16).

All data are collected with a NI data acquisition (DAQ) system (cDAQ-9174) to measure voltage and current signals generated in the test facility. A LabVIEW program is used to log relevant the data generated during tests. Multiple DAQ cards are required as the measurement range is dependent on the sensor, and a summary of the individual measurement module pin-outs, wiring diagrams, Labview program code flow diagram, and general facility procedures are provided in Appendix B.2 – B.4. In the next section, the test section assembly is described in detail.

Figure 3-16:   Accumulator removed from the test facility

3.2.1. Test Section Assembly

The test section is integrated into the test facility to make a hermitic fluidic seal and to enable electrical connectivity to the heater. As shown in Figure 3-17, the electrical connection is made at the contact pads using 24 gauge copper pins embedded in an electrically insulating, precision machined ceramic mount. Reliable contact between the test section and the current conducting wires as the test section thermally expands by using a compliant gasket on the front side of the test section. Thumb screws, which pass though both ceramic components, are tensioned into an aluminum plate to hold the assembly together. All parts have an open view port in the center to allow optical access for both flow visualization and non-contact IR surface temperature measurement. The procedure for installing a test section into this assembly is given in Appendix B.1.1. Once the electrical harness is installed, the test section is then installed into the fluid interface.
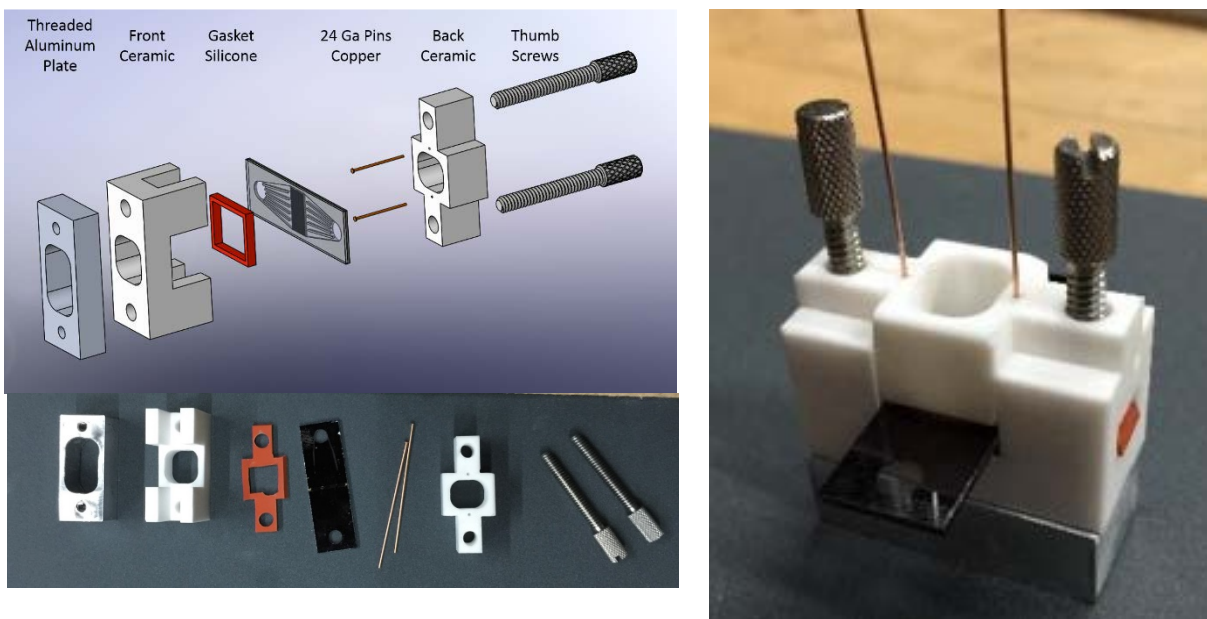
Figure 3-17: Top-Left: Solid model of electrical interface; Bottom-Left: Picture of components; Right: Assembled electrical interface
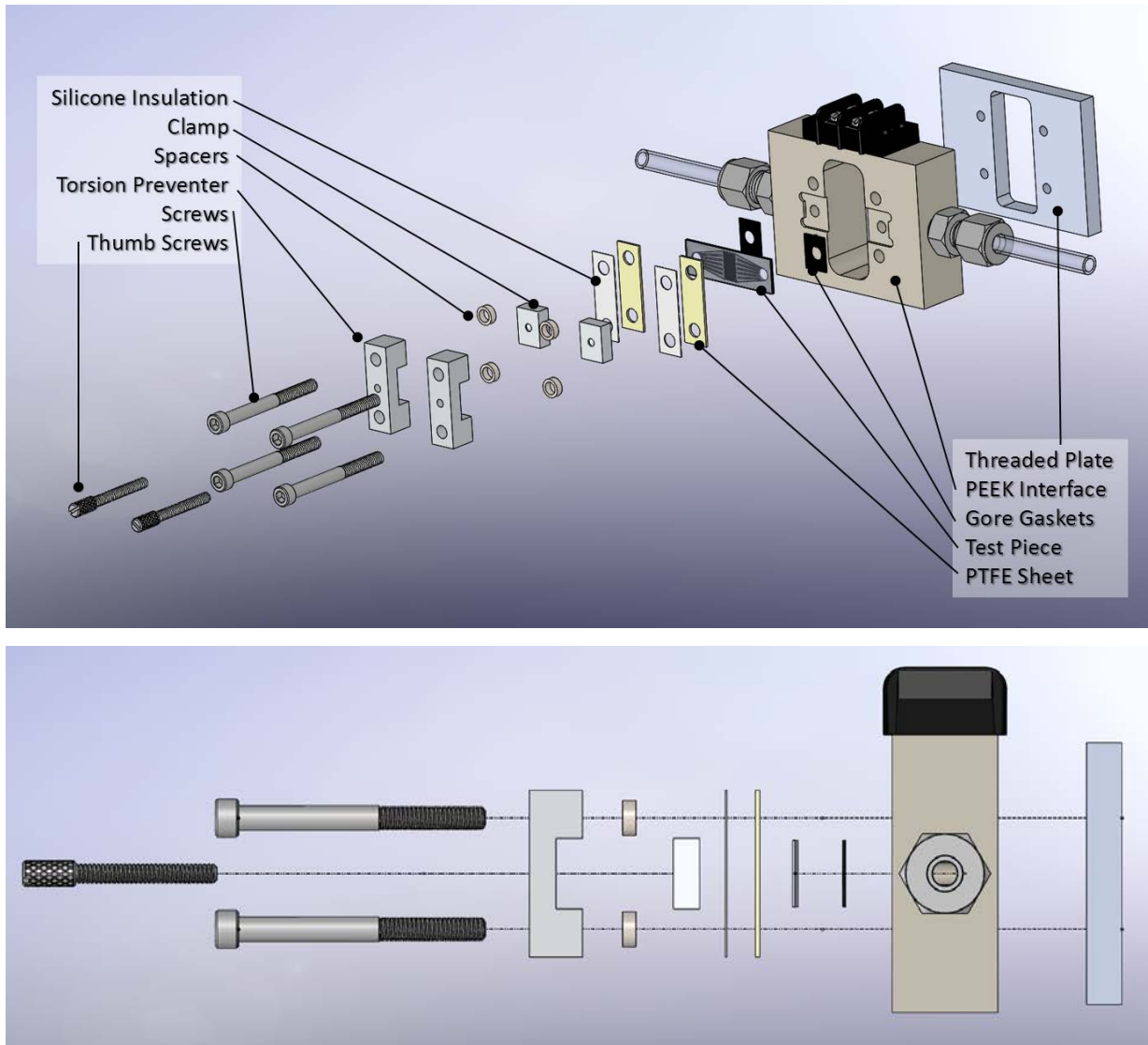
Figure 3-18:   Top: exploded view of fluidic sealing mechanism (electrical harness omitted for clarity); Bottom: side view of assembly

The fluid interface was machined from a solid block of PEEK for its relatively high melting point (343°C), low thermal conductivity (0.25 W m^{-1} K^{-1}), and robust chemical compatibility. Although the test section is very brittle, it is tolerant of large compressive forces, and a clamping mechanism squeezes the part to the fluid interface. To create a hermetic seal between the PEEK and the test section, a compressible Gore-Tex gasket is used. On the reverse side two additional gaskets (silicone foam then rigid PTFE) provide thermal insulation from the clamping hardware and evenly distribute the compressive force. An exploded solid model view of the assembly is

shown in Figure 3-18, and the method for installing the tes22t section into the interface is given in

Appendix B.1.2. The final installed test section is shown in Figure 3-19. The method for measuring

the surface temperature and the transition from single phase cooling to two phase flow boiling is

discussed in the next section.
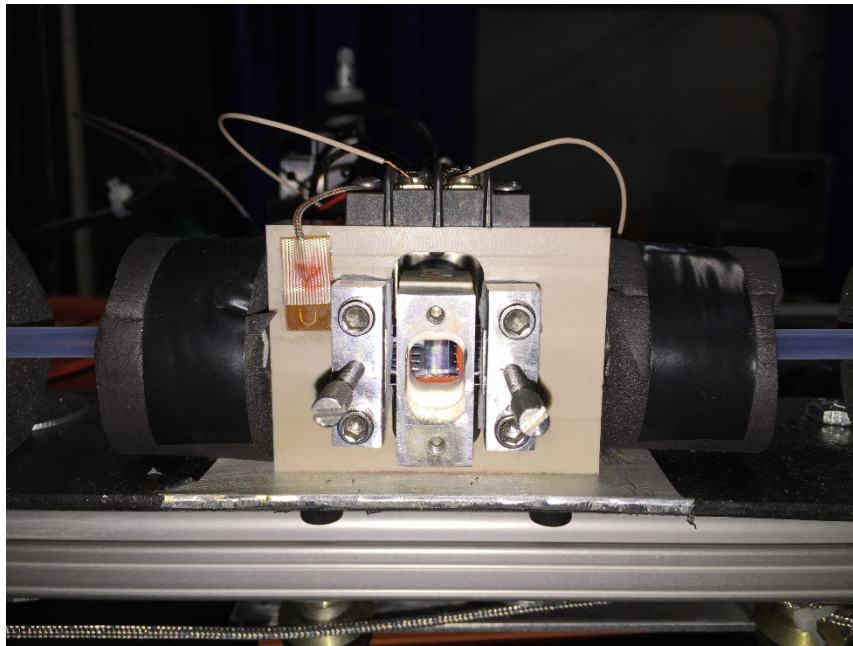
Figure 3-19:   Image of installed test section with electrical harness in the PEEK interface

3.2.2. Test Section Surface Temperature and Two-Phase Transition Location Measurement Techniques

To calculate the flow boiling heat transfer coefficient, both the surface temperature and

heat duty of the test section are required. The surface temperature is directly measured at multiple

positions using the calibrated IR pyrometer. Also, because the fluid enters the test section as a

subcooled liquid, the location where the flow transitions from a single phase mixture to a two

phase mixture is needed. The techniques used for these two measurements are described in this

section.

To ensure that the IR pyrometer measures the surface temperature accurately, the back side of the test section is coated with a thin layer of high emissivity black paint. As shown in Figure 3-2, high temperature paint (Rutland, #81) was brushed onto the surface to create a surface with uniform emissivity. The field of view for the IR pyrometer is small, which minimizes any impact from the surrounding environment. A sensitivity study was conducted to verify that the

Figure 3-20: IR pyrometer with cooling jacket and surface thermocouple

temperature reading was independent of orientation, environmental temperature, and several other factors (see Appendix B.4.2 for a summary). This study found that only the temperature of the
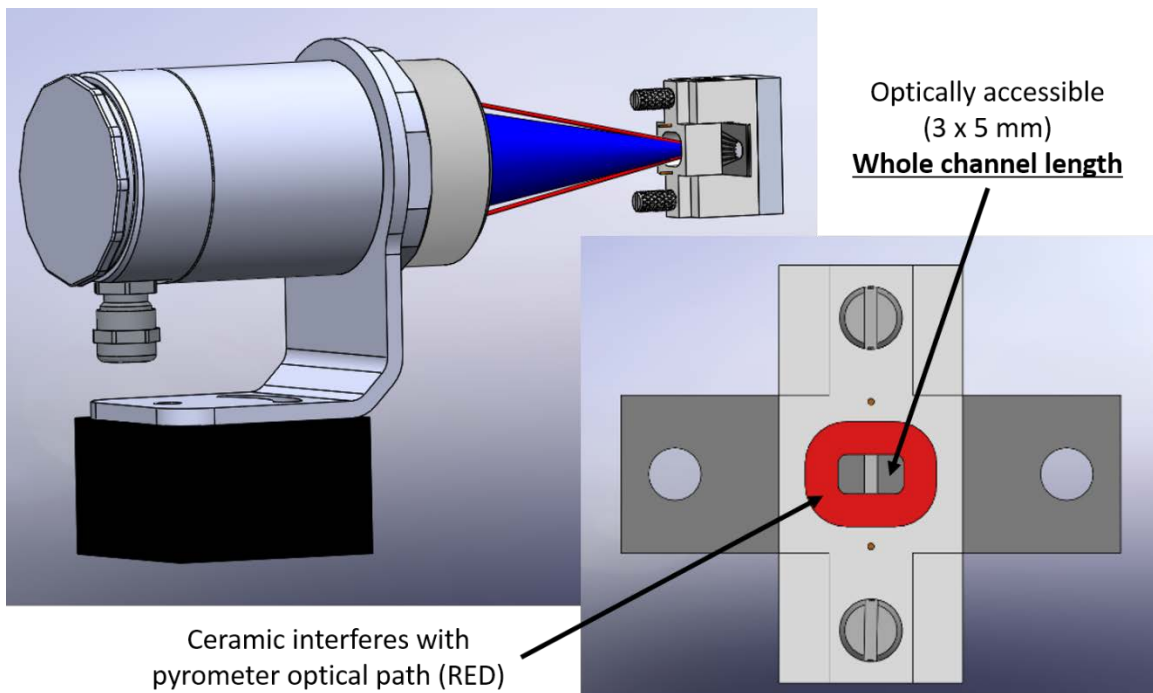
Figure 3-21: Solid model of pyrometer measureable area due to optical interference from the electrical interface; Left: blue cone is the IR path and red lines are 2 lasers which converge on the focal spot; Right: red area shows the immeasurable area due to optical interference from the electrical connector

51
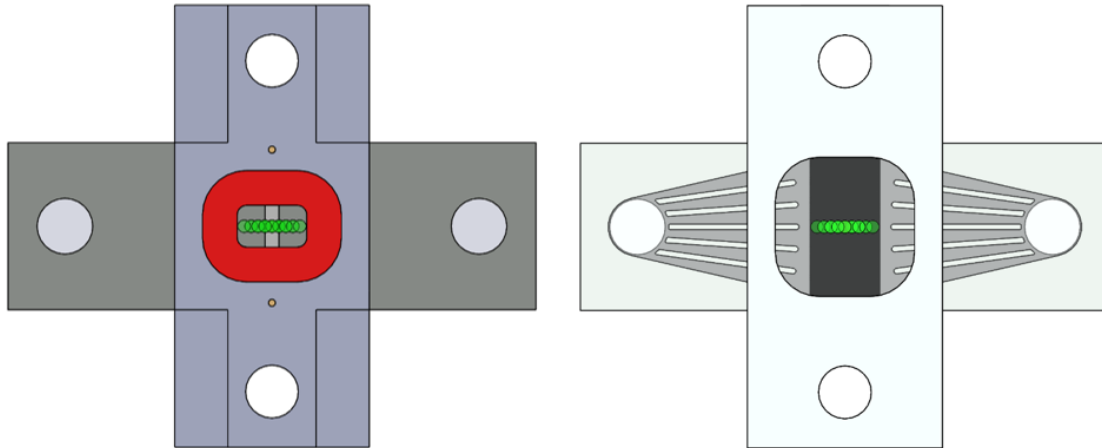
Figure 3-22:   Surface temperature measurement locations along test section channels are shown in green (fluid flow is from right to left); optically inaccessible area shown in red.

pyrometer itself caused a statistically significant effect. As a result, a copper tube that contained a temperature controlled stream of water was wrapped around the pyrometer to control its temperature, which was monitored by a surface thermocouple (Figure 3-20). By circulating chilled water through these tubes, the temperature was maintained at 20°C throughout calibration and during testing. Calibration was performed against at high accuracy platinum RTD in a temperature controlled chamber, which resulted in a surface temperature accuracy of ±0.67°C (Appendix B.4.2). The IR pyrometer was then mounted to a two-axis stage for precisely locating the surface temperature measurement translation on the test section. The procedure for centering the pyrometer on a test section is given in Appendix B.1.5.

The sensor on the pyrometer is 25.4 mm in diameter, which is optically focused onto a 0.9 mm diameter area at a working distance of 70 mm. The conically shaped optical path is required to be kept clear to measure the surface temperature accurately. As shown in Figure 3-21, the electrical interface confined the measureable area on the test section surface to a 3×5 mm window. This area covers the entire length of the channels and 3 mm of the exposed heater (Figure 3-22). During the experiments, it was shown that there was little variation in temperature of the exposed

heater, and flow visualization on the opposite side showed that no channels were blocked

Temperature measurements are taken at consistent locations along the test section using a micrometer stage. To increase temperature profile fidelity, the center of each temperature measurement position is spaced in 0.5 mm increments along the entire flow length, which creates an overlap with the position of neighboring temperature measurement locations on either side by 0.4 mm.

The two-phase transition location is determined by post-processing images extracted from video files taken during testing. The field of view at the highest magnification allows 23 of the 125 channels to be captured in a single image. By adjusting the lighting during the test and using image post processing, the transition between liquid and vapor can be made clearly visible. At the test conditions the flow regime is intermittent; therefore, the transition location is time dependent (it moves back and forth within a given channel) and channel dependent (the location is different from one channel to the next). While these variations are small, they are accounted for by
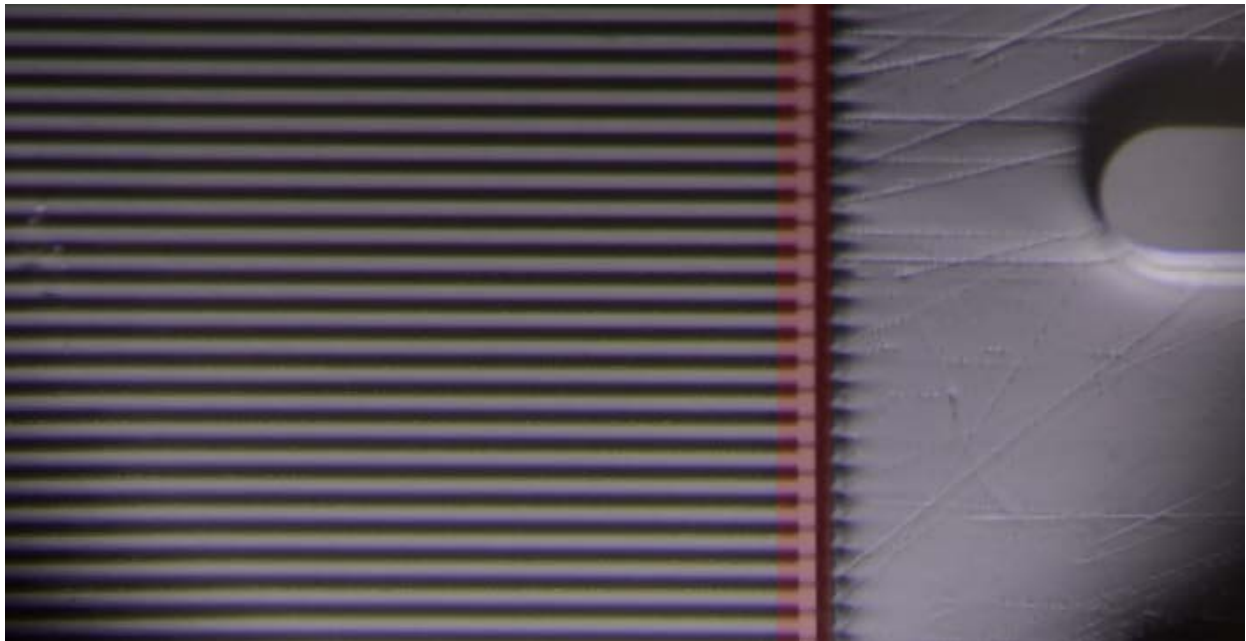
Figure 3-23:   A conversion factor between pixels and physical length was made by measuring the orifice length in the image (highlighted in red)
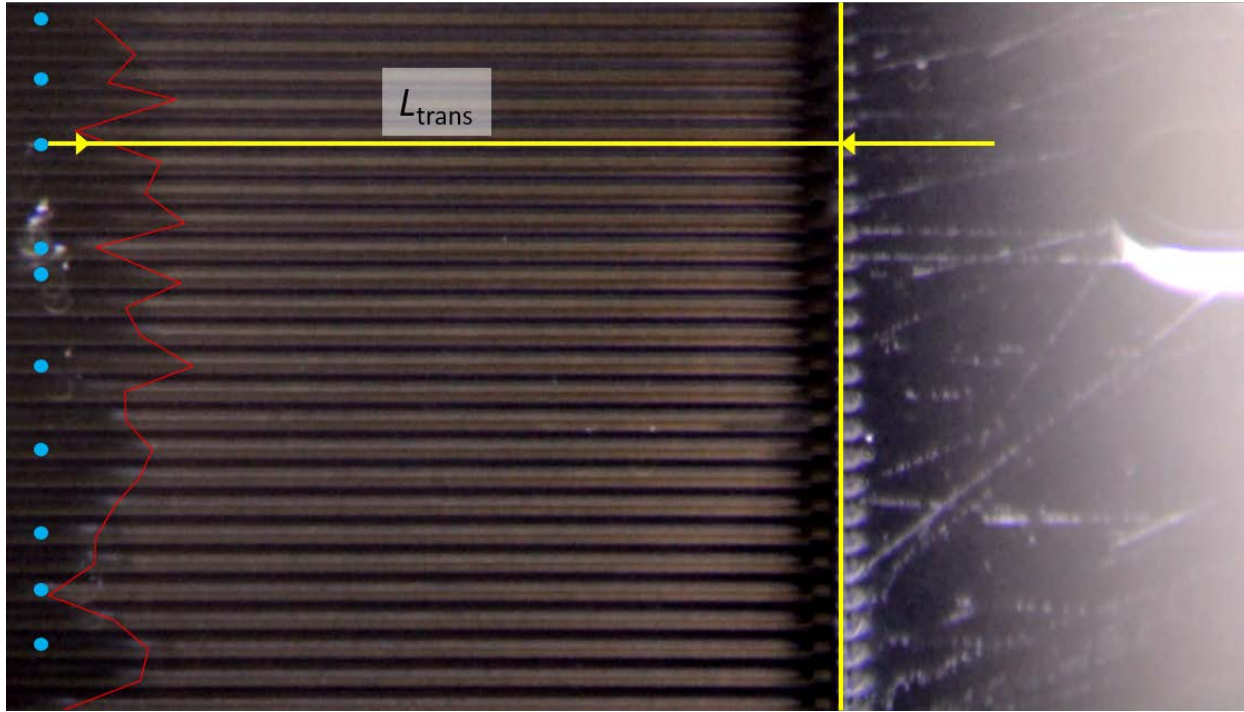
Figure 3-24:   Transition location (red line) for selected individual channels (blue dots); distance
                is measured from the inlet orifice (yellow bar)

determining the transition location from an average of ten channels over three time steps, which

were selected by inspection to account for the widest possible range. A sample data point is used

to illustrate this process. First the scale is determined from the orifice length (highlighted red,

Figure 3-23). Then the light is moved to illuminate the fluid, and the image is analyzed to

determine the transition line, as shown in red in Figure 3-24; this location is then determined

relative to the orifice for ten individual channels, shown by the blue dots. Next, two additional

time steps are chosen where the transition location is visually different, which requires the image

to be magnified. Figure 3-25 shows two representative time steps: the red trace outlines the

previous location of the transition line and the blue trace outlines the current location. The

transition location relative to the heater center is then determined from the 30 samples by:

$$x_{\text{trans}} = \frac{1}{N} \sum_{i=1}^{N} L_{\text{trans}} - 2.5 \qquad\qquad (3.1)$$
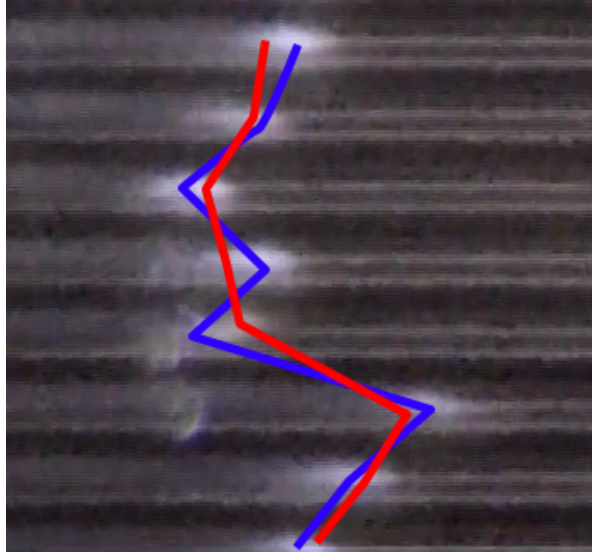
Figure 3-25:   Overlay comparison of two time steps to show transition location variation, red is the previous time step, and blue is the current position

In this case the average transition length (L_{trans}) is 2.3 mm downstream from the orifice entry, which is equivalent to 0.2 mm upstream from the heater center using the above equation. For all the data points for this representative sample, the transition location is within ±172 μm for this location, with a standard deviation of 120 μm. As described later in Section 4.1, this transition location is used to determine the geometry of the numerical model used to extract two-phase heat transfer performance. This model is of the simplest repeating unit of the microchannel array in the two-phase section, a half-channel, as shown in Figure 3-26.

As described in the next section, data from a range of heat duties were taken at specific mass flow rates and saturation temperatures, and the transition location varied at most by ±192 μm from the average for a single mass flow rate over a range of heat inputs. This result – that the transition location is independent of total test section heat duty – is important for determining the local saturation temperature of the fluid, as described in section 3.4.1. In the next section, the experimental test matrix is described.
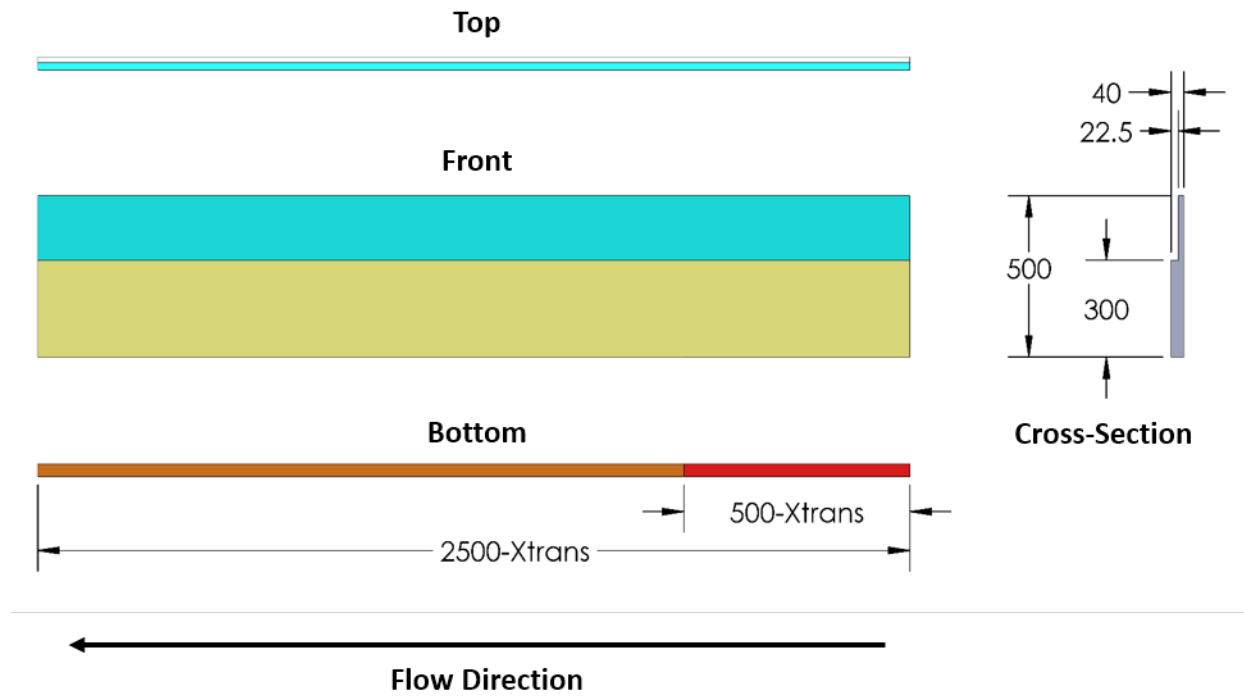
Figure 3-26:   Numerical model geometry (dimensions in μm), blue is the fluid interface, yellow is symmetry, red is the heater, and orange is the unheated section of downstream channels

3.3. Test Matrix

The purpose of the current study is to measure flow boiling heat transfer coefficients for R134a flowing inside channels subjected to base heat fluxes ≥ 1 kW cm^{-2}. In addition, laser diodes can operate near 60°C, which limits the fluid saturation temperature. Furthermore, it was desired to understand the impact of flow rate and saturation temperature on the heat transfer coefficient. Table 3-5 summarizes the test matrix for the current study. By varying the saturation temperature between 15°C and 25°C for R134a, the saturation pressure varies from 489 to 666 kPa. As a result, the saturated vapor density varies between 23.8 and 32.4 kg m^{-3} over this range of pressures, potential yielding an increase in vapor velocity and void fraction as the saturation pressure is reduced for a fixed mass flow rate and vapor quality. At a saturation temperature of 20°C, the mass flow rate was varied from 50 to 150 g min^{-1}. For each of these 5 test cases, the fluid inlet

temperature was subcooled by ~5°C, and the heat duty was increased until the maximum temperature of the heater reached 60°C. In the next section, the methodology used to establish the test condition for each individual data point is described.

Table 3-5:   R134a test matrix summary

x = Sweep heat duty up to T_{he} = 60°C		Flow Rate [g min^{-1}]		
		50	100	150
Saturation Temperature	15		x	
	20	x	x	x
	25		x	

3.4. Test Condition Establishment

As noted by many prior investigations, the flow boiling heat transfer coefficient is a strong function of thermodynamic and transport properties, heat flux, and local vapor quality. In this section, the calculations required to determine these values are described in detail. The method used to calculate the local saturation temperature through the test section is described first. Thereafter, the method used to calculate the total heat transferred to the fluid in the test section and the associated outlet vapor quality is discussed, followed by the estimated uncertainties in these two calculated variables. Because they are dependent on many factors, including heat spreading in the test section, the relative amounts of heat transfer to the single phase and two phase fluid portions of the test section are described in the next chapter, which also includes the method for calculating the flow boiling heat transfer coefficient.

3.4.1. Fluid Saturation Temperature

The saturation temperature of a two-phase mixture is dependent only on its pressure. By determining the local pressure along the entire flow path, the saturation temperature can be calculated. During the experiments, the static pressure and temperature of the fluid is measured upstream and downstream of the test section (Figure 3-27). No local pressure measurements are
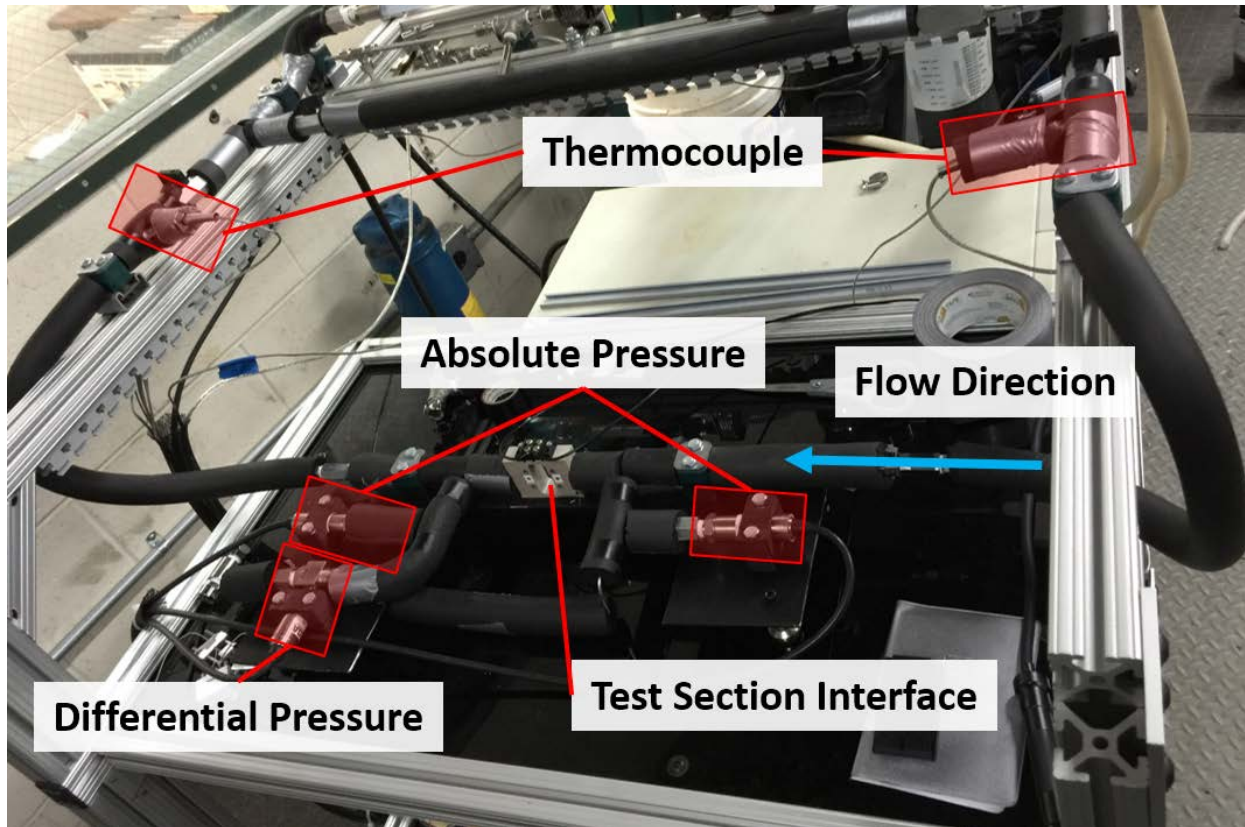
Figure 3-27:   Location of temperature and pressure measurement points in the test section

made within the test section due to the difficulty associated with fabricating it. Therefore, the local

fluid pressure must be calculated from data collected during the tests. As discussed in the previous

section, the fluid enters the channels as a single phase mixture and exits as a two-phase mixture.

Unfortunately, accurate pressure drop models for the outlet heater and tubing and the flow

expansion from the channels to the outlet header do not exist for a liquid-vapor mixture, and it is

exceeding complex to model this process using CFD. Furthermore, because the orifice width is

small relative to the upstream manifold and downstream channels, complex transitions from the

inlet manifold to the orifice and from the orifice to the channels exist, and are also very challenging

to accurately model (Figure 3-10).

As a result, the following approach was utilized to estimate the local pressure in the test

section (Figure 3-28). It was shown in section 3.2.2 that, regardless of downstream boiling, the

transition location is practically constant for a given flow rate, inlet temperature, and pressure. This implies that the pressure drop from the inlet to the transition location is also constant. Because the geometry from the transition location to the pressure transducer is well-defined, it is possible to estimate the single phase pressure drop by estimating all of the pressure drops downstream from the transition location, which can be used to calculate the pressure at the transition location. During testing at a single saturation temperature and flow rate, the heater power was increased until just before the fluid began to boil. At this point, local surface temperatures and inlet and outlet fluid temperature and pressure data were collected. Then, standard correlations for the single phase flow through the channels and the flow expansion into the header and CFD models for the complex outlet header and fluid interface manifold were used to calculate the single phase pressure drop from the transition location to the outlet pressure transducer. These pressure drops were then added to the outlet pressure to calculate the pressure at the transition location, which allowed the pressure drop from the inlet pressure transducer to the transition location to be calculated. Because the transition location is independent of the flow rate, heat duty, and fluid inlet pressure, the fluid pressure at the transition location for all flow boiling tests is determined from the inlet pressure and this calculated pressure drop. A representative calculation using this method is given below.

Characterize single-phase pressure drop just prior to boiling at a given flow rate and inlet subcool (P_{in}, P_{out})	Determine outlet ½ channel and expansion pressure drops, from single-phase correlations (dP_{ch}, dP_{exp})	Estimate outlet manifold, and PEEK interface pressure drop with CFD due to complex geometry $dP_{out} = dP_{man} + dP_{int}$	Estimate pressure at the center of the test piece $P_{trans} = P_{out} + dP_{out} + dP_{man} + dP_{int}$	Estimate saturation temperature $T_{sat} = T_{sat}(P = P_{trans})$

Figure 3-28:   Process flow to estimate the saturation pressure and temperature at the transition location
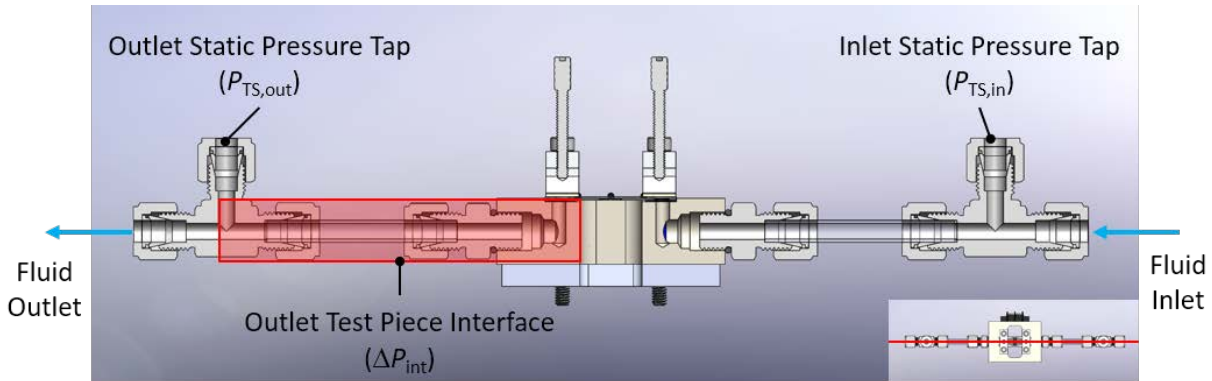
Figure 3-29:   Cross-sectional view of the test section, identifying the pressure taps and outlet test section interface (bottom-right shows section plane, viewing from below)

To demonstrate the procedure used to calculate the local saturation pressure in the test section, two representative data points are needed: one from the single phase characterization, and a two-phase data point at the same flow rate and saturation temperature. The mass flow rate, inlet and outlet temperatures and pressures, outlet vapor quality, test section heat duty, and liquid to two-phase transition location for each of these data points are given in Table 3-6. The two-phase transition location was determined using the procedure described in section 3.2.2.

Table 3-6:   Summary of single phase and sample test point conditions

Parameter	Units	Single Phase	Test Point
Mass flow rate ($\dot{m}$)	g min^{-1}	100.8	99.8
Inlet temperature ($T_{TS,in}$)	°C	14.6	14.5
Outlet temperature ($T_{TS,out}$)	°C	19.4	15.1
Inlet pressure ($P_{TS,in}$)	kPa	618	623
Outlet pressure ($P_{TS,out}$)	kPa	561	480
Test section heat duty (q_{app})	W	19.4	69.75
Liquid to vapor transition, relative to center of heater (x_{trans})	mm	n/a	-0.20

To calculate the pressure at the transition location, the static pressure difference from this location to the outlet pressure transducer is calculated for the single phase test data point first. The individual contributions to this pressure difference include: frictional pressure drop pressure drop in the channels (ΔP_{ch}), outlet test section manifold (ΔP_{man}), and outlet interface (ΔP_{int}) and the

minor losses associated with the expansion from the channel into the manifold (ΔP_{exp}). During this single-phase characterization, the pressure difference due to fluid acceleration and deceleration is accounted for in the CFD models; however, this effect must be explicitly determined when calculating the boiling heat transfer coefficient described in Section 4.1.1. An overview of the test section is shown on Figure 3-29, which identifies the outlet interface, and Figure 3-30 shows a close up of the test section identifying the remaining contributions.
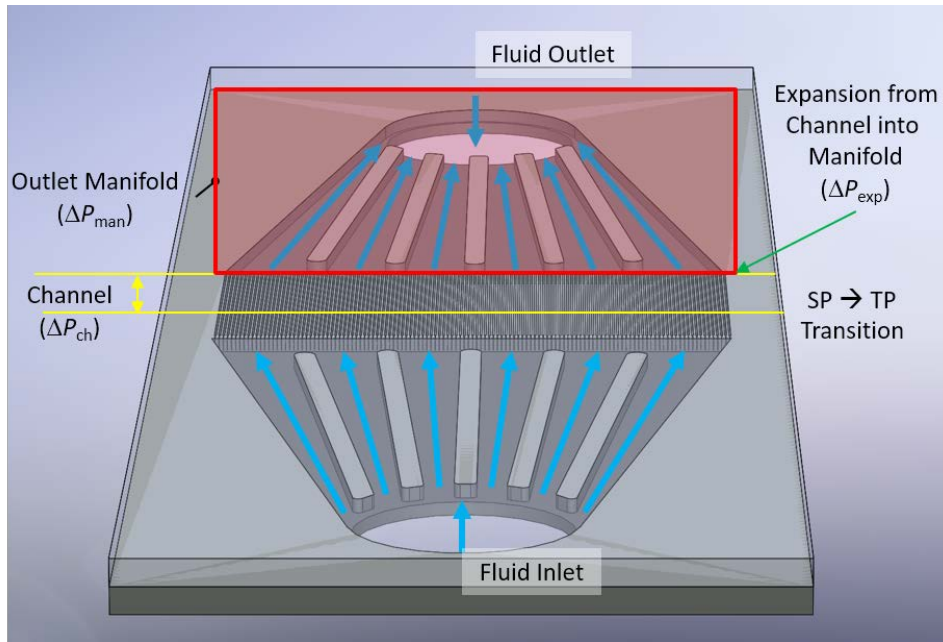
Figure 3-30:   View down the length of the test section, identifying the pressure drops in the direction of the flow path

Starting at the transition location, the frictional pressure drop in the channels is calculated from the following equation:

$$\Delta P_{\text{ch}} = f \frac{(0.0025 - x_{\text{trans}})}{D_{\text{h}}} \frac{\rho_{\text{l}} \bar{u}_{\text{ch}}^{2}}{2} \tag{3.2}$$

The length from the center of the test section to the exit of the channels is 2.5 mm, and, because the transition occurred 0.2 mm upstream of the center in the representative single phase point, the channel length from the transition location to the outlet of the channels is 2.7 mm. The hydraulic

61

diameter (D_H) is 73.4 μm for the 45 × 200 μm channels. The liquid density (ρ_l) is evaluated at the mean temperature and pressure between the inlet and outlet, which are 15.3°C and 590 kPa respectively, for a density of 1243 kg m^{-3}. The average velocity for flow through a single channel is calculated as follows:

$$\bar{u}_{ch} = \frac{\dot{m}}{\rho_l A_{ch} N} \tag{3.3}$$

The channel height and width are 200 μm and 45 μm, respectively, which yields a cross-sectional area of 9 × 10^{-9} m^2, and there are 125 total channels. For a mass flow rate of 99.8 g min^{-1}, the average fluid velocity in the channels is 1.19 m s^{-1}. For all of the data points in the current study, the flow in the channels was laminar, and, therefore, the friction factor was determined from the correlation given by Shah and London [68] for laminar flow in rectangular ducts:

$$f = \frac{96}{Re_l}[1 - 1.3553\alpha + 1.9467\alpha^2 - 1.7012\alpha^3 + 0.9564\alpha^4 - 0.2537\alpha^5] \tag{3.4}$$

The aspect ratio (α) is the ratio of the minimum and maximum dimensions of the channel (*i.e.*, channel width to channel height, respectively), and the Reynolds number is calculated as follows:

$$Re_l = \frac{G_{ch} D_h}{\mu_l} \tag{3.5}$$

where the mass flux (G_{ch}) is calculated by:

$$G_{ch} = \frac{\dot{m}}{A_{ch} N} \tag{3.6}$$

For the representative data point, the mass flux is 1,478 kg m^{-2} s^{-1}, the Reynolds number and α are 532 and 0.225, respectively. It is required that the flow be fully developed to use this single-phase friction factor correlation (equation (3.4)), and to ensure this is the case the laminar entrance length (L_{ent}) is calculated as follows [34]:

$$L_{ent} = 0.05\, Re_1\, D_H \tag{3.7}$$

An evaluation of this expression yields and entrance length of 1.95 mm, which is shorter than the distance from the orifice to the transition location (2.3 mm). Therefore, the flow at the transition location is fully developed. From equation (3.4) the friction factor is 0.14, and finally, using equation (3.2) the pressure drop is estimated to be 4.53 kPa from the transition location to the test section outlet manifold.

Once the fluid exits the channels, it expands into the outlet manifold. It is assumed that the flow expands from the channel into the 80 μm width shown in Figure 3-31, which is referred to as the manifold unit width ($w_{man,unit}$). The minor loss from this expansion is calculated as follows:

$$\Delta P_{exp} = \frac{1}{2} K_{exp} \rho_1 \bar{u}_{ch}^{\ 2} \tag{3.8}$$

The liquid density and average channel velocity are the same as the previous calculation, and the K-factor is calculated from the following [69]:

$$K_{exp} = (1 - \frac{A_{ch}}{A_{man,unit}})^2 \tag{3.9}$$
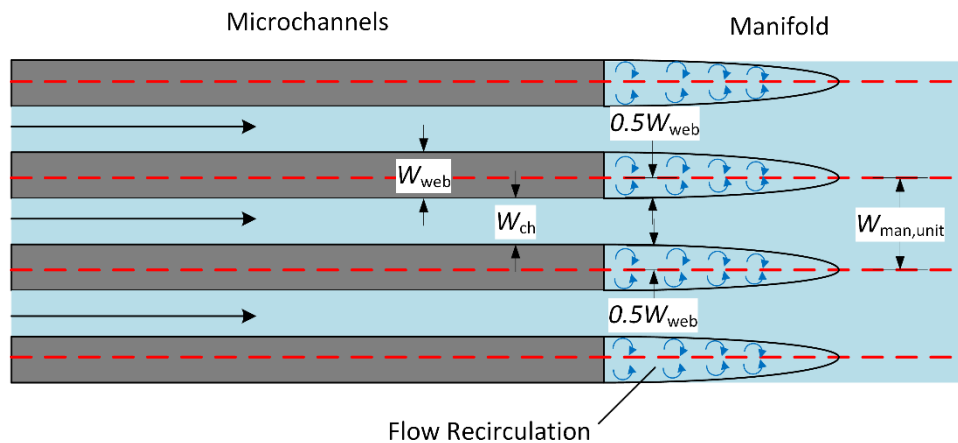
Figure 3-31:   Schematic describing minor loss expansion from microchannels into manifold and depicting the assumed unit width for the manifold section

The channel area is the same as the previous calculation, and the unit area of the manifold is estimated as follows:

$$A_{man,unit} = h_{man}(w_{ch} + w_{web}) \tag{3.10}$$

The depth of the manifold is 230 μm, the channel width is 45 μm, and the web width is 35 μm. This results in a unit manifold cross-sectional area of 1.84×10^{-8} m^2. Therefore, the expansion K-factor is 0.261, and the resulting pressure drop from this expansion is 229 Pa.

The flow through the complex geometry in the test section outlet manifold and test section interface cannot be described by a simple analytical expression or empirical correlation. Therefore, the pressure drop in these locations is determined by using a CFD model (ANSYS CFX [70]). Figure 3-32 shows the modeled geometry and boundary conditions for flow from the outlet of the channels up to the static pressure tap. The manifold and interface regions are connected at the labeled contact area. For simplicity, the geometry was modeled with a half symmetry plane, which assumes that the mass flow rate through all the channels is the same, which is consistent with the
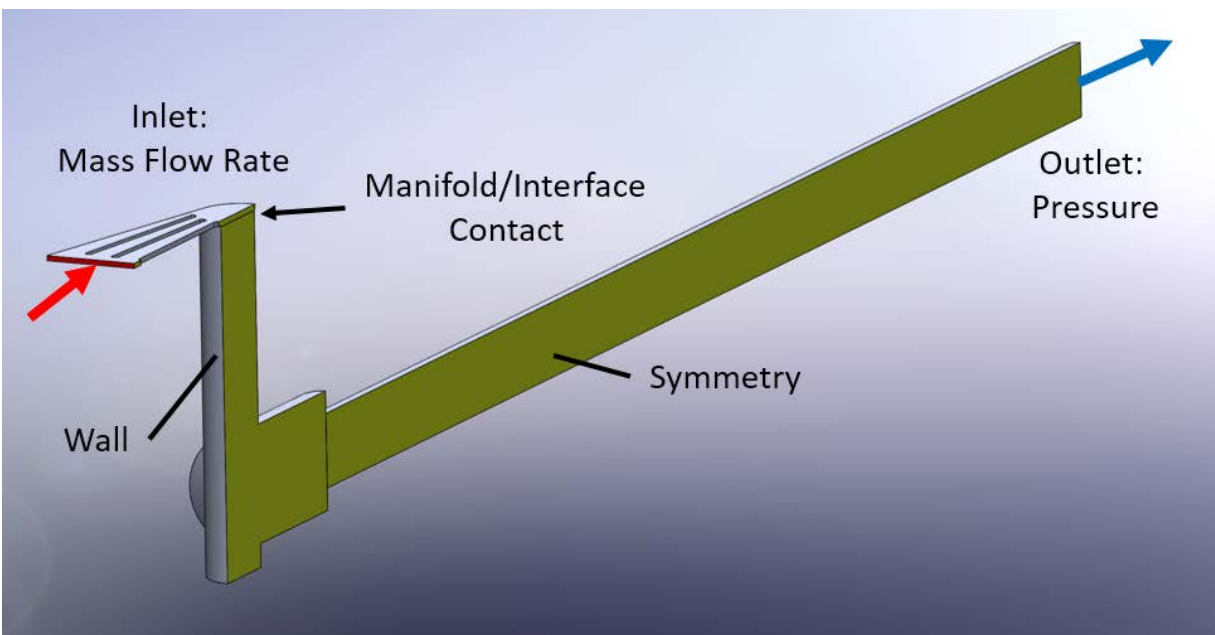
Figure 3-32:   Outlet manifold and interface pressure drop model boundary conditions

experimental observations during two-phase flow. The absolute pressure at the outlet and mass flow rate through the test section were measured during the experiment. For the ANSYS simulation, an isothermal k-ω model with automatic near-wall treatment, was used with a targeted mesh element size of 100 and 500 µm for the manifold and interface areas, respectively. To determine the appropriate first layer thickness (y) which captures the boundary layer, the CFX documentation suggests a y^+ value near 1. This non-dimensional length is defined as:

$$y^+ = \frac{u_* y}{\nu_1} \tag{3.11}$$

This calculation is made for every element in the mesh, and the frictional velocity (u_*) is dependent on the mean velocity, which has a wide range in this geometry (1×10^{-4} to 2.2 m s^{-1}) due to the drastic changes in cross-sectional area. Therefore, an initial guess of the first layer thickness was made, the model was solved, and the mesh was refined as necessary to achieve an average y^+ height near 1 along all wall surfaces. The resulting first layer thicknesses are 1.5 and 20 µm for the manifold and interface areas, respectively; up to 10 layers of inflation were added from this layer, at a standard growth factor of 1.2. These parameters were further verified by a mesh sensitivity study of the element size (Section 3.4.4). This model accounts for the frictional, minor, and acceleration pressure losses, and, for the representative data point the combined pressure drop from the manifold and interface (dP_{out}) is 2.68 kPa.

With all the pressure drops estimated, the pressure at the transition location is calculated from the following equation:

$$P_{trans} = P_{TS,out} + \Delta P_{out} + \Delta P_{exp} + \Delta P_{ch} \tag{3.12}$$

The outlet pressure for this case is 561 kPa, which results in a transition pressure of 568 kPa. The constant inlet pressure drop is then found by the following:

$$\Delta P_{\text{const}} = P_{\text{TS,in}} - P_{\text{trans}} \tag{3.13}$$

The inlet pressure for the single phase data point is 618 kPa; therefore, the constant inlet pressure drop is 50 kPa at the given inlet conditions. For the two-phase data point, equation (3.13) is solved for the transition pressure. At an inlet pressure of 623 kPa the estimated transition pressure is 573 kPa, which from fluid properties is equivalent to a saturation temperature of 20.1°C. In the following section, this saturation temperature is used to estimate the environmental heat transfer losses from the test section.

3.4.2. Environmental Heat Loss

To calculate the heat transferred from the heater to the test section, the heat lost to, or gained from, the environment needs to be estimated. To estimate the heat loss from the test section, it is divided into 7 regions shown in Figure 3-33: test section (4), connection hose (1 and 7), clear sights (2 and 6), and PEEK interface (3 and 5). Heat loss from each region was bounded by assuming the extreme measured temperature at each location applied to the entire surface. To illustrate the calculations for each section, values from the example two-phase data point are used
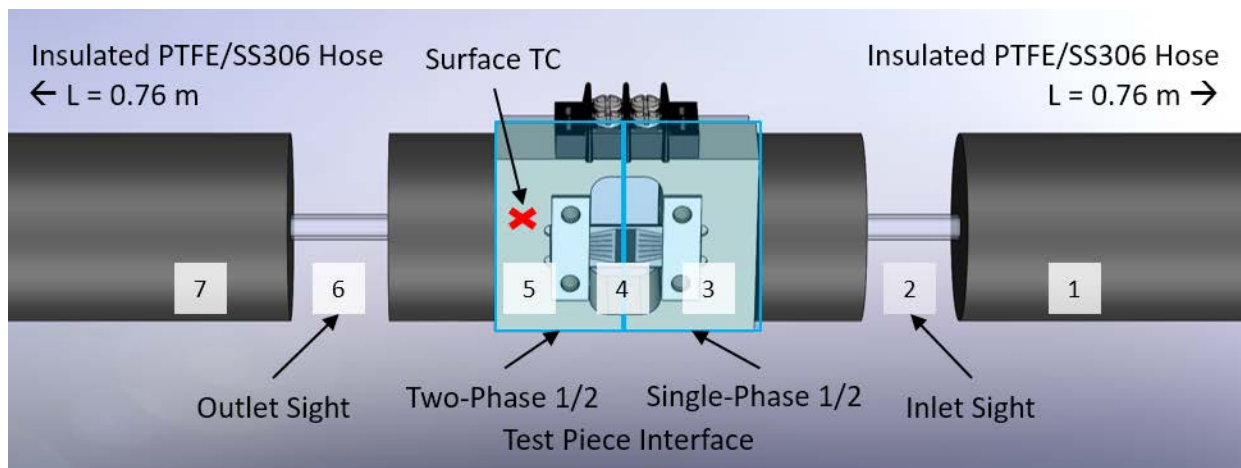
Figure 3-33:   Solid model depicting loss regions in the test section
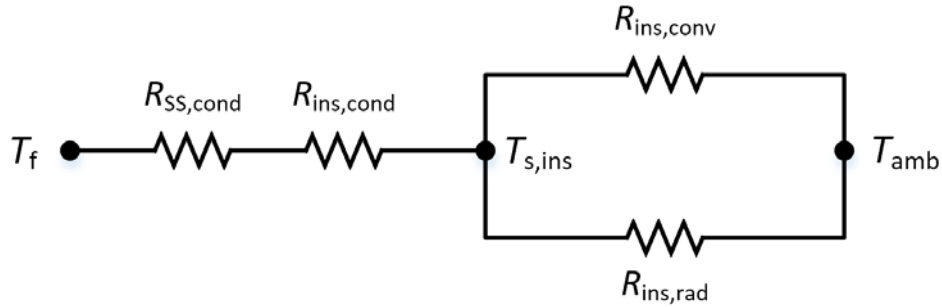
Figure 3-34:　Thermal resistance network for the inlet and outlet hose; for the inlet $T_f = T_{TS,in}$, and for the outlet $T_f = T_{TS,out}$

(Table 3-6). In the following discussion, the calculation methodology for heat loss/gain for each is described in order of the flow direction, beginning with region 1 and ending with region 7.

Starting at the inlet thermocouple (Figure 3-27), the first section is PTFE tube shielded by a stainless steel braid, which was then wrapped in 19 mm thick Buna-N foam insulation (region 1). It is uncertain how thick the PTFE internal tube is, so for a conservative estimate, the entire hose is approximated as stainless steel, and it is assumed that the inside wall temperature for the entire 0.76 m length (L) is at the measured fluid inlet temperature. The thermal resistance network from the fluid to the environment is shown in Figure 3-34, and the equivalent resistance is calculated as follows:

$$R_{eq} = R_{SS,cond} + R_{ins,cond} + \frac{R_{conv}R_{rad}}{R_{conv} + R_{rad}} \tag{3.14}$$

The radial conduction terms are calculated as follows:

$$R_{cond} = \frac{\ln(D_o / D_i)}{2\pi LK} \tag{3.15}$$

For the stainless steel inner tube, the inner and outer diameters are 6.35 and 9.53 mm, respectively. The thermal conductivity of the stainless steel 316 is evaluated at the measured inlet temperature, in this case 14.5°C as, 13.22 W m^{-1} K^{-1}. The resulting conduction resistance through the stainless

steel is 0.0064 K W^{-1}. For the insulation around this tube the inner and outer diameters are 9.53 and 47.6 mm, respectively. The thermal conductivity of the Buna-N foam at 22.2°C is 0.036 W m^{-1} K^{-1}. The resulting conduction resistance through the insulation is 9.33 K W^{-1}.

The convective loss from the outer surface of the insulation is calculated as follows:

$$R_{conv} = \frac{1}{h_{conv} A_s} \tag{3.16}$$

The surface area of the insulation is calculated from the insulation outer diameter (D_o) and hose length (L):

$$A_s = \pi D_o L \tag{3.17}$$

The resulting surface area of the hose insulation is 0.11 m^2. The convection heat transfer coefficient is determined by the following Nusselt number correlation for natural convection from a cylinder [34]:

$$h_{conv} = [0.6 + \frac{0.387 Ra_d^{1/6}}{(1+(\frac{0.559}{Pr_{air}})^{9/16})^{8/27}}]^2 \frac{K_{air}}{D_o} \tag{3.18}$$

The thermal conductivity and Prandtl number are calculated from air properties at the ambient temperature of 22.4°C as, $K_{air} = 0.026$ W m^{-1} K^{-1}, and $Pr_{air} = 0.708$, respectively. The Rayleigh number is calculated from the following:

$$Ra_d = \frac{g \beta_{air} D_o^3 |T_s - T_{amb}|}{\nu_{air} \alpha_{t,air}} \tag{3.19}$$

The volumetric expansion coefficient (β_{air}) was calculated as:

$$\beta_{air} = \frac{1}{T_F} \tag{3.20}$$

where the film temperature (T_F) is calculated as:

$$T_{\mathrm{F}} = \frac{(T_{\mathrm{amb}} + T_{\mathrm{surf}})}{2} \qquad (3.21)$$

The ambient temperature is 295.6 K, which, for a surface temperature of 294.5 K (determined

iteratively), yields a film temperature of 295.1 K and thermal expansion coefficient of 0.0034 K^{-1}.

The thermal diffusivity ($\alpha_{\mathrm{t,air}}$) and dynamic viscosity (ν_{air}) are estimated from fluid properties at

the film temperature ($\alpha_{\mathrm{t,air}} = 2.60\times10^{-5}$ m^2 s^{-1} and $\nu_{\mathrm{air}} = 1.84\times^{-6}$ m^2 s^{-1}). The Rayleigh number and

convection heat transfer coefficient are 8.06×10^3 and 0.142 W m^{-2} K^{-1}, respectively, which results

in a natural convection resistance of 61.9 K W^{-1}. The radiation thermal resistance is calculated as

follows:

$$R_{\mathrm{rad}} = \frac{1}{h_{\mathrm{rad}} A_{\mathrm{s}}} \qquad (3.22)$$

where the radiative heat transfer coefficient is calculated as follows:

$$h_{\mathrm{rad}} = \varepsilon\sigma(T_{\mathrm{surf}} + T_{\mathrm{amb}})(T_{\mathrm{surf}}^2 + T_{\mathrm{amb}}^2) \qquad (3.23)$$

The Stefan-Boltzmann constant (σ) is 5.67×10^{-8} W m^{-2} K^{-4}, and the emissivity (ε) is assumed to

be 1, which ensures that heat loss is over predicted. For a surface temperature of 294.5 K, the

radiation heat transfer coefficient and thermal resistance are 5.82 W m^{-2} K^{-1} and 1.51 K W^{-1},

respectively, which, using equation (3.14), yields an equivalent thermal resistance of 10.8 K W^{-1}.

The total loss rate from the hose is calculated as follows:

$$q_{\mathrm{loss,1}} = \frac{(T_{\mathrm{TS,in}} - T_{\mathrm{amb}})}{R_{\mathrm{eq,1}}} \qquad (3.24)$$

For the representative data point, the heat gain from inlet connection hose is 0.73 W to the fluid

from the environment. Because the convection and radiation heat transfer coefficients are

dependent on the calculated surface temperature, the accuracy of the surface temperature is verified

by re-calculating it using only the thermal convection and radiation thermal resistances as follows:

$$T_s = T_{amb} + q_{loss}\left(\frac{R_{conv}R_{rad}}{R_{conv} + R_{rad}}\right) \qquad (3.25)$$

Using this equation, the calculated surface temperature is 21.3°C, which is the same as the surface temperature used to calculate the thermal resistances.

Next the fluid enters the clear Teflon/PTFE blend flow sight (region 2), which has the following dimensions: inner diameter (D_i) of 3.97 mm, outer diameter (D_o) of 6.35 mm, and length of 76.2 mm. For the Teflon tube it is again assumed that the inner wall temperature is at the fluid inlet temperature ($T_{TS,in}$) to ensure that the heat loss is over predicted (14.5°C). The heat from this section conducts through the tube wall, then naturally convects and radiates to the environment. The equivalent the thermal resistance (Figure 3-35) for this region is calculated as follows:

$$R_{eq} = R_{tef,cond} + \frac{R_{conv}R_{rad}}{R_{conv} + R_{rad}} \qquad (3.26)$$

The conduction thermal resistance is determined from equation (3.15). Using the dimensions of the Teflon tube ($K = 0.25$ W m^{-1} K^{-1}), the conduction thermal resistance is 3.93 K W^{-1}. The convection thermal resistance is calculated from equations (3.16) through (3.20), and the radiation thermal resistance is calculated from equations (3.22) and (3.23). The Teflon surface temperature is determined to be 16.7°C, which is below the ambient temperature and corresponds to a Rayleigh number of 143, natural convection heat transfer coefficient of 0.601 W m^{-2} K^{-1}, and a convection thermal resistance of 1.09×10^3 K W^{-1}. The radiation heat transfer coefficient is 5.63 W m^{-2} K^{-1},
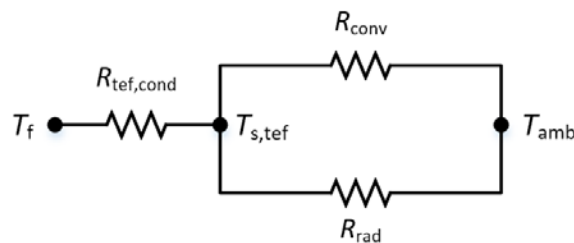
Figure 3-35:   Thermal resistance network for the clear Teflon sight; $T_f = T_{TS,in}$

which yields a radiation thermal resistance of 117 K W^{-1}. Therefore, the equivalent thermal resistance of the Teflon sight is 109 K W^{-1}, and the heat added to the fluid is 0.072 W. Again, there is a small amount of gain from the environment because the fluid temperature is colder than ambient.

Next the fluid enters the single phase section of the PEEK test section interface (region 3) (Figure 3-33). The solid model geometry for this region was used to estimate the total vertical and horizontal surface area (Figure 3-36). For half of the interface manifold, the total surface area is 4.61×10^{-3} m^{-2}, where the vertical portion is 3.83×10^{-3} m^{-2}, and the total horizontal portion is 7.84×10^{-4} m^{-2}. Total heat loss from the single-phase region of the test section interface is estimated by equation (3.24), where the test section inlet and ambient temperatures are both measured. The equivalent thermal resistance is determined from the parallel resistance of the vertical and horizontal surfaces:

$$R_{\text{eq,SP,int}} = \frac{R_{\text{eq,vert}} R_{\text{eq,hori}}}{R_{\text{eq,vert}} + R_{\text{eq,hori}}} \tag{3.27}$$

where both the vertical and horizontal surfaces the equivalent resistance are determined from the parallel resistance of convection and radiation (i = vert or hori):

$$R_{\text{eq,i}} = \frac{R_{\text{conv,i}} R_{\text{rad,i}}}{R_{\text{conv,i}} + R_{\text{rad,i}}} \tag{3.28}$$

The radiation thermal resistance is calculated as follows:

$$R_{\text{rad,i}} = \frac{1}{h_{\text{rad}} A_{\text{S,i}}} \tag{3.29}$$

where the radiation heat transfer coefficient is as follows:

$$h_{\text{rad}} = \varepsilon\sigma(T_{\text{TS,in}} + T_{\text{amb}})(T_{\text{TS,in}}^2 + T_{\text{amb}}^2) \tag{3.30}$$

For a conservative estimate, the surface temperature of the single phase portion of the interface manifold is assumed to be at the measured inlet temperature (14.5°C), which does not require an iterative solution. The emissivity (ε) is assumed to be 1, and, for the representative inlet and ambient temperatures of 14.5°C and 22.4°C, respectively, the radiation heat transfer coefficient is 5.63 W m^{-2} K^{-1}. The resulting radiation thermal resistance is 46.4 K W^{-1} for the vertical surfaces and 227 K W^{-1} for the horizontal surfaces for the single phase portion of the interface manifold.

The convection thermal resistance is calculated as follows:

$$R_{conv,i} = \frac{1}{h_{NC,i} A_{S,i}} \tag{3.31}$$

The vertically oriented surface area was given from the solid model, and the natural convective heat transfer coefficient is determined from [34]:

$$h_{NC,vert} = 0.68 + \frac{0.67 \cdot Ra^{1/4}}{[1+(\frac{0.492}{Pr_{air}})^{9/16}]^{4/9}} \frac{K_{air}}{L_C} \tag{3.32}$$
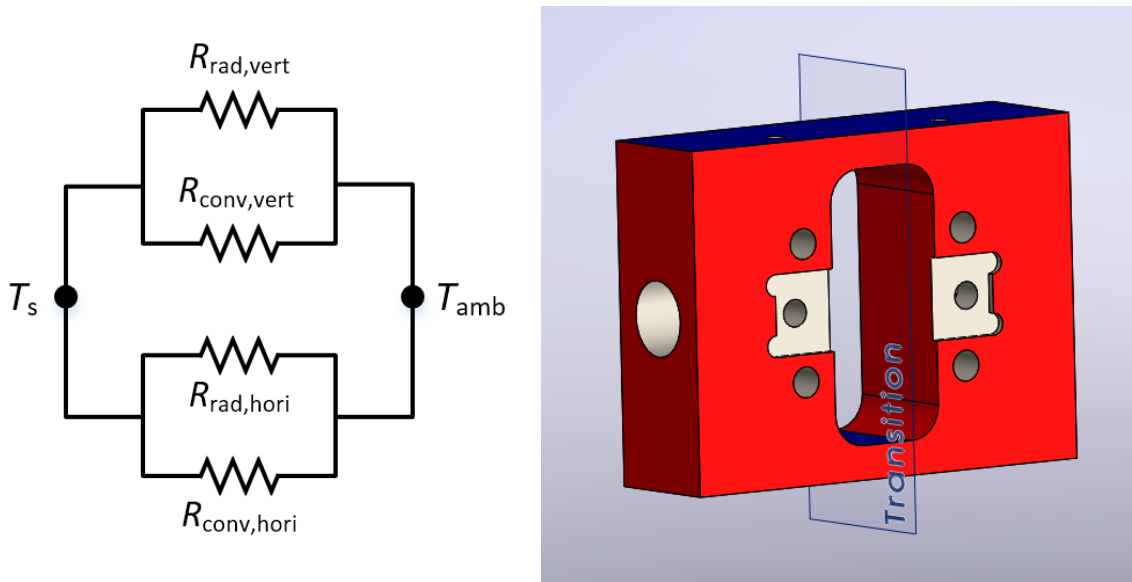
Figure 3-36: Left: Thermal resistance network of the test section interface; Right: Test section interface, vertical area is red, horizontal area is blue; left half is two-phase, right is single-phase

where the thermal conductivity and Prandtl number of air are 0.026 W m^{-1} K^{-1} and 0.708, respectively, for the single phase portion of the test section (T_f = 18.5°C). The vertical characteristic length (L_C) is 0.05 m, and the Rayleigh number is:

$$Ra = \frac{g\beta_{air}L_c^3[T_{TS,in} - T_{amb}]}{\nu_{air}\alpha_{t,air}} \tag{3.33}$$

The volumetric expansion coefficient at the film temperature of the single phase portion of the test facility is 0.0034 K^{-1}, while the kinematic viscosity and thermal diffusivity are 1.80×10^{-5} and 2.55×10^{-5} m^2 s^{-1}, respectively. Therefore, the Rayleigh number is 72.3×10^4, which yields a vertical heat transfer coefficient of 4.69 W m^{-2} K^{-1}, and a convective thermal resistance of 55.6 K W^{-1}. Using the radiation thermal resistance, the equivalent thermal resistance from the vertical surfaces is 25.3 K W^{-1} for the single phase portion of the interface manifold.

For the horizontal surface area, the natural convection heat transfer coefficient is [34]:

$$h_{NC,hori} = 0.54Ra^{1/4}\frac{K_{air}}{L_C} \tag{3.34}$$

The air properties are determined from the film temperature (18.5°C), the length scale is 0.033 m, and the Rayleigh number is calculated from Equation (3.33) and is 2.08×10^4. Therefore, the vertical natural convection heat transfer coefficient is 4.69 W m^{-2} K^{-1}, which is yields a thermal resistance of 252 K W^{-1}. Combined with the radiation thermal resistance, the equivalent horizontal thermal resistance is 119 K W^{-1} for the single phase portion of the interface manifold. Using equation (3.27), the equivalent thermal resistance from this region is 20.9 K W^{-1}, and the heat gain from the environment is calculated from equation (3.24), which is 0.379 W.

At this point, the fluid enters the test section (region 4). To conservatively estimate the loss here it is assumed that the insulating ceramic electrical harness is removed. In addition, the entire back side is assumed to be plain silicon at the heater temperature, and the entire front side glass is

73

assumed to be at the saturation temperature of the fluid at the transition location. For the sample

data point the heater temperature is 51.2°C, and the saturation temperature at the transition location

is 20.1°C. The thermal resistance (Figure 3-37) from the exposed surfaces to the ambient include

both convection and radiation and are calculated as follows:

$$R_{eq,i} = \frac{R_{conv}R_{rad}}{R_{conv} + R_{rad}}$$ (3.35)

These surfaces are both vertically oriented, therefore, the convection thermal resistance, heat transfer coefficient, and Rayleigh number are determined by equations (3.31), (3.32), and (3.33), respectively. The air properties on the silicon and glass side are evaluated at their respective film temperatures of 36.8°C and 21.2°C. These properties are summarized
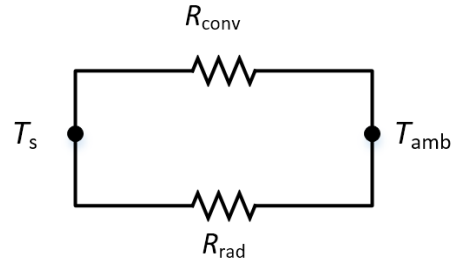
Figure 3-37:   Thermal resistance network of a single side of the test section

on Table 3-7. The surface area of each side of the test section is 2.16×10^{-4} m^2, and the length scale

(L_c) is 12 mm. The surface temperatures were conservatively assumed, and, therefore, an iterative

solution is not required. However, the surface temperature and air properties on each side of the

test section are different, and, thus, the loss from the silicon and glass sides are estimated

individually then summed as follows:

$$q_{loss} = q_{loss,Si} + q_{loss,glass}$$ (3.36)

where each of these losses are:

$$q_{loss,i} = \frac{T_{surf} - T_{amb}}{R_{eq,i}}$$ (3.37)

The equivalent resistance of the glass side is 427 K W^{-1}, where the convection and radiation

thermal resistances are 915 K W^{-1}, and 800 K W^{-1}, respectively. This results in a heat gain of

0.0053 W from the glass side. Similarly, the equivalent resistance of the silicon side is 301 K W^{-1}, where the convection and radiation thermal resistances are 537 K W^{-1}, and 684 K W^{-1}, respectively. This results in a loss of 0.096 W from the silicon side, for a total loss at the test section of 0.091 W.

Table 3-7:   Air properties evaluated at the film temperature on the silicon and glass sides

Property	Unit	Silicon	Glass
Kinematic Viscosity, ν_{air}	m^2 s^{-1}	2.01×10^{-5}	1.83×10^{-5}
Thermal Diffusivity, α_{air}	m^2 s^{-1}	2.85×10^{-5}	2.59×10^{-5}
Thermal Conductivity, K_{air}	W m^{-1} K^{-1}	0.027	0.026
Prandtl Number, Pr$_{air}$	-	0.706	0.708

The next region that transfers heat with the environment is the test section interface that is in close proximity to the two-phase mixture (region 5). The loss in this section is estimated the exact same way as the single-phase region 3, except the surface temperature is conservatively assumed to all be equal to the measured thermocouple temperature (location shown in Figure 3-33). This location was chosen for the thermocouple because the PEEK has the thinnest cross section. The thermal resistances of the horizontal and vertical surfaces are computed from the convection and radiation terms given in equations (3.27) to (3.34), and the heat loss is computed from equation (3.37) using the measured surface temperature and ambient temperatures. For the sample point the measured surface was 16.7°C. For the vertical surfaces the Rayleigh number is 5.13×10^4, corresponding with a convection heat transfer coefficient of 4.35 W m^{-2} K^{-1}, and a convective thermal resistance of 60.1 K W^{-1}. For the horizontal surfaces the Rayleigh number is 1.47×10^4, corresponding with a convection heat transfer coefficient of 4.66 W m^{-2} K^{-1}, and a convective thermal resistance of 274 K W^{-1}. Again, the radiation heat transfer coefficient is the same regardless of surface orientation, which is 5.69 W m^{-2} K^{-1}. The radiation thermal resistance of the vertical surfaces is 45.9 K W^{-1}, and the horizontal surfaces is 224 K W^{-1}. Using the same resistance network shown in Figure 3-36, the resulting equivalent thermal resistance is 21.5 K

W^{-1}, which corresponds to a heat gain from the two-phase region of the test section interface of 0.263 W.

After the fluid leaves the manifold, it enters the outlet Teflon flow sight (region 6), and the loss is estimated in the same way as the upstream flow sight. To overestimate the loss from this region, the temperature of the inner wall was set to the measured outlet temperature ($T_{\text{TS,out}}$, 15.1°C). The thermal resistance network shown in Figure 3-35 also applies to this region. The conduction thermal resistance is determined from equation (3.15), which is 3.93 K W^{-1}. The convection thermal resistance is calculated from equations (3.16) through (3.20), and surface temperature (T_s) is determined iteratively to be 15.4°C. For natural convection, the Rayleigh number is 131, and the heat transfer coefficient is 0.59 W m^{-2} K^{-1}, yielding a convection thermal resistance of 1.10×10^3 K W^{-1}. The radiation thermal resistance is calculated from equations (3.22) and (3.23). The radiation heat transfer coefficient is 5.65 W m^{-2} K^{-1}, which yields a radiation thermal resistance of 116 K W^{-1}. Therefore, the equivalent thermal resistance of the Teflon sight is 109 K W^{-1}, and the final heat gain through this section is 0.066 W.

Finally, the last region to consider is the insulated hose from the Teflon flow sight back to the test facility (region 7). This is calculated using the same methodology used for the insulated hose on the upstream side (region 1). The thermal resistance network shown in Figure 3-34 applies to this region. The individual terms are determined from equations (3.14) to (3.25). In this case, the solution yielded a surface temperature of 21.4°C, which corresponds to a Rayleigh number of 7.45×10^4, natural convection heat transfer coefficient of 0.14 W m^{-2} K^{-1}, and a convection thermal resistance of 63.0 K W^{-1}. The radiation heat transfer coefficient is 5.83 W m^{-2} K^{-1}, which yields a radiation thermal resistance of 1.51 K W^{-1}. Therefore, the equivalent thermal resistance of the downstream hose is 10.8 K W^{-1}, and the final heat gain through this section is 0.667 W.

The total loss in the test section is now calculated from the sum of each individual component as follows:

$$q_{loss,tot} = q_{loss,hose,in} + q_{loss,tef,in} + q_{loss,SP,int} + q_{loss,test} + q_{loss,TP,int} + q_{loss,tef,out} + q_{loss,hose,out}$$

(3.38)

For the representative data point, this yields an overall gain of 2.07 W from the environment to the test fluid. This heat transfer from the environment is used in the energy balance described in the next section to calculate the outlet vapor quality.

3.4.3. Effective Heat Rate and Vapor Quality

The effective heat rate is the joule heating from the heater minus the environmental heat loss. Using this quantity, the outlet vapor quality of the two-phase mixture can be calculated. The methodologies used to calculate both of these are detailed in this section, and the uncertainty of these calculations are detailed in the next section. The same representative data point is used to demonstrate these calculation procedures.

To determine joule heating, the electrical potential drop across and current through the thin film heater are required. To minimize bias in the simultaneous measurement of these two parameters, a 4-wire configuration is used to measure current and voltage separately (Figure 3-38). The electrical leads from the test section electrical harness are connected to a power supply
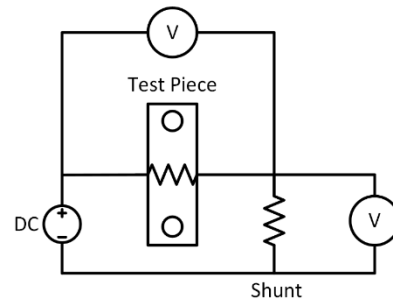
Figure 3-38:   Schematic of the 4-wire voltage measurement scheme

through a high accuracy shunt resistor to measure the current. The wire connecting the electrical harness to the screw terminal is 24 gauge and 0.15 m in length. This length and diameter minimizes both heat loss due to axial heat conduction and power dissipation by joule heating in the wire. Between the screw terminal the wire and the power supply, 12-gauge wire is used to completely

eliminate the possibility of joule heating, as axial conduction of heat is no longer an issue between these two locations. To determine the current through the heater, Ohm's law is applied across the shunt resistor:

$$I_{app} = \frac{V_{shunt}}{R_{shunt}} \tag{3.39}$$

The resistance of the shunt is 0.1 Ω, and the potential difference across the shunt is measured by the DAQ system to be 0.273 V for the representative data point, which yields an applied current of 2.73 A. The applied power (q_{app}) is the product of applied current and potential difference across the heater, less any heat that conducts up the electrical wires, as follows:

$$q_{app} = I_{app}V_{He} - 2q_{wire,cond} \tag{3.40}$$

where the potential difference across the heater (V_{He}) is given by:

$$V_{He} = V_{tot} - 2V_{wire} \tag{3.41}$$

The total potential difference measured by the DAQ system is 25.55 V, while the potential of the wire is calculated from Ohm's law:

$$V_{wire} = I_{app}R_{wire} \tag{3.42}$$

The resistance of the wire is determined from the electrical resistivity of copper and the wire geometry as follows:

$$R_{wire} = \rho_{e,cu}\frac{L_{wire}}{A_{wire}} \tag{3.43}$$

The electrical resistivity of copper is conservatively evaluated at 60°C to be 1.95×10^{-8} Ω m, the length of the wires are 0.15 m, and the cross sectional area (A_{wire}) of a 24 gauge diameter (0.511 mm) is 1.96×10^{-7} m^2. Therefore, the resistance of the wire is 0.015 Ω, which yields a voltage drop

across each wire of 0.041 V. From equation (3.41), the potential difference across the heater is 25.47 V.

For the conductive losses it was assumed that the copper leads were at the measured heater temperature at the heater to wire junction, and that the temperature at the end of the 24 gauge wire was equal to the ambient temperature. This large temperature gradient over predicts the conductive loss, which is calculated as follows:

$$q_{\text{wire,cond}} = K_{\text{Cu}} A_{\text{wire}} \frac{(T_{\text{He}} - T_{\text{amb}})}{L_{\text{wire}}} \tag{3.44}$$

For the sample data point, the heater temperature is 51.2°C, and the ambient temperature is 22.4°C. At the heater temperature, the thermal conductivity of copper is 395 W m^{-1} K^{-1}, and, therefore, the estimated loss to conduction for each wire is 0.015 W. As a result, the applied heat rate (q_{app}) is 69.50 W (equation (3.40)). Finally, the effective heat rate from heater into the test fluid is determined by subtracting the environmental heat loss as follows:

$$q_{\text{He}} = q_{\text{app}} - q_{\text{loss,env}} \tag{3.45}$$

In the previous section, the environmental heat gain was 2.07 W. This heat gain occurred between the two temperature measurement points, where the thermodynamic states are known. By calculating the heat duty using this method, it is assumed that all of this gain (or loss in some test conditions) occurred at the test section. In Section 4.2, an uncertainty of 50% is asserted upon this loss to demonstrate that this assumption does not have a significant effect on the calculated heat transfer coefficient. Using equation (3.45) the effective heat rate into the test section (q_{He}) for the representative data point is 71.57 W.

The vapor quality exiting the test section can now be calculated. Because the fluid enters as a subcooled liquid, heat is first transferred to the fluid to raise the temperature from a subcooled liquid to a saturated liquid at the transition location. Thereafter, the remaining heat is used to boil

the fluid to a liquid-vapor mixture. The vapor quality is the ratio of the mass flow rate of the vapor to the total mass flow rate of the fluid, and fhe following expression is used to determine the outlet vapor quality for the two phase mixture:

$$\chi_{e} = \frac{q_{He} - \dot{m}(h_{trans} - h_{TS,in})}{h_{fg}\dot{m}} \qquad (3.46)$$

The mass flow rate for the sample point is 99.8 g min^{-1}, and the enthalpy at the inlet and transition is evaluated from fluid properties. The inlet enthalpy at a temperature of 14.5°C and 623 kPa is 71.7 kJ kg^{-1}, and at the transition temperature 20.1°C the saturated liquid enthalpy is 79.4 kJ kg^{-1}. The enthalpy of vaporization is evaluated at the mean temperature between the saturation temperature at transition and the measured outlet temperature of 15.3°C, which is 186 kJ kg^{-1}. The resulting outlet vapor quality in this sample data point is 18.95%. Prior to determining the heat transfer coefficient from these quantities, an assessment of uncertainty in this vapor quality and test section heat duty is discussed in the following section.

3.4.4. Uncertainty

To assess the accuracy of the test condition, an uncertainty analysis is performed on each data point. The uncertainty for measured variables, calculated variables, and results from numerical models are each calculated differently, and the methodology for each of these is described. For example, the uncertainty in outlet vapor quality, which is calculated from equation (3.46), depends on a variety of measured variables, including voltage drop across the heater and the shunt resistor and inlet temperature and pressure, as well as the saturation transition pressure, which requires numerical analysis of the flow field in the outlet header.

For measured values, uncertainty is comprised of two components: bias and precision. The total uncertainty for a measured variable is determined from the combined effects of these using the standard propagation of uncertainty as follows:

$$U_{\bar{X}} = \sqrt{B_{\bar{X}}^2 + P_{\bar{X}}^2} \tag{3.47}$$

While the bias is given by the manufacturer or determined through calibration, the precision

uncertainty is due to measurement variation within the data set. It is determined by the standard

deviation, number of samples, and t-statistic as follows:

$$P_{\bar{X}} = t_{\text{stat}} \frac{S_{\bar{X}}}{\sqrt{N}} \tag{3.48}$$

In all cases, the precision uncertainty was calculated at a confidence level (α_s) of 95%. For

example, the measured inlet pressure for the representative data point is 623 kPa, which was an

average based on 82 samples taken over 5 minutes. The data has a two-tailed t-statistic is 1.99 and

a sample standard deviation of 0.39, which yields a precision uncertainty of 0.086. With the

manufacturer reported bias of the instrument (0.08% of full scale: 0.551 kPa), the uncertainty in

inlet pressure is ±0.558 kPa. This process is repeated for all measured values, and a summary of

relevant results is given in Table 3-8.

To estimate the uncertainty in the numerical pressure drop model based on the geometric

discretization, the procedure proposed by Celik et al. [71] was employed. For this method, the

model is solved at three different mesh sizes and the change in value of pressure drop is

determined. In the current study, the grid refinement ratio (r, the ratio of average element size

Table 3-8:   Uncertainty in relevant measured values

Description	Value	Bias	Precision	Uncertainty	Unit
Inlet pressure ($P_{\text{TS,in}}$)	623	0.551	0.086	0.558	kPa
Outlet pressure ($P_{\text{TS,out}}$)	561	0.551	0.752	0.931	kPa
Potential shunt (V_{shunt})	0.273	0.0014	7.62E-6	0.0014	V
Potential heater (V_{He})	25.55	0.092	0.017	0.094	V
Inlet temperature ($T_{\text{TS,in}}$)	14.5	0.36	0.0033	0.36	°C
Outlet temperature ($T_{\text{TS,out}}$)	15.1	0.31	0.01	0.31	°C
Mass flow rate ($\dot{m}$)	99.8	0.50	0.068	0.50	g min^{-1}

between two models) was chosen to be 1.5, which exceeds the minimum suggested value Celik et al. (*i.e.*, 1.3). The approximate relative error between mesh sizes is defined as follows:

$$e_a^{21} = \left| \frac{dP_2 - dP_1}{dP_2} \right|$$

(3.49)

The error in numerical model is then estimated by the fine-grid convergence index:

$$GCI_{fine}^{21} = \frac{1.25 e_a^{21}}{r_{21} - 1}$$

(3.50)

For a ratio of 1.5 between elements sizes, in both the manifold and interface, the approximate relative error is 1.42%, resulting in the fine-grid convergence index of ±3.56% (Table 3-9).

Table 3-9:   Numerical model uncertainty analysis from discretized grid

Mesh	Ave Element Size [μm]	# Elements	dP [kPa]	Relative Error
1	150	3.28×10^5	2.60	-
2	100	7.80×10^5	2.64	1.42%
3	66.7	2.18×10^6	2.61	1.03%

The uncertainty for a calculated quantity "R" is based on the uncertainty in each dependent term "x" weighted by its respective partial derivative as follows:

$$U_R = \sqrt{\sum_{i=1}^{N} (U_{\overline{X}_i} \frac{\partial R}{\partial \overline{X}_i})^2}$$

(3.51)

Using equation (3.46), the following expression is used to evaluate the uncertainty in outlet vapor quality:

$$U_{\chi_e} = \sqrt{(U_{q_{he}} \frac{\partial \chi_e}{\partial q_{he}})^2 + (U_{\dot{m}} \frac{\partial \chi_e}{\partial \dot{m}})^2 + (U_{h_{TS,in}} \frac{\partial \chi_e}{\partial h_{TS,in}})^2 + (U_{h_{trans}} \frac{\partial \chi_e}{\partial h_{trans}})^2 + (U_{h_{fg}} \frac{\partial \chi_e}{\partial h_{fg}})^2}$$

(3.52)

where the partial derivatives for each term are readily evaluated as follows:

$$\frac{\partial \chi_e}{\partial q_{He}} = \frac{1}{h_{fg} \dot{m}} = \frac{1}{(186366 \cdot J \cdot kg^{-1})(0.00166 \cdot kg \cdot s^{-1})} = 0.00323 \cdot W^{-1}$$

(3.53)

$$\frac{\partial \chi_e}{\partial \dot{m}} = -\frac{q_{He}}{h_{fg} \dot{m}^2} = -\frac{71.57 \cdot W}{(186366 \cdot J \cdot kg^{-1})(0.00166 \cdot kg \cdot s^{-1})^2} = -139.4 \cdot s \cdot kg^{-1} \quad (3.54)$$

$$\frac{\partial \chi_e}{\partial h_{trans}} = -\frac{1}{h_{fg}} = -\frac{1}{186366 \cdot J \cdot kg^{-1}} = -5.37 \times 10^{-6} \cdot kg \cdot J^{-1} \quad (3.55)$$

$$\frac{\partial \chi_e}{\partial h_{TS,in}} = \frac{1}{h_{fg}} = \frac{1}{186366 \cdot J \cdot kg^{-1}} = 5.37 \times 10^{-6} \cdot kg \cdot J^{-1} \quad (3.56)$$

$$\begin{aligned}
\frac{\partial \chi_e}{\partial h_{fg}} &= -\frac{q_{He} - \dot{m}(h_{trans} - h_{TS,in})}{\dot{m} h_{fg}^2} \\
&= \frac{71.57 \cdot W - (0.00166 \cdot kg \cdot s^{-1})(79432 \cdot J \cdot kg^{-1} - 71708 \cdot J \cdot kg^{-1})}{(0.00166 \cdot kg \cdot s^{-1})(186366 \cdot J \cdot kg^{-1})^2} \\
&= -1.02 \times 10^{-6} \cdot kg \cdot J^{-1}
\end{aligned} \quad (3.57)$$

The uncertainty in all quantities in equation (3.52) require further analysis, except mass flow rate because it was measured; each of these terms are discussed as follows.

The uncertainty in the effective heat rate (q_{He}, equation (3.45)) is dependent on both shunt and heater potential drops, the environmental loss ($q_{loss,tot}$), and the wire conduction heat loss ($q_{wire,cond}$). The propagated uncertainty is calculated as follows:

$$U_{q_{He}} = \sqrt{(U_{V_{shunt}} \frac{\partial q_{He}}{\partial V_{shunt}})^2 + (U_{V_{He}} \frac{\partial q_{He}}{\partial V_{He}})^2 + (U_{q_{loss,env}} \frac{\partial q_{He}}{\partial q_{loss,env}})^2 + (U_{q_{wire,cond}} \frac{\partial q_{He}}{\partial q_{wire,cond}})^2} \quad (3.58)$$

For a conservative estimate, the uncertainty in the environmental and wire heat conduction losses are asserted to be ±50%. The potential drop across the shunt and heater are measured quantities (Table 3-8), and the resulting uncertainty in effective heat rate is ±0.894 W (±1.28%).

The uncertainty in the test section inlet enthalpy ($h_{TS,in}$) is dependent on the temperature and pressure measurements, as follows:

$$U_{h_{TS,in}} = \sqrt{(U_{T_{TS,in}} \frac{\partial h_{TS,in}}{\partial T_{TS,in}})^2 + (U_{P_{TS,in}} \frac{\partial h_{TS,in}}{\partial P_{TS,in}})^2} \quad (3.59)$$

The uncertainty in both measured quantities was given on Table 3-8, the partial derivatives for the sample case are equivalent to 0.133 and 1384 for the inlet pressure and temperature, respectively. This results in an uncertainty in inlet enthalpy of ±498 J kg^{-1} ($\pm0.70\%$).

The uncertainty in the enthalpy at the transition location is determined first by applying equation (3.51) to equations (3.12) and (3.13) to determine the single phase pressure drop from the transition location to the outlet pressure transducer for the representative single phase data point as follows:

$$U_{dP_{\text{const}}} = \sqrt{(U_{dP_{\text{ch}}} \frac{\partial dP_{\text{const}}}{\partial dP_{\text{ch}}})^2 + (U_{dP_{\text{exp}}} \frac{\partial dP_{\text{const}}}{\partial dP_{\text{exp}}})^2 + (U_{dP_{\text{out}}} \frac{\partial dP_{\text{const}}}{\partial dP_{\text{out}}})^2} \qquad (3.60)$$

The single-phase channel pressure drop (equation (3.2)) uncertainty is estimated from the following:

$$U_{dP_{\text{ch}}} = \sqrt{(U_f \frac{\partial dP_{\text{ch}}}{\partial f})^2 + (U_{x_{\text{trans}}} \frac{\partial dP_{\text{ch}}}{\partial x_{\text{trans}}})^2 + (U_{D_{\text{H}}} \frac{\partial dP_{\text{ch}}}{\partial D_{\text{H}}})^2 + (U_{\rho_{\text{l}}} \frac{\partial dP_{\text{ch}}}{\partial \rho_{\text{l}}})^2 + (U_{u_{\text{ave}}} \frac{\partial dP_{\text{ch}}}{\partial u_{\text{ave}}})^2} \quad (3.61)$$

where the uncertainty in the friction factor (equation (3.4)) is determined from:

$$U_f = \sqrt{\begin{array}{l}(U_{w_{\text{ch}}} \frac{\partial f}{\partial w_{\text{ch}}})^2 + (U_{h_{\text{ch}}} \frac{\partial f}{\partial h_{\text{ch}}})^2 + (U_{\dot{m}} \frac{\partial f}{\partial \dot{m}})^2 + (U_{T_{\text{TS,in}}} \frac{\partial f}{\partial T_{\text{TS,in}}})^2 + \\ (U_{T_{\text{TS,out}}} \frac{\partial f}{\partial T_{\text{TS,out}}})^2 + (U_{P_{\text{TS,in}}} \frac{\partial f}{\partial P_{\text{TS,in}}})^2 + (U_{P_{\text{TS,out}}} \frac{\partial f}{\partial P_{\text{TS,out}}})^2\end{array}} \qquad (3.62)$$

The uncertainty in geometric parameters is estimated as ±5 µm. The other parameters are provided on Table 3-8, and the resulting uncertainty in friction factor is $\pm2.60\%$. The uncertainty in transition location is determined from equations (3.47) and (3.48) where the bias is derived from the resolution of the microscope lens 1.67 µm per pixel, and the precision uncertainty of variation in location ±19.4 µm. The resulting uncertainty in transition location is ±19.5 µm. The uncertainty in hydraulic diameter is determined from:

$$U_{D_H} = \sqrt{(U_{w_{ch}} \frac{\partial D_H}{\partial w_{ch}})^2 + (U_{h_{ch}} \frac{\partial D_H}{\partial h_{ch}})^2} \tag{3.63}$$

where the uncertainty of these measured parameters are again ±5 µm, which yields an uncertainty in hydraulic diameter of ±6.67 µm (±9.07%). The uncertainty in liquid density (ρ_l) is determined from the inlet and outlet temperatures and pressures as follows:

$$U\rho_l = \sqrt{(U_{T_{TS,in}} \frac{\partial \rho_l}{\partial T_{TS,in}})^2 + (U_{P_{TS,in}} \frac{\partial \rho_l}{\partial P_{TS,in}})^2 + (U_{T_{TS,out}} \frac{\partial \rho_l}{\partial T_{TS,out}})^2 + (U_{P_{TS,out}} \frac{\partial \rho_l}{\partial P_{TS,out}})^2} \tag{3.64}$$

The uncertainty in each of these measured parameters is given on Table 3-8, and the resulting uncertainty in the mean density is ± 0.86 kg m^{-3} (±0.069%). The uncertainty in average velocity (u_{ave}, equation (3.3)) is given by:

$$U_{u_{ave}} = \sqrt{(U_{w_{ch}} \frac{\partial u_{ave}}{\partial w_{ch}})^2 + (U_{h_{ch}} \frac{\partial u_{ave}}{\partial h_{ch}})^2 + (U_{\dot{m}} \frac{\partial u_{ave}}{\partial \dot{m}})^2} \tag{3.65}$$

The geometric uncertainties remain at ±5 µm, and the mass flow rate uncertainty is ±0.5 g min^{-1}, which results in an uncertainty of ± 0.14 m s^{-1} (±11.4%). With these terms, the uncertainty in the channel pressure drop, equation (3.61), is evaluated as ±1.45 kPa (31.9%).

The uncertainty in the expansion pressure drop (dP_{exp}, equation (3.8)) is determined from:

$$U_{dP_{exp}} = \sqrt{\begin{array}{l} (U_{w_{ch}} \frac{\partial dP_{exp}}{\partial w_{ch}})^2 + (U_{h_{ch}} \frac{\partial dP_{exp}}{\partial h_{ch}})^2 + (U_{w_{man}} \frac{\partial dP_{exp}}{\partial w_{man}})^2 + (U_{h_{man}} \frac{\partial dP_{exp}}{\partial h_{man}})^2 + \\ (U_{u_{ave}} \frac{\partial dP_{exp}}{\partial u_{ave}})^2 \end{array}} \tag{3.66}$$

The uncertainty in all geometric parameters is ±5 µm, and the uncertainty in average velocity was determined by equation (3.65) to be ± 0.14 m s^{-1}. The resulting uncertainty in expansion pressure drop is estimated as ±105 Pa (45.2%). The uncertainty in the collective pressure drop in the manifold and interface (dP_{out}) is equal to the fine grid convergence index (±3.56%). Finally,

equation (3.60) can be evaluated, which results in a combined uncertainty in the single phase pressure drop of 1.74 kPa (3.51%). Now, the uncertainty in transition pressure (equation (3.13)) is determined as follows:

$$U_{P_{\text{trans}}} = \sqrt{(U_{dP_{\text{const}}} \frac{\partial P_{\text{trans}}}{\partial dP_{\text{const}}})^2 + (U_{P_{\text{TS,in}}} \frac{\partial P_{\text{trans}}}{\partial P_{\text{TS,in}}})^2} \tag{3.67}$$

The inlet pressure uncertainty was calculated to be ±0.558 kPa (0.09%), which results in a transition pressure uncertainty of 1.83 kPa (0.32%). At the transition point the vapor quality is zero, and, thus, the saturated liquid enthalpy at the transition pressure is used. Te uncertainty in this term is solely based on the transition pressure as follows:

$$U_{h_{\text{trans}}} = U_{P_{\text{sat}}} \frac{\partial h_{\text{trans}}}{\partial P_{\text{sat}}} \tag{3.68}$$

This is evaluated as ±145 J kg^{-1} (±0.18%). The final term is the uncertainty in latent heat of vaporization, which is estimated from:

$$U_{h_{\text{fg}}} = \sqrt{(U_{T_{\text{sat}}} \frac{\partial h_{\text{fg}}}{\partial T_{\text{sat}}})^2 + (U_{T_{\text{TS,out}}} \frac{\partial h_{\text{fg}}}{\partial T_{\text{TS,out}}})^2} \tag{3.69}$$

The saturated liquid case condition is used at the mean temperature between the transition and measured outlet temperature. The saturation temperature is determined solely from the pressure at the transition location, and thus, the uncertainty is determined by the following:

$$U_{T_{\text{sat}}} = U_{P_{\text{sat}}} \frac{\partial T_{\text{sat}}}{\partial P_{\text{sat}}} \tag{3.70}$$

This is evaluated as ±0.103°C (±0.51%) for the sample case, which allows equation (3.69) to be evaluated: the uncertainty in heat of vaporization is ±199 J kg^{-1} (±0.11%). Equation (3.52) can now be calculated, which yields an overall uncertainty in outlet vapor quality of ±0.0053 (2.78%). Over all 15 data points the range in relative uncertainty of outlet vapor quality is from ±1.88% to

±12.83% with an average of ±4.67%. The data points with the highest uncertainty were those with relatively low heat duty and vapor quality. In the next section the test conditions for the data collected in the present study are summarized.

3.4.5. Summary of Test Conditions

The test conditions, and corresponding uncertainty, are presented in this section. For the 25°C saturation temperature tests, the exiting vapor quality is plotted as a function of effective test section heat duty in Figure 3-39. Similar plots are found for 20°C and 15°C saturation temperatures in Figure 3-40 and Figure 3-41, respectively. The exiting vapor quality is comparable at similar effective heat rates across the three saturation temperatures. As expected, the exiting vapor quality decreases with increasing mass flow rate (Figure 3-40). With the test conditions established, the next chapter will focus on the methodology for extracting the heat transfer coefficient from this data.
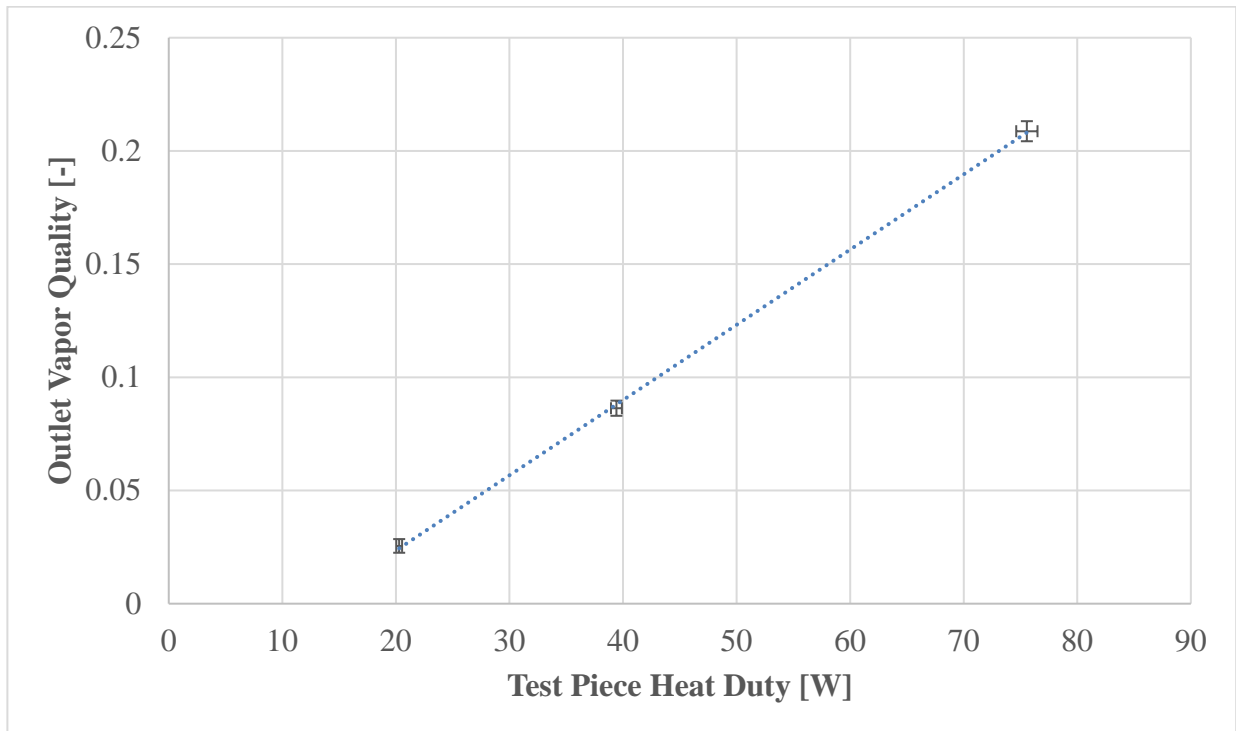
Figure 3-39:   Test conditions at $T_{sat} = 25°C$; $\dot{m} = 100$ g min^{-1}
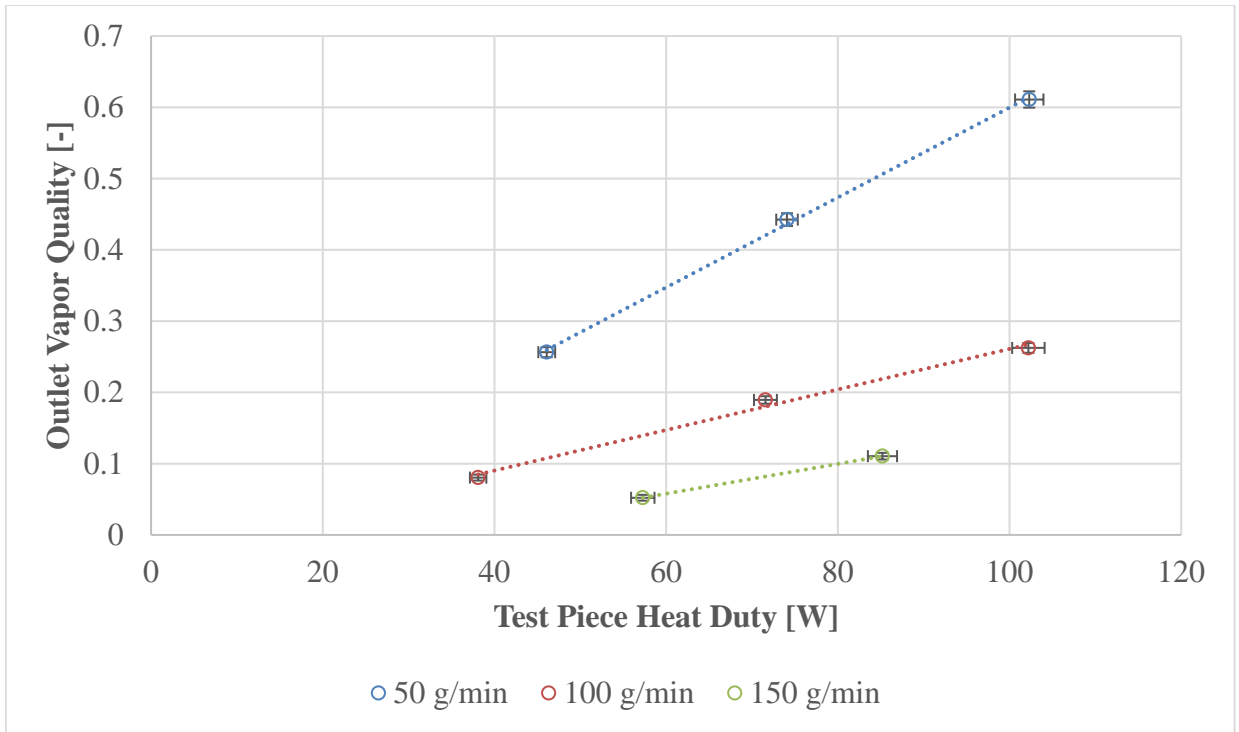
Figure 3-40: Test conditions at $T_{\text{sat}} = 20°C$; $\dot{m} = 50 - 150$ g min^{-1}
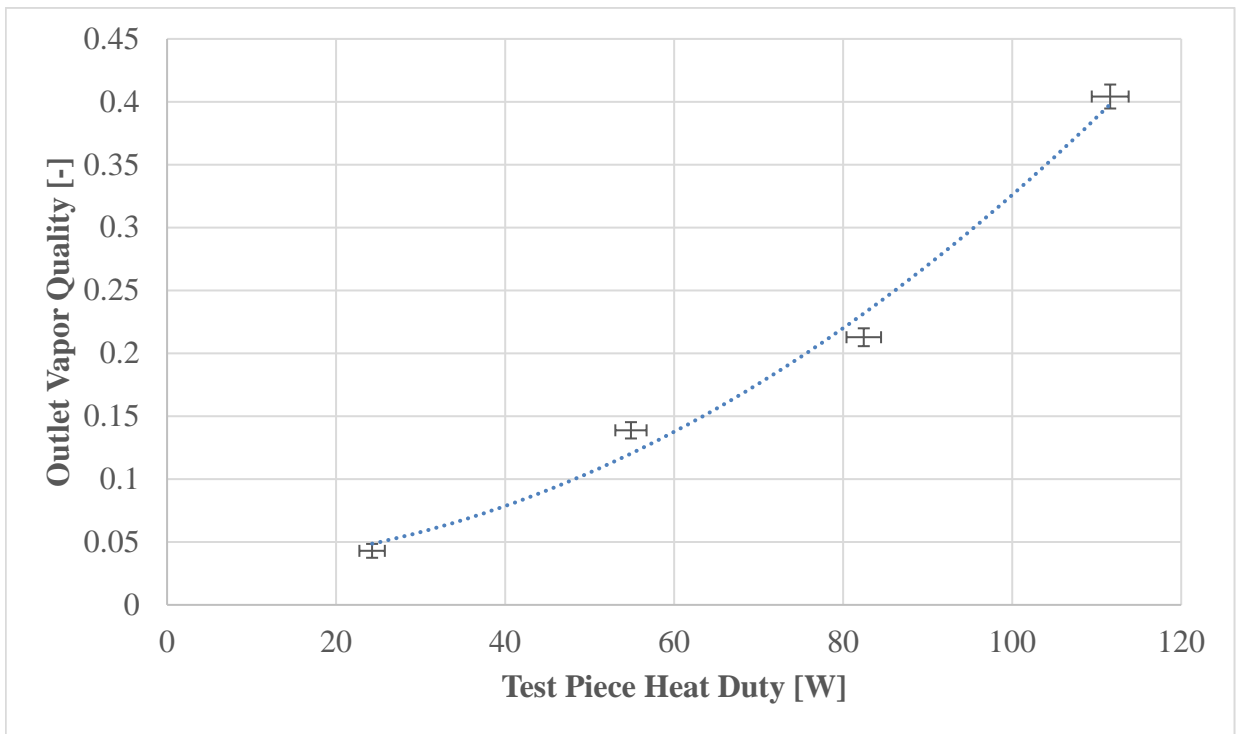
Figure 3-41: Test conditions at $T_{\text{sat}} = 15°C$; $\dot{m} = 100$ g min^{-1}

CHAPTER 4. DATA REDUCTION AND ANALYSIS

In the previous chapter, the methodologies for accurately determining the test section heat duty, outlet vapor quality, surface temperature profile, two-phase transition location, and the transition saturation temperature were discussed. In this chapter, the method for calculating the average heat transfer coefficient from these terms is shown in detail. As discussed in Chapter 2, most prior studies on boiling heat transfer develop correlations that assume uniform heat flux along each channel and/or estimate channel surface temperatures from a 1D conduction analysis. Unfortunately, these approaches are inaccurate for the current study because the small heater dimensions (1 mm $\times$ 10 mm) and high heat fluxes (up to 1.1 kW cm^{-2}) yield significant heat spreading along the microchannel array. As a result, a multi-dimensional numerical method is developed to extract the boiling heat transfer coefficients from the data collected in the present study. In addition, to calculate this heat transfer coefficient, the local fluid saturation temperature must be known. Because the test section used here has complex inlet and outlet manifolds and measurement of the local pressure is impractical, accurately calculating the local fluid saturation temperature is challenging. Therefore, several estimates for extracting the local saturation pressure are made to understand the impact on the calculated boiling heat transfer coefficient.

This chapter is organized as follows. First, the numerical method used to calculate the local boiling heat transfer coefficient is discussed in detail. This section includes an overview of the methods used to calculate the local fluid saturation temperature in the two-phase region, as well as a comparison to the proposed numerical technique and the methods used by prior investigations. To guide the discussion, the calculation methodology for the representative two-phase data point

89

used in chapter 3 is then presented. In the last portion of this chapter, the methodology to calculate

uncertainty in the average flow boiling heat transfer coefficient is presented.

4.1. Numerical Method to Extract Heat Transfer Coefficient

The most significant challenge associated with calculating the boiling heat transfer

coefficient is the heat spreading from within the test section. Heat is added to the test section by

passing current through a thin heater that has the same dimensions of a typical laser diode. As

shown in Figure 4-1, this heat is first conducted through the silicon wall underneath the channels,

then it is transferred to the fluid either through the base of the channel or the silicon fins. Due to

the very small dimensions of the test section and the relatively high thermal conductivity of the

silicon (149 W m^{-1} K^{-1}), heat can spread significantly throughout the test section. Furthermore, the

rate of heat spreading is also dependent on the local boiling heat transfer coefficient. Therefore, to
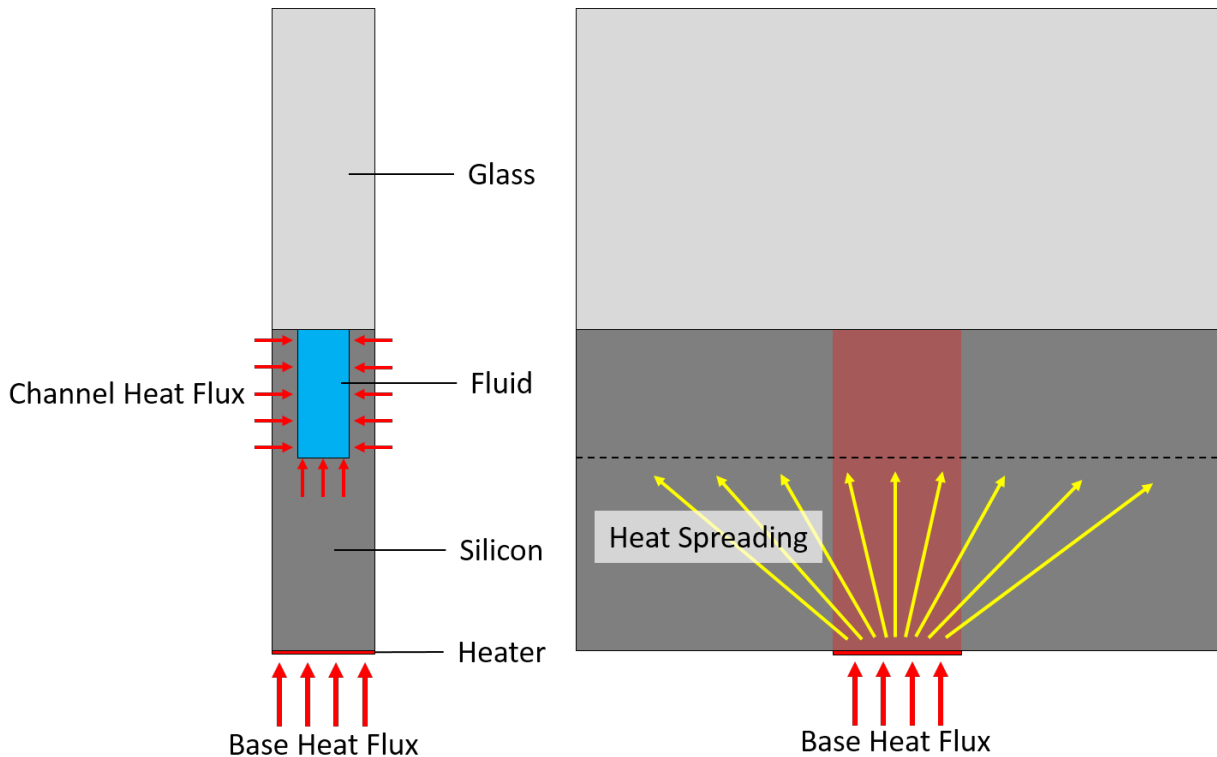
Figure 4-1:   Left: Heat addition through a single channel cross-section; Right: Yellow arrows show heat spreading from the area projected above the heater, red (length not to scale)

90

determine the heat transfer coefficient, it must be calculated iteratively with the 3D conduction heat transfer field using numerical methods.

To minimize computational effort, the following assumptions for the numerical analysis were made:

- The single-phase portion of the test section was not included in the analysis. This assumption was made possible because the transition location was known accurately (within a range of ±192 μm). See Section 3.2.2 for details.

- For the two-phase portion of the channels, an average boiling heat transfer coefficient boundary condition was applied. Although many authors [22, 29, 61] have shown that the heat transfer coefficient is dependent on the local heat flux, this assumption greatly simplified the analysis.

- The microchannel geometry was simplified to the lowest repeating unit: a half channel geometry (Figure 3-26). During the experiments, the heater temperature showed very little variation (within ±3°C in the most extreme case). In addition, there was no visual evidence suggesting flow maldistribution. Therefore, it is assumed that the heat spreading within the array was confined to a single channel along the flow direction and perpendicular to the flow direction and the plane of the heater.

- The heat transfer boundary conditions for the solid domain are as follows (Figure 4-2). The glass interface on the top and the exit end surface of the model (grey) are assumed to be adiabatic. Symmetry boundary conditions are applied to the sides of the repeating unit geometry and on surface at the transition location (yellow). For the bottom surface (orange, red), a polynomial fit to the measured surface temperature profile is applied directly to the

model. At the fluid interface (blue), a convection boundary condition with an average two-phase heat transfer coefficient is applied.

- Heat transfer from the heater to the two-phase fluid is assumed to occur only in the 45 μm × 200 μm channels.

- The fluid flow field for two-phase boiling is very complex. Therefore, no attempt was made to model the fluid domain in the microchannel geometry.

As these assumptions show, the channel surface temperature in contact with the fluid is not specified, and the heat flux is allowed to vary along this surface. This is fundamentally different than the methods used by most studies that assume a uniform heat flux and an average heater temperature. In these prior studies, the channel surface temperature is then determined by 1D conduction analysis, and the heat transfer coefficient is calculated between this temperature and
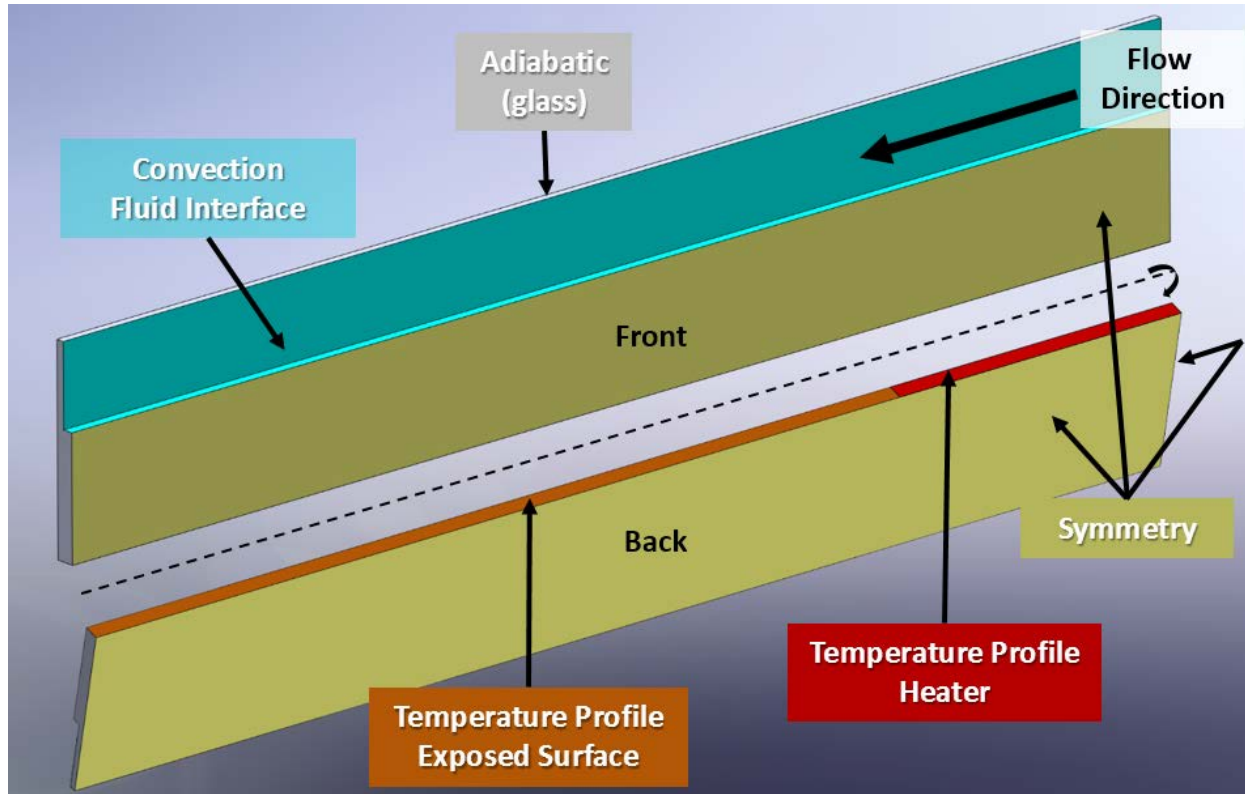
Figure 4-2:   Boundary conditions to the half channel heat transfer model

the estimated fluid temperature. In the current work, the measured surface temperature is applied to the outside surface of the channel, and the heat transfer coefficient is varied in the two-phase portion of the test section until the experimentally measured heat transfer rate matches the scaled heat transfer rate in the numerical model. However, this method requires knowledge of the local fluid saturation pressure and temperature, which is not directly measured here. In the present study, several methods are evaluated to determine the local fluid saturation pressure and temperature. In the next two sections, the methods used for determining the local fluid temperature and the iterative method for calculating the average heat transfer coefficient are discussed in detail.

4.1.1. Fluid Saturation Temperature Profiles

For a fixed two-phase heat duty, the local saturation temperature in the two-phase portion of the channels can strongly affect the required average boiling heat transfer coefficient. In addition, because it is a two-phase mixture, the local saturation temperature is dependent on the local fluid pressure. As shown in Chapter 3, the local saturation pressure at the transition location was calculated, which was based on the test section inlet pressure and the single phase pressure drop determined by analysis of a single phase data point at a heat rate just prior to boiling. The only other pressure measurement taken during the tests was the test section outlet pressure, which is substantially downstream of the channels in the test section (Figure 3-27). Furthermore, no two-phase pressure drop models exist for the geometry investigated in the current study. As a result, three different methods were used to estimate the local saturation pressure (Figure 4-3): (1) constant pressure from the transition location to the exit of the channels, (2) constant pressure drop from the transition location to the exit of the channels equal to the pressure difference between the calculated pressure at the transition location and the measured test section outlet pressure, and (3) the same method as (2) but with a reduction in the channel pressure loss due to fluid acceleration.

Because the saturation temperature decreases with pressure, the first method yields the highest average fluid temperature, and, therefore, the lowest temperature difference between the heater and fluid. At the same rate of heat transfer, this method will yield the highest heat transfer coefficient required to reject the two-phase test section heat duty. In contrast, because channel cross-sectional area is the smaller than the cross sectional area at the outlet pressure transducer, which increases its velocity and decreases its local pressure, the third method yields the largest temperature difference between heater and the fluid. Therefore, this method will predict the lowest average heat transfer coefficient. The second method will predict a value in between these two extremes. By analyzing these three methods, the range of possible heat transfer coefficient can be estimated to understand the maximum possible impact of the local pressure drop.

The outlet pressure is measured directly, and Section 3.4.1 discusses the method used to calculate the pressure at the transition location. Because the cross sectional area is smaller at the exit of the channels, the minimum possible pressure at the channel outlet for the third method is calculated from the following equation:

$$P_{out,min} = P_{TS,out} + dP_{accel} \tag{4.1}$$

The two-phase accelerational pressure drop is determined from the following [32]:

$$dP_{accel} = [\frac{G^2 \chi_e^2}{\rho_v \alpha_f} + \frac{G^2 (1-\chi_e)^2}{\rho_l (1-\alpha_f)}]_{tap} - [\frac{G^2 \chi_e^2}{\rho_v \alpha_f} + \frac{G^2 (1-\chi_e)^2}{\rho_l (1-\alpha_f)}]_{ch} \tag{4.2}$$

The mass flux at each of these locations is computed from:

$$G_i = \frac{\dot{m}}{A_i} \tag{4.3}$$

For the same sample two-phase data point used in chapter 3 (Table 3-6), the mass flow rate is 99.8 g min^{-1} and the cross sectional area of the channels and static pressure tap are 1.13×10^{-6} m^2 and 31.7×10^{-6} m^2, respectively. Thus, the channel mass flux (G_{ch}) is 1,479 kg m^{-2} s^{-1} and the outlet

94

mass flux (G_{tap}) is 52.5 kg m^{-2} s^{-1}. The outlet vapor quality (χ_e) is 18.95%, and the density at the outlet is estimated from saturated fluid properties at the measured temperature, 15.1°C (23.9 kg m^{-3} for the vapor, and 1,243 kg m^{-3} for the liquid). The estimated transition pressure for this sample point is 579 kPa, which yields a saturation temperature of 20.1°C and saturated liquid and vapor densities of 1,224 kg m^{-3} and 28.2 kg m^{-3}, respectively. The void fraction (α_f) of the channels and the pressure tap are computed with different correlations. In the channels, the void fraction is calculated by the following correlation for separated flow [72]:

$$\alpha_{f,ch} = [1 + (1 + 2Fr_1^{-0.2}\alpha_h^{3.5})(\frac{1-\chi}{\chi})(\frac{\rho_g}{\rho_1})]^{-1} \tag{4.4}$$

where the liquid Froude number (Fr_1) is:

$$Fr_1 = \frac{\bar{u}}{\sqrt{g_a L_c}} = \frac{G}{\rho_1 \sqrt{g_a L_c}} \tag{4.5}$$

The characteristic length (L_c) is the depth of fluid in the rectangular channel (200 μm), which yields a liquid Froude number of 26.85 in the channels. The homogeneous void fraction (α_h) is defined as follows [32]:

$$\alpha_h = [1 + (\frac{1-\chi}{\chi})(\frac{\rho_g}{\rho_1})]^{-1} \tag{4.6}$$

The homogeneous void fraction for the representative data point is 0.92, and the resulting void fraction (α_{ch}) in the channels is 0.87. Homogeneous flow was assumed at the outlet pressure tap, and the void fraction (α_{tap}) in this location is determined to be 0.91. This yields an accelerational pressure drop (dP_{accel}) of -12.8 kPa (equation (4.2)). Therefore, for the measured outlet pressure of 481 kPa, the lowest possible pressure at the channel is 468 kPa, which results in a worst case outlet saturation temperature ($T_{out,min}$) of 14.3°C.
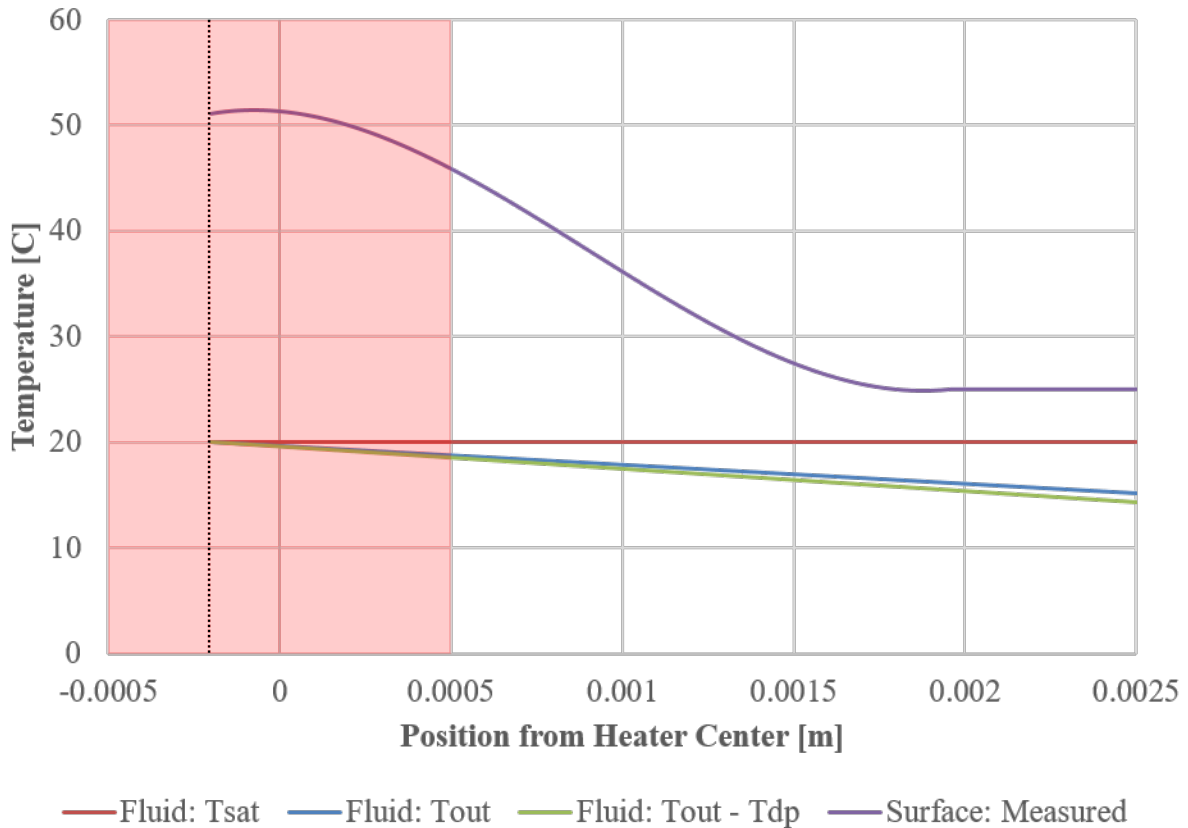
Figure 4-3: Sample temperature profiles, measured surface and all three assumed fluid profiles; the heater location is emphasized in red, the transition was at -0.2 mm

The resulting temperature profiles for these three methods are shown on Figure 4-3, and the equation inputs for the numerical model are shown in Table 4-1. Because the surface temperature profile can only be measured up to the end of the channels, the last 0.5 mm is at the measured average value. Near the junction between the temperature profile and the last measured temperature, the interpolated profile falls below the measured point by 0.14°C. This is not problematic because this accounts for only 1.3 - 2.8% of the temperature difference in this area, and < 11% of the heat is transferred over this area. These profiles are directly applied as boundary conditions in the numerical model as UDFs (User Defined Functions) in ANSYS Fluent. This is accomplished with a C script which first determines the centroid of each element on the applied surface. Then, the given function is evaluated at this location and the value applied to the element.

The next section discusses the iterative process used to calculate the average heat transfer coefficient for each one of these three temperature profiles.

Table 4-1:   Summary of temperature profiles used in the numerical model

Description	Function
Measured surface temperature	$T(x) = 7.14 \times 10^9 x^3 - 1.93 \times 10^7 x^2 - 3.00 \times 10^3 x + 51.3$
Constant T_{sat}	$T(x) = 20.08$
T_{sat} decays to $T_{\text{TS,out}}$	$T(x) = -1829x + 19.71$
T_{sat} decays to $T_{\text{out,min}}$	$T(x) = -2133x + 19.65$

4.1.2. Method for Calculating the Average Flow Boiling Heat Transfer Coefficient

As discussed above, the average two-phase heat transfer coefficient (h_{TP}) is unknown, which requires an iterative solution procedure. The iterative process begins with an initial guess for the average heat transfer coefficient, then solves the heat transfer model until the energy transferred to the fluid matches the experimental results. To calculate the two-phase heat rate ($q_{\text{He,TP,HTM}}$), the surface heat flux on the fluid interface (Figure 3-26) is integrated. This value is compared to the experimental two-phase heat rejection ($q_{\text{He,TP,exp}}$), which is scaled appropriately by:

$$q_{\text{He,TP,exp}} = (q_{\text{He}} - \dot{m}(h_{\text{trans}} - h_{\text{TS,in}})) \frac{w_{\text{HTM}}}{w_{\text{He}}} \tag{4.7}$$

For this representative two-phase data point, the effective heat rate is 71.57 W, the single-phase portion is 12.9 W, and the ratio between heat transfer model and full length is 0.004 (*i.e.*, 1 / 250 half channels, and ½ of the channel width). This results in a scaled experimental two-phase heat duty of 0.235 W. To determine convergence between the model and the experimental data, the residual between the model and experiment is calculated as follows:

$$res = \text{abs}(q_{\text{He,TP,HTM}} - q_{\text{He,TP,exp}}) \tag{4.8}$$
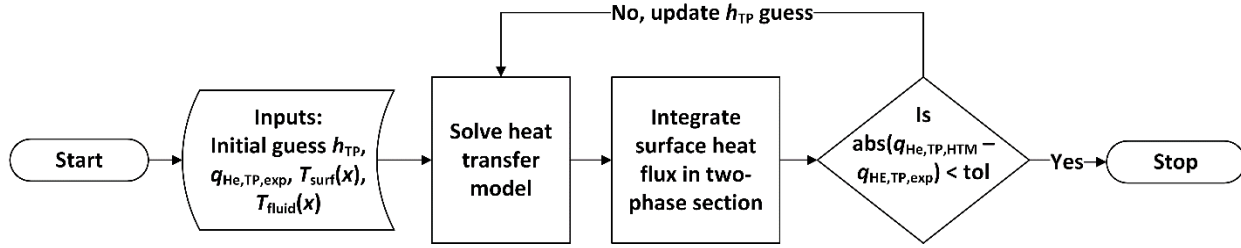
Figure 4-4:   Basic iterative solution process flow

The heat transfer coefficient guess is updated and the model is re-solved until the residual is smaller than the tolerance (1×10^{-4}). This process is required for each temperature profile method outlined in the previous section. Therefore, it was automated by Python scripting as summarized on Figure 4-4. The resulting heat transfer coefficients from the three different temperature profiles are then averaged together to estimate the performance at a given test condition. For the sample point, the flow boiling heat transfer coefficient ranged from 31.9 to 41.2 kW m^{-2} K^{-1}, with an average of 35.4 kW m^{-2} K^{-1} which was calculated from the following:

$$\bar{h}_{TP} = \frac{1}{N} \sum_{i=1}^{N} h_{TP,i}$$
(4.9)

The uncertainty associated with this average calculate heat transfer coefficient is discussed in the next section.

4.2. Estimated Heat Transfer Coefficient Uncertainty

The uncertainty of the numerically calculated heat transfer coefficient is estimated from the sensitivity to changes in fluid temperature profile, input values, and geometric discretization error from the meshing process. Two methodologies where used to estimate the uncertainty in the average heat transfer coefficient. The first methodology is more complex, requiring multiple numerical models to estimate the partial derivatives of heat transfer coefficient with respect to each variable. The second method is much simpler: it conservatively estimates the maximum possible

98

range of heat transfer coefficients by changing all variables simultaneously to yield minimum and maximum values. As shown below for a more extreme representative data point (Table 4-2), which yields the largest possible change in the calculated heat transfer coefficient, the simpler method yields a larger uncertainty, and is therefore used for all data points. The uncertainty associated with mesh size is also included for this simpler method.

Table 4-2:   Sample data point for uncertainty analysis method comparison

Parameter	Value	Units
Two-phase heat duty ($q_{He,TP}$)	95.01	W
Mass flow rate ($\dot{m}$)	50.64	g min^{-1}
Average heater surface temperature (T_{He})	62.32	C
Saturation temperature (T_{sat})	20.86	C
Measured outlet temperature ($T_{TS,out}$)	13.52	C
Worst case outlet temperature ($T_{out,min}$)	12.74	C
Transition location (x_{trans})	-0.2	mm
Outlet vapor quality (χ)	61.0	%

The more complex first method follows the procedure for estimating uncertainty in measured and calculated values presented in Section 3.4.4. The uncertainty in heat transfer coefficient is dependent on the applied power, surface temperature profile, fluid saturation, measured and minimum outlet temperatures, transition location, width of the channel/web, and the height of the channel. Therefore, the propagation of uncertainty is calculated as follows:

$$U_{h_{TP}} = \sqrt{ \begin{array}{l} (U_{q_{He,TP}} \frac{\Delta h_{TP}}{\Delta q_{He,TP}})^2 + (U_{T_{surf}} \frac{\Delta h_{TP}}{\Delta T_{surf}})^2 + (U_{T_{sat}} \frac{\Delta h_{TP}}{\Delta T_{sat}})^2 + \alpha(U_{T_{TS,out}} \frac{\Delta h_{TP}}{\Delta T_{TS,out}})^2 \\ \beta(U_{Tout,min} \frac{\Delta h_{TP}}{\Delta T_{out,min}})^2 + (U_{x_{trans}} \frac{\Delta h_{TP}}{\Delta x_{trans}})^2 + (U_{w_{ch/web}} \frac{\Delta h_{TP}}{\Delta w_{ch/web}})^2 + (U_{h_{ch}} \frac{\Delta h_{TP}}{\Delta h_{ch}})^2 \end{array} } \qquad (4.10)$$

The coefficients α and β are either 0 or 1 depending on the fluid temperature profile (Figure 4-3) as shown in the following table.

Table 4-3:   Individual uncertainty analysis coefficients

Fluid Temperature Profile	α	β
Constant T_{sat}	0	0
Linear from T_{sat} to $T_{\text{TS,out}}$	1	0
Linear from T_{sat} to $T_{\text{out,min}}$	0	1

To calculate the uncertainty in two-phase heat transfer coefficient, the partial derivative of the heat transfer coefficient with respect to each variable is required. To estimate these derivatives, each input variable was independently changed by the magnitude of its uncertainty estimate, and the resulting change heat transfer coefficient was determined. This requires 16 solutions to 7 unique heat transfer model geometries (normal, ± channel/web, ± channel height, and ± transition location). A summary of the resulting values from this process for the extreme sample point are provided on Table 4-4. The notable results from the individual analyses are that the surface temperature profile and heat duty had the strongest effect on heat transfer coefficient. However, the saturation temperature and transition location had the strongest effect on the estimated uncertainty, because the heat transfer coefficient is more sensitive to a change these parameters.

Using these results, the uncertainty in the heat transfer coefficient can be determined each saturation temperature profile method: constant saturation temperature, linear decline from the transition location to the measured outlet pressure, and the linear decline to the minimum temperature based on the acceleration losses. From equation (4.10), these are ±6.88%, ±9.65%,

Table 4-4:   Individual uncertainty analysis sample results

Inputs	Value	Uncertainty	Units	Max	Min	Δx	Δh_{TP}	$\Delta h_{\text{TP}}/ \Delta x$
$q_{He,\text{TP}}$	95.01	1.71	W	96.72	93.3	3.42	5971	1746
T_{surf}	62.32	0.67	C	61.65	63.00	1.34	6452	4815
T_{sat}	20.79	0.068	C	20.86	20.72	0.14	1636	12029
$T_{\text{TS,out}}$	13.52	0.3	C	13.82	13.22	0.60	1294	2157
$T_{\text{out,min}}$	11.81	0.31	C	12.11	11.51	0.60	1123	1872
x_{trans}	-0.2	0.022	mm	-0.18	-0.22	0.044	1310	29773
$w_{\text{ch}}/w_{\text{web}}$	45/35	5	μm	40/40	50/30	10	3590	359
h_{ch}	200	5	μm	195	205	10	2020	202

and $\pm9.93\%$, respectively (Table 4-5). As expected the uncertainty is highest for the two linear decay temperature profiles because they have uncertainty propagated for more input variables than the constant saturation temperature case.

Table 4-5:   Resulting individual uncertainty for the extreme sample point from individually shifting each variable

Fluid Temperature Profile	h_{TP}	Uncertainty in h_{TP}	
	[kW m^{-2} K^{-1}]		[%]
Constant T_{sat}	72.2	4.97	6.88
Linear from T_{sat} to $T_{TS,out}$	51.9	5.00	9.65
Linear from T_{sat} to $T_{out,min}$	50.4	5.00	9.93

The average heat transfer coefficient is estimated by taking the linear average of these three values at each temperature profile (equation (4.9)). The uncertainty in this result is the propagation of the individual values as follows:

$$U_{\bar{h}_{TP}} = \sqrt{\sum_{i=1}^{N}(U_{h_{TP,i}} \frac{\partial \bar{h}_{TP}}{\partial h_{TP,i}})^2} \tag{4.11}$$

where N is 3, for each of the three heat transfer coefficients, and the value of the partial derivative is 1/3 for all three values. In the representative case, the average is 58.1 kW m^{-2} K^{-1} with an uncertainty of $\pm 4.91\%$. As shown, this process requires 7 individual models, 16 solutions, and up to 25 iterations per solution for each data point, which takes a considerable amount of computational effort. Therefore, this result was compared to a more economical and conservative solution.

Table 4-6:   Average flow boiling heat transfer coefficient in kW m^{-2} K^{-1}, extreme values for each temperature profile and the associated percent difference

Temp. Profile	T_{sat}		$T_{TS,out}$		$T_{out,min}$	
Nominal	72.2	n/a	51.9	n/a	50.4	n/a
Max	85.2	18.0%	59.6	14.9%	57.7	14.6%
Min	62.1	-13.9%	45.6	-12.1%	44.4	-11.9%

In this method, heat transfer coefficients were calculated by shifting all of the parameters at once to either maximize or minimize the heat transfer coefficient. To maximize the heat transfer coefficient, the variables were shifted to minimize temperature gradient in the silicon and surface area and to maximize the power input (max and min columns in Table 4-4). For example, to maximize the heat transfer coefficient, the heat input, transition location, and fluid temperatures were all increased while the surface temperatures, the channel height, and channel width were decreased. The opposite was used to minimize the heat transfer coefficient. This method reduced the computational load to 2 models per test condition and 6 solutions per data point, and resulted in a more conservative estimate of the uncertainty. Table 4-6 shows the normal, minimum, and maximum heat transfer coefficients for the three saturation temperature profiles. For all data points, the maximum difference between the nominal and extreme estimates was used to determine the uncertainty in the average heat transfer coefficient. In this case, the uncertainty in the heat transfer coefficients are assumed to be ±18.0%, ±14.9%, and ±14.6% for the three saturation temperature methods. Using equation (4.11) the uncertainty in the average heat transfer coefficient is ±9.65%, which is larger than the uncertainty for the more complex method. This procedure is repeated for all 15 data points, and the total uncertainty includes these values and the uncertainty from meshing in the heat transfer model.

Next, the procedure proposed by Celik et al. [71] was employed to estimate the geometric discretization error. For the heat transfer coefficient, the numerical model for the nominal data point was solved at two different mesh sizes. The grid refinement ratio (r), ratio of average element size between two models, was chosen to be 1.5, which exceeds the minimum suggested value by Celik et al. of 1.3. The approximate relative error between mesh sizes for the heat transfer coefficient is again defined as follows:

$$e_a^{21} = \left| \frac{h_{TP,1} - h_{TP,2}}{h_{TP,1}} \right| \tag{4.12}$$

The error in numerical model is estimated by the fine-grid convergence index:

$$GCI_{fine}^{21} = \frac{1.25 e_a^{21}}{r_{21} - 1} \tag{4.13}$$

The *GCI* was determined for all three saturation temperature profile methods. Table 3-9 shows a summary for the representative (more exteme) data point. For each data point, the maximum *GCI* was used to estimate the total uncertainty. As shown in Table 4-7, the worst case fine-grid convergence index for the representative data point is ±0.14%. The propagation of uncertainty with the *GCI* is calculated as follows:

$$U_{\bar{h}_{TP}} = \sqrt{U_{\bar{h}_{TP,in}}^2 + GCI^2} \tag{4.14}$$

The uncertainty in this average heat transfer was ±9.65%, which yield a total uncertainty of ±9.65%. Clearly, the GCI had little effect on the uncertainty.

Table 4-7:   Numerical model uncertainty analysis from discretized grid

Mesh	Size [μm]	# Elements	h_{TP} [kWm^{-2}K^{-1}]			GCI [%]		
			T_{sat}	$T_{TS,out}$	$T_{out,min}$	T_{sat}	$T_{TS,out}$	$T_{out,min}$
1	10	48,800	72.20	51.90	50.40		-	
2	6.67	164,520	72.22	50.93	50.41	0.08	0.14	0.06

As shown in Table 4-8, the average uncertainty in the flow boiling heat transfer coefficient for all 15 data points is ±11.9%. The points which had consistently high uncertainty were those with relatively low test section heat duty, heat transfer coefficient, and vapor quality; as these parameters increased, the uncertainty was reduced.

Table 4-8:   Summary of uncertainty and heat transfer coefficient for all 15 data points; sorted by heat duty

Two-Phase Heat Duty	Vapor Quality	Saturation Temp.	Mass Flow Rate	Average Heat Transfer Coefficient		
				Value	Uncertainty	
W	-	°C	g min^{-1}	kW m^{-2} K^{-1}	kW m^{-2} K^{-1}	%
7.67	0.03	25.01	99.7	6.28	1.01	16.0%
13.63	0.04	15.33	101	12.1	2.48	20.5%
24.49	0.05	19.95	150	14.0	1.74	12.4%
25.18	0.08	19.97	101	18.0	2.08	11.5%
26.02	0.09	25.36	100	19.7	2.13	10.8%
39.77	0.26	19.95	50.4	32.6	3.61	11.1%
44.33	0.14	14.83	101	28.0	3.38	12.0%
51.63	0.11	20.29	149	29.9	3.30	11.1%
58.71	0.19	20.08	99.8	35.4	3.33	9.42%
62.72	0.21	25.22	99.7	62.5	8.90	14.2%
67.93	0.21	16.51	101	37.7	4.05	10.7%
67.97	0.44	19.9	49.9	51.1	5.32	10.4%
81.16	0.26	20.64	99.6	43.1	4.07	9.46%
95.01	0.61	20.79	50.6	58.1	5.61	9.65%
99.89	0.40	17.07	78.5	53.3	5.21	9.77%

In the next chapter, the heat transfer results are discussed further, and compared to exiting correlations. This analysis directs the development of a new correlation to predict the data in the present study more accurately, and is used to analyze a suggested test section geometry for future laser diode cooling systems.

CHAPTER 5. RESULTS AND DISCUSSION

In the previous section, the process for extracting the average heat transfer coefficient from the experimental data was presented. In this section, a summary of the results from the 15 two-phase data points is presented first, including a discussion of how the results compare to other investigations. The heat transfer performance of the test section in this study is then compared to the state of the art laser diode cooler. Next, the heat transfer coefficients are then compared to representative correlations by prior investigators, and it is shown that no existing method achieves acceptable accuracy. Therefore, a new correlation is generated for the range of operating parameters in the current investigation. The new correlation is then used to mathematically optimize the heat sink geometry that targets the desired 10× increase in brightness over the state of the art.

5.1. Overview of Results

In general, the heat transfer coefficients determined in the present study follow trends observed in previous investigations with lower heat fluxes and larger channel diameters. As shown in Figure 5-1, the average flow boiling heat transfer coefficient increases with applied heat flux. The calculated heat transfer coefficient is primarily a function of the two-phase test section heat duty for all the data points collected in the present study. These results agree with Kuo and Peles [39]: varying saturation temperatures of water between 46°C and 100°C demonstrated very little effect on flow boiling heat transfer. All of the data points are in confined flow by the criteria defined by Harirchian and Garimella (*i.e.*, $Co < 160$) [18]. In confined flow, it is expected that the convective boiling dominates nucleate boiling, and, as shown in Section 5.4, this trend is confirmed by an increase in the nucleate boiling suppression factor for the modified correlation.
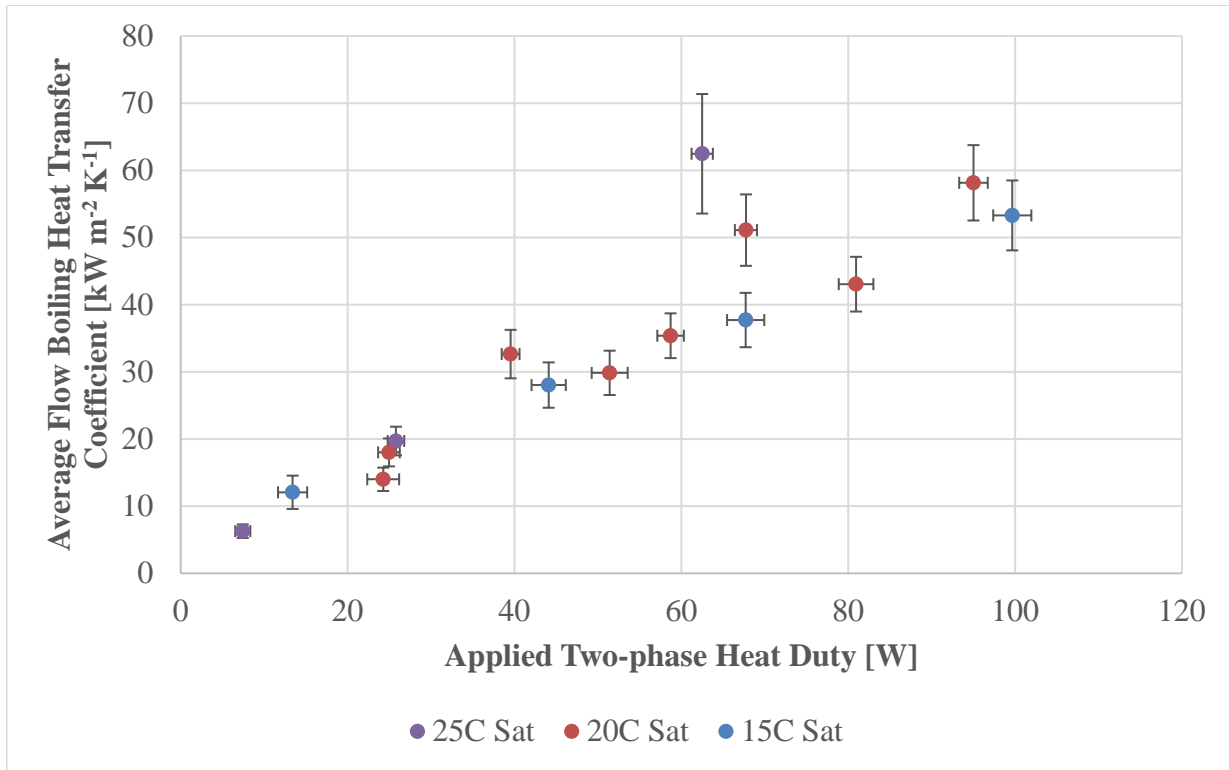
Figure 5-1:   Average flow boiling heat transfer coefficient vs. applied two-phase heat duty for each saturation temperature

The highest base heat flux rejected in this study is 1.10 kW cm^{-2}, which is the highest known heat rejection for saturated boiling for a microchannel heat sink. The highest average heat transfer coefficient in the present study is 62.5 kW m^{-2} K^{-1}, which occurred at 751 W cm^{-2} and a saturation temperature of 25°C. This exceeds the typical performance found in literature for a plain wall microchannel heat sink by > 20% [10-12]. Kuo and Peles [22] showed that using reentrant cavities yielded a heat transfer coefficient of 135 kW m^{-2} K^{-1}, and Li et al. [52] used silicon nanowires grown from the floor to achieve 95 kW m^{-2} K^{-1}. However, it is unclear if these results are accurate. Kuo and Peles have placed local temperature measurements between their heater and the microchannel array, and then they compute a 'local heat flux' using this measurement and the average heater temperature. This is incorrect because their average heater temperature is determined over the entire microchannel length (Section 4.1), and, thus, the resulting heat transfer
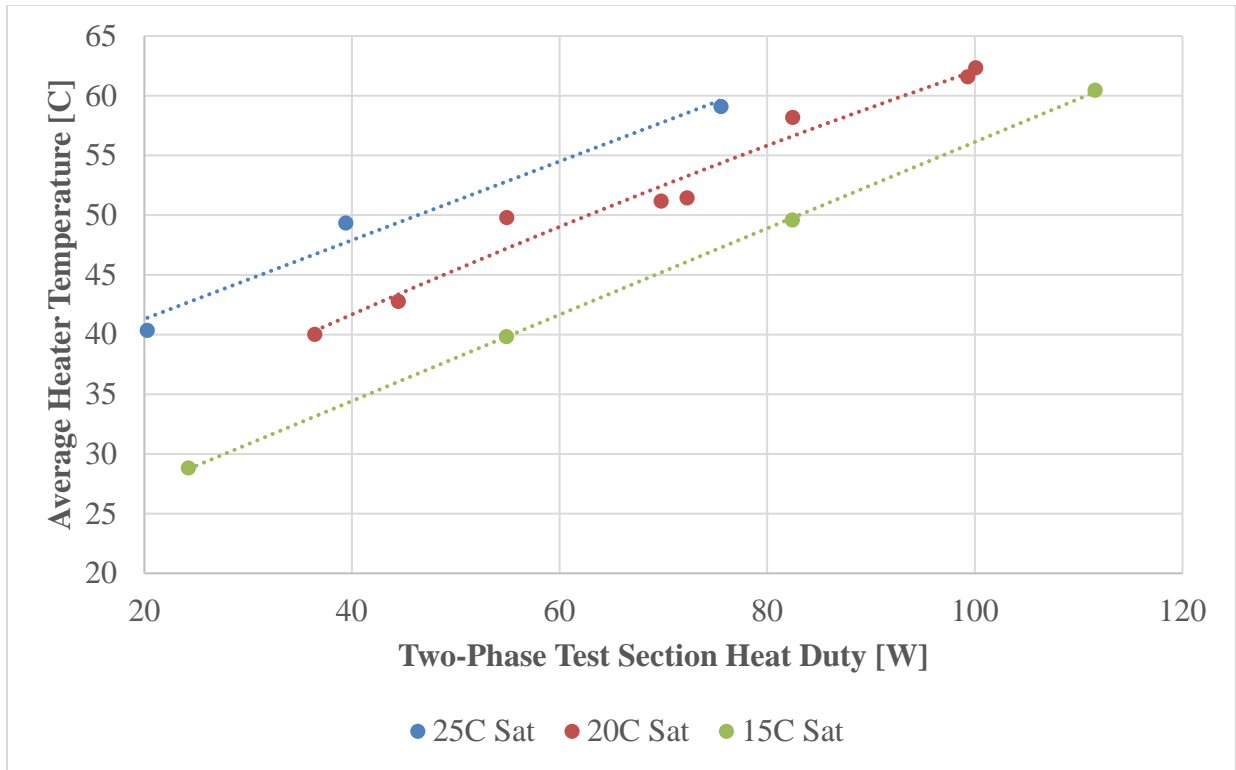
Figure 5-2:   Average heater temperature vs. two-phase applied heat duty for each saturation temperature

coefficient may be over predicted.   In the case of Li et al, even though they assumed the temperature at the center of the array was the average over the whole area, which could underestimate the heat transfer coefficient, they calculated the wall surface temperature for a plain channel and neglected the area enhancement from the nanowires.

In the present study, data was collected for three different nominal saturation temperatures at the single-phase to boiling transition location: 15, 20, and 25°C. Figure 5-2 shows that as the saturation temperature reduces the temperature of the heater reduces at the same heat flux, which is consistent with prior investigations [39, 49]. As a result, when the test fluid is at a lower saturation temperature, it can reject more heat at a fixed heater temperature. For example, at a heater temperature of nominally 60°C, the test section heat duty was 75.6 W at a saturation
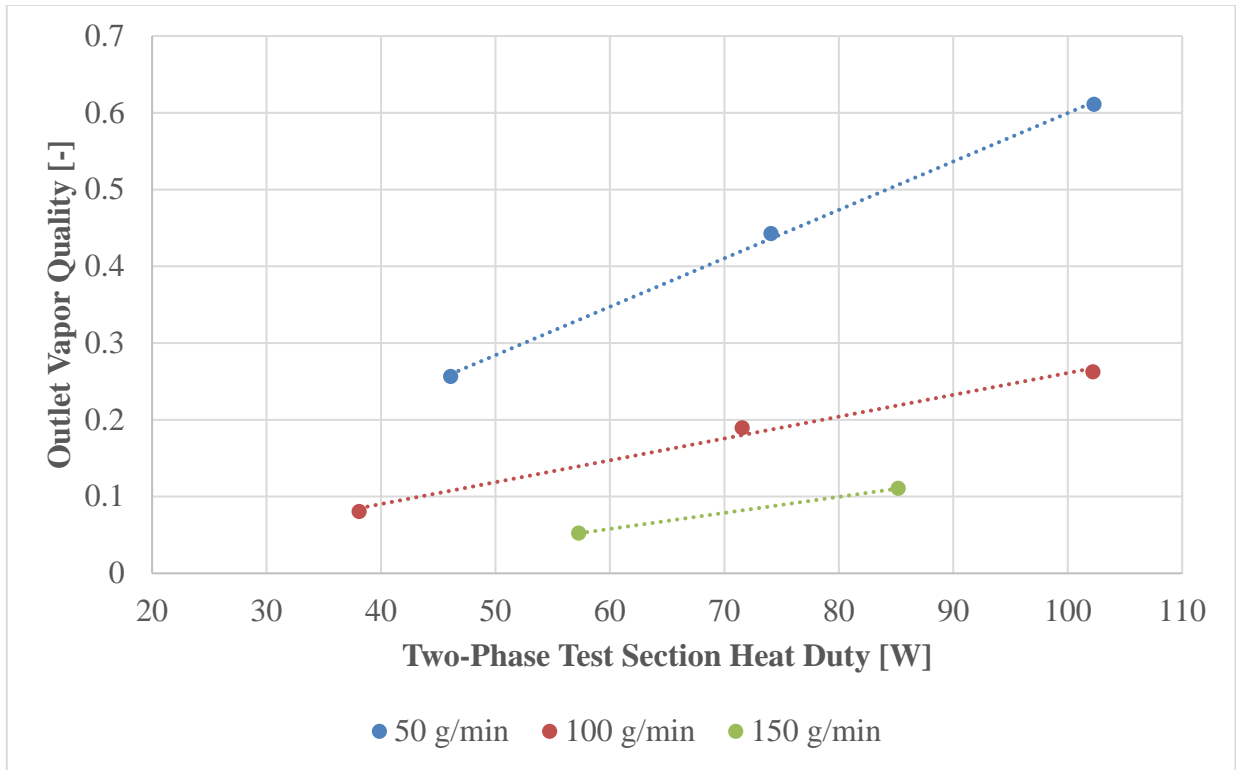
Figure 5-3:   Outlet vapor quality as a function of two-phase test section heat duty at a saturation temperature of 20°C

temperature of 25°C, and increased to 112 W at 15°C. This effect occurred because the heat transfer coefficient did not change substantially with an increase in saturation temperature.

To observe the effect of mass flow rate, Figure 5-3 shows a plot of heat transfer coefficient as a function of vapor quality at a saturation temperature of 20°C for all three flow rates tested (50 – 150 g min⁻¹). As expected, the vapor quality increases with reducing mass flow rate. In addition, the heat transfer coefficient appears to be a very weak function of thiks flow rate. As shown in Figure 5-2, the heater temperature increases almost linearly w an increase in heat duty for all the 20°C data points. This means that the heat transfer coefficient does not change substantially with flow rate.
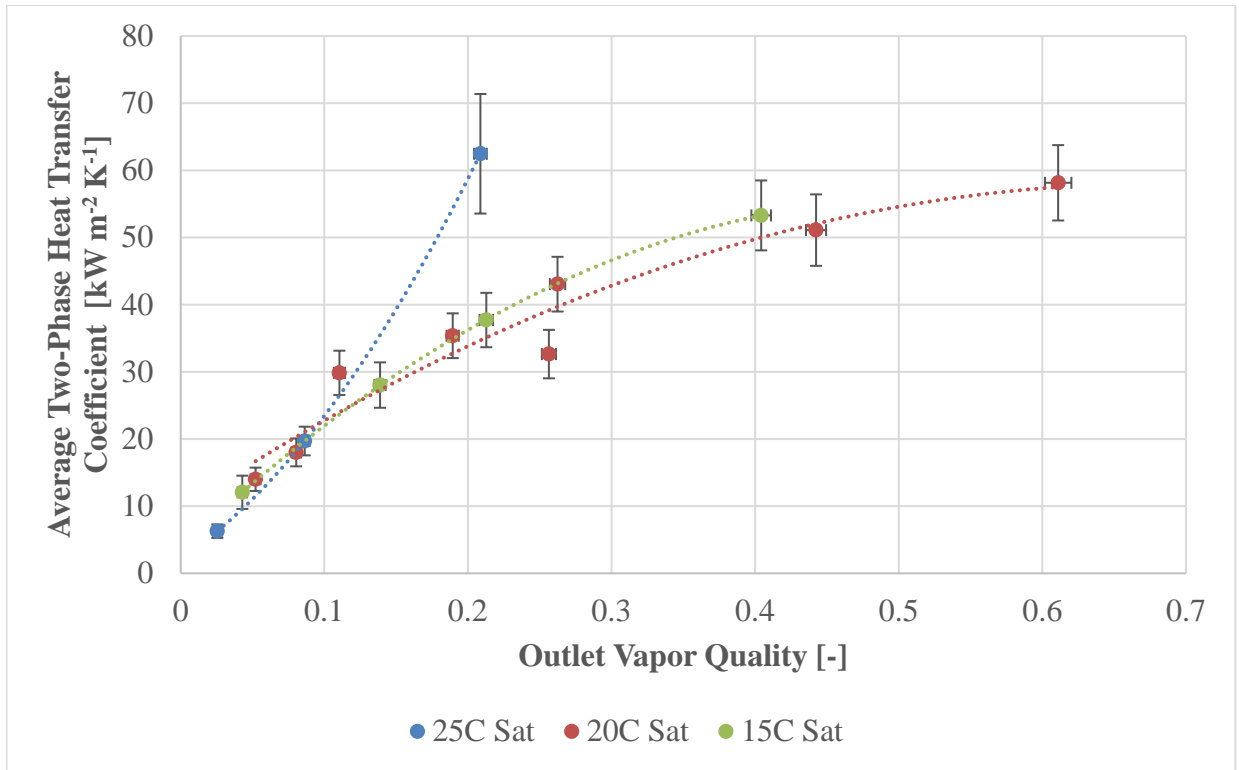
Figure 5-4: Average two-phase heat transfer coefficient vs. outlet vapor quality for each saturation temperature

A number of previous investigators have shown that the heat transfer coefficient peaks at vapor qualities near 20% [11, 49, 51, 73-76], while others have not observed this trend [77, 78]. As shown in Figure 5-4, the average heat transfer coefficient increases with vapor quality for all the experimental data gathered in the present study. However, as the vapor quality increases, the rate of increase in the heat transfer coefficient reduces. For example, at a transition saturation temperature of 20°C, the heat transfer coefficient increase from 14.0 to 35.4 kW m^{-2} K^{-1} as the vapor quality increases from 5.2% to 18.9%. When the outlet vapor quality increases further to 61.1%, the heat transfer coefficient increases to only 58.1 kW m^{-2} K^{-1}. The data point at the nominal conditions of 25°C saturation temperature with an average heat transfer coefficient of 62.5 kW m^{-2} K^{-1} was eliminated due to an experimental error. The IR pyrometer rests on four pins to enable a rapid removal in the event of a test section rupture, and, during the installation

procedure of a test section, the pyrometer is centered on the heater (Section B.1.5). For this particular data point the center location was incorrect, and the resulting temperature profile was not measured correctly. Compared to all remaining data collected during these experiments, the surface temperature profile for this point appears to be shifted such that it yields a smaller difference between it and the fluid. This yields an artificially high heat transfer coefficient. Excluding this data point, it is clear that there was no observed peak at any particular vapor quality.

During testing, significant fouling was observed in the test section beginning at an average heater temperature of 70°C. As shown in Figure 5-5, the R134a appeared to decompose once this heater temperature was reached. Several attempts were made to clean the test section by soaking in both isopropyl alcohol and acetone, but the residue remained and, therefore, these sample test sections were discarded. As discussed further in Section 5.5.2, this result was a primary reason for considering alternative working fluids.
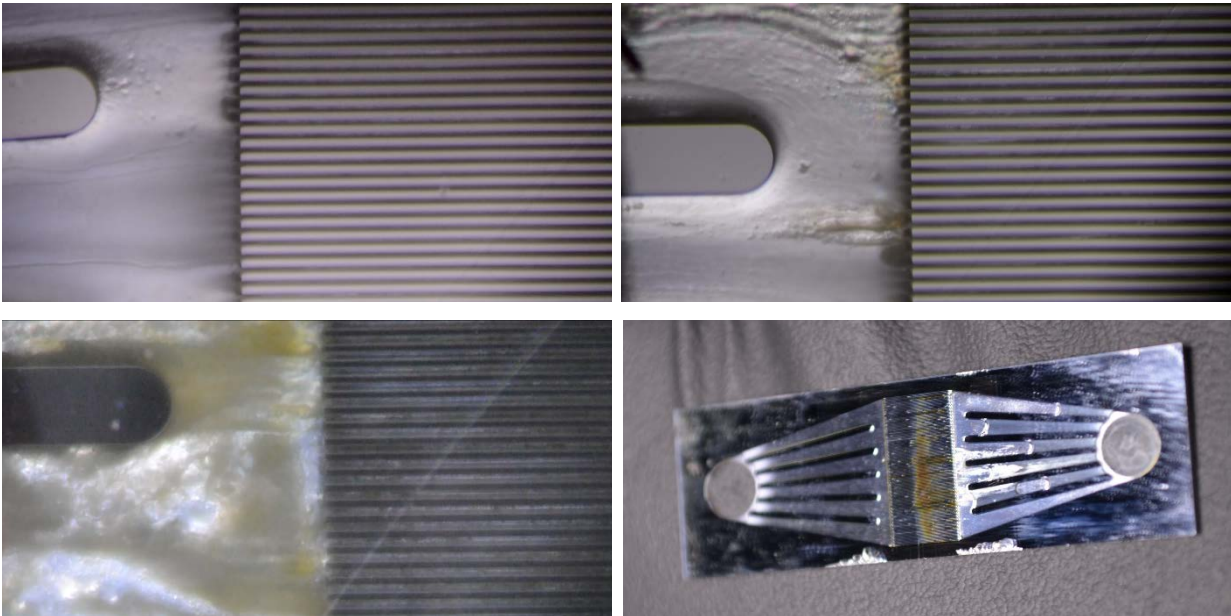
Figure 5-5:   Progression of R134a breakdown; Top-Left: prior to formation at lower temp; Top-Right: early formation, insignificant effect on dP_{tot} or T_{he}; Bottom-Left: significant channel blockage; Bottom-Right: full test section showing blockage

As discussed in Chapter 4, significant heat spreading was observed in the test section, and a numerical technique was required to determine the average two-phase flow boiling heat transfer coefficient. For all of the data points, the relative amount of heat spreading from the two-phase region was calculated by the average energy through the projected area ($\overline{q}_{\text{TP,proj}}$), from each of the three temperature profiles, as follows:

$$\gamma = 1 - \frac{\overline{q}_{\text{TP,proj}}}{q_{\text{He,TP}}} \qquad (5.1)$$

The projected area above the heater included only the two-phase flow boiling portion (Figure 4-1), and the amount of heat rejected through the area projected above the heater was determined from the numerical model results for each of the three different methods used to predict the fluid saturation temperature. For the same two-phase sample point used in Chapter 3 (Table 3-6), the projected two-phase heat transfer in the model from each of the fluid profiles are 112 mW, 98.5
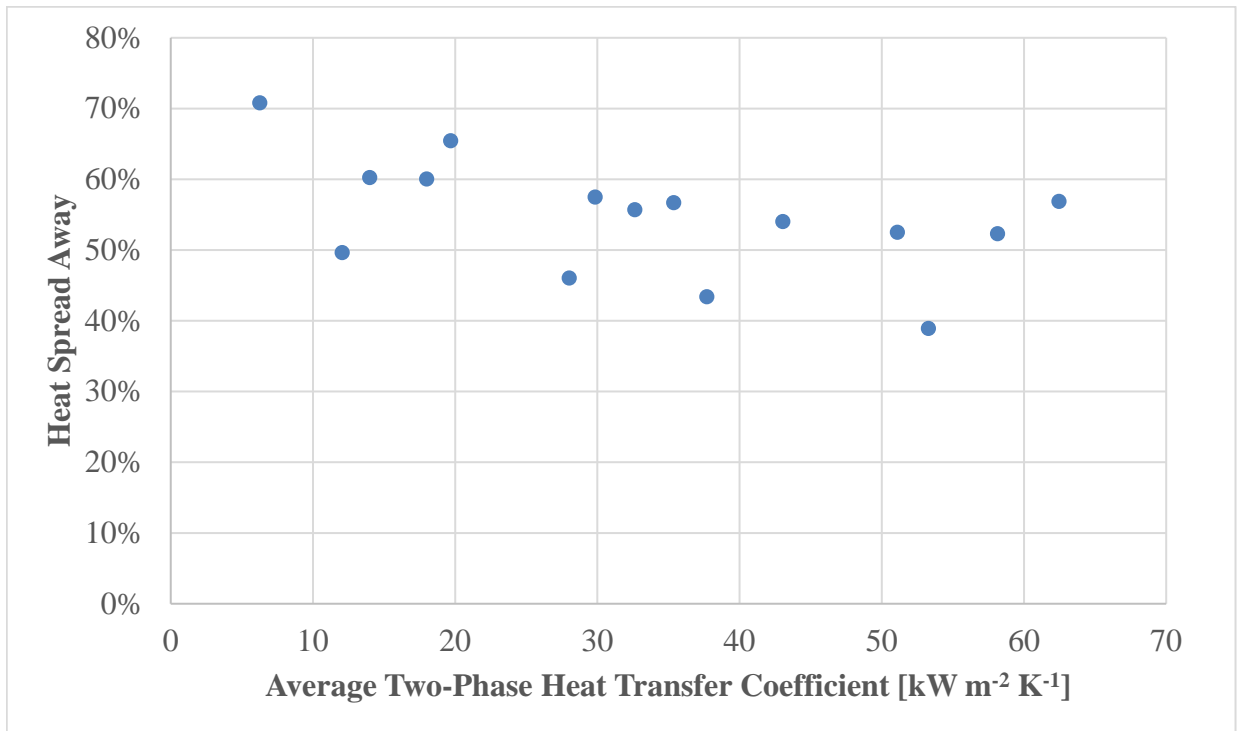
Figure 5-6:   Heat spread away from the projected area vs. average two-phase heat transfer coefficient

mW and 96.6 mW of the total 236 mW transferred, which is yields $\gamma = 56.7\%$. Figure 5-6 shows

γ for all the data points in the current study as a function of average flow boiling heat transfer

coefficient. The heat spreading decreases with increasing heat transfer coefficient from a peak of

70.8% to a minimum of 38.9%. Interestingly, the four points where heat spreading was lowest all

occurred at a saturation temperature of 15°C.

One method to reduce heat spreading is to decrease the thickness of the wall. This may

increase the overall thermal resistance of the test section by decreasing the effective heat transfer

area. However, this also reduces the thermal resistance of the floor if all of the heat is transferred

through the area projected vertically from the heater, which is calculated as follows:

$$R_{th} = \frac{t_{si}}{K_{si} A_{he}} \tag{5.2}$$

In the test section for the current study, the silicon ($K = 149$ W m^{-1} K^{-1}) floor thickness is 300 μm,

which, over the 0.1 cm^2 heater area, yields a thermal resistance of 0.2 K W^{-1}. Reducing this floor

thickness to 100 μm yields a thermal resistance of 0.07 K W^{-1}, which could potentially reduce the

heater temperature for a fixed fluid saturation temperature and flow rate. However, this lower floor

thickness also reduces the amount of heat spreading, which can increase the thermal resistance.

Additional investigation on this effect is warranted. Another method to reduce the overall thermal

resistance is to eliminate subcooling prior to the fluid reaching the area directly above the heater.

During the experiments, the fluid entering the test section had between 5°C and 10°C of subcooling

below the saturation temperature at the transition location. Single-phase heat transfer coefficients

are much lower than flow boiling heat transfer coefficients at the same mass flow rate through the

same geometry. For example, single-phase convective heat transfer coefficient is well

characterized by Nusselt number correlations for rectangular ducts. Kakac et al. has characterized

the heat transfer from a rectangular duct with 3 heated sides and 1 insulated side as a function of aspect ratio, which is the case for the current work [79]. Their correlation is as follows:

$$Nu_D = -29.426\alpha^6 + 76.489\alpha^5 - 59.895\alpha^4 - 0.0637\alpha^3 + 23.341\alpha^2 - 11.99\alpha + 5.2409 \quad (5.3)$$

For the current study, the aspect ratio is nominally 0.225 (45 μm / 200 μm), which results in a Nusselt number of 3.61. The heat transfer coefficient is then calculated from hydraulic diameter and fluid properties as follows:

$$h_{SP} = \frac{K_1 Nu_D}{D_H} \quad (5.4)$$

For the sample case the thermal conductivity of the liquid (K_1) is evaluated at the saturation temperature (20.1°C), to be 0.086 W m^{-1} K^{-1}, which yields a single phase heat transfer coefficient of 4.21 kW m^{-2} K^{-1}, which is much smaller than the average flow boiling heat transfer coefficient for this case: 35.4 kW m^{-2} K^{-1}. A portion the heater is cooled by single phase cooling in the channel
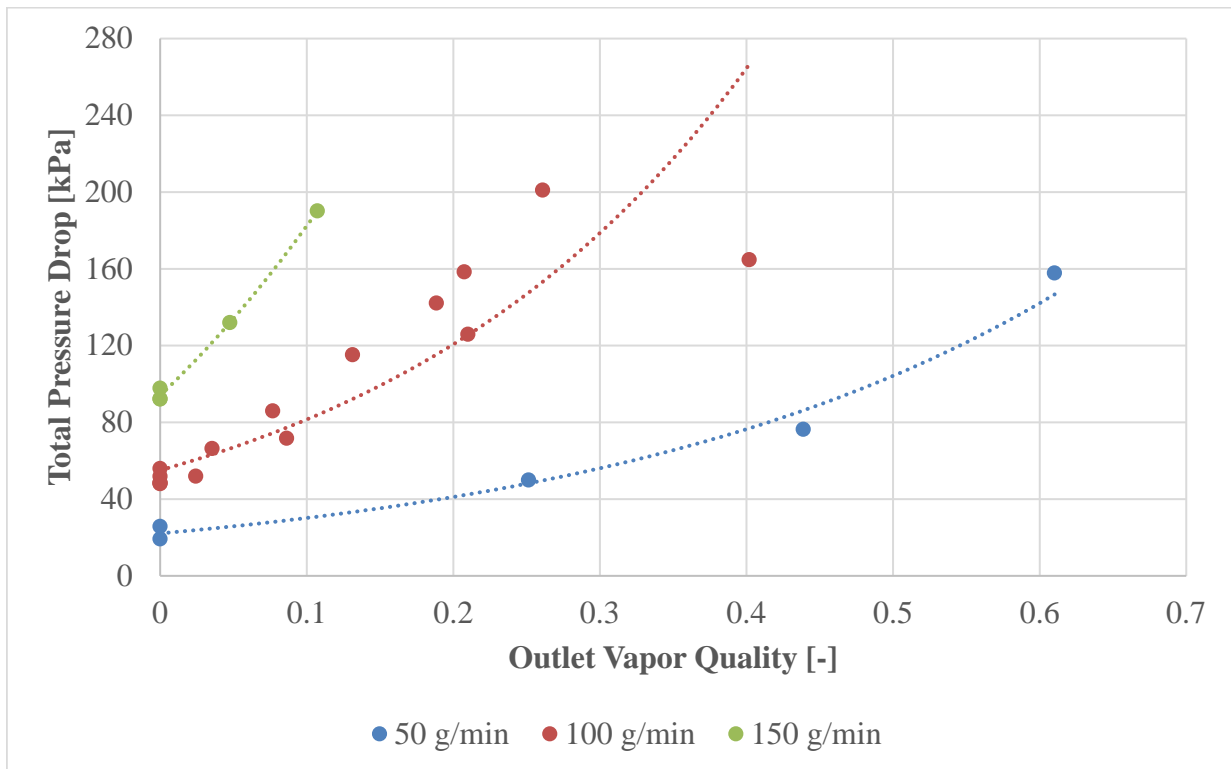
Figure 5-7:   Total pressure drop vs outlet vapor quality as a function of mass flow rate

113
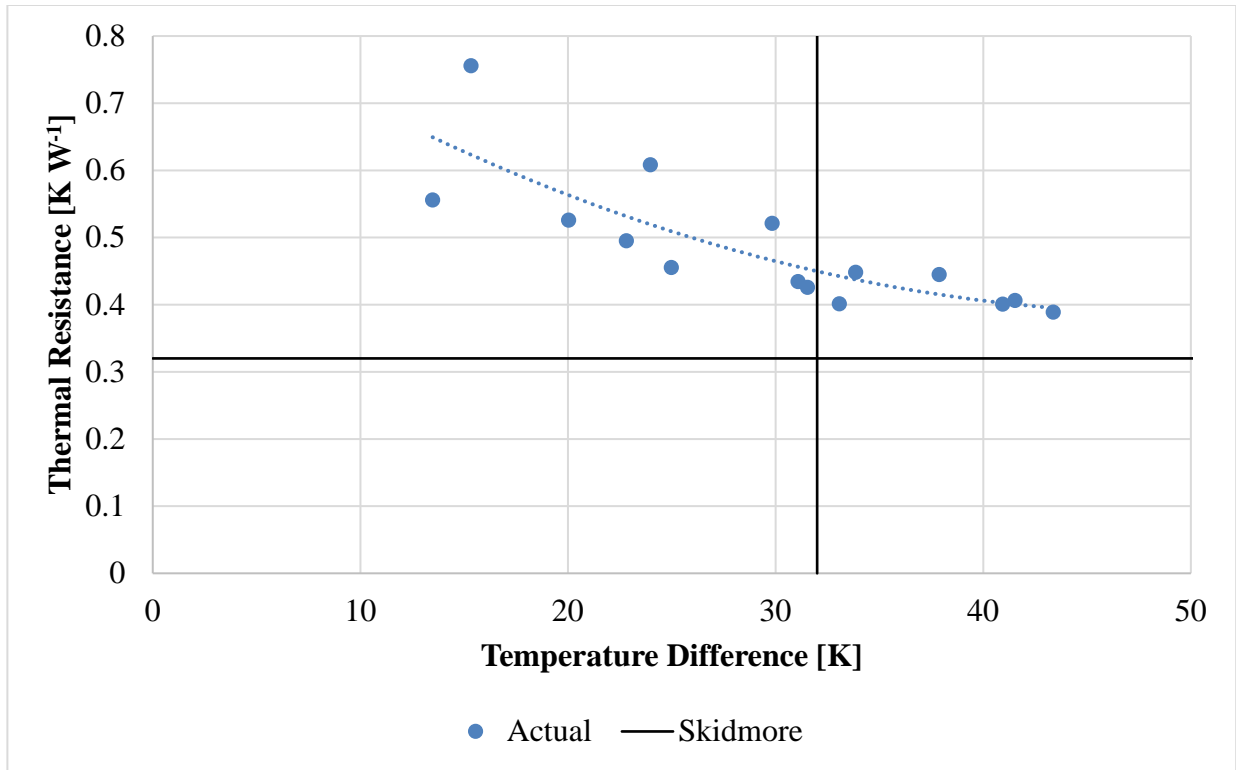
Figure 5-8:   Thermal resistance vs. average temperature difference between heater and fluid; bottom left quadrant would superior to Skidmore et al.

during the experiments in the present study. Therefore, it is possible that the heater temperature could be lowered by reducing the inlet subcooling and moving the liquid-vapor transition location further upstream.

Because the fluid is a two-phase liquid-vapor mixture, the saturation temperature is only dependent on the fluid pressure. As shown in Chapter 4, the calculated heat transfer coefficient is strongly dependent on the fluidic pressure drop in the channel. As shown in Figure 5-7, the measured total pressure drop through the test section and inlet/outlet manifolds can increase significantly when the fluid is evaporated in the test section. For example, at a mass flow rate of 100 g min^{-1}, the pressure drop increase from 48 kPa to 201 kPa when the outlet vapor quality increases from 0 to 0.26. When the vapor quality increases, the outlet velocity increases because there is more vapor, which reduces the local pressure. Using the procedure in Section 4.1.1 (*i.e.,*
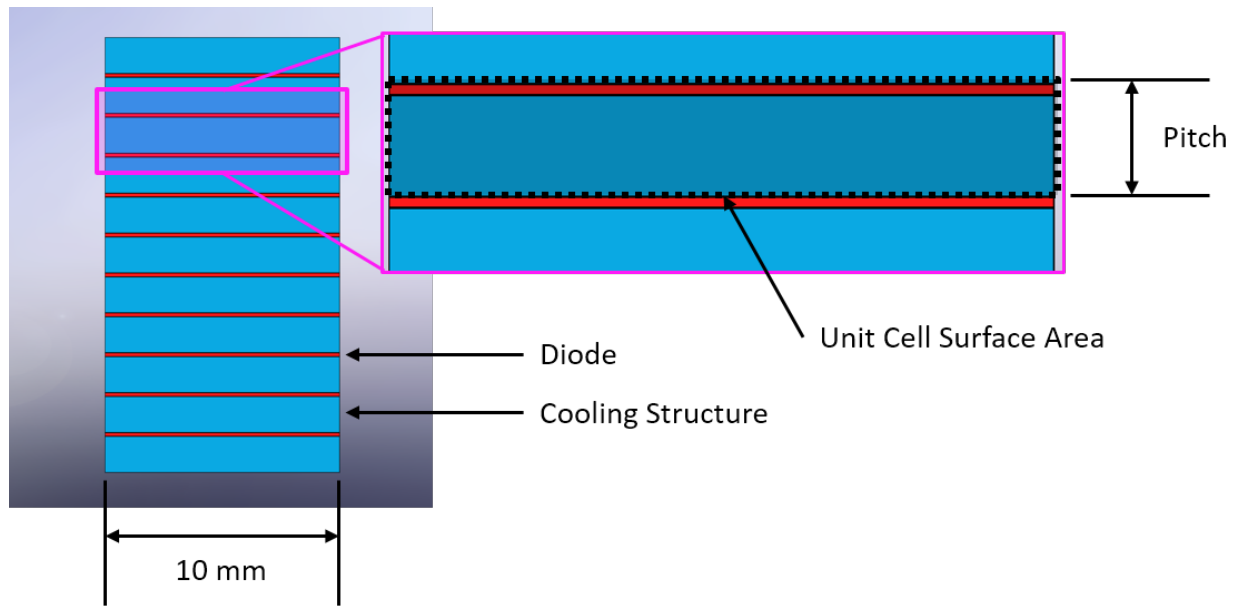
Figure 5-9:   Front face of a 10-bar diode array, showing the unit cell area and dimensions

equations (4.2) through (4.6)), the difference in pressure due to acceleration as the outlet vapor

quality increases from 0 to 0.61 is 12.0 kPa, which clearly demonstrates that this increase in

pressure drop cannot be attributed solely to this effect. There are many two-phase pressure drop

correlations in the literature for flow through microchannels [30, 80, 81]. Unfortunately, none of

these prior investigations covered the high flowrates ($739 < G_{ch} < 2,224$ kg m^{-2} s^{-1}) and small

hydraulic diameter (73.4 μm) for single component fluids similar to R134a [82]. Therefore, future

studies that accurately measure local pressure drop are warranted.

5.2. Comparison to the State of the Art Laser Diode Cooler

Skidmore et al. [5] rejected a heat duty of 100 W per diode in a 10-bar array via single-

phase cooling with a temperature difference of 32°C between the cooling fluid and the diode

surface. Using these values, they calculated the thermal resistance to be 0.32 K W^{-1} per diode bar[3].

Their v-grooved mounting arrangement (Figure 1-4) yields a diode pitch of 1.7 mm. The results

---

[3] They achieved a thermal resistance of 0.032 K W^{-1} for the 10-bar array.

from the current work are compared to this performance using two key metrics: thermal resistance and diode array brightness.

In the current work, the thermal resistance is calculated by the temperature difference from heater to fluid saturation temperature, and the effective heat rate into the test section as follows,

$$R_{th} = \frac{\Delta T}{q_{He}} = \frac{T_{He} - T_{sat}}{q_{He}} \tag{5.5}$$

For the sample case, the average heater temperature is 51.6°C, the saturation temperature is 20.1°C, and the effective heat rate is 71.6 W, which yields a thermal resistance of 0.43 K W^{-1}. Figure 5-8 summarizes the thermal resistance as a function of temperature difference for comparison to the results of Skidmore et al.: unfortunately, no conditions in the current study were at a lower thermal resistance. As the temperature difference increased, the thermal resistance decrease, and the lowest thermal resistance in the current study is 0.39 K W^{-1}.

Although the thermal resistance of the state of the art diode cooler is lower than the current study, the critical metric for laser diode arrays is brightness. Laser diodes are typically 50% efficient, which means that, for example, 100 W of heat generated by the diode corresponds to 100 W of light emissive power emanating from the diode. For convenience, the simplified brightness (*Br*) is calculated by dividing the light emissive power at the edge emitting face of the diode by the surface area encompassing a unit cell ($A_{array,unit}$) for a diode bar as follows (Figure 5-9):

$$Br = \frac{q_{light}}{A_{array,unit}} = \frac{q_{He}}{A_{array,unit}} \tag{5.6}$$

For the study by Skidmore et al., the unit cell surface area is 0.17 cm^2, which yields a simplified brightness of 588 W cm^{-2} at a heat rate and light power of 100 W. Figure 5-10 shows a hypothetical unit cell using the test section dimensions in the present study, which assumes a diode bar thickness of 150 μm and a total silicon thickness of 600 μm and yields a diode pitch of 0.75 mm. (The total

silicon thickness is actually 500 µm in the present study. An additional 100 µm is added as a capping layer to create a hermetic seal.) At a fluid to heater temperature difference of 33°C, the maximum heat duty that test section in the present study can reject is 82.4 W at a saturation temperature of 15°C and a fluid flow rate of 100 g min^{-1}. This yields a simplified brightness of 1.1 kW cm^{-2}, which is 1.87× larger than the state of the art. If the diode temperature is increased 60°C, the maximum rejected heat rate is 111.6 W. Although this increases the fluid to diode temperature difference to 43.4°C, this yields a brightness of 1.49 kW cm^{-2}, which is 2.53× brighter that shown by Skidmore and coworkers. The volumetric heat duty in these cases are 11 kW cm^{-3}, and 14.9 kW cm^{-3}, respectively; both cases are substantially higher than that of Skidmore et al. (5.88 kW cm^{-3}). Further increases in brightness are possible by reducing the floor thickness, or increasing the heat transfer coefficient and surface area by reducing the channel hydraulic diameter. To assess these scenarios, an accurate heat transfer coefficient correlation is required. In
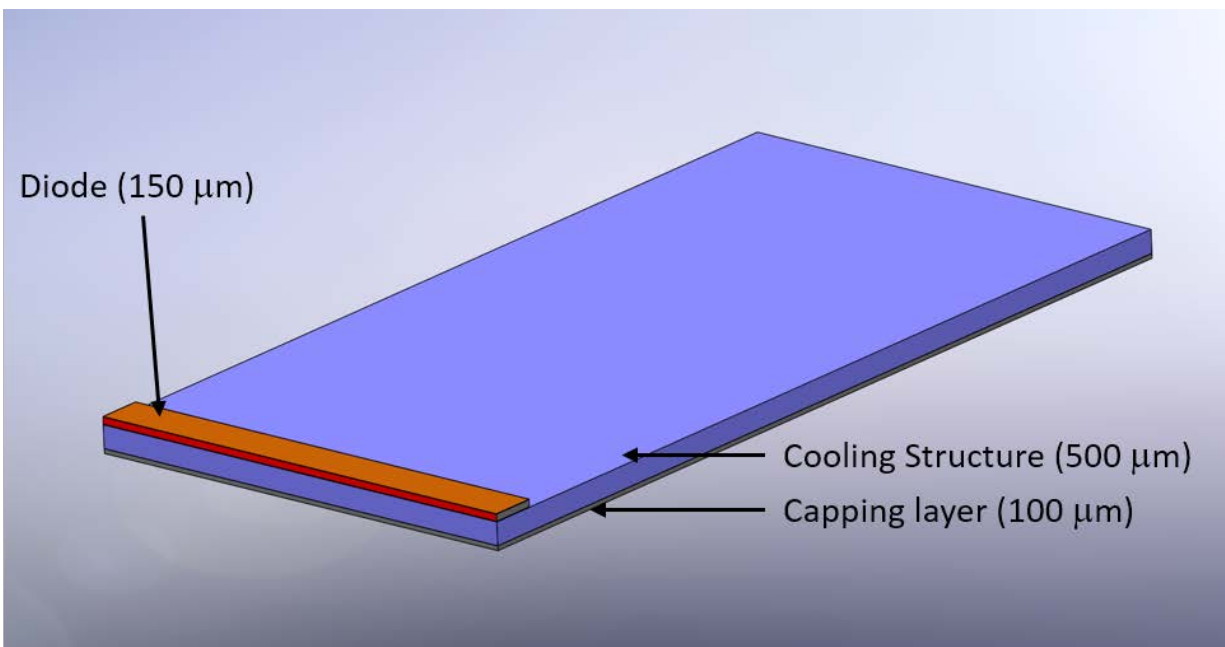
Figure 5-10:   Representative microchannel cooling structure
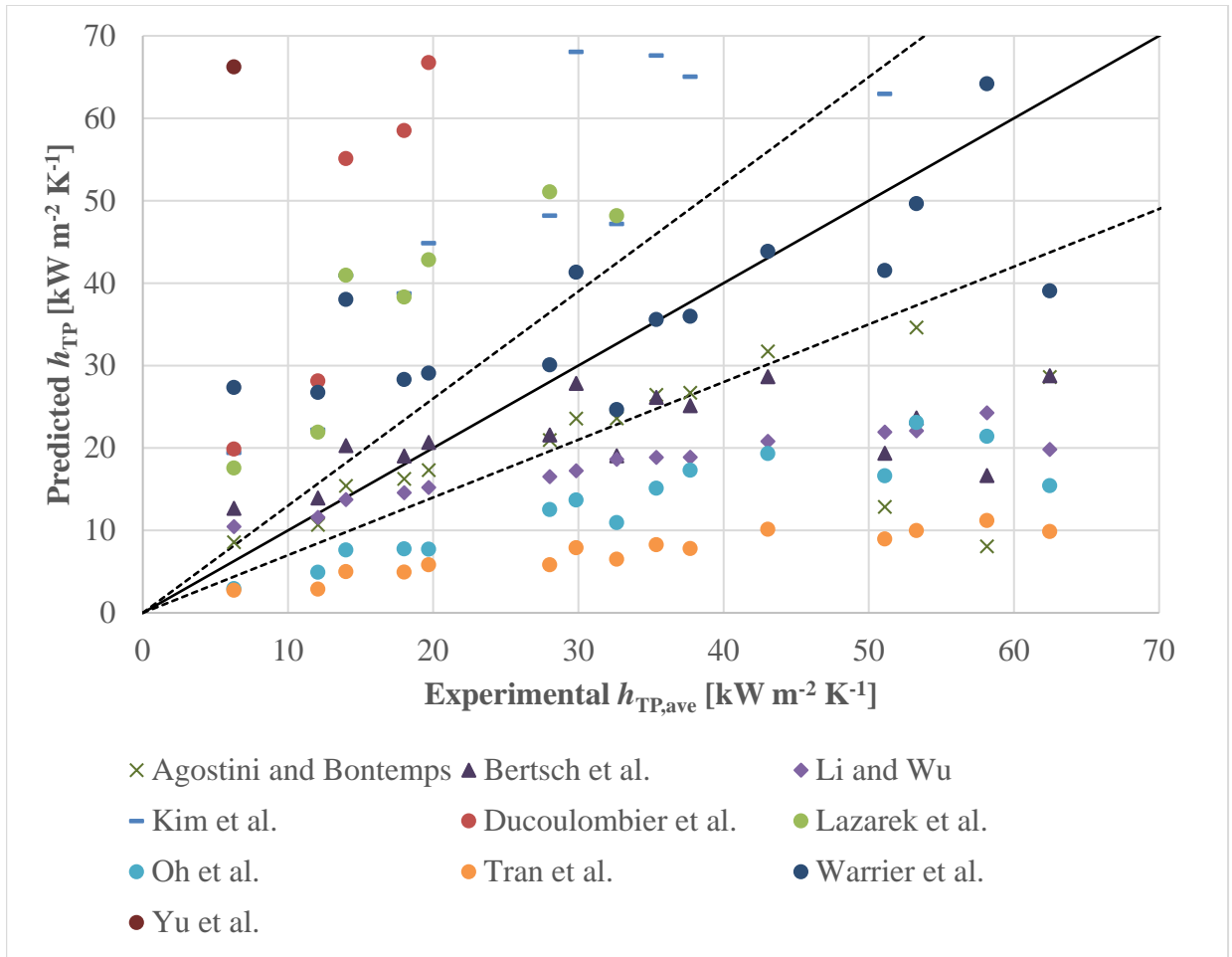
Figure 5-11: Predicted flow boiling heat transfer coefficient vs. experimental flow boiling heat transfer coefficient; the dashed lines are ±30% from the experimental data

the next section, the test data collected in the present study are compared to correlations available in the literature.

5.3. Comparison of Date to Existing Correlations

Relevant flow boiling heat transfer coefficient correlations were compared to the data collected in the present study. A summary of the correlations, including a representative calculations for a sample data point, are provided in Appendix C.1. The predicted heat transfer coefficients at the experimental conditions for each data point are compared to the values determined from the procedure outlined in Chapter 4. Figure 5-11 shows that none of the correlations predicted all 15 data points within ±30% of the measured values in the present study.

To quantify the accuracy of each correlation, the mean absolute error (*MAE*) is calculated for all 15 two-phase data points as follows:

$$MAE = \frac{1}{N} \sum_{i=1}^{N} \frac{\left| h_{\text{TP,cor}} - h_{\text{TP,exp}} \right|}{h_{\text{TP,exp}}} \tag{5.7}$$

As shown in Table 5-1, there are three correlations which predict the experimental flow boiling heat transfer coefficient within an *MAE* ≤ 42.1%: Agostini and Bontemps [83] (32.3%), Bertsch et al. [11] (38.7%), and Li and Wu [12] (42.1%). All three of these correlations were developed for rectangular minichannel and microchannel channel arrays. Agostini and Bontemps used R134a flowing in a parallel array of 11 channels at a hydraulic diameter of 2.01 mm, while the other two correlations used a large database of fluids and conditions. Bertsch et al. used a database of 3,899 data points for multiple fluids (including R134a), hydraulic diameters (160 – 2920 µm), heat fluxes (0.4 – 115 W cm^{-2}), and mass fluxes of (20 – 3000 kg m^{-2} s^{-1}). Li and Wu similarly used a large database of 3,744 data points from different studies spanning hydraulic diameters from 0.16 mm to 3.1 mm for numerous fluids, which also include R134a. Because significant heat spreading was observed in the current experiment, the channel heat flux was lower than expected, and the highest value was 71.7 W cm^{-2}, which is within the bounds for these three correlations. However, these correlations are still not directly applicable due to the significantly lower hydraulic diameter in the current work (73.4 µm) as compared to the smallest in the correlation databases (160 µm). The Agostini and Bontemps and Li and Wu correlations are generated by fitting empirical constants to non-dimensional parameters with no regard for asymptotically approaching liquid or vapor heat transfer coefficients. In contrast, the correlation by Bertsch et al. yields the appropriate single phase convection heat transfer coefficients at both extremes (saturated liquid and vapor). However, asymptotically approaching the correct limits is

not always successful: Kim et al. have also used a similar approach, but their correlation predicted the data in the current study poorly (*MAE* of ±90.1%). The more important factors for improving fit appears to be the fluid selection and the geometry.

Because no study predicted the data in the present investigation less than an *MAE* of ±32.3%, a new correlation was developed to more accurately predict flow boiling heat transfer coefficients for the conditions in the present study. In the following section, the new correlation is discussed in detail.

5.4. New Flow Boiling Heat Transfer Model

There are two primary objectives for the proposed flow boiling heat transfer model: (1) improve prediction accuracy for the current operating conditions ($D_H = 73.4 \ \mu$m and $q_B'' \leq 1.1$ kW cm^{-2}), and (2) correctly account for the fin effects in the calculation of average heat flux. In the following discussion, the structure of the correlation is presented first. The method for modifying the average heat flux is subsequently presented, followed by two case studies that show why this method leads to a more accurate prediction of heat transfer performance. Then, the experimental data is used to determine required constants, which are determined through a minimization of the *MAE*. Finally, this model is compared to the model it was based upon: the Bertsch correlation.

Although the correlation presented by Agostini and Bontemps fit the data the best, Bertsch et al. used many different fluids, geometries, and operating conditions that potentially captured the impact of these parameters in a more universal fashion. Therefore, the method proposed by Bertsch et al. is used in the present study to develop a new correlation. In their method, the flow boiling heat transfer coefficient is determined from the contributions from nucleate and forced convective boiling as follows:

$$h_{FB} = h_{NB}(1-\chi) + h_{CB}[1+80(\chi^2 - \chi^6)\exp(-0.6\,\text{Co})] \tag{5.8}$$

Table 5-1:   Summary of correlation fit to experimental data; sorted by *MAE*

Correlation	Sample Data Point h_{TP} [kW m^{-2} K^{-1}]	Percent Error		
		MAE	Max	Min
(Actual Data)	35.4	-	-	-
Agostini and Bontemps [85]	26.45	32.3%	86.1%	9.7%
Bertsch et al. [11]	26.15	38.7%	101.9%	4.9%
Li and Wu [12]	18.87	42.1%	68.3%	1.9%
Oh et al. [86]	15.11	58.7%	75.3%	45.5%
Warrier et al. [87]	35.58	59.0%	335.6%	0.6%
Tran et al. [78]	8.26	75.6%	84.2%	56.4%
Kim et al. [61]	67.62	90.1%	209.5%	23.2%
Lazarek et al. [77]	70.51	95.6%	192.5%	28.8%
Ducoulombier et al. [88]	135.84	250.3%	335.4%	133.1%
Yu et al. [80]	183.06	457.7%	955.2%	235.7%

The nucleate boiling correlation of Cooper was used due to its agreement with various microchannel experiments [49, 84]:

$$h_{NB} = 55(-\log_{10}\text{Pr})^{-0.55}\,\text{Pr}^{0.12-0.2\log_{10}R_p}\,\frac{q_H''^{0.67}}{M^{0.5}} \tag{5.9}$$

The two-phase forced convective heat transfer coefficient (h_{TP}) includes the contributions from the liquid and vapor phases. To ensure that the correlation asymptotically approached liquid and vapor single phase heat transfer coefficients at vapor qualities of 0 and 1, respectively, the following equation was used to calculate the forced convective boiling heat transfer coefficients:

$$h_{CB} = h_{conv,l}(1-\chi) + h_{conv,v}\chi \tag{5.10}$$

The liquid and vapor heat transfer coefficients are determined separately using the Hausen correlation [89]:

$$h_{conv,i} = \frac{k_i}{D_H}[3.66 + \frac{0.0668\dfrac{D_H}{L}\,Re_i\,Pr_i}{1+0.04[\dfrac{D_H}{L}\,Re_i\,Pr_i]^{2/3}}] \tag{5.11}$$

where the Reynolds numbers for each phase are calculated as follows:

$$Re_{\text{i}} = \frac{G_{\text{ch}}D_{\text{H}}}{\mu_{\text{i}}} \tag{5.12}$$

When developing this model (*i.e.*, equations (5.8) through (5.12)), Bertsch et al. used an average heat flux in equation (5.9), normalized by the total heated channel surface area as follows:

$$q_{\text{H}}^{''} = \frac{q_{\text{He}}}{A_{\text{H}}} = \frac{q_{\text{He}}}{N(\,w_{\text{ch}} + 2h_{\text{ch}}\,)L_{\text{ch}}} \tag{5.13}$$

This formulation for average heat flux assumes that the surface temperature of the entire fin is equal to that of the base temperature, yielding a fin efficiency of 1. This assumption is assumed by every correlation in the literature, and, while it is adequate for some studies, it is insufficient when the fin efficiency is reduced due to low fin thermal conductivity, large aspect ratio, or a high heat transfer coefficient. In the proposed model for the current study, the average heat flux is calculated using the effective surface area, which includes the fin efficiency as follows:

$$A_{\text{H,act}} = N(w_{\text{ch}} + 2h_{\text{ch}}\eta_{\text{fin}})L_{\text{ch}} \tag{5.14}$$

Assuming a rectangular cross-section and an adiabatic fin tip at the top of the channels, the fin efficiency is calculated as follows [90]:

$$\eta_{\text{fin}} = \frac{\tanh(mL_{\text{c}})}{mL_{\text{c}}} = \frac{\tanh(mh_{\text{ch}})}{mh_{\text{ch}}} \tag{5.15}$$

The fin parameter (*m*) is defined as follows:

$$m = \sqrt{\frac{2h_{\text{TP}}}{K_{\text{Si}}w_{\text{web}}}} \tag{5.16}$$

Because the fin efficiency is between 0 and 1, the surface area calculated by equation (5.14) will always be lower than the total channel surface area. Therefore, the method proposed here to calculate the average heat flux will always yield a higher value, and the increase in the heat flux (ϕ) is calculated by:

Figure 5-12:   Difference in average heat flux vs. average two-phase heat transfer coefficient

$$\phi = \frac{q''_{H,act} - q''_H}{q''_H} \qquad (5.17)$$

For the two-phase sample point (Table 3-6), the effective heat flux ($q''_{H,act}$) is 15.4% higher than

the normalized heat flux (q''_H). The percent difference for all 15 data points are summarized as a

function of average flow boiling heat transfer coefficient on Figure 5-12. As the heat transfer

coefficient increases, the fin efficiency decreases, which causes the surface area utilization to also

decrease. As the surface area utilization decreases, the required heat transfer coefficient also

increases. This effect diminishes until the thermal resistance matches the required thermal

resistance measured during the experiment. In the current study, the maximum difference between

the normalized and effective surface area is 26.2%. As expected, as the heat transfer coefficient

increases the discrepancy between the normalized and corrected heat flux values also increases.

To further demonstrate the problem with using the normalized area, two case studies are considered. In the first case, the channel dimensions are assumed are equal to those used in the current study (45 μm wide and 200 μm tall channels, 35 μm wide webs, 125 channels). Assuming no heat spreading, a heat duty of 100 W and flow boiling heat transfer coefficient of 50 kW cm^{-2} K^{-1} are applied to a channel that is 1 mm long in the flow direction (Figure 5-13). The fin efficiency is then calculated for three different materials that are the most common for microchannel geometries: silicon, copper, and stainless steel. Using this fin efficiency, the normalized and effective average heat flux from the channels are then calculated. As shown in Table 5-2, the corrected effective heat flux is to 143% higher than the normalized heat flux for stainless steel. The difference is due to the low thermal conductivity of stainless steel, which yields a low fin efficiency (35%). For silicon and copper this is effect is less due to their higher fin efficiencies (79% and 91%, respectively). For the second case, the same imposed heat duty and flow boiling heat transfer coefficient are used as in the previous case (Figure 5-13). However, the thickness of the web between channels and the channel width are both varied simultaneously from 10 to 1,000 μm, which encompasses the range considered in all previous studies in the literature. For a fixed diode width of 10 mm, the number of channels is recalculated for each point and rounded to the nearest integer value as follows:

$$N = round(\frac{w_{\mathrm{d}}}{w_{\mathrm{ch}} + w_{\mathrm{web}}}) = round(\frac{w_{\mathrm{d}}}{2w_{\mathrm{web}}}) \tag{5.18}$$

Decreasing the web and channel width increases the total amount of surface area (*i.e.*, more channels), but it decreases the fin efficiency. The latter effect is dominant, and the net effect is a decrease in active surface area. This lower area results in the corrected heat flux being substantially higher than the normalized heat flux. As shown on Table 5-3, the effective heat flux is 79.0% higher than for the normalized heat flux at the smallest fin and channel thickness (10

124
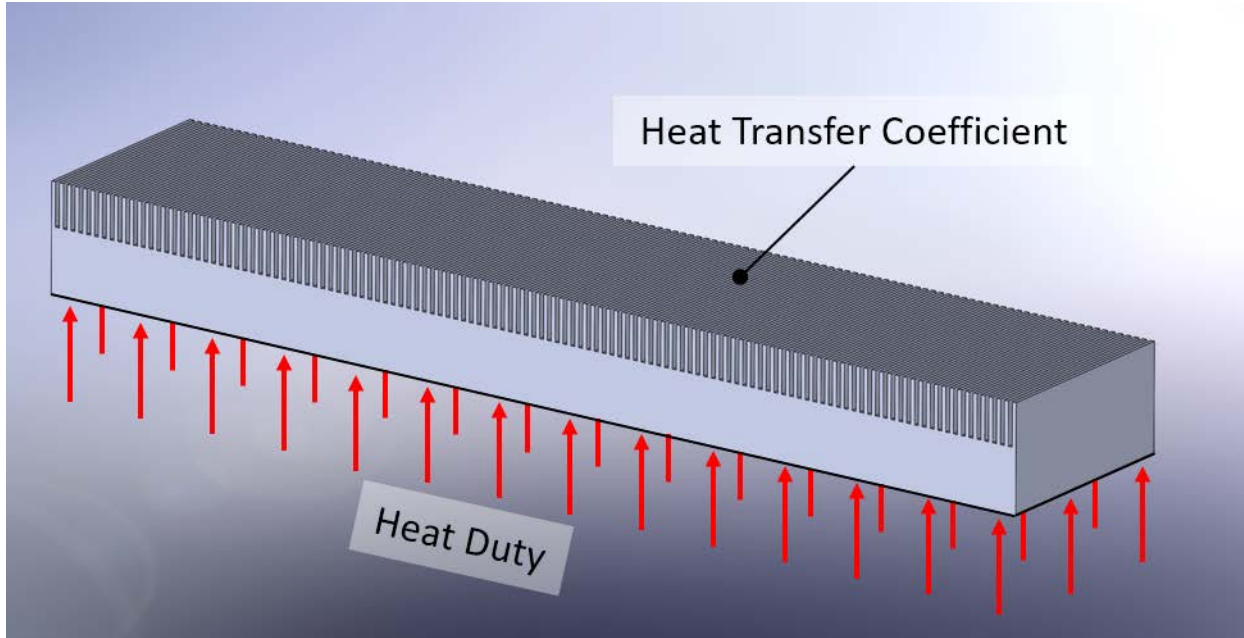
Figure 5-13: Sample geometry: 1 mm channel length, uniform base heat flux and flow boiling heat transfer coefficient applied to all wetted surfaces except the capping layer (not shown for clarity)

µm). This result shows that as the hydraulic diameter is reduced, and more channels are added, the surface area efficiency is much more important than in previous studies at larger dimensions. Considering both of these cases, it is clear that the normalized heat flux is inadequate for the current study, and for many existing microchannel heat transfer studies. By using the normalized heat flux, the reported heat transfer coefficient is artificially suppressed from its true value, and using the corrected heat flux is more realistic. For a fixed heat flux and the temperature difference between the fluid and the heater, the heat transfer coefficient is calculated from the following equation:

$$h = \frac{q_i^{''}}{\Delta T}$$
(5.19)

For example, using the same dimensions from the first case (45 μm wide and 200 μm tall channels, 35 μm wide webs, 125 channels) for a silicon microchannel array, the normalized and effect heat fluxes are 180 and 221 W cm^{-2}, respectively, for a heat duty of 100 W. At a fixed temperature

difference of 40 K, this yields heat transfer coefficient of 45 and 55.3 kW m^{-2} K^{-1} for the normalized and effective areas, respectively.

Table 5-2:   Case 1: variation in heat sink material; material properties evaluated at 50°C

q_{tot}	h_{TP}	Mat'l	K	η_{fin}	$q_H^{''}$	$q_{H,act}^{''}$	ϕ
[W]	[kW m^{-2} K^{-1}]	[-]	[W m^{-1} K^{-1}]	[–]	[W cm^{-2}]		[%]
100	50	Copper	395	0.91	180	195	8.43
		Silicon	137	0.79		221	23.2
		SS316	13.8	0.35		436	143

Table 5-3:   Case 2: variation in web width; material properties evaluated at 50°C

q_{tot}	h_{TP}	w_{web}, w_{ch}	N	η_{fin}	$q_H^{''}$	$q_{H,act}^{''}$	ϕ
[W]	[kW m^{-2} K^{-1}]	[μm]	[–]	[–]	[W cm^{-2}]		[%]
100	50	10	500	0.55	48.8	87.3	79.0
		50	100	0.84	222	259	16.4
		100	50	0.91	400	430	7.52
		1,000	5	0.99	1430	1433	0.28

These two studies show that the normalized heat flux is insufficient for comparing the heat transfer performance of many studies that have different heat sink geometry and materials. The proposed effective heat flux accounts for these effects, and is included in the development of the new correlation, which based on the formulation used by Bertsch et al. (equations (5.8) through (5.13)). For the proposed correlation, new coefficients are used for equation (5.8) as follows:

$$h_{TP} = a \cdot h_{NB}(1-\chi) + h_{conv,TP}(1+b \cdot (\chi^c - \chi^d)\exp(e \cdot Co)) \tag{5.20}$$

To determine these constants, the *MAE* (equation (5.7)) is minimized using the conjugate direction method for 14 of the 15 flow boiling data points. Using the remaining 14 data points, the resulting correlation is as follows:

$$h_{TP} = 0.24 \cdot h_{NB}(1-\chi) + h_{conv,TP}(1+70 \cdot (\chi^{1.18} - \chi^{100})\exp(-0.062 \cdot Co)) \tag{5.21}$$

126

As shown in this equation, the nucleate boiling term (h_{NB}) is suppressed by a factor of 0.24, which is consistent with previous studies that have suggested confined flow boiling to be dominated by convective heat transfer (Figure 2-3) [61]. In addition, the convective term is not strongly dependent on the vapor quality, which makes coefficient 'd' unnecessary. However, it was kept because this value allows the correlation to collapse to the single phase correlations for a quality of zero or 1. The average *MAE* of this proposed correlation is substantially lower (±8.1%) than for the Bertsch et al. correlation (±38.7%). The predictions for both correlations are plotted against the experimental heat transfer coefficient on Figure 5-14. As shown in the figure, 93% of the experimental data is predicted within ±15% for the proposed correlation. (The data point excluded due to experimental error at 62.5 kW m^{-2} K^{-1} is shown as a black square.) In the next section, this
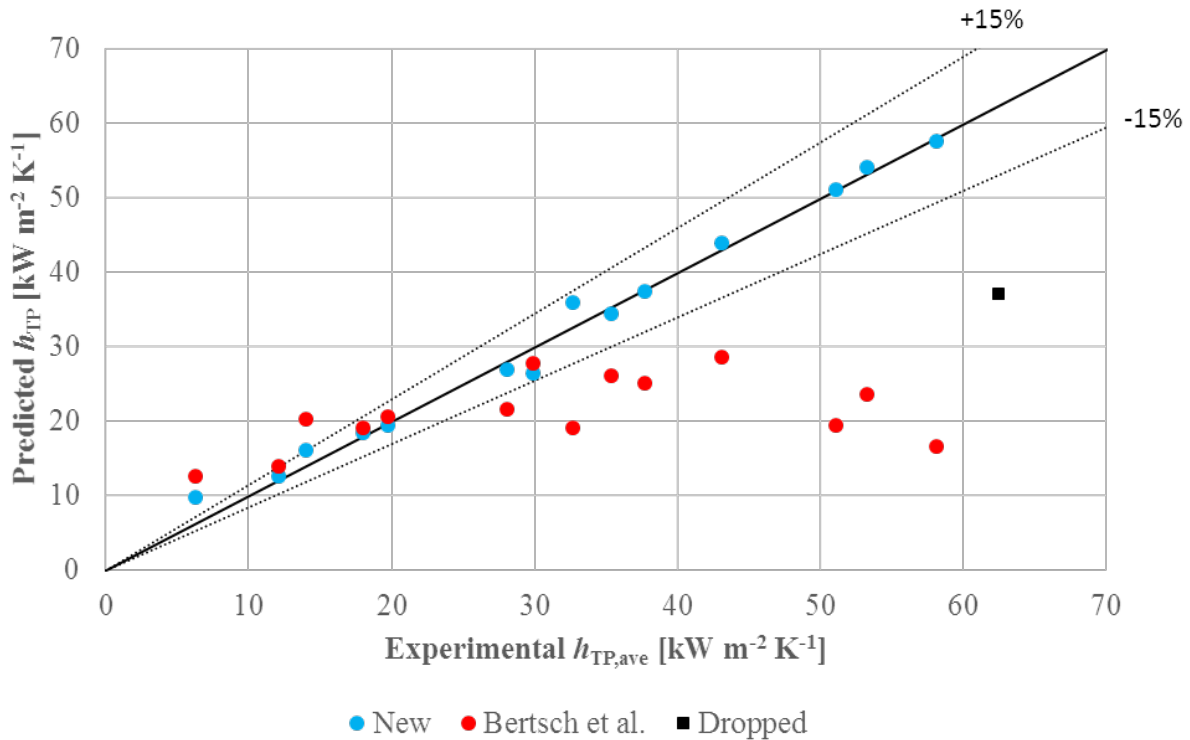
Figure 5-14: Predicted heat transfer coefficient from the Bertsch et al. and the proposed correlations as a function of the experimental heat transfer coefficient

new correlation is used to explore alternative parameters with the potential to reach a 10× increase in brightness over the state of the art.

5.5. Test Section Modifications

As discussed above in Section 0, the data from the current study shows that the laser diode brightness can increase by 1.87× over the state of the art at the same $\Delta T = 32°C$ using the current fluid, operating parameters, and geometry. By changing the operating parameters and geometry, it is possible to improve this performance by maximizing the heat transfer coefficient and surface area, and therefore, lowering the heater temperature for a fixed heat load. With the new correlation, it is possible to explore this potential effect. Because R134a broke down at temperature (70°C) near the imposed diode temperature limit (60°C), alternative working fluids are explored. In addition, the geometry of the heat sink is also modified to show potential for reaching a 10× improvement in diode array brightness for a few candidate fluids. In the following sections, the operating parameter, working fluid, and heat sink geometry options that warrant further investigation are discussed.

5.5.1. Operating Parameters

In general, flow boiling heat transfer coefficients are larger than subcooled liquid flow heat transfer coefficients. If the fluid enters the microchannels downstream of the orifice at the target saturation temperature, the diode temperature could be lower and the total heat rejection rate has the potential to be higher. In the current study, the inlet fluid temperature was set at sufficient large degree of subcooling to prevent cavitation in the test section prior to applying power to the heater. As discussed Section 3.4.1, this was done to enable calculation of the pressure at the transition from single-phase to boiling. The consequence is a 5-10°C temperature rise of the fluid is required before the onset of boiling, which, at the nominal flow rate of 100 g min^{-1}, yields

128

between 10.8 and 21.3 W of heat dissipated to the single phase fluid. During the experiments, the onset of boiling occurred near the heater center, which limits the heat transfer in the region that is most important. By eliminating subcooling of the working fluid, it is possible to reduce the heater temperature further. However, it should be noted that subcooled boiling could be happening at a microscopic level, which increases the local heat transfer coefficient, and further investigation is warranted.

To accomplish this in the current configuration of the test facility and still extract the average flow boiling heat transfer coefficient, a different method must be used to determining the transition pressure, and one possible method is described here. First, the inlet fluid temperature could be set at the target saturation temperature, and the inlet pressure set well above the saturation pressure. Then, the inlet pressure could be gradually lowered until a two-phase flow is observed in the channels. If the single-phase pressure drop is known just prior to this point, the pressure at the observed transition location can be calculated. As the heater power is increased, the transition location can be observed, and the single phase pressure drop up to that location can be estimated. It is expected that the high flow boiling heat transfer coefficient would be applied to a larger area, which reduces the effective thermal resistance from the heater to the fluid and, therefore, could lower the heater temperature for a fixed flow rate. To achieve improved performance, different working fluids are also explored in the next section.

5.5.2. Working Fluid

To increase performance beyond that demonstrated in the existing test section, alternative fluids were considered. Assuming that the operating parameters and microchannel geometry are fixed, a database of fluids is considered: organics, alcohols, refrigerants, and engineered fluids. From the application specific requirements, and inspection of many existing two-phase heat

129

transfer correlations, the following generalized set of constraints was developed primarily to increase heat transfer performance and secondarily enable implementation in a range of applications:

- Maximize the following fluid properties: enthalpy of vaporization, specific heat, thermal conductivity, and liquid and vapor Prandtl numbers. The enthalpy of vaporization affects the vapor quality of the fluid at a given heat duty and flow rate, and a lower vapor quality is typically associated with a lower pressure drop, which is advantageous for some systems. A higher specific heat enables the fluid to dissipate more energy at a fixed flow rate, and increasing the thermal conductivity of the fluid increases its ability to transfer heat from the wall into the fluid in both single-phase and two-phase flows. High Prandtl numbers for each phase also yields high convective heat transfer, which is dominant in confined flow regimes.

- Minimize the following fluid characteristics: phase slip ratio (ρ_l / ρ_v), flammability, material incompatibility, toxicity/health hazards environmental impact. The phase slip ratio determines two-phase flow stability, and is potentially a limiting factor for reaching the critical heat flux. The other considerations are straightforward: liquid-vapor phase change thermal management of laser diodes is more appealing if the working fluid does not require special attention to ensure the safety of operating personnel.

- Utilize a fluid with a moderate pressure at a saturation temperature of 10°C. If the saturation pressure is very low, *e.g.* water (1.2 kPa), flow in a recirculating loop is difficult to sustain because downstream pressure drop from the test section are of similar, or greater, magnitude than shown in the present study. Conversely, if the saturation pressure is too high, *e.g.* CO_2 (4.5 MPa), the test section will not be able to contain the working fluid.

- Be easily attainable/available. For this solution to be scalable to large arrays the working fluid must be readily available.

For an initial comparison of thermophysical properties, the database in the software package Engineering Equation Solver (EES) [91] and the web-based material property database MatWeb [92] were utilized. It was found that the following fluids have potential to exceed the current performance of R134a (alphabetical, not ranked):

- Ammonia

- Carbonyl sulfide

- Hydrocarbons (Trans-2-butene, isobutene)

- Propylene

- Refrigerants (R125, R218, R143a, Rc318, and R161)

- Water

Unfortunately, many of these options are flammable and/or toxic to humans and the environment. The NFPA (National Fire Protection Association) ratings for health, flammability, and instability are used to assess the danger of each fluid. This system rates the danger from 0 (benign) to 4 (extreme danger), and it is asserted, in the current study, that any fluid with a rating of 4 in any category is rejected as a possible option. For their extreme flammability, the following fluids are dropped from consideration: carbonlyl sulfide, hydrocarbons, propylene, and R143a. While ammonia is toxic (level 3) and corrosive, it is also commonly used in many industrial processes; thus, compatible materials are well known and handling procedures are established. The wetted materials in the test facility are also fully compatible with ammonia [93], but it would require the addition of a fume hood or other containment system to prevent exposure. The refrigerants R218 (octafluoropropane) and Rc318 (octafluorocyclobutane) are commonly used in plasma etching of

silicon, and it is unclear if these refrigerants alone would cause accelerated erosion. Because these refrigerants are relatively safe, further investigation on material compatibility is warranted. Refrigerant R125 (pentafluoroethane) is commonly found in fire extinguishers, has low toxicity, and, therefore, is considered. Water is an excellent candidate in all categories except slip ratio and saturation pressure at 10°C. The potential for using water as the working fluid is more promising with a modified heat sink design (Section 6.1). Table 5-4 shows the relevant thermophysical properties of the following fluids: ammonia, R218, Rc318, R125, R161, water, and R134a. As shown, ammonia and water have the most ideal properties in three categories, while the remainder have the best properties in at most 1 category. Ammonia has the most consistently promising properties, but, to date, no known, single-component microchannel boiling research has been conducted. In the following section, the performance of these alternative fluids are all considered in an alternative geometry that is predicted to achieve a 10× brightness improvement.

Table 5-4:   Thermophysical properties of selected alternative fluids at a 10°C saturation temperature; the best fluid for each property is bolded

Fluid	h_{fg}	C_p	K_l	K_v	P_{sat}	ρ_l	ρ_v	ρ_l/ρ_v	Pr_l	Pr_v
Units	kJ kg^{-1}	kJ kg^{-1} K^{-1}	W m^{-1} K^{-1}	W m^{-1} K^{-1}	kPa	kg m^{-3}	kg m^{-3}	-	-	-
Ammonia	1226	**4.674**	0.529	**0.024**	615.3	624.8	4.87	128.3	1.35	**1.09**
R218	84.71	1.108	0.049	0.012	568.8	1406	54.9	**25.6**	4.80	0.93
Rc318	110.6	1.077	0.071	0.011	**187.8**	1557	17.14	90.83	5.60	0.77
R125	124.7	1.301	0.066	0.013	909.2	1272	**57.75**	22.02	3.36	0.95
R161	364.2	2.191	0.118	0.014	599.2	740.6	13.95	53.1	2.67	1.04
Water	**2477**	4.188	**0.567**	0.018	1.228	999.7	0.0094	1.06×10^5	**9.65**	1.01
R134a	190.7	1.37	0.090	0.013	414.9	**1261**	20.24	62.3	3.56	0.82

5.5.3. Heat Sink Geometry

The prototype test section realized a 1.87× improvement in diode array brightness over the state of the art at comparable conditions. To reach the target improvement of 10×, the following dimensions are modified: channel width and depth, web width, and floor thickness. A thermal

132

resistance model of the test section is made using the proposed heat transfer correlation, which allows the performance at alternative dimensions and fluids to be predicted. Alternative dimensions are then proposed which are expected to improve performance.

The thermal resistance of the test section was modeled as conduction through the floor, and convection to the fluid at the flow boiling heat transfer coefficient, without heat spreading in the flow direction as follows:

$$R_{th} = R_{th,FB} + R_{th,floor} = \frac{1}{h_{TP} N L_{ch}(w_{ch} + 2h_{ch}\eta_{fin})} + \frac{t_{Si}}{K_{Si} A_{He}} \qquad (5.22)$$

The heat transfer coefficient (h_{TP}) is calculated by the proposed correlation (equation (5.21)), with the appropriate fin efficiency equations ((5.15) and (5.16)). Using this thermal resistance model, the temperature of the diode (T_{Di}) is predicted from the saturation temperature of the fluid and heat duty as follows:

$$T_{Di} = T_{sat} + q_{He} R_{th} \qquad (5.23)$$

This model assumes that there is no single-phase cooling or heat spreading along the flow direction. At a dissipation of 71.6 W, by only flow boiling yields a predicted heat transfer coefficient of 45 kW m^{-2} K^{-1}. Using the dimensions in the current study (Table 5-5), and the experimental two-phase length for this case (2.7 mm), the thermal resistance is 0.177 K W^{-1}. For the saturation temperature of 20.1°C, this yields a diode temperature of 47.2°C. Therefore, it is suggested that the diode temperature would be reduced by ~4°C, from the experimental temperature of 51.2°C, by eliminating single-phase cooling.
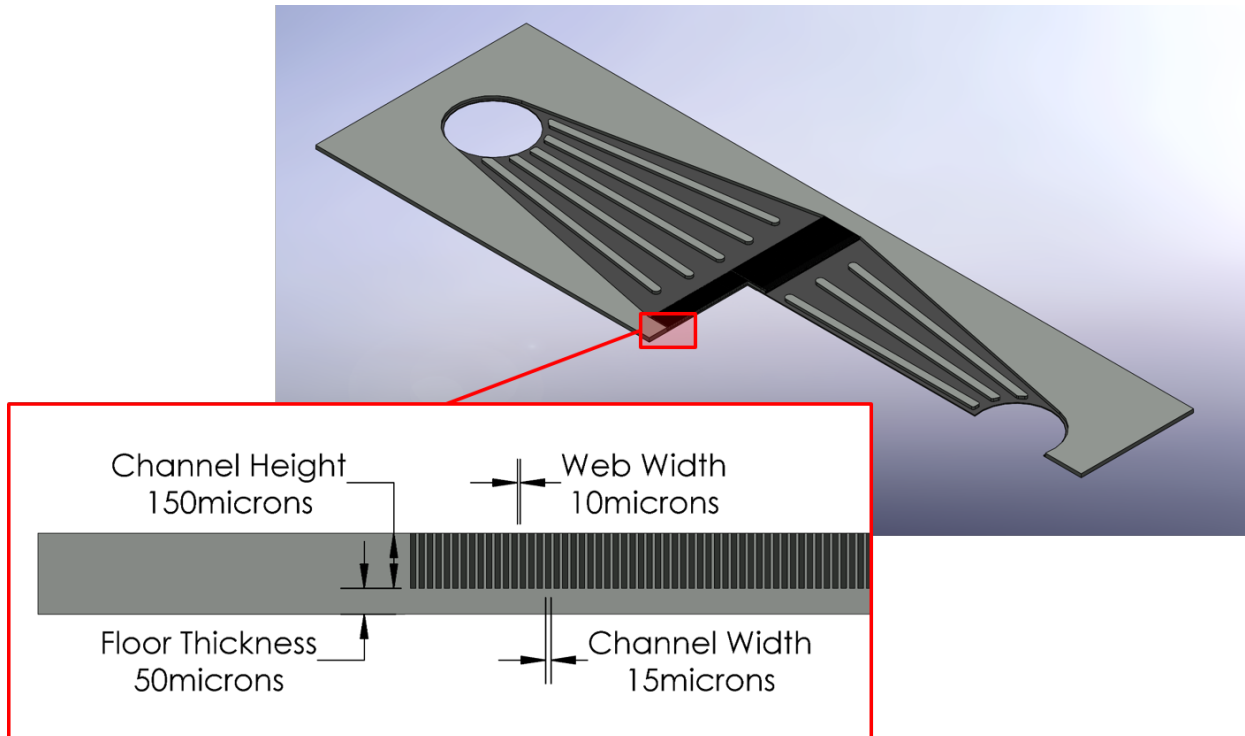
Figure 5-15:　Solid model cut-away showing the proposed microchannel dimensions in the test section

New proposed dimensions are given on Table 5-5 and shown in Figure 5-15, where the channel and web widths have both been reduced to include additional channel surface area. (The heater remains the same 1 mm × 10 mm footprint at the center of this microchannel array, as shown in Figure 5-16. The heaters design is also kept same as the current work.) The hydraulic diameter has been reduced from 73.4 µm to 27.3 µm, and, to avoid a significant increase in pressure drop, the microchannel length has been shortened from 5 mm to 2 mm. Additionally, the channel height has been reduced from 200 µm to 150 µm to reduce the diode pitch. Furthermore, to retain the effect of the inlet restriction, orifice, the width has been reduced from 10 µm to 7.5 µm, and the length has been increased from 50 µm to 250 µm. Finally, the floor thickness is reduced from 300 µm to 50 µm which decreases the conduction thermal resistance. For a given fluid, the heat transfer coefficient does not change substantially in the proposed geometry. Instead, the effective heat transfer resistance reduction is dominated by an increase in surface area. For example, in the

current geometry with R134a at 10°C saturation temperature and 60°C diode temperature, the flow boiling heat transfer coefficient is 66.9 kW m^{-2} K^{-1} using the proposed correlation, which yields a fin efficiency of 75.7%. These same conditions in the proposed geometry yield a predicted heat transfer coefficient of 63.1 kW m^{-2} K^{-1} and a fin efficiency of 63.8%. However, the effective heat transfer surface area is 2× higher for the proposed geometry, which enables the heat duty to increase by nearly 2× for the same surface temperature. Furthermore, if the proposed correlation is valid for ammonia in the proposed geometry, it is expected that the heat transfer coefficient increases to 109.5 kW m^{-2} K^{-1}, but at a fin efficiency of 52.2%. This increase is attributed to a substantial increase in nucleate boiling, which enables an increase in heat duty. As a result of the higher heat transfer coefficient for ammonia and this larger surface area for the proposed test section, this yields a 3× higher heat duty than the original geometry with R134a.

Table 5-5:   Summary of current and proposed microchannel geometry

Description	Current	Proposed	% Change	Unit
Channel width (w_{ch})	45	15	-66.7	μm
Channel height (h_{ch})	200	150	-25.0	μm
Channel hydraulic diameter (D_H)	73.4	27.3	-62.8	μm
Channel length (L_{ch})	5	2	-60.0	mm
Web width (w_{web})	35	10	-71.4	μm
Orifice width (w_{orf})	10	7.5	-25.0	μm
Orifice length (L_{orf})	50	250	400	μm
Floor thickness (t_{Si})	300	50	-83.4	μm
Number of channels (N)	125	400	220	–

It is desirable to minimize pressure drop both for pumping power and temperature uniformity. The latter is negatively affected by a large pressure drop because the saturation temperature is determined by it pressure for a liquid-vapor mixture. Because the proposed operating conditions call for the elimination of subcooling, the two-phase pressure drop is predicted by the correlation by Lee and Garimella (Appendix C.2) [30]. Unfortunately, the hydraulic diameter in the current work is smaller than the conditions used for this correlation, and
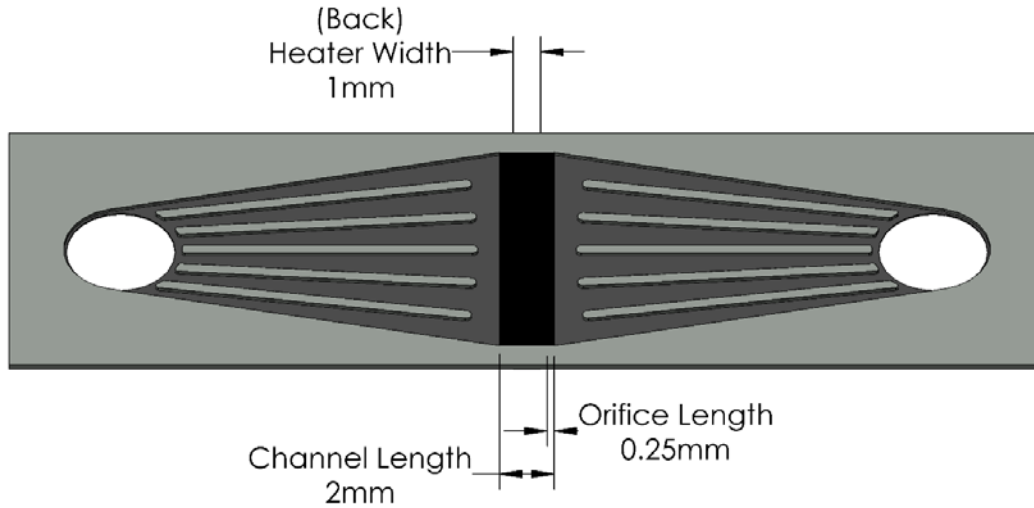
Figure 5-16:   Solid model overview of the new proposed heat transfer test section geometry.

the complex geometry of the outlet manifold and test section interface precludes an accurate

validation of this pressure drop correlation. As a result, this correlation was only used to compare

the relative change in pressure drop from the R134a data collected in the present study. It is also

asserted that the two-phase pressure drop over the 1 mm heater be limited to 100 kPa, and this

constraint is used to determine the optimal flow rate for each fluid in each geometry. For all of the

alternative fluids, the highest heat duty possible at the 60°C diode temperature limit are calculated

for both the current and proposed geometries. In both cases it is assumed that there is no heat

spreading, *i.e.* the heated length is constrained to 1 mm, and the saturation temperature of the fluid

is 10°C. To determine the best mass flow rate for each condition, the diode power was maximized,

while still subject to the temperature constraint.

The change in brightness relative to the state of the art is computed as:

$$\theta = \frac{Br_{\text{current}}}{Br_{\text{Skidmore}}}$$ (5.24)

where the simple brightness (*Br*) is calculated from equation (5.6). Table 5-6 shows the predicted

performance of the heat sink for each fluid and geometry. As shown, all suggested working fluids

are predicted to exceed the 10× improvement in brightness over Skidmore et al. in the proposed geometry. The best expected performance in the current geometry is ammonia, at a potential improvement of 7.1× compared to Skidmore et al. The two-phase pressure drop in the channel section is significantly higher in the proposed geometry in all cases, and the 100 kPa limit was reached in each case except for R134a. The prediction of pressure drop for water is substantially higher than is likely to be realistic: the saturated vapor density is very low at 10°C, (9.4×10^{-3} kg m^{-3}), which causes the model to predict an extremely high frictional pressure drop. Because the surface efficiency is lower at these smaller dimensions, the average heated channel heat flux is elevated from the current study, which introduces the possibility of reaching the CHF condition. Unfortunately, due to R134a breaking down, the CHF was not experimentally characterized, and experimental dryout correlations are inapplicable at the conditions used in the present study. Furthermore, while the current correlation predicts that heat transfer coefficient will remain high with shrinking hydraulic diameter indefinitely, this trend may not hold due to increasing bubble confinement. Therefore, in future studies, it is suggested that several hydraulic diameters between the current and proposed geometry are investigated.

Table 5-6: Predicted performance comparison between current and proposed geometry for the alterative working fluids; cases where the brightness improvement exceed 10× are bolded

Fluid | Geometry		Mass Flow Rate, $\dot{m}$	Vapor Quality, χ	Heat flux, $q_{H,act}$	Heat Duty, q_{He}	Brightness Change, θ	Pressure Drop, dP_{ch}
Unit		g min^{-1}	%	W cm^{-2}	W	-	kPa
Ammonia	Current	13.8	44.8	344	125	6.3	1.79
	Proposed	**55.4**	**11.25**	**542**	**338**	**16.9**	**100****
R218	Current	129	64	295	115	5.8	6.13
	Proposed	**313**	**63.4**	**388**	**280**	**14.0**	**100****
Rc318	Current	101	57.5	263	107	5.4	11.9
	Proposed	119	87.2	216	191	9.6	100**
R125	Current	99.6	57.4	305	117	5.9	4.2
	Proposed	**277**	**49.3**	**398**	**284**	**14.2**	**100****
R161	Current	36	46.9	244	101	5.1	2.86
	Proposed	**206**	**16.8**	**246**	**209**	**10.5**	**100****
R134a	Current	62.6	54	262	106	5.3	4.91
	Proposed	**157**	**44.3**	**268**	**222**	**11.1**	**84.1**
Water	Current	5	45.13	216	93.2	4.7	237*
	Proposed	**20**	**27.6**	**281**	**229**	**11.5**	**5964***

Notes:
* Vapor density is low, causing predicted pressure drop to be exceedingly high
** Pressure drop limited to 100 kPa

CHAPTER 6. CONCLUSION AND RECOMMENDATIONS

The current study is the first part of a multi-year heat sink development effort to yield a 10× increase in laser diode array brightness over the existing state of the art. The principle limit for achieving higher brightness is thermal management. State of the art laser diodes generate heat fluxes in excess of 1 kW cm^{-2} on a plane parallel to the light emitting edge. As the laser diode bars are packed closer together, it becomes increasingly difficult to remove large amounts of heat in the diminishing space between neighboring diode bars. In existing laser diode systems, the heat transfer fluid is a single phase liquid, and energy from the diode is dissipated by increasing the liquid temperature. As heat rejection requirements increase, the flow rate and, therefore, pressure drop, of the cooling fluid increases to keep the diode temperature within acceptable limits and minimize its temperature gradient. In contrast, flow boiling heat sinks utilize liquid-vapor phase change, which allows heat transport to occur with a negligible increase in temperature and, due to a high enthalpy of vaporization, at comparatively low mass flow rates. However, there had been no prior investigations at the conditions required for high brightness edge emitting laser diode arrays: >1 kW cm^{-2} and >10 kW cm^{-3}.

The current investigation is the first study to characterizing flow boiling heat transfer in a microchannel array of with D_H < 100 µm subjected to a base heat flux of up to 1.1 kW cm^{-2}. To investigate the flow boiling heat transfer characteristics at these conditions, a microchannel heat sink was fabricated in silicon through a series of MEMS processing techniques. The test section withstood a continuous static pressure of 1.03 MPa, and, during some extreme instances, severe temperature gradients that approached 50°C mm^{-1}. During testing, a glass layer bonded to the silicon enabled flow visualization to identify the location where the fluid began to boil. Inlet

restrictions upstream of each channel ensured that the flow through the channels was stable and uniformly distributed throughout the microchannel array. On the reverse side of the silicon, a thin film heater was deposited in the center of the microchannel array to simulate a diode (1 mm × 10 mm). At the extremes ends of this heater, contact pads (1 mm × 1 mm) provided a site for electrical communication between the test facility and the heater, ensured that the heating was confined to the heater, and allowed a uniform heat generation rate across the heater. Joule heating in the heater was controlled by a power supply, and the current was measured accurately using a high precision shunt resistor. The test section was also designed with quick-release connections to facilitate changes to the part interface for new geometries. The entire facility was hermetically sealed to the test section using gaskets and a custom clamping interface. A positive displacement pump circulated the working fluid in the loop, and its flow rate was accurately measured using a Coriolis flow meter. The system pressure was set by pressurized nitrogen in an accumulator, and the temperature of the fluid at the test section inlet was controlled by a recirculating chiller through a heat exchanger upstream of the test section. To interface electrically with the test section, a harness clamps around it prior to installation in the fluidic interface. The surface temperature of the heater and surrounding silicon were accurately measured by a calibrated infrared pyrometer (±0.67°C).

During the experiments, a set of computer program scripts was used to automate data collection and to establish steady state (±1% in average heater temperature over a 5-min period). From this data, the average value and its associated uncertainty (95% confidence level) of each measured quantity was determined. These measured quantities are then used to conservatively estimate the ambient heat transfer to the environment, which was shown to be small: on average 3% and at most 4.5% of the total test section heat duty. This heat duty was then used to determine the outlet vapor quality from an energy balance across the test section. The location where the

fluid transitioned from single phase to boiling was determined from scaled images, which allowed both the local fluid pressure and average flow boiling heat transfer coefficient to be determined.

The average flow boiling heat transfer coefficient was determined from a numerical model that accounted for heat spreading and the non-uniformities in both surface temperature and heat flux. This method did not use typical assumptions used by prior investigators – uniform heat flux, uniform heater temperature, and no axial conduction in the test section – yielding a more accurate calculation of the average heat transfer coefficient. Unfortunately, the fluid pressure in the channels downstream of the transition location is uncertain due to two reasons: the flow rates and geometry have not been investigated previously, and significant minor and frictional losses were present in the outlet manifold and several sudden expansions. As a result, three fluid temperature profiles were used to calculate the average heat transfer coefficient, and these results were average to estimate the final value. The uncertainty in average heat transfer coefficient from this method was determined to be an average of ±11.1%, and at most ±17%.

The resulting average flow boiling heat transfer coefficients were then used to compare the current study to the state of the art diode cooler by Skidmore and coworkers. It was found that, for a comparable 32°C temperature difference, their thermal resistance of 0.32 K W^{-1} was lower than the minimum thermal resistance observed in the present study (0.39 K W^{-1}). However, by if the floor of the test section was reduced from 300 µm to 100 µm, it is possible that the thermal resistance in the current study would be lower than the presented by Skidmore et al., which warrants further investigation. Nevertheless, the geometry in the present study allows the pitch between diodes to decrease significantly, and, consequently, the brightness in the current work was 1.87× greater than the state of the art, at a comparable temperature difference.

The average heat transfer coefficients measured in the present study were compared to ten representative correlations, and it was found that none of these predicted the experimental performance to within ±32.3%. As a result, a new correlation was generated from the current study that was based on the formulation of Bertch and coworkers. Additionally, the average heat flux in the new correlation uses a corrected heat transfer area that includes the effect of fin efficiency. In prior investigations, the average heat flux normalized by the surface area was used, which leads to inaccurate results. For example, when the heat transfer coefficient is high, heat sink thermal conductivity is low, or the aspect ratio of the webs between channels is high, significant differences between the actual effective and area-average normalized heat fluxes occurred. Two cases were presented that showed not using the effective heat flux yields a significant difference for the geometry and material used in the present study. By using the effective heat flux and different constants for the correlation presented by Bertsch et al., the proposed correlation predicted the experimental performance to with ±8.1%.

The proposed correlation, and results from experimentation, were then used to propose alternative operating parameters, working fluids, and microchannel dimensions to reach the 10× target improvement in brightness over the state of the art. The results call for an elimination of inlet subcooling to contain heat spreading. This maximizes the heat transfer coefficient in this area, as opposed to the current operation where approximately half of the heated area is cooled by single phase fluid. To make this change, a new empirical method of estimating saturation temperature in the test section, for determining heat transfer coefficient, was proposed. Because R134a began to foul the channels at a heater temperature of 70°C, alternative working fluids were considered: ammonia, R218, Rc318, R125, R161 and water. New geometric dimensions were considered to increase the heat transfer surface area, and extrapolations of the current heat transfer

model with these fluids show that a proposed next generation test section design and operating conditions are expected to improve brightness up to 12× over the state of the art with R134a. If ammonia is used at the working fluid, the brightness could potential increase by more than 19× over the state of the art.

In summary, this work has yielded a more accurate characterization technique for assessing flow boiling heat transfer performance at the dimensions and scales relevant to laser diode cooling. While the measured thermal resistance was higher than the state of the art, it was shown that a laser diode array that is forced convectively cooling by a liquid-vapor phase change fluid moving inside the geometry used in the present study can yield a brightness increase of 1.87×. Using the new proposed method, it was shown that >10× improvement in brightness is possible with new microchannel dimensions and alternative working fluids. In the following section, recommendations for future research are discussed further.

6.1. Recommendations for Future Research

In addition to investigating alternative working fluids, eliminating inlet subcooling, and reducing the length, channel and web width, and floor thickness, the follow are recommended for future research:

- Significant heat spreading was observed in the test section, which made extraction of the average heat transfer coefficient difficult. It is recommended that new geometries are considered that minimize heat spreading, and that a variety of channel hydraulic diameters are investigated. Using this larger pool of data, the development of a heat transfer correlation that is applicable over this whole range should improve its prediction capability over a wider range of conditions. In addition, it is recommended that tests with more robust fluids are conducted so that critical heat flux is understood. This will enable the

performance limitations in future microchannel designs and operating conditions to be more accurately predicted.

- Because there is significant pressure drop in the test section, it is suggested that new outlet manifold geometries are considered. For example, the interface manifold could be modified to add a secondary flow across the outlet manifold that creates a venturi effect to provide active suction at the channel outlet. This could potentially alleviate accelerational pressure drop, which could enable water to continuously operation at very low pressures. This could be implemented by modifying the PEEK interface in the current facility without modifying the test section. This could also potentially eliminate the need for an inline condensing heat exchanger by condensing the fluid with a cold liquid at a higher pressure.

- The Deep Reactive Ion Etching (DRIE) process can cause localized undercutting of the vertical channels in the silicon, forming a corrugated side wall (Figure 3-5). This scalloping of the silicon has the potential to significantly increase heat transfer area. For example, a repeating scallop of 2 µm radius over a channel depth of 200 µm would yield 50 individual curves, each with a length of 6.28 µm ($\pi \cdot r_{scallop}$). Therefore, the total length on a single wall would be increased by 57.1% to 314 µm; the overall effect on heated perimeter area is a 51.3% increase. In Section 5.5.3, it was found that surface area is expected to have a strong effect on overall heat transfer; therefore, this additional area is expected to lower the diode temperature. By using a lower passivation time step relative to etching time step, the scallops would yield deeper undercutting. In addition, increasing the frequency of etch steps could produce more scallops of shallower depth. Optimizing the frequency, passivation, and etch time steps could yield improved heat transfer performances, and further investigation is warranted.

REFERENCES

[1]   S. L. Matthias Pospiech, "Laser Diodes: an Introduction," U. o. Hannover, Ed., ed. Germany, 2004.

[2]   S. O. Kasap, *Optoelectronics and Photonics: Principles and Practices*: Prentice Hall, 2001.

[3]   M. Leers and K. Boucke, "Cooling approaches for high power diode laser bars," in *Electronic Components and Technology Conference, 2008. ECTC 2008. 58th*, 2008, pp. 1011-1016.

[4]   "Laser Programs: The First 25 Years (1972-1997)," L. P. D. Services, Ed., ed: University of California, p. 20.

[5]   J. A. Skidmore, B. L. Freitas, J. Crawford, J. Satariano, E. Utterback, L. DiMercurio*, et al.*, "Silicon monolithic microchannel-cooled laser diode array," *Applied Physics Letters,* vol. 77, pp. 10-12, 2000.

[6]   R. Beach, W. J. Benett, B. L. Freitas, D. Mundinger, B. J. Comaskey, R. W. Solan*, et al.*, "Modular Microchannel Cooled Heatsinks for High Average Power Laser Diode Arrays," *IEEE J. Quantum Electron,* vol. 28, pp. 966-976, 1992.

[7]   R. Feeler, J. Junghans, G. Kemner, and E. Stephens, "Next-generation microchannel coolers," *Proceedings of SPIE, the International Society for Optical Engineering,* vol. 6876, pp. 687608-687608-8, 2008.

[8]   Y. Karni, G. Klumel, M. Levy, Y. Berk, Y. Openhaim, Y. Gridish*, et al.*, "Active cooling solutions for high power laser diodes stacks," *High-Power Diode Laser Technology and Applications VI,* vol. 6876, 2008.

[9]   S. K. Roy and B. L. Avanic, "A Very High Heat Flux Microchannel Heat Exchanger for Cooling of Semiconductor Laser Diode Arrays," *IEEE Trasactions on Components, Packaging, and Manufacturing Technology - Part B,* vol. 19, pp. 444-451, 1996.

[10]   S.-M. Kim and I. Mudawar, "Review of databases and predictive methods for heat transfer in condensing and boiling mini/micro-channel flows," *International Journal of Heat and Mass Transfer,* vol. 77, pp. 627-652, 10// 2014.

[11]   S. S. Bertsch, E. A. Groll, and S. V. Garimella, "A composite heat transfer correlation for saturated flow boiling in small channels," *International Journal of Heat and Mass Transfer,* vol. 52, pp. 2110-2118, 2009.

[12]   W. Li and Z. Wu, "A general correlation for evaporative heat transfer in micro/mini-channels," *International Journal of Heat and Mass Transfer,* vol. 53, pp. 1778-1787, 4// 2010.

[13]   M. Traub, M. Giesberts, J. Geiger, C. Johnigk, and H. D. Hoffmann, "High Peak Power Fiber Coupled Super-Pulsed Diode Lasers," in *High-Power Diode Laser Technology and Applications Vii*. vol. 7198, M. S. Zediker, Ed., ed Bellingham: Spie-Int Soc Optical Engineering, 2009.

[14]   J. Collins. (2015, February). *World's most powerful laser diode arrays deployed*. Available: http://www.gizmag.com/worlds-highest-power-laser-diode-arrays/36535/

[15]   S.-M. Kim and I. Mudawar, "Universal approach to predicting saturated flow boiling heat transfer in mini/micro-channels – Part I. Dryout incipience quality," *International Journal of Heat and Mass Transfer,* vol. 64, pp. 1226-1238, 9// 2013.

[16]   D. B. Tuckerman and R. F. W. Pease, "High-performance heat sinking for VLSI," *Electron Device Letters, IEEE,* vol. 2, pp. 126-129, 1981.

[17]   S. G. Kandlikar, S. Colin, Y. Peles, S. Garimella, R. F. Pease, J. J. Brandner, *et al.*, "Heat Transfer in Microchannels—2012 Status and Research Needs," *Journal of Heat Transfer,* vol. 135, p. 091001, 2013.

[18]   T. Harirchian and S. V. Garimella, "Boiling Heat Transfer and Flow Regimes in Microchannels—A Comprehensive Understanding," *Journal of Electronic Packaging,* vol. 133, pp. 011001-011001, 2011.

[19]   S. V. Garimella, "Advances in mesoscale thermal management technologies for microelectronics," *Microelectronics Journal,* vol. 37, pp. 1165-1185, 2006.

[20]   M. Asadi, G. Xie, and B. Sunden, "A review of heat transfer and pressure drop characteristics of single and two-phase microchannels," *International Journal of Heat and Mass Transfer,* vol. 79, pp. 34-53, 2014.

[21]   M. Fabbri, S. Jiang, and V. K. Dhir, "A Comparative Study of Cooling of High Power Density Electronics Using Sprays and Microjets," *Journal of Heat Transfer,* vol. 127, pp. 38-48, 2005.

[22]   C. J. Kuo and Y. Peles, "Local measurement of flow boiling in structured surface microchannels," *International Journal of Heat and Mass Transfer,* vol. 50, pp. 4513-4526, 11// 2007.

[23]   S. Szczukiewicz, N. Borhani, and J. R. Thome, "Two-phase flow operational maps for multi-microchannel evaporators," *International Journal of Heat and Fluid Flow,* vol. 42, pp. 176-189, 8// 2013.

[24]   A. E. Bergles, J. H. Lienhard, G. E. Kendall, and P. Griffith, "Boiling and Evaporation in Small Diameter Channels," *Heat Transfer Engineering,* vol. 24, p. 18, 2003.

[25]   T. Harirchian and S. V. Garimella, "A Comprehensive Flow Regime Map for Microchannel Flow Boiling With Quantitative Transition Criteria," *Int. J. Heat Mass Transfer,* vol. 53, pp. 2694-2702, 2010.

[26]   R. K. Sarangi, A. Bhattacharya, and R. S. Prasher, "Numerical modelling of boiling heat transfer in microchannels," *Applied Thermal Engineering,* vol. 29, pp. 300-309, 2// 2009.

[27]   A. Cioncolini and J. R. Thome, "Algebraic turbulence modeling in adiabatic and evaporating annular two-phase flow," *International Journal of Heat and Fluid Flow,* vol. 32, pp. 805-817, 8// 2011.

[28]   J. Lee and I. Mudawar, "Low-Temperature Two-Phase Microchannel Cooling for High-Heat-Flux Thermal Management of Defense Electronics," *Components and Packaging Technologies, IEEE Transactions on,* vol. 32, pp. 453-465, 2009.

[29]   S. S. Bertsch, E. A. Groll, and S. V. Garimella, "Refrigerant flow boiling heat transfer in parallel microchannels as a function of local vapor quality," *International Journal of Heat and Mass Transfer,* vol. 51, pp. 4775-4787, 2008.

[30]   P.-S. Lee and S. V. Garimella, "Saturated flow boiling heat transfer and pressure drop in silicon microchannel arrays," *International Journal of Heat and Mass Transfer,* vol. 51, pp. 789-806, 2// 2008.

[31]   V. V. Kuznetsov, A. S. Shamirzaev, I. A. Kozulin, and S. P. Kozlov, "Correlation of the Flow Pattern and Flow Boiling Heat Transfer in Microchannels," *Heat Transfer Engineering,* vol. 34, pp. 235-245, 2013.

[32]   V. P. Carey, *Liquid-Vapor Phase-Change Phenomena*. London: Taylor & Francis, 1992.

[33]   S. S. Bertsch, E. A. Groll, and S. V. Garimella, "A composite heat transfer correlation for saturated flow boiling in small channels," *International Journal of Heat and Mass Transfer,* vol. 52, pp. 2110-2118, 2009.

[34]   F. P. Incropera, D. P. Dewitt, T. L. Bergman, and A. S. Lavine, *Fundamentals of Heat Mass Transfer*, 6th ed.: John Wiley & Sons, 2007.

[35]   T. Zhang, S. Chen, and E. N. Wang, "A separated-flow model for predicting flow boiling critical heat flux and pressure drop characteristics in microchannels," in *ASME 2012 10th International Conference on Nanochannels, Microchannels, and Minichannels*, Rio Grande, Puerto Rico, 2012, pp. 1-10.

[36]   R. Revellin and J. R. Thome, "A theoretical model for the prediction of the critical heat flux in heated microchannels," *International Journal of Heat and Mass Transfer,* vol. 51, pp. 1216-1225, 2008.

[37]   R. Revellin and J. R. Thome, "Experimental investigation of R-134a and R-245fa two-phase flow in microchannels for different flow conditions," *International Journal of Heat and Fluid Flow,* vol. 28, pp. 63-71, 2007.

[38]   G. Hetsroni, "Boiling in micro-channels," *Bulletin of the Polish Academy of Sciences. Technical sciences,* vol. 58, pp. 155-163, 2010.

[39]   C. J. Kuo and Y. Peles, "Critical Heat Flux of Water at Subatmospheric Pressures in Microchannels," *Journal of Heat Transfer,* vol. 130, pp. 072403-072403, 2008.

[40]   R. Revellin, J. M. Quiben, J. Bonjour, and J. R. Thome, "Effect of Local Hot Spots on the Maximum Dissipation Rates During Flow Boiling in a Microchannel," *Components and Packaging Technologies, IEEE Transactions on,* vol. 31, pp. 407-416, 2008.

[41]   P. Jung Eung, J. R. Thome, and B. Michel, "Effect of inlet orifice on saturated CHF and flow visualization in multi-microchannel heat sinks," in *Semiconductor Thermal Measurement and Management Symposium, 2009. SEMI-THERM 2009. 25th Annual IEEE*, 2009, pp. 1-8.

[42]   J. J. Brandner and S. Maikowske, "Influence of Fluid Flow Distribution in Micro-Channel Arrays to Phase Transition Processes," *Experimental Heat Transfer,* vol. 25, pp. 172-180, 2012.

[43]   I. Mudawar and M. B. Bowers, "Ultra-high critical heat flux (CHF) for subcooled water flow boiling—I: CHF data and parametric effects for small diameter tubes," *International Journal of Heat and Mass Transfer,* vol. 42, pp. 1405-1428, 4// 1999.

[44]   W. Hailei and R. B. Peterson, "Enhanced Boiling Heat Transfer in Parallel Microchannels With Diffusion Brazed Wire Mesh," *Components and Packaging Technologies, IEEE Transactions on,* vol. 33, pp. 784-793, 2010.

[45]   F. J. d. Nascimento, H. L. S. L. Leao, and G. Ribatski, "Flow Boiling Heat Transfer of R134a in a Microchannel Heat Sink," in *ASME 2012 10th International Conference on Nanochannels, Microchannels, and Minichannels*, Rio Grande, Puerto Rico, 2012, pp. 1-10.

[46]   G. Hetsroni, A. Mosyak, E. Pogrebnyak, and Z. Segal, "Explosive boiling of water in parallel micro-channels," *International Journal of Multiphase Flow,* vol. 31, pp. 371-392, 4// 2005.

[47]   S. N. Ritchey, J. A. Weibel, and S. V. Garimella, "Local measurement of flow boiling heat transfer in an array of non-uniformly heated microchannels," *International Journal of Heat and Mass Transfer,* vol. 71, pp. 206-216, 4// 2014.

[48]   S. Szczukiewicz, N. Borhani, and J. R. Thome, "Two-phase heat transfer and high-speed visualization of refrigerant flows in 100×100 μm2 silicon multi-microchannels," *International Journal of Refrigeration,* vol. 36, pp. 402-413, 3// 2013.

[49]   S. S. Bertsch, E. A. Groll, and S. V. Garimella, "Effects of heat flux, mass flux, vapor quality, and saturation temperature on flow boiling heat transfer in microchannels," *International Journal of Multiphase Flow,* vol. 35, pp. 142-154, 2009.

[50]   T. Chen and S. V. Garimella, "Measurements and high-speed visualizations of flow boiling of a dielectric fluid in a silicon microchannel heat sink," *International Journal of Multiphase Flow,* vol. 32, pp. 957-971, 8// 2006.

[51]   T. Chen and S. V. Garimella, "A Study of Critical Heat Flux During Flow Boiling in Microchannel Heat Sinks," *Journal of Heat Transfer,* vol. 134, pp. 011504-011504, 2011.

[52]   D. Li, G. S. Wu, W. Wang, Y. D. Wang, D. Liu, D. C. Zhang*, et al.*, "Enhancing Flow Boiling Heat Transfer in Microchannels for Thermal Management with Monolithically-Integrated Silicon Nanowires," *Nano Letters,* vol. 12, pp. 3385-3390, 2012/07/11 2012.

[53]   E. Costa-Patry, J. Olivier, B. A. Nichita, B. Michel, and J. R. Thome, "Two-phase flow of refrigerants in 85 μm-wide multi-microchannels: Part I – Pressure drop," *International Journal of Heat and Fluid Flow,* vol. 32, pp. 451-463, 4// 2011.

[54]   P. K. Buchling and S. G. Kandlikar, "Enhanced flow boiling of ethanol in open microchannels with tapered manifolds in a gravity-driven flow," presented at the ASME 2015 Internaltional Technical Conference and Exhibition on Packaging and Integration of Electronic and Photonic Microsystems, San Fracisco, CA, 2015.

[55]   W. Qu and I. Mudawar, "Measurement and correlation of critical heat flux in two-phase micro-channel heat sinks," *International journal of heat and mass transfer,* vol. 47, pp. 2045-2059, 2004.

[56]   T. Chen and S. V. Garimella, "Measurements and High-Speed Visualizations of Flow Boiling of a Dielectric Fluid in a Silicon Microchannel Heat Sink," *International Journal of Multiphase Flow,* vol. 32, pp. 957-971, 2006.

[57]   C. J. Kuo and Y. Peles, "Flow Boiling Instabilities in Microchannels and Means for Mitigation by Reentrant Cavities," *Journal of Heat Transfer,* vol. 130, pp. 072402-072402, 2008.

[58]   E. Costa-Patry, J. Olivier, B. A. Nichita, B. Michel, and J. R. Thome, "Two-phase flow of refrigerants in 85 μm-wide multi-microchannels: Part I – Pressure drop," *International Journal of Heat and Fluid Flow,* vol. 32, pp. 451-463, 4// 2011.

[59]   Q. Cai and A. Bhunia, "High heat flux phase change on porous carbon nanotube structures," *International Journal of Heat and Mass Transfer,* vol. 55, pp. 5544-5551, 10// 2012.

[60]   S. Szczukiewicz, N. Borhani, and J. R. Thome, "Fine-resolution two-phase flow heat transfer coefficient measurements of refrigerants in multi-microchannel evaporators," *International Journal of Heat and Mass Transfer,* vol. 67, pp. 913-929, 12// 2013.

[61]   S.-M. Kim and I. Mudawar, "Universal approach to predicting saturated flow boiling heat transfer in mini/micro-channels – Part II. Two-phase heat transfer coefficient," *International Journal of Heat and Mass Transfer,* vol. 64, pp. 1239-1256, 9// 2013.

[62]   J. C. Chen, "Correlation for boiling heat transfer to saturated fluids in convective flow," *I&EC Process Des. Dev.,* vol. 5, pp. 322-329, 1966.

[63]   R. Revellin and J. R. Thome, "A theoretical model for the prediction of the critical heat flux in heated microchannels," *Int. J. Heat Mass Transfer,* vol. 51, pp. 1216-1225, 2008.

[64]   S. D. Senturai, *Microsystem Design*. New York: Kluwer Academic Publishers, 2002.
[65]   G. K. Fedder, "MEMS Fabrication," presented at the ITC International Test Conference, 2003.
[66]   (2013, Sep. 26). *Hivatec*. Available: http://hivatec.ca/wp-content/uploads/2012/08/Pic1.png
[67]   J. E. Park, J. R. Thome, and B. Michel, "Effect of inlet orifices on saturated CHF and flow visualisation in multi-microchannel heat sinks," *IEEE Semiconductor Thermal Measurement and Management (SEMI-THERM) Symposium,* vol. 25, 2009.
[68]   R. K. Shah and A. L. London, *Laminar flow forced convection in ducts* vol. 1: Academic Press, 1978.
[69]   F. M. White, *Fluid Mechanics*, 7 ed.: McGraw-Hill, 2010.
[70]   "ANSYS CFX," 15 build 2013.10.10-08.49-130242 ed, 2013.
[71]   I. B. Celik, U. Ghia, P. J. Roache, and C. J. Freitas, "Procedure for Estimation and Reporting of Uncertainty Due to Discretization in CFD Applications," *Journal of Fluids Engineering,* 1993.
[72]   Y. Xu and X. Fang, "Correlations of void fraction for two-phase refrigerant flow in pipes," *Applied Thermal Engineering,* vol. 64, pp. 242-251, 3// 2014.
[73]   Y. Yan and T. Lin, "Evaporation heat transfer and pressure drop of refrigerant R-134a in a small pipe," *International Journal of Heat and Mass Transfer,* vol. 41, pp. 4183-4194, 1998.
[74]   S. Lin, P. A. Kew, and K. Cornwell, "Two-phase heat transfer to a refrigerant in a 1mm diameter tube," *International Journal of Refrigeration,* vol. 24, pp. 51-56, 2001.
[75]   H. J. Lee and S. Y. Lee, "Heat transfer correlation for boiling flows in small rectangular horizontal channels with low aspect ratios," *International Journal of Multiphase Flow,* vol. 27, pp. 2043-2062, 2001.
[76]   S. Saitoh, H. Daiguji, and E. Hihara, "Effect of tube diameter on boiling heat transfer of R-134a in horizontal small-diameter tubes," *International Journal of Heat and Mass Transfer,* vol. 48, pp. 4473-4984, 2005.
[77]   G. M. Lazarek and S. H. Black, "Evaporative heat transfer, pressure drop and critical heat flux in a small vertical tube with R-113," *International Journal of Heat and Mass Transfer,* vol. 25, pp. 945-960, 7// 1982.
[78]   T. N. Tran, M. W. Wambsganss, and D. M. France, "Small circular- and rectangular-channel boiling with two refrigerants," *International Journal of Multiphase Flow,* vol. 22, pp. 485-498, 6// 1996.
[79]   S. Kakac, R. K. Shah, and W. Aung, *Handbook of single-phase convective heat transfer*, 1 ed.: Wiley-Interscience, 1987.
[80]   W. Yu, D. M. France, M. W. Wambsganss, and J. R. Hull, "Two-phase pressure drop, boiling heat transfer, and critical heat flux to water in a small-diameter horizontal tube," *International Journal of Multiphase Flow,* vol. 28, pp. 927-941, 6// 2002.
[81]   R. W. Lockhart and R.C. Martinelli, "Proposed correlation of data for isothermal two-phase, two-component flow in pipes," *Chem. Eng. Prog.,* pp. 39–48, 1949.
[82]   B. Todd, "Electrochemical-Thermal Modeling and Microscale Phase Change for Passive Internal Thermal Management of Lithium Ion Batteries," Doctor of Philosophy, Mechanical Engineering, Georgia Institute of Technology, 2011.

[83] B. Agostini, M. Fabbri, J. Park, L. Wojtan, J. Thome, and B. Michel, "State of the Art of High Heat Flux Cooling Technologies," *Heat transfer engineering,* vol. 28, pp. 258-281, 2007.

[84] M. G. Cooper, "Heat Flow Rates in Saturated Nucleate Pool Boiling—A Wide-Ranging Examination Using Reduced Properties," *Adv. Heat Transfer,* vol. 16, pp. 157-239, 1984.

[85] B. Agostini and A. Bontemps, "Vertical flow boiling of refrigerant R134a in small channels," *International Journal of Heat and Fluid Flow,* vol. 26, pp. 296-306, 4// 2005.

[86] H.-K. Oh and C.-H. Son, "Evaporation flow pattern and heat transfer of R-22 and R-134a in small diameter tubes," *Heat and Mass Transfer,* vol. 47, pp. 703-717, 2011/06/01 2011.

[87] G. R. Warrier, V. K. Dhir, and L. A. Momoda, "Heat transfer and pressure drop in narrow rectangular channels," *Experimental Thermal and Fluid Science,* vol. 26, pp. 53-64, 4// 2002.

[88] M. Ducoulombier, S. Colasson, J. Bonjour, and P. Haberschill, "Carbon dioxide flow boiling in a single microchannel – Part II: Heat transfer," *Experimental Thermal and Fluid Science,* vol. 35, pp. 597-611, 5// 2011.

[89] H. Hausen, "Darstellung des Wärmeüberganges in Rohren durch verallgemeinerte Potenzbeziehungen," *Z. VDI Beiheft Verfahrenstechnik,* vol. 4, pp. 91-102, 1943.

[90] T. L. Bergman, A. S. Lavine, F. P. Incropera, and D. P. DeWitt, *Fundamentals of Heat and Mass Transfer*, 7th ed.: John Wiley & Sons, 2011.

[91] S. A. Klein, "Engineering Equation Solver," ed: F-Chart Software, 1992-2014.

[92] (2015, Oct 25). *Material Property Database*. Available: http://www.matweb.com/

[93] Cole-Parmer. (2015). *Chemical Compatibility Database*. Available: http://www.coleparmer.com/Chemical-Resistance

[94] G. M. Lazarek and S. H. Black, "Evaporative heat transfer, pressure drop and critical heat flux in a small vertical tube with R-113," *International Journal of Heat and Mass Transfer,* vol. 25, pp. 945-960, 1982.

[95] T. N. Tran, M. W. Wambsganss, and D. M. France, "Small circular and rectangular channel boiling with two refrigerants," *International Journal of Multiphase Flow,* vol. 22, pp. 485-498, 1996.

APPENDIX A. TEST SECTION HEATER DESIGN

In this appendix, the method for designing the heater and predicting its resistance are presented, which enables an appropriate power supply to be selected. In addition, current and heat generation rate distribution in the heater and the contact pads are estimated using a finite element analysis (FEA) model built in ANSYS Workbench.

During the experiments, a bench-top power supply sends current through the heater, which is measured using a high accuracy shunt resistor (Figure 3-38). The target heat transfer rate for the test section was 200W, and the resistance of the heater was estimated for the contributions from each layer (Table 3-2). The electrical resistance for each of these layers was estimated as follows:

$$R_{e,He} = \frac{\rho_e L}{A_{He}}$$ (A.1)

As shown in Table A-1, the length is the total distance in the direction of current flow, and the area is perpendicular to this direction. For example, the electrical resistivity (ρ_e) is 1.02×10^{-7} Ω m, the length is 10 mm, and the cross sectional area is 200×10^{-6} mm^2 (1 mm $\times$ 200 nm) for the platinum layer in the heater, which yields a resistance of 5.12 Ω. To estimate the effective resistance of the heater, a parallel resistance network model is used, which yields an equivalent resistance calculated as follows:

$$\frac{1}{R_{e,He}} = \frac{1}{R_{e,pt}} + \frac{1}{R_{e,ti}}$$ (A.2)

As a first approximation, current flows through the layers in the first contact pad in series. After leaving the contact pad, the current is then assumed to flow through the heater and the in second contact pad in series, which yields an overall system resistance as follows:

$$R_{e,tot} = R_{e,He} + 2(2R_{ti,cp} + R_{pt,cp} + R_{au,cp} + R_{ni,cp}) \qquad (A.3)$$

Each contact pad has two layers of titanium, and, using the individual results from Table A-1, the resulting total resistance ($R_{e,tot}$) of the system is 5.01 Ω at the lowest inlet temperature (10°C). However, during operation, the resistances change as the heater temperature increases. To ensure that the power supply could provide the desired power at elevated temperature, the change in heater resistance was predicted as follows:

$$R_{e,tot,f} = \sum R_{e,i,o}[1 + \alpha_i \Delta T] \qquad (A.4)$$

Because each layer has a different temperature coefficient of resistance, each resistance was individually scaled, and then the changes were summed to estimate the resistance at elevated temperature. A temperature difference of 150°C is considered the worst case scenario as this is a factor of safety of 3× over the expected temperature difference of 50°C (10°C inlet fluid → 60°C heater). Table A-1, summarizes the resistance of each layer at ambient and elevated temperatures. From equation (A.4), the resistance of the heater is expected to increase from 5.01 Ω to 8.12 Ω. As shown on the table, the thin layer of titanium for adhesion and the platinum heater have the highest resistance (99% of the total), and the electrical resistance of the layers in the contact pads are negligible.

Table A-1:   Heater design individual layer resistances

Material	Resistivity [Ω-m]	Desc.	Length [μm]	Width [μm]	Depth [μm]	R_{inlet} [Ω]	α_e [1/C]	$R_{elevated}$ [Ω]
Titanium	4.59×10^{-7}	Heater	10,000	1,000	0.01	459	0.0038	723
		Pad	0.01	1,000	1,000	4.59×10^{-9}		7.23×10^{-9}
Platinum	1.02×10^{-7}	Heater	10,000	1,000	0.2	5.01	0.0039	8.12
		Pad	0.2	1,000	1,000	2.05×10^{-8}		3.25×10^{-8}
Nickel	9.22×10^{-8}	Pad	0.5	1,000	1,000	4.61×10^{-8}	0.0031	6.75×10^{-8}
Gold	2.13×10^{-8}	Pad	0.5	1,000	1,000	2.13×10^{-9}	0.0034	3.22×10^{-9}

The power dissipated in the heater and the voltage drop across the heater are calculated as follows:

$$q_{\mathrm{H}} = I^2 R_{e,tot} \tag{A.5}$$

$$V_{\mathrm{H}} = I R_{e,tot} \tag{A.6}$$

These equations are used to calculate the current and voltage drop across the heater. At the minimum inlet temperature (10°C), 6.29 A at 31.8 V are required to deliver 200 W, and at the elevated temperature (160°C), 5.00 A at 40.1 V are required to deliver the same heater power. The chosen power supply is the Instek SPS-606 DC, which has operational limits of 6 A at 60 V. A heater temperature ≥ 36°C is required to deliver 200 W, which is sufficient for this particular heater
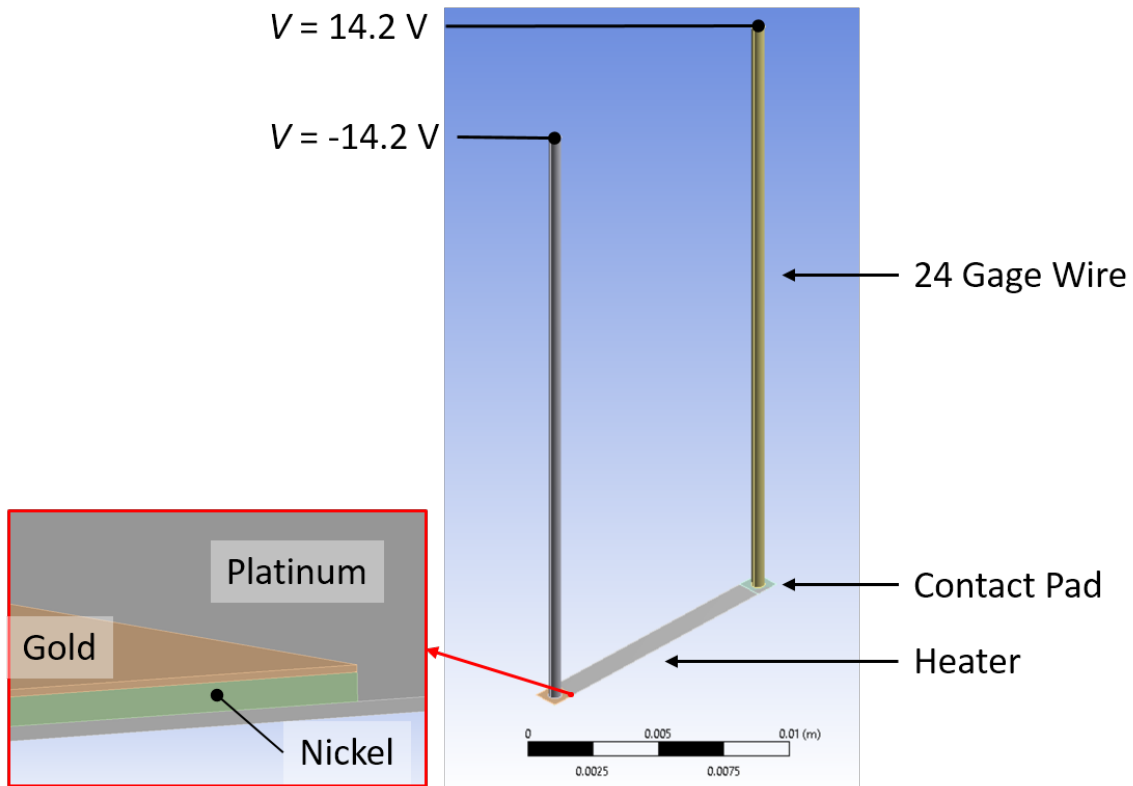
Figure A-1:   Current crowding model at 100 W power dissipation for a 60°C heater; the resistance of each layer was evaluated at this temperature and the appropriate potential difference was applied across the wire ends

design. The output for this power supply is regulated to within 0.01% of the set point (constant

current or voltage output operation). As discussed in Section B.3, a remote sense line on the power supply allows it to be disabled very quickly.

One final concern for the design of the heater is current crowding near the interface between the contact pads and the heater. If there is a high concentration of current in this region, significant joule heating can occur in the contact pads. To verify that this does not occur, a FEA model for the heater, contact pads, and 24 gauge wires was created. As shown in Figure A-1, each layer was modeled (except for the titanium adhesion layers) and the resistance was set appropriately to simulate a specific heater temperature. Then a potential difference was applied across the wire ends to result in a specific power dissipation. For a range of power inputs (10 – 200 W), the heater had uniform current density. Figure A-2 shows a sample result at 100 W and 60°C heater temperature, which shows that heat is generated uniformly in the thin film heater region. In addition, the volumetric heat generation rate in the heater is many orders of magnitude larger than the rates in the wire and contact pads (8.7×10^{13} W m^{-3} vs 7.4×10^6 W m^{-3}). As a result, the heat generation in the wire and contact pads is negligible compared to that of the heater.
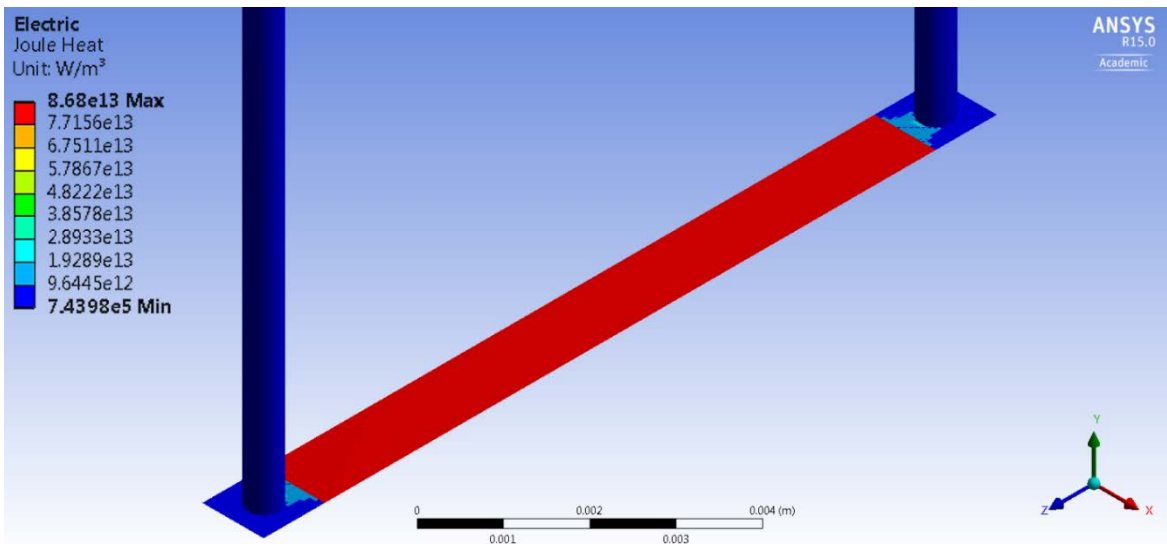
Figure A-2:   Ansys current density plot for 100 W for a 60°C thin film heater

APPENDIX B. TEST FACILITY DOCUMENTATION AND EQUIPMENT CALIBRATION

This appendix summarizes the test facility operation, and documents the data acquisition system, auto protect system, and calibration methodology for all required components.

B.1. General Facility Procedures

In the following sections, operating procedures for installing the electrical harness on the test section, installing the test section into the facility, evacuating and charging the system, locating the pyrometer, and executing an experiment are described.

B.1.1. Electrical Harness Installation

To facilitate joule heating in the thin film heater, the electrical harness must be installed on the test section prior to installation in the test facility. The installation procedure is as follows, and Figure B-1 provides a visualization of each step:

1. Measure the resistance of the heater on the desired test section by touching the probes with a digital multi-meter directly to the contact pads. The resistance of the produced thin film heater exceeds the estimated value (5.01 Ω) by ~2×, which is attributed to residual stress in the film which is deposited at elevated temperature. Furthermore, the resistance is found to exhibit variation from part to part, and with temperature cycling on a single test section. Therefore, each part must be individually measured every time the harness is changed, and the value recorded for comparison in step 8.

2. Set the threaded aluminum front plate down on a flat surface and then place the front ceramic piece on top. Install the gasket.

3. Place the test section glass side down into the front ceramic piece. Be careful not to apply torsion to the 4 ceramic pillars (circled in blue in Figure B-1).

4. Aim both of the electrical wires toward the screw terminal in the final installation (Figure B-2):

   a. Orient the assembly so that the test section identifier is on the left side. This corresponds with the downstream side of the part; which ensures that orifice is on the correct side of the PEEK interface.

   b. The wires should point toward the assembler, with the longer wire on top. This ensures that both wires can reach the screw terminal. Once the thumb screws are tightened, do not spin the wires: this could damage the contact pads. This step ensures they are aimed correctly.

5. Slide the back ceramic piece with pins and electrical wires in between the pillars on the front piece. Visually align the heater with the electrical pins in the ceramic, (circled in purple in Figure B-1). Again, be careful not apply any torsion to the pillars.

6. Install the thumb screws through both ceramic pieces and carefully hand-tighten them into the aluminum front plate. Tighten both screws at the same time to load the piece in compression only until the electrical wires no longer spin freely. Avoid over tightening because the ceramic and test sections are fragile.

7. Check the electrical connection by measuring the resistance across the leads, compare to the resistance measured in step 1. If the resistance is significantly different, disassemble and realign part with pins, and repeat steps 4-8.
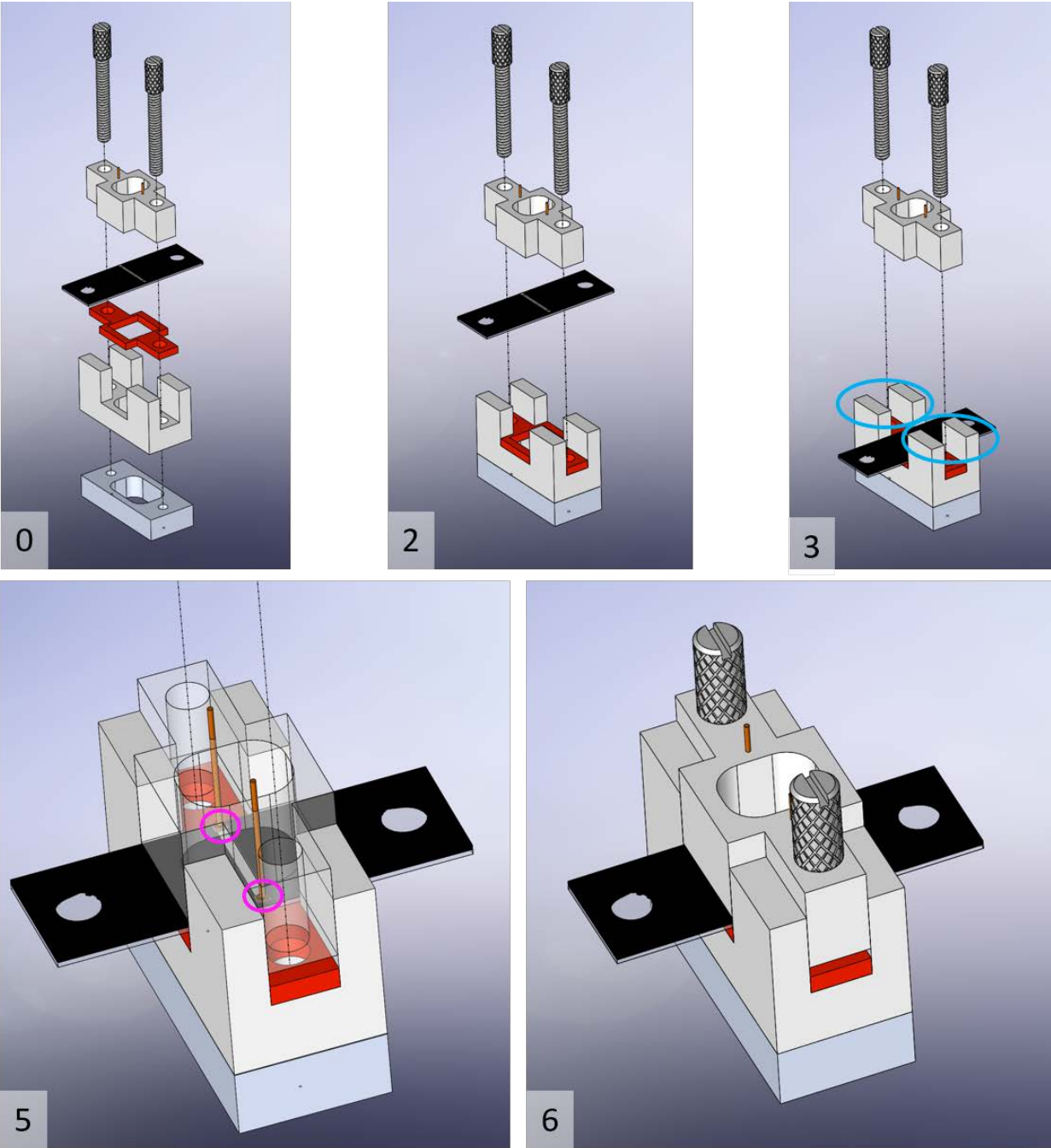
Figure B-1: Electrical clamp install: (0) fully exploded view, (2) place the front ceramic structure on the aluminum clamp and install the gasket, (3) install the part into the front ceramic piece, (4) see Figure B-2, (5) slide back ceramic piece (rendered transparent) into the opening in the front ceramic piece and align the heater with the pins, and (6) install the thumb screws to tighten the structure around the part
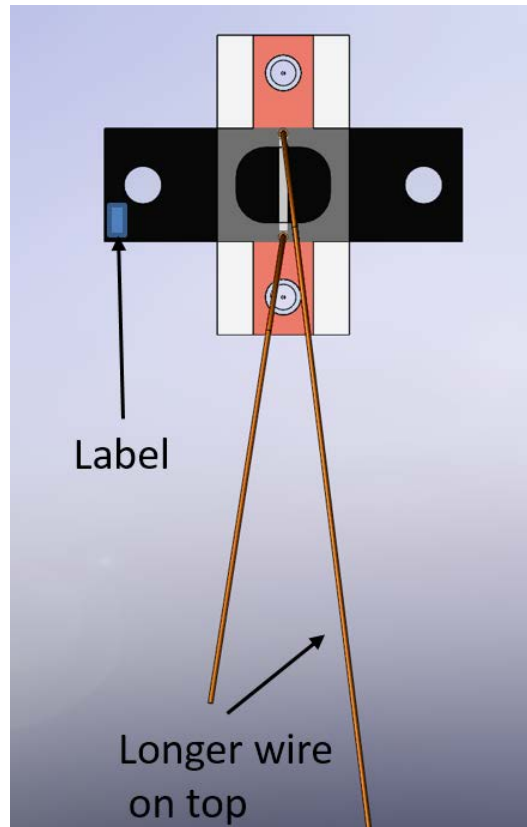
Figure B-2:   Step 4 visualization from the top looking down, with the back ceramic part rendered transparent

B.1.2. Test Section Installation

Once the electrical harness has been installed on the test section, it is ready to install in the test facility. A picture of the completed installation was provided on Figure 3-19, and the following process details the installation. This process assumes that the test section area is open to the environment, while the remainder of the test facility is either filled with fluid or open to the environment. Figure B-3 and Figure B-4 show illustrations to augment the instructions.

1. Wet the back side of the Gore sealing gaskets and install them onto the PEEK interface.

2. Hold the threaded aluminum back plate against the back side of the PEEK interface, and pass the wires through the center of both the PEEK and aluminum.
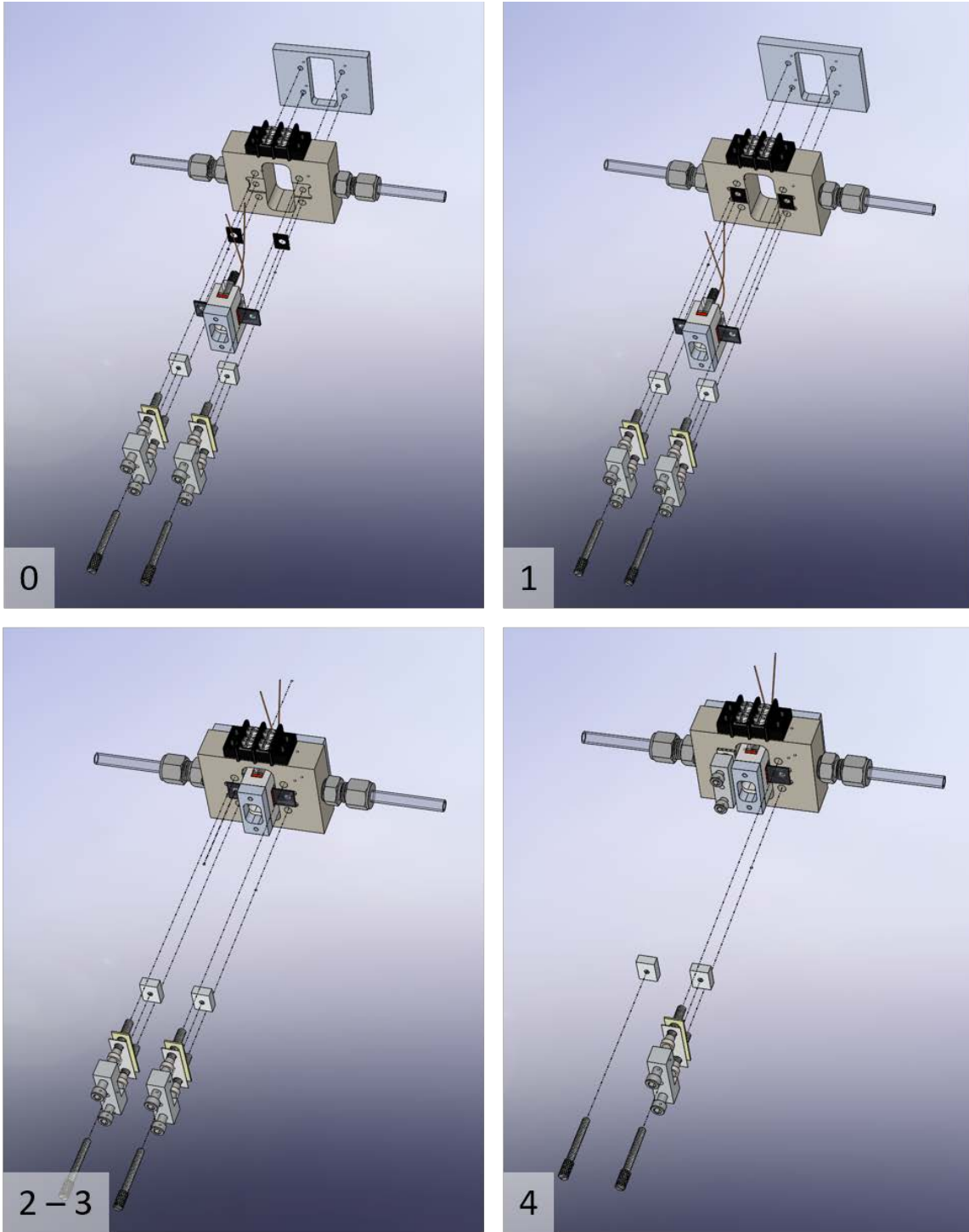
Figure B-3:   Steps 0 $\rightarrow$ 4 of the test section installation: (0) exploded view of all parts, (1) Gore-Tex gaskets installed in the recesses of the PEEK manifold, (2 – 3) threaded aluminum plate brought in contact with PEEK manifold and test section wires passed through the opening in both, and (4) hold the test section while installing the 1st clamping structure

3. Install the test section into the PEEK interface while aligning the fluid holes. Hold the assembly in place with one hand and compress the test section onto the interface through the hole axis.

4. Assemble the 1st clamping structure with the center piece removed, as shown in Figure B-3, and install it by passing the Allen screws through the PEEK and threading them into the aluminum back plate, while holding the test section in place. Tighten enough such that the silicone and PTFE gaskets of the installed clamp will hold the test section in place, allowing the assembler to let go of the part.

5. Check the alignment of the test section in the PEEK interface relative to the fluid ports. Adjust as necessary.

6. Install the second clamping structure with center piece removed.

7. Tighten the four Allen screws in a cross pattern (like changing a tire) to finalize the clamping structure, as shown in Figure B-4.

8. Install the center aluminum pieces that compress the gasket and create the seal between the PEEK and test section. They should easily slide in between the clamp and part, highlighted blue in Figure B-4.

9. Lightly tighten each thumb screw which presses the center piece in contact with the part. Ensure the screw seats into the recess on the center piece.

10. Firmly tighten each thumb screw at the same time, and compress the gaskets evenly. The seal is verified during the evacuation process, and can be tightened during this as deemed necessary.

11. Connect the electrical wires to the screw terminal onto the PEEK interface.
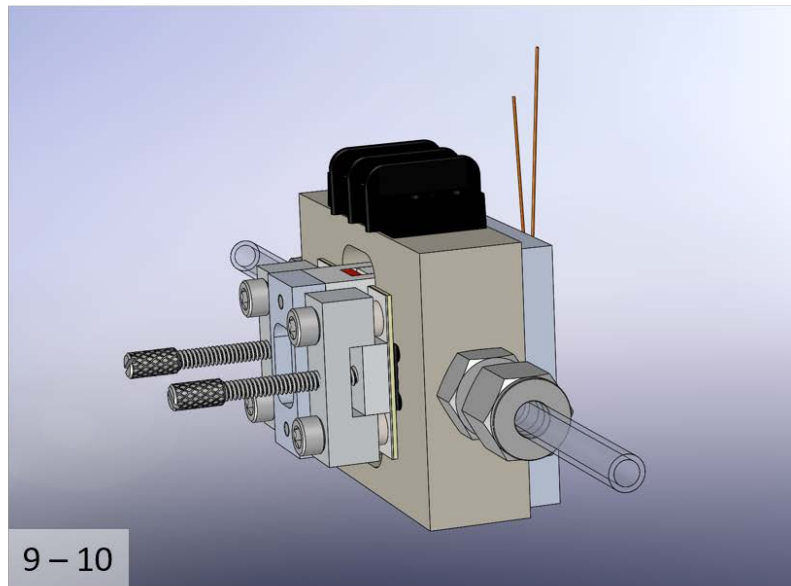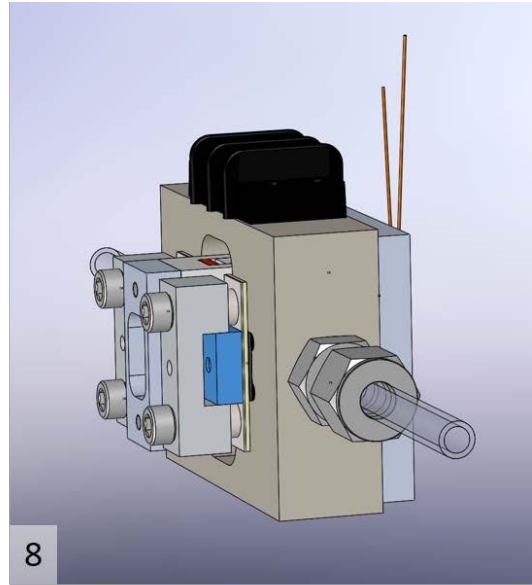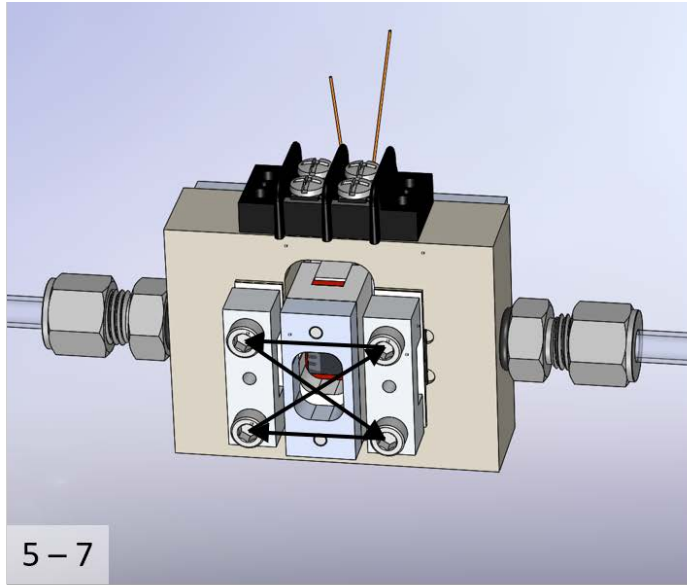
Figure B-4:   Steps 5 $\rightarrow$ 10 of the test section installation: (5 – 7) install the 2nd clamping structure and tighten in a repeating cross-pattern, (8) install the center clamping pieces (the spacers ensure they are easy to slide in), and (9 – 10) install thumb screws and ensure the screw seats into the recess on the center piece, tighten both sides simultaneously

B.1.3. System Evacuation

Prior to evacuating the system, the choice of working fluid must be determined. In the test facility, there are two pressure transducers that can be installed at the test section outlet. A vacuum transducer that operates over the range of 0-5 psia (34.47 kPa) can be used for fluids that have a low vapor pressure at 10°C (*e.g.,* water). The burst pressure on this transducer is 30 psia (206.8 kPa). The other transducer is for fluids with a high vapor pressure at 10°C (*e.g.,* R134a), and it has a range of 0-100 psia (689.5 kPa). Installing the correct transducer is critical, and it must be completed prior to the evacuation process. The following procedure assumes that the correct transducer and the test section has been installed.

1. Open the LabVIEW program and begin data collection to monitor the pressure within the facility.

2. Open the discharge valve on the facility.

3. Close the valves before and after the gear pump to protect the gears.

4. Open the bypass line in the facility.

5. Pressurize the accumulator with nitrogen at ~50 psia (344.8 kPa) to empty the bladder.

6. Close the bladder valve on the accumulator. The vacuum pump will damage the bladder if this is not done.

7. Close all valves to the environment including the vacuum lines.

8. Open all valves in the fluid loop including at the gear pump.

9. Ensure that there is no fluid in the cold trap, and empty if necessary.

10. Fill the Dewar around the cold trap with liquid nitrogen.

11. Turn on the vacuum pump and open the valve on the unit. This will evacuate the clear vacuum lines to three locations within the facility.

12. Open the three vacuum ports on the test facility to evacuate it from all liquids and/or air.

    a. The heat exchangers are where the working fluid pools. Continue evacuating until they warm up to room temperature. This can take multiple hours depending on how much fluid is present.

    b. Monitor the pressure of the facility with the LabVIEW program.

    c. Periodically open and close all of the internal ball valves in the loop to remove trapped condensate.

13. Once the pressure in the facility stabilizes below < 0.5 psia (3.44 kPa) close the valves to the bypass, and to and from the test section. This isolates the test section pressure transducers, which enables the user to determine if the Gore-Tex surface gaskets on the test section are leaking.

14. Close the vacuum ports, close the valve on the vacuum pump, and turn the vacuum pump off.

15. Ensure that the facility does not increase in pressure by more than 1 kPa in 15 min. This is approximately double the resolution of the $0 - 100$ psia (689.5 kPa) transducers. If there is a leak it is typically located at the test section – tighten the thumbscrews on the clamps and repeat steps 11-15.

B.1.4. System Charging

Once the facility is evacuated, it is ready to be charged with a working fluid. This process differs slightly depending on the fluid. For water and other fluids that are liquid ambient temperature and pressure, a process tank pressure vessel is used to interface with the facility. For high vapor pressure fluids, it is assumed that they are in a pressure vessel. The following details the process of filling the facility, and a sample image is provided on Figure B-5:

1. Ensure that the proper pressure transducer was installed prior to system evacuation.

2. Take note of the fluid vapor pressure at the ambient temperature.

3. Set the pressure in the accumulator (with nitrogen) to be 10 psia (68.9 kPa) above the fluid vapor pressure at ambient temperature.

4. Open the valve between the accumulator bladder and facility, which had been closed to prevent the bladder from ripping during evacuation.

5. Close the valves on both sides of the gear pump to protect the gears.

6. Ensure the test section and bypass lines are both open.

7. Install the test facility interface tube connected to the filter and quick-disconnect hardware to the fluid tank, (see Figure B-5) for pressure vessels keep the valve on the tank closed at this time.

8. Connect the quick-disconnect to the vacuum pump adapter to evacuate the charging lines.

9. Evacuate the charging lines for approximately 5 minutes.

10. Connect the quick-disconnect to the charging port and ensure the tank is setup to discharge fluid (typically upside down for refrigerants).

11. Open the valve on the pressure vessel to fill the system, and visually observe the fill level by the flow sights on both heat exchangers and on either side of the test section.

12. Once these lines are full, open the valves on both sides of the gear pump.

13. Slowly decrease the nitrogen pressure in the accumulator until it begins to fill. The target fill is ~10-20%. It is desired to have a small amount of fluid in the bladder, but not full.

14. Shut-off the valve to the fluid tank and detach the quick-disconnect from the facility.
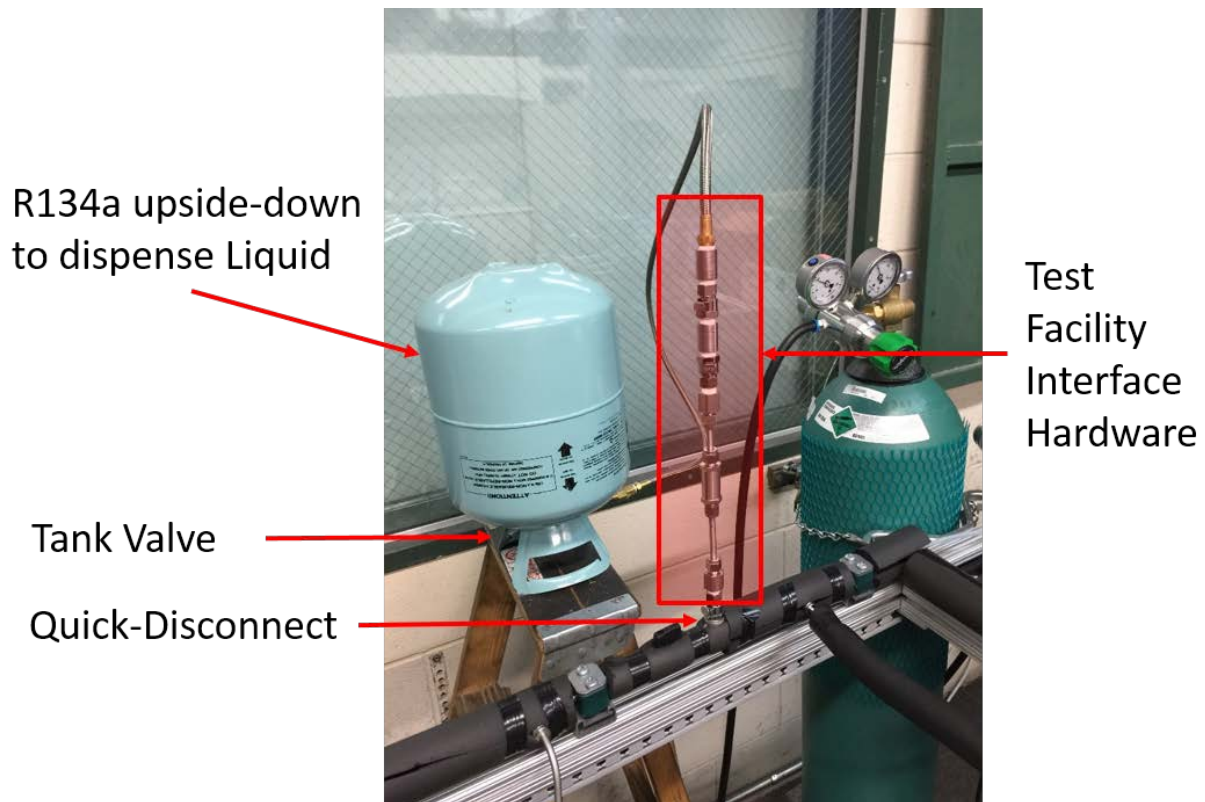
Figure B-5:   Filling the test facility with R134a; annotated with items called out in the procedure

B.1.5. Pyrometer Alignment

Every time a new test section is installed or the pyrometer is moved off the mount, it must be re-centered onto the heater. The performance of the autonomous kill switch and accuracy of temperature sweeps depend on locating the pyrometer properly. The test section is mounted to accommodate thermal growth, and the pyrometer mount is not fixed to the test section to ensure it could be quickly removed if a part were to break and was leaking. As a result, the mount rests on four pins which locate it on the test section. During single-phase testing without any subcooled boiling, the center of the heater is the hottest spot. This location is found by the following procedure:
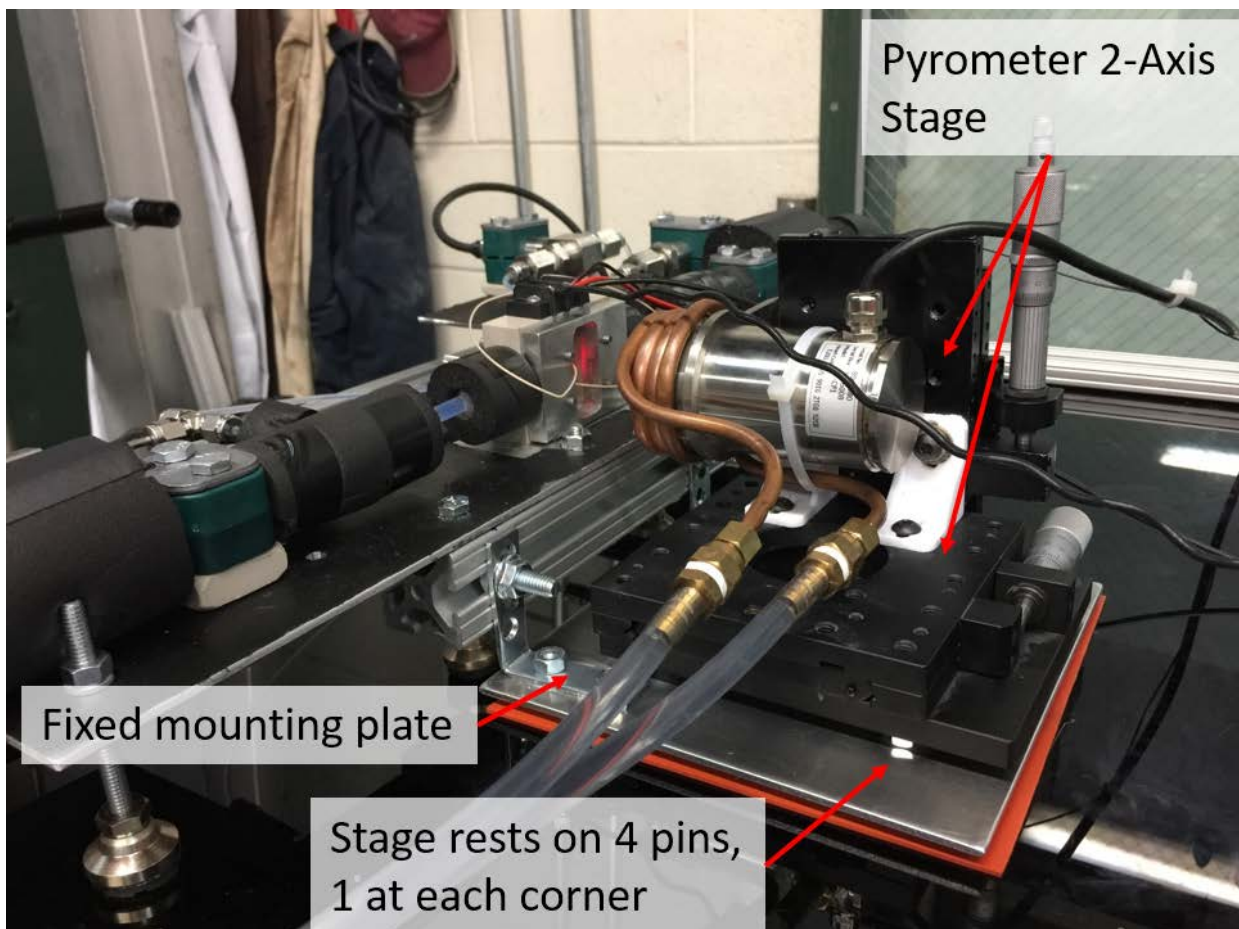
Figure B-6:   Annotated image of the back side of the test section, showing that the mounting plate is fixed to the test section; the 2-axis pyrometer stage rests on 4-pins

1. Ensure pyrometer has clear line of sight to the test section; bend the electrical wires out of the way if required.

2. Circulate the cooling fluid through the test section. Ensure that the fluid remains single phase and that the pyrometer is focused on the last known center location.

3. Apply power to the heater to reach a temperature of 10 to 15°C higher than the entering fluid temperature. Ensure that the fluid remains in single phase at the test section outlet.

4. Sweep the location of the pyrometer upstream and downstream until the hottest spot is approximately located.

5. Move the pyrometer upstream and downstream in 0.05 mm increments. There is a 0.1 mm range where the temperature is nearly constant. The center of this range is center of the heater. (There is some variation in temperature reading at a constant position; take an average over a few samples.)

6. Sweep the location perpendicular to the flow direction in both directions to ensure that the temperature along the heater is constant. If a temperature variation of more than 3°C is observed, rotate the mount as needed and repeat steps 3-5.

B.1.6. Executing a Test

Once the electrical clamping structure is installed on the test section and it has been installed into a leak-free and charged facility, and the pyrometer has been centered on the test section, data collection can begin. The procedure for executing a test is as follows:

1. Determine target mass flow rate and saturation temperature.

2. Turn on the gear pump and achieve target flow rate by setting gear pump speed.

3. Turn on chiller to lower the working fluid temperature to the desired subcooling at the test section inlet. Adjust chiller temperature and needle valves between heat exchangers as necessary.

4. Once temperature and flow rate are stabilized near the target values, apply current to the heater to find the highest input that remains single-phase. Watch for vapor in the outlet sight.

5. Just prior to boiling initiation, record data for the single-phase pressure drop calculation.

6. Increase the power of the heater slightly, and locate the approximate boiling transition location. Calculate the approximate single-phase pressure drop from the inlet pressure transducer to the transition location.

7. Determine the target inlet pressure (saturation pressure plus the single-phase pressure drop, equation (3.13)) and set the inlet pressure with the accumulator.

8. Continue flow boiling tests in increments of increased applied power.

   a. Modify pressure, flow, and temperature controls as required to maintain the desired flow rate and transition location saturation pressure.

   b. During the tests, ensure that the fluid into the gear pump inlet is single-phase. Adjust the chiller bypass valve between heat exchangers to increase condenser heat exchanger flow rate if necessary.

At each data point, ensure that the test facility stabilizes (*i.e.*, <1% change over 5-min interval). Collect data using the procedure outline in Appendix B.2. Record the test section surface temperature by sweeping pyrometer position. Minimize time spent with pyrometer aimed anywhere but the heater: the auto protect circuit will not protect the part during that time.
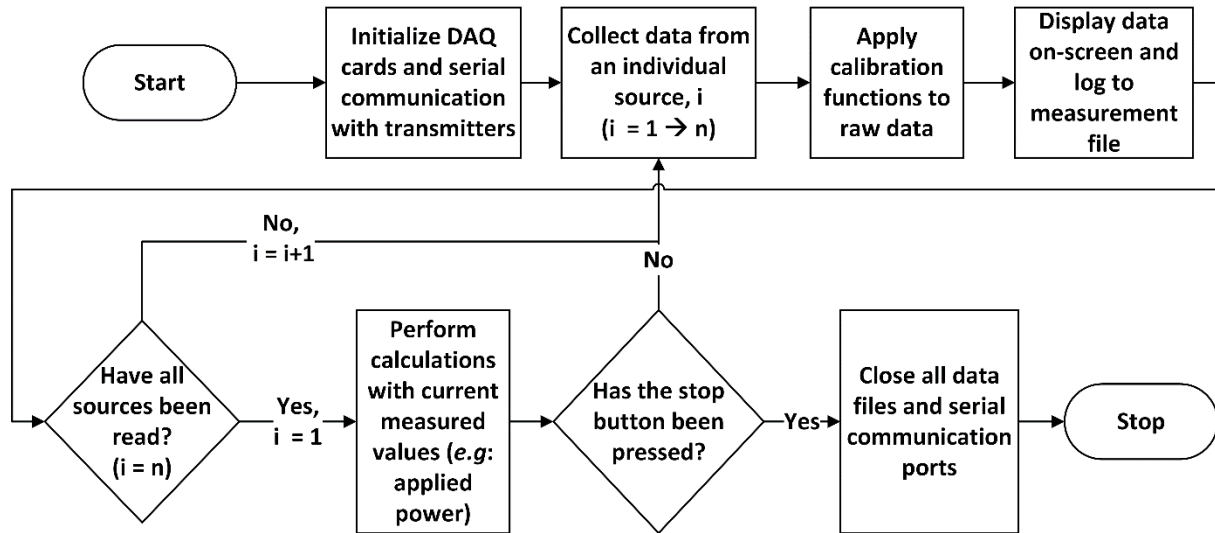
Figure B-7:   Labview code flow diagram.

B.2. Data Acquisition

This section discusses the data acquisition system and LabVIEW program that collects the data during tests. Because it is necessary to accurately measure a wide range of analog potential difference and current flow in this test facility, many separate measurement devices are utilized. NI (National Instruments) makes a system called CompactDAQ, where a chassis has multiple slots for individual measurement modules. They make modules for many different purposes and ranges, with each having a variation in number of channels, sample frequency, and accuracy. The NI measurement chassis and each of the measurement modules is described in the following section, along with schematic diagrams and pin outs for the complete system. The digital signal from the Rheonik mass flow meter are acquired via serial communication. To enable both forms of data acquisition (analog and digital) a dedicated computer was integrated into the test facility, and all signals were acquired and logged with NI LabVIEW (Figure B-7).

For analog signals, a NI cDAQ 9174 chassis was chosen for its 4-slot capacity and USB interface. This system is ideal for the test facility and enables measurement flexibility. Three module units are currently in use: NI 9207, 9221, and 9214. For measuring current and midrange voltage, a NI 9207 employs a 24-bit A/D converter on 16-channels with limits of ±20 mA and ±10 V. For measuring voltage,
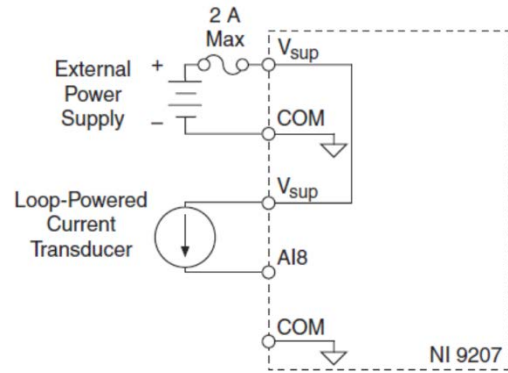
Figure B-8: NI 9207 loop-powered current measurement

the module has an accuracy of ±0.52% of reading and ±0.00416 V from its range. For measuring current, the module has an accuracy of ±0.87% of reading and ±0.011 mA from its range. This module is used to measure pressure transducer output, voltage drop across the shunt resistor, and pyrometer output. The pressure transducers have 4-20 mA output and require 24 V excitation (Figure B-8). Excitation voltage is provided by an Emmerson SOLA 24V DC power supply. The shunt and pyrometer measurements are potential difference measurements between 0-1 V and 0-10 V, respectively. These are also measured by the NI 9207, as shown in Figure B-9 and the pin-out on Table B-1. For larger voltages, a NI 9221 allows +/-60 V over 8-channels at 12-bit resolution, and this module was used for measuring the potential difference across the heater. The accuracy of this module is ±0.25% of reading plus a ±0.156 V offset. This module only allows for single ended voltage measurements. Therefore, the lower side of the heater resistor was connected to the common terminal of this unit as shown in Figure B-10. The pin-out is shown on Table B-2.
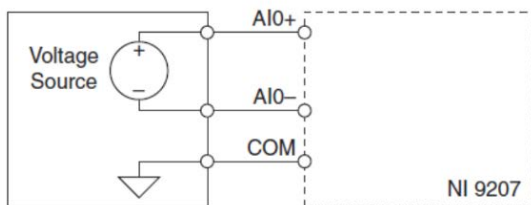
Figure B-9: NI 9207 differential voltage measurement

The NI 9214 module is used to measure temperature. This module measures the small potential difference from the Seebeck effect and converts it into a temperature relative to an internal cold-junction compensation IC component. In high resolution mode, this is the slowest data acquisition step in the system: 52 ms per channel. However, this mode increases the accuracy to ±0.15% of the reading plus ±15 μV (from the instrument range). The resulting accuracy is ±0.37°C for measurements between 0°C and 100°C. Thermocouple wires installed into the module via screw terminals. All thermocouple components were calibrated as a system against a high accuracy Fluke reference standard (±0.0012°C). The pin-out is provided on Table B-3.

Figure B-10: NI 9221 voltage measurement diagram

Table B-1: Pinout for the NI9207 low voltage DAQ module

Input #	Terminals	Location	Manufacturer Calibration #
AI 08	11,30	CH Out	431141
AI 09	12,31	PH In	432909
AI 10	13,32	TS Out High	431110
AI 11	14,33	TS In	432891
AI 12	15,34	TS Diff	436707
AI 13	16, 35	TS Out Low	415397
AI 00	01,20	Shunt Voltage Drop	n/a
AI 01	02, 21	Pyrometer Object	n/a
AI 03	03, 22	Pyrometer Sensor	n/a
Excitation	10,19	24 Vdc	n/a

Table B-2: Pinout for the NI9221 high voltage DAQ module

Input #	Terminals	Description
AI 01	0,9	Supply Voltage

Table B-3:   Pinout for the NI9214 thermocouple DAQ module

Input # & TC Cal #	Location
0	Gear Pump Inlet (Chiller Outlet)
1	Preheater Inlet
2	Preheater Supply
3	Preheater Return
4	Test Section Inlet
5	Test Section Outlet
6	Chiller Return
7	Chiller Supply
12	Pyrometer Surface
13	Ambient
14	PEEK Interface

Finally, for serial communication over an RS232, the Rheonik mass flow transmitter required a custom cable. To communicate with the PC, this required a USB-to-RS232 interface (Prolific, PL2303). For the mass flow meter transmitter, only three connections are required: read and transmit lines and the ground pins. Standard male and female DB9 connectors were used with 20-gauge solid hook-up wire soldered to the appropriate pins. As described in the following section, the flow transmitter also served as an input to autonomously shut off the power supply when the pyrometer temperature increased rapidly during dryout or if the flow rate suddenly dropped.

B.3. Autonomous Protection Circuit

The silicon and glass in the test section have different coefficients of thermal expansion, which, under sufficiently high temperatures, can cause these brittle materials can fail. This condition can occur once the CHF condition is reached or if there is an insufficient cooling fluid flow rate in the test section. To prevent part failure, an autonomous kill switch was designed to continually monitor heater temperature and fluid flowrate and disengage the power supply when needed to prevent part failure. A dedicated Arduino microcontroller is implemented to perform

this function. The auto kill switch interfaces with the power supply via remote sense line as shown in Figure B-11. If the remote sense lines are shorted together, the circuit is closed and the power supply is enabled. The Arduino microcontroller can be programmed to selectively open or close the remote sense
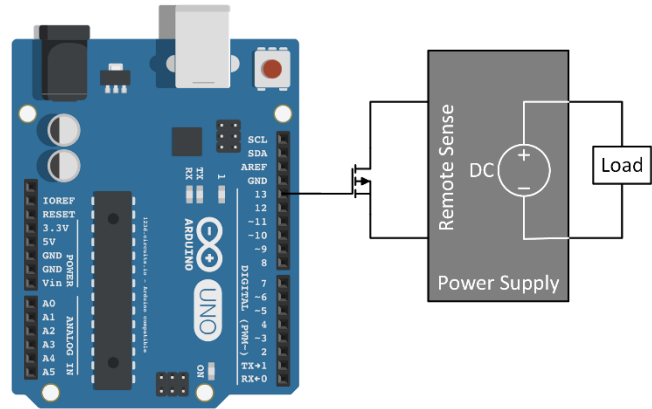
Figure B-11: Arduino to power supply control circuit

circuit by controlling the potential applied to the gate pin. To automatically shut the power supply off if the test section is in danger of failing, the heater temperature and mass flow rate are input from their respective transmitters.

The pyrometer transmitter has programmable low and high alarms that control an onboard relay, and this functionality is employed for communication with the Arduino. A potential of 5 V from the Arduino supply line is connected to one pin of the relay while the other is connected to ground through a 1 MΩ resistor. An analog input pin on the Arduino is also connected to the grounded pin on the controller relay, as shown in Figure B-12. If the measured voltage on the sense pin is sufficiently greater than 0 V, the alarm is tripped causing the relay to open, which deactivates the heater. Using this alarm relay is superior to reading the temperature value because the range can be adjusted on the controller instead of having to modify the operating code to change the
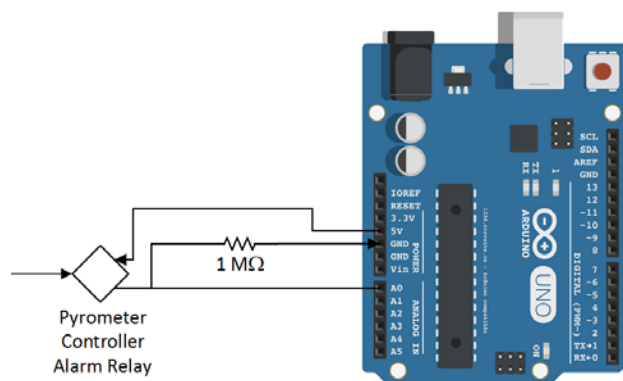
Figure B-12: Pyrometer alarm read circuit

set point. Because the resistance in this circuit is large, the current draw is minimal and the power dissipation is concentrated in the resistor. Therefore, the sense pin read approximately 5 V when the relay is open, which ensures that the signal-to-noise is excellent.

The flow rate of the working fluid is interfaced with the Arduino via a 4-20

Figure B-13:   Coriolis transmitter read circuit.

mA signal output on the Rheonik transmitter. This signal is converted to a potential difference so that it can be monitored by the Arduino microcontroller. This was accomplished by placing a 220 Ω resistor across the output pins and measuring the potential drop across the resistor. The maximum voltage that the Arduino can read is 5 V. At 20 mA current across a 220 Ω resistor, the signal is 4.4 V. The low set point of fluid flow was set to 20% of the target mass flow rate for a given test. The mass flow meter is connected to the Arduino as shown in Figure B-13.

Figure B-14:   Kill button read circuit.

The final shutoff method that was implemented in the auto kill switch is a manual button located near the computer. This button enables the operator to interrupt power to the test section manually. A 5 V potential is held across the normally open button through a 1 MΩ resistor. A digital input pin on the Arduino is connected to this side of the button. The

opposing terminal on the button is grounded, as shown in Figure B-14. When the button is pressed, the circuit is completed, current flows, the sense pin reads low, and the program interrupts power to the heater.

With these circuits, the framework for the Arduino code to automatically interrupt power is in place. The code flow diagram is shown in Figure B-15. Prior to implementation of this system it was tested by turning the power supply to full output power. Turning it on abruptly increases temperature of the heater. This process was repeated 50×, and the auto protect circuit interrupted power before part failure in all cases. The interrupt time was measured via high speed video (240 fps) to be on the order of 300 ms from power on to off. After this implementation, no parts have been damaged from thermal runaway. An image overview of the system and close-up of the Arduino and breadboard circuits are shown in Figure B-16.

Figure B-15: Arduino flow diagram

B.4. Calibration

All instrumentation was calibrated prior to use in the test facility. Many suppliers provided equipment with NIST traceable records of calibration. However, this was not the case for the thermocouples and pyrometer. These were calibrated against a Fluke 5615 platinum resistance device (RTD) with a Fluke 1502A readout that yields a combined accuracy ±0.0012°C. All thermocouples expect the surface mount thermocouples were calibrated in a PolyScience MX7L heated recirculating bath. The surface thermocouples and the pyrometer were calibrated in a

Figure B-16:   Left: Autonomous kill switch overview; Right: Arduino and breadboard circuits.

furnace. The methodology, procedures, and resulting calibration are presented in the following sections.

B.4.1. Process Thermocouple Calibration

The K-type thermocouples used to measure flow processes in the closed loop were calibrated over a nominal range of 5°C to 135°C. This enables accurate measurement over the entire range of expected conditions. During calibration, the temperature was controlled using a PolyScience MX7L heated bath filled with silicone oil. This bath has a temperature stability of ±0.1°C, and continuous recirculation minimizes thermal gradients in the bath.   The Fluke temperature probe and all thermocouples were submersed in the fluid and the bath was covered with a lid. This bath also has an internal coil that can be connected to an external chiller to reduce fluid temperature. During calibration, a PolyScience recirculating chiller was used to decrease the bath temperature down to 5°C, and calibration was conducted in 10°C increments up to 135°C. At each condition, the measurements were allowed to reach steady state (< 1% change in reading over 5 min), and ~100 samples of the temperature measurement were taken for all thermocouple probes over a 2 min period in LabVIEW.

Table B-4:   Summary of thermocouple calibration data

Thermocouple ID	0	1	2	3	4	5	6	7
Slope (m)	0.99	0.99	0.99	0.99	0.99	0.99	0.99	0.99
Intercept (b)	0.21	0.19	0.13	0.17	0.20	0.16	0.17	0.14
Sum Sq. Error (SSE)	77.75	66.88	34.89	55.41	68.44	48.67	49.02	37.68
Sum Exp. Error (SEE)	0.19	0.18	0.13	0.16	0.18	0.15	0.15	0.13
Count [-]	2092	2092	2092	2092	2092	2092	2092	2092
Deg. Freedom [-]	2090	2090	2090	2090	2090	2090	2090	2090
Bias (standard) [C]	0.0012	0.0012	0.0012	0.0012	0.0012	0.0012	0.0012	0.0012
Bias Uncertainty [C]	0.38	0.35	0.26	0.33	0.36	0.31	0.31	0.27

After collecting data, a linear regression was applied to the thermocouple output versus Fluke standard temperature measurement, and the coefficients of determination were near unity in all cases. The uncertainty of the calibration is then calculated as the combination of bias and precision uncertainties. The source of bias is the uncertainty associated with the Fluke standard temperature device, and precision uncertainty emanates from the record data. The bias uncertainty of calibration was determined by the following equation:

$$U_{cal} = \sqrt{U_{std}^2 + 4SEE^2} \tag{B.1}$$

The Sum of Experimental Error (*SEE*) is determined from the linear regression and calibration data as follows:

$$SEE^2 = \frac{\sum_{i=1}^{N}[Y_i - (aX_i + b)]^2}{N - 2} \tag{B.2}$$

For example, the *SEE* for the thermocouple ID 0 (chiller outlet, names given in Table B-3) was 0.193°C and the bias from the standard was 0.0012°C, which yields a calibration uncertainty of ±0.386°C. Table B-4 shows the uncertainties of all of the process flow thermocouples used during the experiments. The range of accuracy is from ±0.26°C to ±0.38°C. The values in this table are

bias uncertainties, and the data taken with these thermocouples will have additional precision uncertainty associated with it, as was demonstrated with a sample calculation in Section 3.4.4.

B.4.2. Surface Thermocouples and IR Pyrometer

The surface thermocouples were used to measure the pyrometer face, PEEK test section interface, and ambient temperatures and the IR pyrometer was used to measure the temperature of heater and surrounding silicon. These sensors were calibrated in a furnace that could achieve a temperature of 210°C. To ensure that thermal gradients in the oven did not affect calibration, a separate set of calibrated surface thermocouples were used as the standard. These T-type surface thermocouples were calibrated against the Fluke temperature reference standard to sufficient accuracy (±0.23°C) using a similar procedure as described in the previous section. Because IR temperature measurement techniques are notorious for sensitivity to environmental factors, a sensitivity study was conducted prior to calibration. In the following discussion, the sensitivity study and the calibration methodology and results are described.

The purpose of the sensitivity study was to show that the pyrometer measurement is statistically invariant to the angle of the sensor relative to the part surface, the distance between the part and sensor, and ambient illumination for the painted surface with a base material of silicon or platinum. To perform this study, a viewport with a sliding cover was added to the furnace door (Figure B-17). This allows direct line-of-sight between the test section and the pyrometer. In addition, a pass through for the Fluke reference probe positioned the temperature standard in contact with the test section. The pyrometer was placed at the correct working distance from the silicon (70 mm) and oriented normal to the part surface. During the sensitivity study, the angle of sensor relative to the surface was varied ±20°, and the distance from part was varied ±12.7 mm. In addition, tests were conducted that compared the measurement with and without ambient lighting

imparted into the furnace enclosure. During each test, the furnace was allowed to achieve steady state conditions (*i.e.*, <1% change in temperature over 5 min), and then the sliding door was opened for 5 sec to allow data collection before closing again. This process was repeated ~5 × per test case. The resulting data is
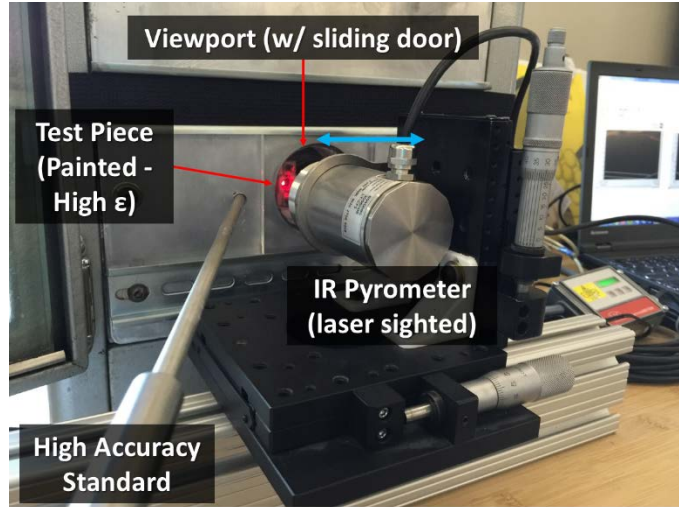
Figure B-17:   Pyrometer and modified furnace.

summarized in Table B-5. The mean difference between the data sets is on the order of 1°C for all test cases, with the deviation from the normal configuration being 0.2°C different in the worst case. The variance for all of these data are very low < 0.07°C, at a 95% confidence level. These tests were conducted at a fixed furnace temperature of nominally 56°C.

To assess the significance of these results, statistical T-tests and an Analysis of Variance (ANOVA) were performed on the data to a significance level of 0.05. It was found that both the T-tests and ANOVA failed to reject the null hypothesis, meaning that the deviation in test groups was not statistically significant at a confidence level of 0.05. This implies that a single calibration curve for the pyrometer in the normal configuration is sufficient for describing its performance in relation to the reference standard. However, it was determined that this result only holds true if the temperature of the pyrometer is held constant; if the temperature of the pyrometer housing changes relative to the calibration, the measurement accuracy is affected. To alleviate this issue, a cooling jacket was fabricated for the pyrometer, and a calibrated surface thermocouple was

placed on the pyrometer face normal to the test section.   A chiller supplied cooling fluid through this cooling coil to hold the pyrometer surface temperature at 20°C (Figure 3-20).

Table B-5:   Pyrometer sensitivity analysis descriptive statistics

Temperature Reference Standard: Fluke 1502A + 5615				
Pyrometer: Micro-Epsilon CTL-1 (emissivity and transmissivity set to unity)				
Description	# Data Sets	Descriptive Stats		
		Mean Difference	Deviation from Normal	Variance
Normal (centered on heater)	9	1.036	0	0.037
Base material (Si vs. Pt)	9	1.115	0.078	0.022
Out of Focus (Close)	4	1.196	0.159	0.023
Out of Focus (Far)	4	1.020	-0.016	0.007
Dark enclosure around	5	1.102	0.066	0.062
Light directly into sensor	5	1.036	-0.001	0.056
CW Angle (~20°)	5	1.237	0.200	0.063
CCW Angle (~20°)	4	1.030	-0.007	0.018

All thermocouples, surface mount and process plug type, were calibrated against the Fluke temperature reference standard. The surface thermocouple with the lowest uncertainty (±0.23°C), was then used as the reference standard for calibrating the pyrometer. This was done because abruptly opening the viewport to the furnace was causing the temperature of the pyrometer to increase, thereby skewing the results. The furnace door was open during the entire calibration procedure, and
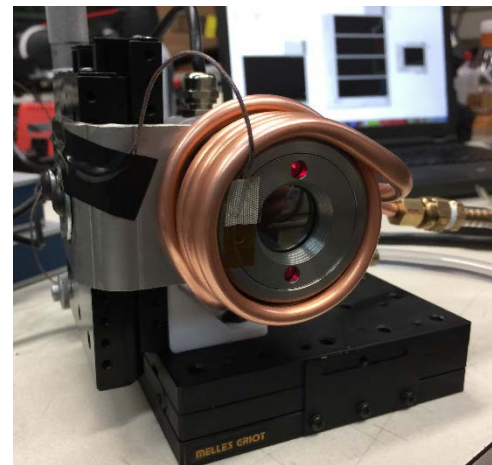
Figure B-18: IR pyrometer with cooling jacket and surface thermocouple.

sufficient flow of cooling fluid to the pyrometer maintained the required 20°C surface temperature. To ensure that the part temperature was known, and not the air around it, as is the case for the Fluke probe, the surface thermocouple was applied to the part, next to the painted surface. The

calibration procedure for the thermocouples is described next, followed by the procedure for the pyrometer.

During calibration of the thermocouples, they were placed in contact with the Fluke calibration standard probe in the furnace, and the viewport was closed for the entire calibration. When calibrating the surface thermocouples, the oven was set to 5 temperature set points: 40.92°C, 81.93°C, 134.9°C, 160.7°C, and 211.5°C. All measurements were allowed to achieve steady state prior to collecting ~100 data points during a 3 minute interval. An additional point at 4.99°C was also added by submerging the thermocouples and the standard in the PolyScience recirculating oil bath with the fluid being cooled by an external chiller. The data was linearly regressed against the Fluke standard RTD to generate the calibration curves. The accuracy of the calibrations is computed in the same manner as in section B.4.1. The surface thermocouple that was utilized in the pyrometer calibration achieved a calibrated accuracy of ±0.233°C.

During calibration of the pyrometer, the silicon test section was painted with high emissivity paint (Figure 3-2) and placed in the furnace with the calibrated thermocouple adhered to the surface (Figure B-19). In addition, the sliding access panel was left open during the entire calibration process to minimize temperature that significantly increase the

Figure B-19: Test section with thermocouple adhered to the silicon surface and place in heated cavity

time to reach steady state. Cooling fluid was circulated through the pyrometer cooling jacket to maintain the surface temperature of 20°C ±0.29°C regardless of the temperature of the furnace.

The pyrometer was calibrated at four temperatures: 30.84°C, 65.95°C, 92.44°C, and 123.1°C. Similar to the surface thermocouples, a fifth point was added by submerging the test section up in silicone oil at 5.04°C in the PolyScience bath. The measurements were allowed to stabilize at each of these conditions and ~100 data points were taken at each temperature. The accuracy of the pyrometer calibration from this process is ±0.671°C, which exceeds manufacturer specified performance (±1°C) and ensures that it correctly accounts for the emissivity of the surface.

APPENDIX C. SAMPLE DATA

In this appendix, the heat transfer and pressure drop correlations use in the current study are given. Each correlation is coupled with a sample calculation. Table C-1 shows the representative data point used for these calculations.

C.1. Heat Transfer Correlations

The heat transfer correlations that were compared to the experimental performance are summarized on Table C-3, Many of the input parameters to these correlations (Reynolds number, heat flux, etc.) are common, and, therefore, these are shown and calculated in Table C-2. The fluid properties are evaluated at the mean pressure between transition and measured outlet pressure (P_m). Because heat spreading is significant, it is assumed that the heat transfer area for these correlations includes the entire two-phase portion (from transition location to the channel exit), which is 2.7 mm for the representative case. The experimentally measured heat transfer coefficient using the methodology from the current work is 35.4 kW m^{-2} K^{-1}.

C.2. Pressure Drop Correlations

The pressure drop correlations that were used in the experimental analysis are summarized on Table C-4 for the same data point summarized on Table 3-6. The single phase properties are evaluated at the mean temperature between inlet and outlet (15.2°C), and the two-phase properties are evaluated at the transition pressure (574 kPa), both were shown on Table 3-6.

Table C-1: Summary of the representative data point

Parameter	Units	Test Point
Length, (L)	mm	2.7
Liquid to vapor transition, relative to center of heater (x_{trans})	mm	-0.20
Mass flow rate ($\dot{m}$)	g min^{-1}	99.8
Pressure, mean ($P_{m} = \left(P_{trans} + P_{TS,out}\right)/2$)	kPa	527
Pressure, test section outlet ($P_{TS,out}$)	kPa	480
Pressure, transition (P_{trans})	kPa	574
Test section heat duty, two-phase ($q_{He,TP}$)	W	58.71
Outlet vapor quality (χ)	%	18.95

Table C-2: Common calculated parameters for heat transfer correlations at the respective data point

Parameter	Units	Sample Value
Boiling number ($Bo = \dfrac{q_{H}^{"}}{Gh_{fg}}$)	-	0.0014
Bond number ($Bd = \dfrac{g(\rho_{l} - \rho_{v})D_{h}^{2}}{\sigma_{l}}$)	-	0.0071
Channel heat flux ($q_{H}^{"} = \dfrac{q_{He,TP}}{N(w_{ch} + 2h_{ch})L_{ch}}$)	W cm^{-2}	39.1
Confinement number ($Co = \sqrt{\dfrac{\sigma_{l}}{g(\rho_{l} - \rho_{v})D_{H}^{2}}}$)	-	11.9
Density, liquid ($\rho_{l} = \rho(P = P_{m}, \chi = 0)$)	kg m^{-3}	1235
Density, vapor ($\rho_{l} = \rho(P = P_{m}, \chi = 1)$)	kg m^{-3}	25.6
Heat of vaporization ($h_{fg} = h(P = P_{m}, \chi = 1) - h(P = P_{m}, \chi = 0)$)	kJ kg^{-1}	185

Table C-2 (Cont.): Common calculated parameters for heat transfer correlations at the respective data point

Parameter	Units	Sample Value
Hydraulic diameter ($D_{\mathrm{H}} = \dfrac{4A_{\mathrm{ch}}}{P_{\mathrm{ch}}}$)	μm	73.4
Martinelli parameter ($X_{\mathrm{vv}} = [\dfrac{\mu_{\mathrm{l}}}{\mu_{\mathrm{v}}}]^{0.5}[\dfrac{1-\chi}{\chi}]^{0.5}[\dfrac{\rho_{\mathrm{l}}}{\rho_{\mathrm{v}}}]^{0.5}$)	-	1.27
Martinelli parameter, Turbulent-Turbulent ($X_{\mathrm{tt}} = [\dfrac{\mu_{\mathrm{l}}}{\mu_{\mathrm{v}}}]^{0.1}[\dfrac{1-\chi}{\chi}]^{0.9}[\dfrac{\rho_{\mathrm{l}}}{\rho_{\mathrm{v}}}]^{0.5}$)	-	0.70
Mass flux ($G = \dfrac{\dot{m}}{NA_{\mathrm{ch}}}$)	kg m^{-2} s^{-1}	1478
Perimeter, fluid ($P_{\mathrm{F}} = 2(w_{\mathrm{ch}} + h_{\mathrm{ch}})$)	m	4.9×10^{-4}
Perimeter, heated ($P_{\mathrm{H}} = w_{\mathrm{ch}} + 2h_{\mathrm{ch}}$)	m	4.45×10^{-4}
Prandtl number, liquid ($Pr_{\mathrm{l}} = Pr(P = P_{\mathrm{m}}, \chi = 0)$)	-	3.43
Prandtl number, vapor ($Pr_{\mathrm{v}} = Pr(P = P_{\mathrm{m}}, \chi = 1)$)	-	0.831
Reduced pressure ($P_{\mathrm{R}} = \dfrac{P_{\mathrm{m}}}{P_{\mathrm{crit}}}$)	-	0.130
Reynolds number, liquid ($Re_{\mathrm{l}} = \dfrac{GD_{\mathrm{H}}}{\mu_{\mathrm{l}}}$)	-	508
Reynolds number, superficial ($Re_{\mathrm{f}} = \dfrac{GD_{\mathrm{H}}(1-\chi)}{\mu_{\mathrm{l}}}$)	-	411
Reynolds number, vapor ($Re_{\mathrm{v}} = \dfrac{GD_{\mathrm{H}}}{\mu_{\mathrm{l}}}$)	-	9338
Thermal conductivity, liquid ($K_{\mathrm{l}} = K(P = P_{\mathrm{m}}, \chi = 0)$)	W m^{-1} K^{-1}	0.087
Thermal conductivity, vapor ($K_{\mathrm{v}} = K(P = P_{\mathrm{m}}, \chi = 1)$)	W m^{-1} K^{-1}	0.014

Table C-2 (Cont.):   Common calculated parameters for heat transfer correlations at the respective data point

Parameter	Units	Sample Value
Velocity, average channel ($\bar{u}_{ch} = \dfrac{\dot{m}}{\rho_l N A_{ch}}$)	m s^{-1}	1.20
Weber, liquid ($We_l = \dfrac{G^2 D_H}{\rho_l \sigma}$)	-	14.4

Table C-3:   Saturated flow boiling microchannel heat transfer coefficient correlations

Author(s) and Conditions	Correlation	Sample Evaluation
Bertsch et al. [11] Compilation of data (3,899 points) over 12 fluids G = 20 – 3000 [kg m^{-2} s^{-1}] D$_h$ = 160 – 2,920 [µm] $q_h^{"}$ = 0.4 – 155 [W cm^{-2}]	$h_{TP} = h_{NB} \cdot (1-\chi) + h_{conv,TP} \cdot [1 + 80 \cdot (\chi^2 - \chi^6) \cdot \exp(-0.6 \cdot Co)]$ $h_{NB} = 55 \cdot Pr^{0.12-0.2 \cdot \log(R_p)} \cdot (-\log(Pr_l))^{-0.55} \cdot M^{-0.5} \cdot (q_H {"})^{0.67}$ $h_{CB} = h_{conv,l} \cdot (1-\chi) + h_{conv,v} \cdot \chi$ $h_{conv,l/v} = (3.66 + \dfrac{0.0668 \cdot \dfrac{D_H}{L} \cdot Re_{l/v} \cdot Pr_{l/v}}{1 + 0.04 \cdot [\dfrac{D_H}{L} \cdot Re_{l/v} \cdot Pr_{l/v}]^{2/3}}) \cdot \dfrac{k_l}{D_H}$	h_{TP} = 25.6 kW m^{-2} K^{-1} h_{NB} = 25.4 kW m^{-2} K^{-1} h_{CB} = 5.00 kW m^{-2} K^{-1} $h_{conv,l}$ = 5.84 kW m^{-2} K^{-1} $h_{conv,v}$ = 1.43 kW m^{-2} K^{-1}
Kim and Mudawar [61] Compilation of data (10,805 data points) over 18 fluids G = 19 – 6,500 [kg m^{-2} s^{-1}] D$_h$ = 190 – 6,500 [µm] $q_h^{"}$ = 0.4 - 155 [W cm^{-2}]	$h_{TP} = \sqrt{h_{NB}^2 + h_{CB}^2}$ $h_{NB} = [2345(\dfrac{P_H}{P_F})^{0.70} P_R^{0.38} (1-\chi)^{-0.51}](0.023 Re_f^{0.8} Pr_l^{0.4} \dfrac{k_l}{D_H})$ $h_{CB} = [5.2(Bo \dfrac{P_H}{P_F})^{0.8} We_l^{-0.54} + 3.5(\dfrac{1}{X_{tt}})^{0.94} (\dfrac{\rho_v}{\rho_l})^{0.25}](0.023 Re_f^{0.8} Pr_l^{0.4} \dfrac{k_l}{D_H})$	h_{TP} = 64.7 kW m^{-2} K^{-1} h_{NB} = 63.1 kW m^{-2} K^{-1} h_{CB} = 14.1 kW m^{-2} K^{-1}

Table C-3 (Cont.): Saturated flow boiling microchannel heat transfer coefficient correlations

Author(s) and Conditions	Correlation	Sample Evaluation
Li and Wu [12] Compilation of data (3,744 data points) $G = 23.4 - 3,750$ [kg m^{-2} s^{-1}] $D_h = 160 - 3,100$ [μm] $q_h^{"} = 1 - 115$ [W cm^{-2}]	$$h_{TP} = 334 Bo^{0.3} (Bd \cdot Re_f^{0.36})^{0.4} \frac{k_1}{D_H}$$	$h_{TP} = 18.8$ kW m^{-2} K^{-1}
Warrier et al. [87] 17 data points FC84 $G = 557 - 603$ [kg m^{-2} s^{-1}] $D_h = 750$ [μm] $q_h^{"} = 0 - 4$ [W cm^{-2}]	$$h_{TP} = E \cdot h_{SP}$$ $$h_{SP} = 0.023 Re_1^{0.8} Pr_1^{0.4} \frac{k_1}{D_H}$$ $$E = 1.0 + 6.0 Bo^{1/16} - 5.3(1 - 855 Bo)\chi^{0.65}$$	$h_{TP} = 35.1$ kW m^{-2} K^{-1} $h_{SP} = 6.51$ kW m^{-2} K^{-1} $E = 5.40$
Agostini et al. [85] 715 points R134a $G = 90 - 295$ [kg m^{-2} s^{-1}] $D_h = 2,010$ [μm] $q_h^{"} = 0.6 - 0.31$ [W cm^{-2}]	$$h_{TP} = 28 q_H^{"2/3} G^{-0.26} \chi^{-0.1} \text{ for x} < 43\%$$ $$h_{TP} = 28 q_H^{"2/3} G^{-0.64} \chi^{-2.08} \text{ for x} > 43\%$$	$h_{TP} = 26.5$ kW m^{-2} K^{-1}
Lazarek and Black [94] 728 points R113 $G = 125 - 750$ [kg m^{-2} s^{-1}] $D_h = 310$ [μm] $q_h^{"} = 1.4 - 38$ [W cm^{-2}]	$$h_{TP} = (30 Re_1^{0.857} Bo^{0.714})(\frac{k_1}{D_H})$$	$h_{TP} = 68.9$ kW m^{-2} K^{-1}

Table C-3 (Cont.):   Saturated flow boiling microchannel heat transfer coefficient correlations

Author(s) and Conditions	Correlation	Sample Evaluation
Tran et al. [95] 296 points R12, R113 $G = 44 - 832$ [kg m^{-2} s^{-1}] $D_h = 2460 - 2920$ [μm] $q_h^{"} = 0.36 - 12.9$ [W cm^{-2}]	$$h_{TP} = 8.4 \times 10^5 (Bo^2 We_l)^{0.3} (\frac{\rho_v}{\rho_l})^{0.4}$$	$h_{TP} = 7.79$ kW m^{-2} K^{-1}
Yu et al. [80] >100 points Water, ethylene glycol $G = 50 - 200$ [kg m^{-2} s^{-1}] $D_h = 2980$ [μm] $q_h^{"} = 5 - 30$ [W cm^{-2}]	$$h_{TP} = 6.4 \times 10^6 (Bo^2 We_l)^{0.27} (\frac{\rho_v}{\rho_l})^{0.2}$$	$h_{TP} = 176$ kW m^{-2} K^{-1}
Ducoulombier et al. [88] 2,710 Points CO$_2$ $G = 200 - 1200$ [kg m^{-2} s^{-1}] $D_h = 529$ [μm] $q_h^{"} = 1 - 3$ [W cm^{-2}]	$$h_{TP} = \max(h_{NB}, h_{CB})$$ $$h_{NB} = 131 P_R^{-0.0063} (-\log_{10} P_R)^{-0.55} M^{-0.5} q^{"0.58}_H$$ $$h_{CB} = [1.47 \times 10^4 Bo + 0.93(\frac{1}{X_{tt}})^{2/3}](0.023 Re_l^{0.8} Pr_l^{1/3} \frac{k_l}{D_H}) \text{ for } Bo > 1.1E\text{-}04$$ $$h_{CB} = [1 + 1.8(\frac{1}{X_{tt}})^{0.986}](0.023 Re_f^{0.8} Pr_l^{0.4} \frac{k_l}{D_H}) \text{ for } Bo < 1.1E\text{-}04$$	$h_{TP} = 133$ kW m^{-2} K^{-1} $h_{NB} = 24.6$ kW m^{-2} K^{-1} $h_{CB} = 133$ kW m^{-2} K^{-1}
Oh and Son [86] ≥ 30 points R22, R134a $G = 100 - 600$ [kg m^{-2} s^{-1}] $D_h = 1,770 - 5,350$ [μm] $q_h^{"} = 0.2 - 1.2$ [W cm^{-2}]	$$h_{TP} = 0.034 Re_f^{0.8} Pr_l^{0.3} [1.58(\frac{1}{X_{tt}})^{0.87}] \frac{k_l}{D_H}$$	$h_{TP} = 15.4$ kW m^{-2} K^{-1}

Table C-4:   Pressure drop correlations

Author(s) and Notes	Correlation	Sample Evaluation
Shah and London [68] Friction factor for ducts	$$\Delta P_{SP} = f \frac{L}{D_H} \frac{\rho_l \bar{u}_{ch}^2}{2}$$ $$f = \frac{96}{Re_l}(1 - 1.355\alpha + 1.9467\alpha^2 - 1.7012\alpha^3 + 0.9564\alpha^4 - 0.2537\alpha^5)$$ $$\alpha = \frac{w_{ch}}{h_{ch}}$$	ΔP_{SP} = 4.53 [kPa] ρ_l = 1243 [kg m^3] $\bar{u}_{ch}$ = 1.19 [m s^{-1}] f = 0.14 α = 0.225
Total two-phase pressure drop	$$\Delta P_{TP} = \Delta P_{TP,f} + \Delta P_{TP,a}$$	ΔP_{TP} = 11.5 [kPa]
Lockhart and Martinelli [81] Two-phase frictional pressure drop	$$\Delta P_{TP,f} = \int_0^\chi 2\phi^2 f G^2 \frac{(1-\chi)^2}{\rho_l D_h} d\chi$$ $$\phi = \sqrt{1 + \frac{C}{X_{VV}} + \frac{1}{X_{VV}^2}}$$ $$C = 2566 G^{0.5466} D_h^{0.8819}(1 - \exp(-319 D_h))$$	$\Delta P_{TP,f}$ = 8.45 [kPa] ϕ = 1.48 C = 0.726
Lee and Garimella [30] (Two-phase accelerational pressure drop) 129 Points Deionized water G = 368 – 738 [kg m^{-2} s^{-1}] D$_h$ = 162 – 571 [µm] $q_h^{''}$ = 0 – 80 [W cm^{-2}]	$$\Delta P_{TP,a} = \frac{G^2}{\rho_l}[\frac{\chi^2}{\alpha_0 \frac{\rho_l}{\rho_v}} + \frac{(1-\chi)^2}{1-\alpha_0} - 1]$$ $$\alpha_0 = [1 + (\frac{1-\chi}{\chi})(\frac{\rho_v}{\rho_l})^{2/3}]^{-1}$$	$\Delta P_{TP,a}$ = 3.02 [kPa] α_0 = 0.76